

Molecular beam epitaxial growth of InSb quantum well heterostructures for applications in topological quantum computing

by

Yinqiu (Peyton) Shi

A thesis
presented to the University of Waterloo
in fulfillment of the
thesis requirement for the degree of
Doctor of Philosophy
in
Physics (Nanotechnology)

Waterloo, Ontario, Canada, 2021

© Yinqiu (Peyton) Shi 2021

Examining Committee Membership

The following served on the Examining Committee for this thesis. The decision of the Examining Committee is by majority vote.

External Examiner: Michael Santos
Professor, Dept. of Physics and Astronomy,
University of Oklahoma

Supervisor(s): Zbigniew R. Wasilewski
Professor, Dept. of Electrical and Computer Engineering,
University of Waterloo

Internal Member: Jan Kycia
Professor, Dept. of Physics and Astronomy,
University of Waterloo

Internal-External Member: Jonathan Baugh
Professor, Dept. of Chemistry,
University of Waterloo

Other Member(s): Dayan Ban
Professor, Dept. of Electrical and Computer Engineering,
University of Waterloo

Author's Declaration

I hereby declare that I am the sole author of this thesis. This is a true copy of the thesis, including any required final revisions, as accepted by my examiners.

I understand that my thesis may be made electronically available to the public.

Abstract

The small effective mass, large Landé g -factor, and strong spin-orbit coupling of InSb make high-quality InSb [quantum well \(QW\)](#) structures particularly appealing for the experimental realization of [Majorana bound states \(MBS\)](#) in the pursuit of topological quantum computing. However, suitable InSb [QWs](#) have not yet been realized owing to outstanding challenges in material development. In this thesis, InSb [QW](#) heterostructures on GaAs substrates have been developed by [molecular beam epitaxy \(MBE\)](#) and optimized to achieve reduced defect densities, smooth surface morphology, and improved transport properties.

Metamorphic buffers consisted of AlSb or GaSb as the first intermediate buffer and ternary AlInSb as the second-stage buffer to bring the lattice constant of the material structure from that of the GaAs substrate to that of the InSb [QW](#) are investigated using a broad range of characterization techniques. The optimization of the [interfacial misfit \(IMF\)](#) growth mode for the GaSb buffers is presented. We further report an effective dislocation filtering by the $\text{Al}_x\text{In}_{1-x}\text{Sb}/\text{Al}_y\text{In}_{1-y}\text{Sb}$ interlayer buffers. InSb [QW](#) structures with a [threading dislocation density \(TDD\)](#) of $\sim 1 \times 10^8 \text{ cm}^{-2}$ have been achieved, tolerable for [MBS](#) devices.

Hillock-decorated surface morphologies on different buffers have been studied under various growth parameters and also as a function of GaAs (001) substrate offcut angle. A toy model to demonstrate the offcut-dependent morphological transitions is discussed. The optimal substrate offcut angle for a hillock-free surface was found, which has also been shown to suppress the [micro-twins \(MT\)](#) formation. On GaAs (001) substrates with a 0.55° offcut towards $[\bar{1}10]$ direction, we have successfully grown hillock-free, [MT](#)-free, and atomically smooth InSb [QW](#) heterostructures.

The magneto-transport properties of InSb [QWs](#) are studied with samples fabricated in either [van der Pauw \(vdP\)](#) or hall bar geometries. The optimization of the doping profile and the study on the effect of the buffer structures are presented for the structures with a standard [high-electron-mobility transistor \(HEMT\)](#) active region. We also present a comprehensive study on the parallel conduction and reproducibility problems accompanying the growth of the InSb [QW](#) heterostructures. The development of InSb [QW](#) structures in an inverted [HEMT](#) design achieved through either modulation doping or a Si-doped back gate is presented. First InSb true surface [QW](#) structures are reported and the top gate-ability on which has also been demonstrated with a HfO_2 gate dielectric.

Acknowledgements

I would like to express my sincerest gratitude to who made this thesis possible. First, I especially would like to thank my supervisor, Prof. Zbig Wasilewski, for his continual guidance, support and encouragement throughout the duration of my Ph.D. program. I have been constantly feeling inspired by his enthusiasm towards science, extensive knowledge and experience, as well as his considerate kindness. I am grateful to have Prof. Jonathan Baugh as the collaborator for my PhD project and one of my committee members, who has provided invaluable insights and guidance for my research. Many thanks are owed to my other two committee members, Prof. Jan Kycia and Prof. Dayan Ban, whose generous help have been indispensable for me to complete my Ph.D. program. I extend my thanks to Prof. Michael Santos for acting as my external examiner and all those enjoyable encounters and discussions at conferences.

I also would like to thank all the members involved in the Majorana project for their great contributions to the project and all the fruitful discussions. Thanks are especially owed to Emma (Annelise) Bergeron and Dr. Francois Sfigakis, who have offered extensive help on the sample fabrication and measurements. I would like to thank every member I have worked with in the QNC-MBE group for all his/her time and contribution in maintaining and continuously improving the lab and making even the most nasty troubleshooting a enjoyable experience. I would especially like to thank Dr. Denise Gosselink, our former lab manager, and Chis Deimert, Ph.D student and our current lab coordinator, for their generous help. I owe my gratitude to all the staff members and students who helped me using the many characterization tools involved in my project. In particular, I would like to thank Dr. Nina Heinig and Dr. Lei Zhang for their help with SEM and STEM studies, Dr. Sandra Gibson for her help with AFM analysis.

I further would like to thank my husband, Ziwei Ding, for his unending love, patience and understanding. Without him, it would have been impossible for me to walk through this long Ph.D. journey, not even mentioning while being well fed and happy. I would also like to express my gratitude to my parents who have been giving me love, care and support more than I could have ever imagined. Special thanks are extended to my friends at Waterloo, my Canadian family, for their love, support and all the great times we have spent together.

Dedication

This is dedicated to my husband, Ziwei Ding, and our deceased rabbit, Nala.

Table of Contents

List of Figures	xii
List of Tables	xxi
List of Abbreviations	xxiii
1 Introduction	1
1.1 Motivation	1
1.2 Outline	3
2 Crystals and epitaxial growth	5
2.1 Crystal structure	5
2.2 Basics of Crystal defects	7
2.2.1 Types of defects	7
2.2.2 Burgers vectors and movement of dislocations	9
2.3 Crystal growth	11
2.3.1 Fundamental theories	11
2.3.2 Surface kinetics	12
2.3.3 Crystal morphology	14
2.4 Epitaxial growth	15
2.4.1 Pseudomorphic epitaxy	15
2.4.2 Generation of misfit dislocations	16
2.4.3 Sources of threading dislocations in III-Vs	20

3	Electronic properties of semiconductors	23
3.1	Semiconductors: some basic concepts	23
3.1.1	Band theory	23
3.1.2	Heterostructure	25
3.1.3	Two-dimensional electron gas	26
3.1.4	Modulation doping	27
3.1.5	Length scales in quantum transport	28
3.2	Magnetotransport	29
3.2.1	Classical Hall effect	30
3.2.2	Landau Quantization	32
3.2.3	Shubnikov de-Haas oscillations	33
3.2.4	Integer quantum Hall effect	35
3.3	Majorana devices	37
3.3.1	Majorana bound states and topological quantum computing	37
3.3.2	Systems hosting Majorana modes	38
3.3.3	Ingredients for the Rashba nanowire model	39
4	Experimental setup	42
4.1	Molecular beam epitaxy	42
4.1.1	GEN10™ MBE system	42
4.1.2	Ultra-high vacuum environment	44
4.1.3	Material beams	46
4.1.4	Substrate mounting	48
4.2	<i>In-situ</i> monitoring	49
4.2.1	Reflection high-energy electron diffraction (RHEED)	50
4.2.2	Desorption mass spectrometry (DMS)	54
4.2.3	Substrate temperature monitoring	55
4.3	<i>Ex-situ</i> characterization	60

4.3.1	Nomarski differential interference contrast (DIC) microscope . . .	60
4.3.2	Atomic force microscopy (AFM)	60
4.3.3	Scanning electron microscopy - electron channeling contrast imaging (SEM-ECCI)	61
4.3.4	Scanning transmission electron microscopy (STEM)	62
4.3.5	Defect selective etching (DSE)	62
4.3.6	Secondary ion mass spectrometry (SIMS)	63
4.3.7	High-resolution x-ray diffractometry (HD-XRD)	63
4.4	Transport characterization	69
4.4.1	Hall measurements	69
5	Minimizing the defect densities	73
5.1	Challenges and buffer designs	73
5.2	Defect characterization	75
5.2.1	Atomic force microscopy (AFM)	76
5.2.2	Scanning electron microscopy - electron channeling contrast imaging (SEM-ECCI)	77
5.2.3	Defect selective etching (DSE)	79
5.3	Interfacial misfit (IMF) growth mode	80
5.3.1	A literature review	80
5.3.2	The observed RHEED patterns	82
5.3.3	Factors affecting the growth mode	85
5.3.4	Effectiveness of the technique	90
5.4	Dislocation filtering by Interlayers	92
5.5	Conclusions	95

6	Improving the surface morphology	97
6.1	Threading dislocation mediated surface morphology	97
6.2	Surface hillocks on antimonides/GaAs and their disadvantages	98
6.3	Influence of growth conditions	101
6.4	Effect of substrate offcut	106
6.5	Conclusions	113
7	Magneto-transport Analysis	115
7.1	InSb QW standard structure	115
7.1.1	Doping profile	116
7.1.2	Effect of buffer structures	119
7.1.3	Variations in growth conditions	122
7.1.4	Issues with parallel conduction and growth reproducibility	125
7.2	InSb QW inverted structure	127
7.2.1	Structures with modulation doping	127
7.2.2	Structures with back gates	132
7.2.3	Top gate-ability	135
7.3	Conclusions	136
8	Summary and outlook	139
8.1	Summary	139
8.2	Future work and outlook	142
	Letters of Copyright Permission	144
	References	151
	APPENDICES	164

A	Device fabrication	165
A.1	van der Pauw	165
A.2	Hall-bar	165
B	Supplementary transport data	171

List of Figures

2.1	Schematic drawing for (a) face-centered cubic (fcc) (a) zinc-Blende crystal structures. Examples of a (111) plane and one [110] direction are shown in (a). Atoms of the two different elements are represented by different colors in (b).	6
2.2	(a) Burgers circuits around (a) an edge dislocation and (b) a left-handed screw dislocation, also with the same circuits in a perfect crystal, depicting the Burgers vectors. [Adapted from [29] with permission]	8
2.3	Plastic deformation by the glide of (a) edge and (b) screw dislocations under the shear stress.	10
2.4	Schematic drawing to illustrate the surface kinetic processes during crystal growth, including impingement, evaporation, and surface migration of atoms on the surface, as well as atoms attaching to step and kink sites either from upper or lower terraces and formation of 2D nuclei on the terraces.	12
2.5	Schematic illustration for (a) the Ehrlich–Schwoebel effect with the adatom potential energy profile and (b) the knock-out effect. The atoms represented in cubes. The light gray atoms in (a) are moving along the surface with potential bonds with nearest neighbors depicted by dashed lines and the dark gray atoms are attached to the surface with bounds represented by solid lines to the nearest neighbors. The light gray atom in (b) is being freshly deposited towards the surface.	14

2.6	The generation of a misfit dislocation (MD) segment at the epilayer interface from a threading dislocation (TD) that is initially extended from the lower layer to the upper layer. The thick continuous and thick dashed lines represent the intersection of the ($\bar{1}11$) slip plane with the top surface of the upper layer and the bottom surface of the lower layer respectively. The thick dotted line is the intersection of the ($\bar{1}11$) slip plane with the interface of the two layers. The fine continuous line is the dislocation line with its burgers vector F_ϵ is the force exerted by the misfit strain and F_l is the tension in the dislocation line. [Adapted from [47] with permission]	17
2.7	The schematic drawing of the nucleation and glide of 60° dislocation half loops on the 111 plane and the generation of 60° misfit segment at the interface between the GaAs layer and the Si substrate. [Adapted from [49] with permission]	18
2.8	Schematic diagram showing the strain relaxation of an island on the surface by the introduction of MDs at its edges. [Adapted from [54] with permission]	20
3.1	(a) The band structure of InSb calculated using the pseudo-potential method. (Adapted from Chelikowsky and Cohen [75] with permission). The band indices are represented by the number in the subscript. (b) The first Brillouin zone of a fcc lattice showing the corresponding representations for the high symmetry lines and points in (a).	24
3.2	Density of states for 3D, 2D, 1D and 0D systems. [Adapted from [77] with permission]	27
3.3	The basic setup for classical Hall effect.	31
3.4	The evolution of the two-dimensional electron gas (2DEG) density of states (top) and the corresponding ρ_{xy} and ρ_{xx} curves (bottom) as the magnetic field increases from (a) to (e).	34
3.5	(a) Graphic illustration of the energy level bending higher at the edge of the sample. The extended bulk and edge states as well as the localized bulk states which lie in the gaps of the extended bulk states are also included in the drawing. (b) The electrostatic potential landscape of the sample as well as the chirality of the edge states and the impurity states. The equipotential lines at the edge of the samples are open and hence the edge states are extended states. The charged impurity states are localized as their equipotential lines are closed.	35

3.6	(a) Experiment setup for the Rashba nanowire model. (b-f) The energy spectrum of a Rashba nanowire generated using the kwant Python package [87], demonstrating the process of its topological phase transition controlled by the four ingredients given in the model.	41
4.1	The schematics of the front and back views of the growth module (GM) of the GEN10™ molecular beam epitaxy (MBE) system at the University of Waterloo. The part of the substrate manipulator that is inside the GM is represented in a gray shade. This diagram is modified based on the GM figure in the system manual provided by Veeco Instruments Inc. [88]. . .	44
4.2	Schematic overview of the stacking sequence of the cleaved substrate, retainer plates, and securing ring on the full 3" substrate holder for (a) the normal mounting and (b) the sapphire plate mounting configuration. . .	49
4.3	(a) The wafer polishing-induced surface bowing at the edge of the substrate. (b) Cross-section along the solid line in (a). Surface morphology at positions close to the edge on the front polished side of the wafer (region indicated by a black curve) are studied as a function of substrate offcut angle.	50
4.4	Schematics of both the (a)side view and (b) top view of the reflection high-energy electron diffraction (RHEED) diffraction geometry and the Ewald sphere construction [adapted from [89] with permission].	51
4.5	RHEED diffraction patterns acquired during growth of the AlInSb and InSb layers at different substrate temperatures and group V/III flux ratios as specified in (a)-(d).	53
4.6	The partial pressure of Sb measured by Inficon residual gas analyzer (RGA) during a typical deposition process of an AlSb layer.	55
4.7	Schematic illustration for the substrate mounting configuration used for the calibration of integrated spectral pyrometry (ISP) with the GaAs substrate exposed in only a small opening enclosed by the Mo plate and the InAs substrate.	58
4.8	(a) The schematic overview of a typical InSb quantum well (QW) heterostructure and (b) the plot of the substrate temperature measured by the thermocouple (T_c), band-edge thermometry (BET), and ISP during the growth with the four growth stages indicated in (a).	59

4.9	Rotation and translation axes enabled by the Jordan Valley QC3 diffractometer	64
4.10	A schematic of the Ewald sphere in the reciprocal space defined by the diffraction conditions for a (001) orientated single-crystal material. The light area represents the area from which a diffraction spot is physically possible for the machine and the hatched regions are not accessible due to the limited range of the diffractometer in use. The orange dash line represents a rocking curve. The blue solid lines together constitute an reciprocal space map (RSM) with each one of the lines representing a coupled scan.	66
4.11	Symmetric and asymmetric RSMs of a typical InSb heterostructure studied in this thesis with the main layer peaks labeled.	69
4.12	Circuit diagram of the 1/10 000 voltage divider used in the gate measurements in the pin-off regime. The resistance of the shunt resistor (10Ω in this case) must be much less than the resistance of the sample R_{DUT}	70
4.13	Schematic diagram of the (a) van der Pauw and (b) Hall bar geometries used in this study.	71
5.1	Bandgap energy versus lattice constant of various III-V semiconductors at room temperature (Reprint from Schubert (adopted from Tien, 1988)[107]	74
5.2	Schematics of the buffer structures consisted of a first intermediate buffer of either kind (a) or (b) and a second-stage buffer of design (c) or (d). . . .	75
5.3	Atomic force microscopy (AFM) images of buffers with a different number of interlayers (N) on GaAs (001) substrates as well as their surface hillock density (HD)s and threading dislocation density (TDD)s. The white ellipse in (c) shows a signature of micro-twins (MT)s observed on all buffers. . .	78
5.4	AFM images of $1 \times 1 \mu\text{m}^2$ of the N=3 buffer showing the step insertions on the hillock sidewalls in both (a) [110] and (b) $[1\bar{1}0]$ directions.	79
5.5	scanning electron microscopy (SEM)-electron channeling contrast imaging (ECCI) images revealing the TDs (examples pointed by two thin arrows in (c)) and MTs defects (examples indicated by two ellipses) on the (a) N = 0, (b) N = 1, and (c) N = 3 buffers, with their TDDs quoted. Two TDs with opposite signs are indicated by two circles with thick black-white arrows above representing the opposite directions of the dark-light contrasts. . .	79

5.6	Nomarski differential interference contrast (DIC) optical images of the N = 3 buffer surface after subsequent diluted sirtl-like mixture with light (DSL) etching for (a) 15s and (b) additional 15s. The second etching results primarily in the enlargement of the existing pits. Several new pits can also be detected. The quoted threading etch pit density (EPD) in the image is measured from the square-shaped etch pits.	81
5.7	RHEED pattern observed on GaAs surface at different substrate temperatures as cooling down from 590 °C to 450 °C under no fluxes	83
5.8	The RHEED patterns of the Sb-terminated GaAs surface under different conditions as specified.	84
5.9	The SEM-ECCI images of the GaSb interfacial misfit (IMF) buffers grown at different growth conditions and additional treatments as specified as well as the RHEED patterns during the island formation stage for the GaSb IMF buffer growths in (a)-(d). The RHEED patterns for (e)-(h) are similar to their corresponding ones above, i.e, (a)-(d) respectively. The growth number and the counted TDD for each growth is indicated in its SEM-ECCI image.	87
5.10	The schematics of the InSb QW structures for (a) G0637 with a 100nm AlSb buffer and (c) G0792 with a 600nm GaSb buffer instead. The two structures share the same QW region and the only difference between them is the first intermediate buffer as highlighted in light gray. The characterization of TDD using SEM-ECCI for the structures in (a) and (c) are shown in (b) and (d) respectively.	91
5.11	The cross-sectional scanning transmission electron microscopy (STEM) image of the buffer structure with 3 interlayers (N = 3). Each layer of the buffer is indicated to the right of the image. The dislocations are identified as the white lines, many of which are observed to stop at the interlayer interfaces.	93
5.12	The schematics of the InSb QW structures for (a) G0637 with a single-composition buffer and (c) G0704 with an interlayer buffer. The two structures share the same QW region and the only difference between them is the second-stage buffer as highlighted in gray. The characterization of TDD using SEM-ECCI for the structures in (a) and (c) are shown in (b) and (d) respectively. Note that the ECCI image in (a) is the same as the one shown earlier in Figure 5.10(b) and is simply presented here again for easier comparison with (d).	94

6.1	Schematic illustration of the surface spirals as a result of (a) one single dislocation with a screw component; (b) a pair of dislocations of opposite signs; (c) a pair of dislocations of similar signs and (d) a group of dislocations of similar signs, as predicted by the Burton, Cabrera, and Frank (BCF) theory (adapted from the BCF paper, 1951 [40])	98
6.2	5×5 and 1×1 μm ² AFM images showing the morphological features of spiral hillocks on (a) AlSb of 1 μm thick on GaAs substrate; (b) GaSb of 600 nm thick on GaAs substrate; and (c) Al _{0.12} In _{0.88} Sb of 1 μm thick grown on top of a 1 μm AlSb layer on GaAs substrate	99
6.3	1×1 μm ² AFM image showing different forms of hillocks due to their interactions with each other on an AlSb surface. The spiral steps of some hillocks are highlighted for easy comparison to the predictions in Figure 6.1.	100
6.4	AFM height scans of 10×10 μm ² (up) and 1×1 μm ² (down) in size showing the surface morphology of AlSb buffers grown at (a) 500 °C and (b) 550 °C using thermal oxide desorption; (c) 550 °C and (d) 600 °C using Indium assisted oxide desorption.	102
6.5	AFM height scans of 5×5 μm ² (up) and 1×1 μm ² (down) in size showing the surface morphology of GaSb buffers grown at (a) 400 °C, (b) 450 °C and (c) 510 °C.	103
6.6	Nomarski and 1×1 μm ² AFM images showing the surface morphology of Al _{0.1} In _{0.9} Sb buffers grown at (a) 350 °C, (b) 380 °C and (c) 420 °C.	104
6.7	20×20 μm ² (up) and 1×1 μm ² (down) AFM images of (a) 2 μm-thick and (b) 12 μm-thick Al _{0.12} In _{0.88} Sb buffers grown at 420 °C under the same growth conditions on AlSb nucleation buffers on GaAs (001) substrates.	105
6.8	5×5 and 1×1 μm ² AFM images showing (a) the transition of the surface morphology of the AlSb layer on GaAs (001) substrate with offcut angle increasing from 0° to 1.68° in [110] direction at the very edge of the wafer, and (b) the surface morphology of AlSb layer grown directly on GaAs (001) substrate with 2°-offcut towards [110] direction.	108

6.9	(a) Nomarski and (b) AFM images of $20 \times 20 \mu\text{m}^2$ and $1 \times 1 \mu\text{m}^2$ in size showing the transition of the $\text{Al}_{0.12}\text{In}_{0.88}\text{Sb}$ surface morphology as a function of the effective substrate offcut angle at the edge of the wafer. The approximate AFM scan positions in (b) are indicated by label (ii)-(v) in (a) correspondingly. The effective offcut are calculated using the $1 \times 1 \mu\text{m}^2$ AFM images. The insert in (b) panel (v) is a magnified view to show the step-bunching effect.	109
6.10	Graphic illustration of the growth mechanism that results in a morphological transition with increasing substrate offcut angle. The black curves are surfaces parallel to the substrate. The medium gray regions represent the hillocks formed on the surface. The light gray and dark gray regions are the ‘suppressed parts’ and the ‘over-suppressed parts’ of the hillocks, respectively. Hillock-free and smooth surface can be achieved when the substrate offcut angle agrees with the hillock sidewall angle.	111
6.11	The Surface morphology of the InSb QW under Nomarski at (a) the center and (b) the edge of the wafer. The insert in (a) shows a dramatic illustration of the side-view of the InSb QW structure. Label (ii)-(vi) in (b) corresponds to the approximate positions of the AFM scans in Figure 6.12.	112
6.12	$20 \times 20 \mu\text{m}^2$ and $1 \times 1 \mu\text{m}^2$ AFM images showing the transition of the InSb surface morphology as a function of effective substrate offcut angle. The insert in the panel (vi) is a magnified view to show the step-bunching effect. The approximate AFM scan positions are indicated by label (ii)-(vi) in Figure 6.11(a) correspondingly.	112
6.13	The surface morphology of InSb QW grown on the GaAs offcut substrate observed with (a) Nomarski microscope at the center of the wafer and $20 \times 20 \mu\text{m}^2$ and $1 \times 1 \mu\text{m}^2$ AFM scans both (b) at the center and (c) at the edge of the wafer. The insert in (c) is a magnified view to show the step-bunching effect, similar to that in Figure 6.9(b) panel (v) and Figure 6.12 panel (vi).	113
7.1	(a) Schematic overview of the active region for InSb QW standard structures with a single Si δ -doping layer and (b) The mobility as a function of carrier density at 1.4 K for the InSb QW standard structures listed in Table 7.1 except for G0721c.	116

7.2	The Longitudinal (ρ_{xx} , left axis) and transverse (ρ_{xy} , right axis) resistivity as a function of magnetic field B at T = 1.4 K for (a) G0597, (c) G0602 and (d) G0637. (b) The weak anti-localization effect measured at B = 0 T in G0597 which was also observed with the other standard InSb QW structures.	120
7.3	The Longitudinal (ρ_{xx} , left axis) and transverse (ρ_{xy} , right axis) resistivity as a function of magnetic field B at T = 1.4K for (a) G0692 and (b) G0704, both showing parallel conduction.	121
7.4	The longitudinal (ρ_{xx} , left axis) and transverse (ρ_{xy} , right axis) resistivity as a function of magnetic field B at T = 1.4K for (a) G0729, (b) G0730 and (c) G0735.	124
7.5	(a) The Longitudinal (ρ_{xx} , left axis) and transverse (ρ_{xy} , right axis) resistivity as a function of magnetic field B at T = 1.4K for G0742. The fitting to the slope of the Hall resistance (b) in the low field range for determination of the 2DEG carrier density and (c) in the high field range for determination of the total carrier density.	125
7.6	The Longitudinal (ρ_{xx} , left axis) and transverse (ρ_{xy} , right axis) resistivity as a function of magnetic field B at T = 1.4K for (a) G0736, (b) G0746 and (c) G0747, all showing parallel conduction.	126
7.7	(a) Schematic overview of the InSb QW active region for the inverted structures with five Te δ -doping layers. (b) The mobility as a function of carrier density at 1.4 K for all the conductive inverted InSb QW structures are listed in Table 7.2. The inset at the bottom right corner is a plot of the longitudinal resistivity ρ_{xx} (left axis) and the transverse resistivity ρ_{xy} (right axis) as a function of magnetic field B at T = 1.4 K for G0414, which serves as a representative of the magneto-transport data for all the samples in this plot. Additional data can be found in Appendix B.	129
7.8	nextnano++ simulation results of (a) G0414 and (b-d) the possible modifications in the G0414 structure with the doping densities adjusted accordingly to achieve single-channel conduction at the InSb QW in the structure. The conduction band edge is represented by a solid blue line and the Fermi level is fixed at 0eV as shown by an orange solid line. The distribution of the electron densities in the structure is depicted by a gray dashed line.	131
7.9	The schematics of the back-gated InSb QW structures	133
7.10	The secondary ion mass spectrometry (SIMS) spectra measured for G0797.	134

7.11	Carrier density of G0414 as a function of top gate voltage sweeping from -1 V to +0.8 V and back that show minimal hysteresis in the gating [Adapted from the E. Bergeron' s MSc thesis [94]].	135
8.1	Reuse and permissions license for Figure 2.2.	145
8.2	Reuse and permissions license for Figure 2.6 and Figure 2.8.	146
8.3	Reuse and permissions license for Figure 2.7.	147
8.4	Reuse and permissions license for Figure 3.1a.	148
8.5	Reuse and permissions license for Figure 3.2.	149
8.6	Reuse and permissions license for Figure 4.4.	150
A.1	Schematic illustration of the step-by-step process of Ohmic contact definition, demonstrating the advantageous of the undercut features on the photo-resist sidewalls.	167
A.2	Schematic diagram showing the 45° deposition of Ti/Au making contact with the sidewalls of the QW in the etched region, where the populated 2DEG is indicated by a dashed line.	169
A.3	Schematic diagram showing a finished Hall bar device for a structures with a backgate layer.	170
B.1	Plot of the longitudinal resistivity ρ_{xx} (left axis) and the transverse resistivity ρ_{xy} (right axis) as a function of magnetic field B at T = 1.4 K for (a) G0381mid, (b) G0383mid, and (c) G0387mid.	171

List of Tables

5.1	A summary of the GaSb interfacial misfit (IMF) buffer growths with different surface preparation methods, various substrate temperatures to initiate the Sb soak, diverse growth conditions, and other applied growth techniques. "A-E" and "A-D" stand for the "anion exchange" and "As desorption" surface preparation methods receptively. "PG-A" and "I-A" stand for other applied growth techniques of "post-growth annealing" and "inserted annealing", respectively.	85
7.1	A summary of the growths of InSb quantum well (QW) standard heterostructures with varying Al compositions x and doping densities n_d , different buffer structures as well as diverse growth conditions, which include the substrate temperature T_s and the group V/III ratio. The number before and after the ' $'$ ' are for the $\text{Al}_x\text{In}_{1-x}\text{Sb}$ metamorphic buffer and the InSb QW active region respectively. Buffer structures labeled by 'G' 'A' 'S' 'T' refer to GaSb, AlSb, single composition, and interlayer AlInSb buffers as shown in Figure 5.2(a)-(d) respectively. The measurement geometry (either Hall bar (HB) or van der Pauw (vdP)) as well as the measured low magnetic field electron mobilities μ and charge carrier densities n_e are included in the table for all the conducting wafers, except for G0597, the mobility and density were not measured (as denoted by not available (N/A)). G0617 was non-conducting (N.C.). The 'c' and 'e' following the growth number indicate the sample cleaved from the center and the edge respectively. If not specified, a central piece was measured.	117

7.2	<p>A summary of the InSb surface QW growths using the modulation doping approach with their corresponding low magnetic field electron mobilities μ and charge carrier densities n_e. The materials used for the cap layer are listed. The doping densities n_d was estimated based on the location of the cleaved sample on the wafer. The term ‘hi’ ‘mid’ or ‘low’ behind the growth numbers are used to indicate that the sample is cleaved from a high, mid or low doping area, respectively. All growth except G0414 has a gradient doping density for each δ-doping layer. ‘eqw’ is short for etched quantum well. The material used for the cap layer is also listed. For G0414eqw, the InSb cap was etched away as represented with an additional pair of round brackets.</p>	128
7.3	<p>A summary of the growths of InSb QW back-gated structures with varying Si-doping densities n_d for the back-gate layer, Al composition x in the $\text{Al}_x\text{In}_{1-x}\text{Sb}$ barrier layer and thickness of the $\text{Al}_x\text{In}_{1-x}\text{Sb}$ spacer, as well as the corresponding two-dimensional electron gas (2DEG) isolation to the back gate $R_{2deg-bg}$ in the structure.</p>	133

List of Abbreviations

- 2DEG** two-dimensional electron gas [xiii](#), [xix](#), [xx](#), [xxii](#), [2](#), [26–29](#), [33](#), [34](#), [115](#), [116](#), [118–120](#), [122](#), [124](#), [125](#), [127–130](#), [132–134](#), [136](#), [137](#), [142](#), [169](#)
- AFM** atomic force microscopy [xv](#), [xvii](#), [xviii](#), [60](#), [61](#), [76–80](#), [90](#), [92](#), [95](#), [96](#), [98–100](#), [102–113](#), [139](#), [140](#)
- ALD** atomic layer deposition [135](#), [166](#)
- AsB** angle-selective backscatter [61](#)
- BCF** Burton, Cabrera, and Frank [xvii](#), [14](#), [97–100](#), [103](#), [107](#), [113](#)
- BCS** Bardeen-Cooper-Schrieffer [38](#)
- BdG** Bogoliubov-de Gennes [38](#)
- BEP** beam equivalent pressure [47](#), [48](#)
- BET** band-edge thermometry [xiv](#), [56–59](#), [83](#), [122](#), [123](#)
- BFM** beam flux monitor [47](#), [48](#)
- BOE** buffered oxide etch [166](#), [167](#)
- BSE** back-scattered electrons [61](#), [77](#)
- CCD** charge-coupled device [50](#)
- CCW** counter-clockwise [29](#)
- CT** cluster tool [42](#), [43](#)

CW clockwise 29

DIC differential interference contrast [xvi](#), 60, 63, 81, 95

DMS desorption mass spectrometry 54

DOS density of states 26, 27, 33, 37

DSE defect selective etching 62, 63, 79, 80, 95, 139

DSL diluted sirtl-like mixture with light [xvi](#), 63, 79, 81

EBSD electron back-scatter diffraction 61

ECCI electron channeling contrast imaging [xv](#), [xvi](#), 61, 77–80, 85–95, 139, 140

EP etch pit 63, 79, 80

EPD etch pit density [xvi](#), 80, 81, 95

ES Ehrlich–Schwoebel 104, 105, 110

fcc face-centered cubic [xii](#), [xiii](#), 6, 7, 10, 11, 19, 24, 52

GM growth module [xiv](#), 42–45, 54, 57, 89

HAADF high-angle angular dark-field 62

HB Hall bar [xxi](#), 117

HD hillock density [xv](#), 78, 95

HD-XRD high-resolution x-ray diffractometry 48, 63, 68, 75, 76, 90, 96, 125

HEMT high-electron-mobility transistor [iv](#), 2, 115, 127, 139, 142

HV high vacuum 44, 45

HVP heated view ports 56, 57

IMF interfacial misfit [iv](#), [xvi](#), [xxi](#), 3, 21, 80–83, 85–90, 95, 96, 120, 136, 140, 142

IOD In-assisted oxide desorption 101

IQHE integer quantum Hall effect 35

ISP integrated spectral pyrometry xiv, 57–59, 122, 123

LL load lock 42, 43, 48

MBE molecular beam epitaxy iv, xiv, 1–3, 14, 42–50, 55, 56, 59, 60, 71, 90, 96, 103, 107, 109, 126, 139, 140

MBS Majorana bound states iv, 1–3, 37, 115, 139, 142, 143

MD misfit dislocation xiii, 16–22, 73, 80–83, 87

MOCVD metal-organic chemical vapor deposition 82, 107

MT micro-twins iv, xv, 73, 77–79, 101, 111, 114, 139, 140

MZM Majorana zero modes 37, 40

N.C. non-conducting xxi, 117, 119, 128

N/A not available xxi, 117

PAS pinned atomic step 76, 95, 107

PID proportional-integral-derivative 44, 46, 55

PM preparation module 42, 43

PP partial pressure 54, 55

Q2" quarter of a two-inch 48, 57

Q3" quarter of a three-inch 48, 49, 108, 121, 122

QD quantum dot 88

QW quantum well iv, xiv, xvi, xviii–xxii, 2–4, 26, 28, 42, 49, 55, 58, 59, 67–70, 73, 76, 90–92, 94–96, 101, 102, 110–123, 125–142, 165, 166, 168, 169, 171

RGA residual gas analyzer xiv, 45, 54, 55

RHEED reflection high-energy electron diffraction [xiv](#), [xvi](#), [50–54](#), [81–84](#), [86–89](#)

RMS root-mean-square [82](#)

RSM reciprocal space map [xv](#), [66–69](#), [125](#)

S-N superconductor-normal [132](#)

SdH Shubnikov-de Haas [33](#), [34](#), [70](#), [118](#), [119](#), [121](#), [123](#), [124](#), [136](#)

SEM scanning electron microscopy [xv](#), [xvi](#), [61–63](#), [77–80](#), [85–95](#), [139](#), [140](#)

SIMS secondary ion mass spectrometry [xix](#), [63](#), [134](#), [138](#), [141](#)

SNS superconductor-normal-superconductor [142](#)

STEM scanning transmission electron microscopy [xvi](#), [62](#), [92](#), [93](#), [96](#), [139](#), [140](#)

TD threading dislocation [xiii](#), [xv](#), [16](#), [17](#), [19–22](#), [73](#), [76–81](#), [87–90](#), [92](#), [93](#), [95–97](#), [99](#), [101](#), [106](#), [107](#), [110](#), [111](#), [139](#)

TDD threading dislocation density [iv](#), [xv](#), [xvi](#), [3](#), [17](#), [20–22](#), [76–81](#), [85–98](#), [106](#), [113](#), [120](#), [123](#), [139–142](#)

TEM transmission electron microscopy [19](#), [52](#), [61](#), [62](#), [75–77](#), [85](#), [86](#), [88](#), [90](#), [92](#), [93](#), [96](#)

TLK terrace-ledge-kink [12](#)

TOD thermal oxide desorption [101](#), [102](#)

UHV ultra-high vacuum [42](#), [43](#), [45](#), [46](#), [48](#), [49](#)

UV ultraviolet [168](#)

vdP van der Pauw [iv](#), [xxi](#), [71](#), [117](#), [119](#), [122](#), [139](#), [165](#)

Chapter 1

Introduction

1.1 Motivation

As the desire for device functions in the modern semiconductor industry has significantly exceeded that offered by Silicon technologies, developments have rapidly branched out into other compound semiconductors, especially III-Vs made by combining elements from group III and group V elements of the periodic table, enabling improved device performance and a much wider range of applications. Under the growing demand on components of ever smaller structures and faster operating speed, the quantum mechanical effect becomes more and more significant in the development of complex nanoscale semiconductor devices, which opens up new horizons for solid-state researches and industrial applications. The development of the [molecular beam epitaxy \(MBE\)](#) technique has further sped up such evolution by allowing high-purity and nanoscale-precision growths of semiconductor heterostructures.

Among all the binary III-V semiconductors, InSb has the smallest electron effective mass ($0.014m_e^*$), the narrowest band gap (0.17 eV at 300 K), and the highest room-temperature electron mobility ($78\,000\text{ cm}^2/\text{Vs}$), which makes it particularly appealing for high-performance advanced electronic devices [1-3]. Recently, due to the strong spin-orbit coupling and the large Landé g-factor (~ -51), InSb quantum structures have also drawn significant interest by being one of the most desirable material systems when coupled with superconductors for realizing [Majorana bound states \(MBS\)](#) [4, 5]. The non-Abelian property of [MBS](#) has been demonstrated to enable topologically protected qubits for robust quantum information processing. [6-9].

While much of the early work demonstrating the signatures of **MBS** has employed self-assembled InSb nanowires [10–14], the top-down fabrication from a **two-dimensional electron gas (2DEG)** is a much more scalable and cleaner approach. [15, 16] By applying negative top gates, the area where the **2DEG** is uncovered by the superconducting layer can be depleted, leaving only 1D conducting channels strongly coupled to the superconducting material. This motivates a thorough investigation of the high-quality InSb **quantum well (QW)** structures grown by **MBE**. **MBE** also has the advantages of offering the most desirable clean semiconductor-superconductor interfaces in high crystalline quality by depositing epitaxial superconducting Al directly on the InSb **QW** surface for future development of Majorana devices.

However, InSb **2DEG** structures are far less developed comparing to GaAs systems. The low-temperature mobility measured with InSb **QW** structures (so far all below $400\,000\text{ cm}^2/\text{Vs}$) also have been far from ideal compared to the behavior of InSb bulk materials. The challenges come from both epitaxial growth and fabrication processes. One of the growth challenges is the lack of III-V semi-insulating substrates lattice-matched to InSb. High-quality and economical GaAs commercial substrates with the use of thick metamorphic buffers have paved a reliable path but the large lattice-mismatch between GaAs and InSb ($\sim 14.6\%$) leads to both a high density of structural defects, [17–23] and a rough surface morphology [24–26], which strongly influence the performance of the InSb active region in the structures. In addition, reported InSb **QW** heterostructures are often plagued with parallel conduction channels which prevents full depletion as required in split-gate quantum structures and low-bandgap materials are also notoriously difficult for electrostatic gating. Moreover, InSb **QWs** are known to have a low thermal budget, posing further challenges in the fabrication of InSb-based devices.

The development of InSb **QW** heterostructures has been so far mostly narrowed to the standard **high-electron-mobility transistors (HEMTs)** where the InSb **QWs** are buried beneath the doped barrier layer and protected from impurities and crystal disorders at the surface. However, for systems suitable for hosting **MBS**, near-surface InSb **QW** structures in an inverted fashion such that the doping is below the **QW** must be developed to achieve the proximity-induced superconductivity in the InSb **QW** from the superconductor deposited on the surface of the structure. Such near-surface **QWs** are known to suffer a much lower performance from the higher degree of surface scatterings and are much susceptible to surface treatment and handling during processing compared to buried **QWs**.

1.2 Outline

This thesis is part of a joint project on the experimental realization of [MBS](#) on readily scalable semiconductor-superconductor hybrid platforms in collaboration with Prof. Jonathan Baugh's research group with expertise in nano-device fabrication and quantum transport measurements. This thesis focuses on the development of InSb [QW](#) heterostructures as the underlying material systems for this purpose and is structured as follows:

In [chapter 2](#), the fundamental theory of crystalline materials and crystal growth are covered, together with brief reviews on the literature results which serve as useful references for the studies presented later in the thesis on the epitaxial growth, surface morphology, and dislocations of the grown material structures.

In [chapter 3](#), the basic concepts in semiconductor physics and related electronic properties of semiconductors are addressed which are fundamental to the design of the InSb [QW](#) heterostructures, as well as the device simulations and magneto-transport measurements covered in this thesis. A brief introduction on [MBS](#) and topological quantum computing are given for a clear understanding of the potential application of the InSb [QW](#) heterostructures developed in this thesis.

In [chapter 4](#), the experimental setup and metrology involved in the epitaxial growth and characterization of the material structures developed in this thesis are presented, including the [MBE](#) system and its in-situ monitoring tools, the extensive ex-situ material characterization methods, and the magneto-transport measurement setups. Please note that a small portion of the materials in this section are adapted from our publication [\[27\]](#) with permission.

In [chapter 5](#), the challenges in the growths of InSb [QW](#) heterostructures on GaAs substrates and the development of metamorphic buffers are discussed. Different characterization techniques were used and compared for studying the [threading dislocation densitys \(TDDs\)](#) reaching the top surface of the grown material structures. The metamorphic buffers were optimized by using the technique reported to promote the formation of the [interfacial misfits \(IMFs\)](#) and the design of interlayer buffer structures for dislocation filtering. The results on their effectiveness in reducing the defects are discussed. Please note that some materials of this chapter are reused, with permission, from our publications Ref. [\[25, 28\]](#).

In [chapter 6](#), the effect of the dislocations on the surface morphology in high lattice-mismatched III-Sb/GaAs systems and the disadvantages of the resultant rough surface

surface morphologies are discussed. The surface morphologies were studied as a function of growth conditions as well as substrate offcut angles and a significantly improved surface morphology was achieved for InSb QW heterostructures. Please note that some materials of this chapter are reused, with permission, from our publications Ref. [26]

In [chapter 7](#), the results of magneto-transport measurements for both InSb QW standard and inverted structures are discussed. The transport properties of InSb QW standard structures were studied with varying buffer structures and growth conditions. Parallel conduction and irreproducibility issues were observed during the growth campaign and the possible reasons for their rising were examined.

Lastly, [chapter 8](#) summarized the main results and conclusions from this thesis with potential future work suggested.

Chapter 2

Crystals and epitaxial growth

A crystal or a crystalline solid is a material that has its constituent atoms arranged in a three-dimensional periodic pattern. For noncrystalline materials which lack such long range order are termed *amorphous*. A crystalline material is a *single crystal* if the period pattern is perfect throughout the entire specimen. On the other hand, if the crystalline material is composed of many single-crystal domains separated by boundaries, then it is called *polycrystalline*.

2.1 Crystal structure

The arrangement of atoms inside a crystalline material is described by the crystal structure and the geometric form of the crystal structure which consists of three-dimensional array of points representing the atom positions in space is called a lattice. The *Bravais lattice* is usually used to describe the crystal lattice structure, which consists of discrete points generated by its primitive translation vectors that span the space. The *reciprocal lattice*, which is the momentum space, also known as k-space, is especially useful for studying the important physics of waves in solids and understanding and characterizing the material properties (more in [chapter 3](#) and [chapter 4](#)). The reciprocal lattice vectors G obey the relationship with the real lattice vector R as

$$e^{iG \cdot R} = 1. \quad (2.1)$$

In order to more conveniently describe the crystal structure, the concept of *unit cell* is introduced, which are small entities that represent the repeating pattern of the

crystal such that all the atom positions may be generated by its translations. The physical dimension of the unit cell is called *lattice constant*. The choice of a unit cell is not unique and all the unit cells do not have to have the same volume. The smallest unit cell, which contains exactly one lattice point, is called a *primitive cell*. *Wigner-Seitz cell* is an example of a primitive unit cell, which is constructed by drawing perpendicular planes at the midpoint of the lines connecting the central lattice point to its nearest neighbors. The primitive cell of the reciprocal lattice is called the first *Brillouin zone*.

In practice, the Wigner–Seitz cell is rarely used as a description of real space, where the conventional unit cells, larger than the primitive cell, are usually used, which are generated by translational basis vectors as in Bravais lattices. The crystallographic planes and crystallographic directions as specified by three *Miller indices*, h , k , and l , as expressed in terms of the basis vectors. A (111) plane and one $[110]$ direction are drawn in Figure 2.1(a) as examples. For a family of equivalent planes, the round brackets, ‘()’, around the indices are replaced with the curly ones, ‘{}’, and the angle brackets, ‘<>’, are used for a family of equivalent crystalline directions.

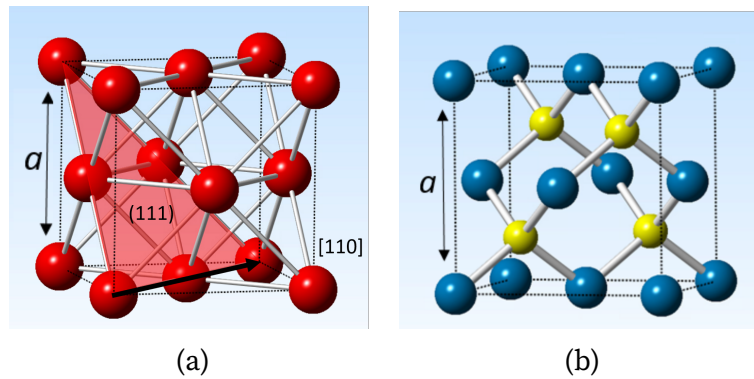


Figure 2.1: Schematic drawing for (a) **face-centered cubic (fcc)** (a) zinc-Blende crystal structures. Examples of a (111) plane and one $[110]$ direction are shown in (a). Atoms of the two different elements are represented by different colors in (b).

There are many different possible crystal structures and hence it is useful to divide them into groups called crystal systems based on their Bravais lattice unit cell configurations. For three-dimensional crystals, there are seven crystal systems and a total of fourteen distinct types of Bravais lattices, as classified by their translational and rotational symmetry. All crystalline materials must, by definition fit in one of these arrangements. Many semiconductors adapt the **fcc** form (Figure 2.1(a)), as one of the three in the cubic crystal system. The compound III-V semiconductors involved in this

thesis, like GaAs and InSb, all share the same zinc-blende structure, which consists of two interpenetrating fcc lattices formed by the Group III and Group V atoms respectively, as shown in [Figure 2.1\(b\)](#).

2.2 Basics of Crystal defects

2.2.1 Types of defects

In reality, perfect crystals described in the above section don't exist – all crystals contain different amounts and various types of crystalline defects or imperfections. A crystalline defect refers to a local disturbance in the regular arrangement of the atoms. Their existence can significantly alter the properties of crystalline solids. Though not all crystalline imperfections are undesirable, some can be especially detrimental in many ways.

There are mainly four types of crystalline defects associated with different dimensionality of crystal irregularity. A point defect is a case in zero-dimension including the vacancy kind (a missing atom at a normally occupied site), the self-interstitial kind (an extra atom at a normally unoccupied site), and impurity kind (a foreign atom introduced either substitutionally or interstitially).

A dislocation is a one-dimensional or linear defect in which case the atoms around the dislocation line are misaligned. One basic type of dislocation is termed an edge dislocation which is a result of an extra insertion of a half-plane of atoms with the edge of the plane that terminates within the crystal and defines the dislocation line. As shown in the left panel in [Figure 2.2\(a\)](#), the edge dislocation, represented by a symbol \perp , is perpendicular to the plane of the page. The lattice distortion due to edge dislocations decreases with increasing distance from the line and the lattice far away is essentially perfect. Another basic type of dislocation is a screw type, for which one side of the crystal is displaced by one atom spacing to the other side in the direction parallel to the dislocation line under shear stress, as shown in the left panel in [Figure 2.2\(b\)](#). The arrangement of atoms around a screw dislocation can be simply described by one surface helicoid and a symbol \odot is usually used to denote a screw dislocation with its spiral direction. Looking down the dislocation line, if the helix advances clockwise around it, the screw dislocation is right-handed and otherwise a left-handed one, like the one shown in [Figure 2.2\(b\)](#). In real crystals, other than the two basic types of dislocations, many dislocations actually consist of components of both edge and screw types. They are hence called mixed dislocations, for example, a 60° dislocation ([subsection 2.4.2](#)).

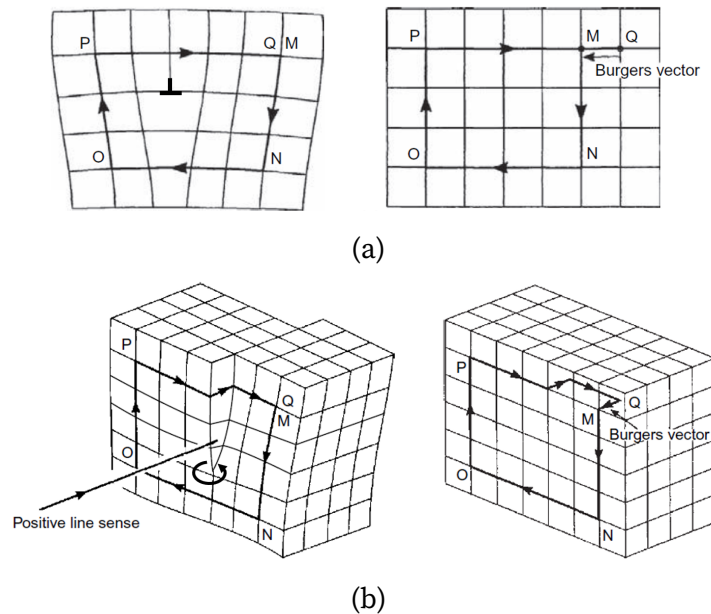


Figure 2.2: (a) Burgers circuits around (a) an edge dislocation and (b) a left-handed screw dislocation, also with the same circuits in a perfect crystal, depicting the Burgers vectors. [Adapted from [29] with permission]

Planar or interfacial defects are two-dimensional boundaries that separate regions of the crystals with different structures and/or orientations, include external surfaces, grain boundaries, phase boundaries, stacking faults, and micro-twins. Micro-twins and stacking faults are often observed in III-V hetero-structures and can sometimes be hard to be distinguished during imaging without close inspection. A stacking fault is an interruption in the stacking sequence of atomic layers. For example, in a regular sequence of ABCABCABC..., a stacking fault may result in a sequence of ABCBCABC... instead with a layer of A removed. A micro-twin is a boundary with one side undergoing a homogeneous shear and consequently showing a mirror image of the lattice on the other side. For the same ABCABCABC... regular sequence, a sequence containing a micro-twin could become ABCBACBA... for one example.

Bulk or volume defects are three-dimensional defects such as precipitates, voids, and bubbles that occur under certain growth conditions; as well as pores, cracks, foreign inclusions, and other phases which are sometimes introduced during processing and fabrication steps.

This thesis is primarily concerned with dislocations, as they dominate the hetero-

epitaxial growth of III-V materials and the ones that reach the active region in the structure may significantly deteriorate the electronic properties.

2.2.2 Burgers vectors and movement of dislocations

The magnitude and direction of the lattice distortion due to the presence of dislocation is expressed in terms of a *Burgers vector* and it can be determined using the *Burgers circuit*. First, an arbitrary atom-to-atom closed loop needs to draw around a dislocation line, then the vector needed to complete the exact same circuit redrawn in a dislocation-free crystal is the Burgers vector, b , as indicated in [Figure 2.2](#) (a) and (b) for edge and screw dislocations, respectively. The types of dislocations can also be determined from the angle between its Burgers vector and the dislocation line. For an edge dislocation, the Burgers vector is perpendicular to its dislocation line; the Burgers vector and the dislocation line are parallel for a screw-type; while for a mixed dislocation, the angle is in between $0-90^\circ$. Dislocations with opposite Burgers vectors will annihilate if they meet with each other and annihilate. Moreover, a few important rules need to be noted with dislocations:

1. Dislocations can only end at the surface of a crystal or grain boundaries but it can never end inside a crystal unless they form closed circuits.
2. The Burgers vector of dislocation always stays fixed even though the dislocation changes its type or direction.
3. The Burgers vector is conserved and when more than one dislocations meet and react, the sum of Burgers vectors of incoming dislocation must equal to the sum of the Burgers vectors of the ones coming out.

Crystals can be deformed elastically under stress and such deformation is non-permanent ([subsection 2.4.1](#)). However, under large enough stress, permanent plastic deformation will happen, which involves the creation and movement of dislocations ([subsection 2.4.2](#)). The stress required to move the dislocations by overcoming the lattice resistance is called the Peierls-Nabarro stress. While sessile dislocations cannot move, glissile dislocations can move in two basic ways. One is the *glide* motion, which occurs when the dislocation moves in the *slip plane*; and the other one is the *climb* motion, which is when the dislocation moves out of the slip plane. The slip planes are certain crystallographic planes in the crystal that allow the dislocation to move more easily. In

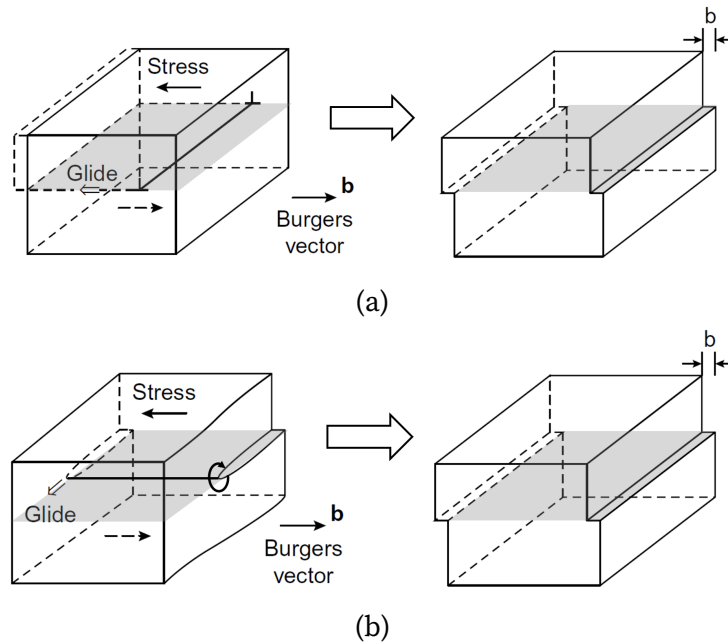


Figure 2.3: Plastic deformation by the glide of (a) edge and (b) screw dislocations under the shear stress.

the slip plane, there are also preferred crystallographic directions for the dislocations to travel and such directions are termed *slip directions*. A slip plane and a slip direction in the plane establish a *slip system*. The slip system depends on the crystal structure and usually is such that the lattice distortion due to the dislocation movement is minimized. For a particular crystal structure, the slip planes are normally the plane that has the densest atomic packing, i.e. the highest planer density, and the directions of slip correspond to the direction in this plane that has the shortest atomic spacing, i.e, the highest linear density. For an **fcc** structure, the most closely packed atomic planes are the $\{111\}$ family and the direction for the shortest atomic spacing is the $\langle 110 \rangle$ directions. Therefore, $\{111\}\langle 110 \rangle$ represents the slip system for **fcc** and there are 12 slip systems in total, including four individual $\{111\}$ slip planes and three independent $\langle 110 \rangle$ directions within each plane.

For the motion of edge-type dislocations, the slip plane is uniquely defined as the plane which contains both the dislocation line and the Burgers vector of the dislocation, as shown in [Figure 2.3\(a\)](#). However, for a pure screw-type dislocation, the dislocation line and the Burgers vector do not define a unique glide plane ([Figure 2.3\(b\)](#)), and hence the

glide of a screw dislocation is not restricted to a specific plane and cross slip can happen. For example, screw dislocations in an fcc structure can glide to another neighboring $\{111\}$ plane as long as it contains its Burgers vector under local stresses. As shown in Figure 2.3(b), the shear stress still acts on the slip plane parallel to the Burgers vector but the screw dislocation line glides in the perpendicular direction to the applied shear stress. The continued gliding of dislocations may eventually lead to a result of *slip*, which is one of the most common manifestations of plastic deformation, which are shown in Figure 2.3 for both the edge type and screw type dislocations.

2.3 Crystal growth

2.3.1 Fundamental theories

Crystal growth describes the process of forming crystalline materials and is determined by both thermodynamics and kinetics. Crystal growth can be considered as phase transformation during which crystalline solids develop from disordered gas or liquid phases. Phase transitions are described by Gibbs thermodynamic principles [30] which essentially determines the driving force for crystal growth. The phase to be formed when the system reaches its equilibrium state is determined by the given thermodynamic conditions and a phase diagram can be prepared experimentally. When a system departs from its equilibrium condition, the chemical potential difference between the phases provides the thermodynamic driving force for crystallization to occur, which can either be supersaturation or supercooling. Supersaturation is the difference of the chemical potential of the new solid phase relative to that of the infinitely large mother phase (gas or liquid) as a function of pressure or concentration at a particular temperature. Supercooling, also known as undercooling, can be regarded as the difference of the chemical potentials of the infinitely large mother and crystal phases as a function of temperature at a certain concentration or pressure.

However, the above thermodynamic considerations are purely macroscopic. Crystals do not grow instantly and the elementary processes of the actual motion of the individual building units (which can be atoms, molecules, or ions, but for simplicity and the interest of this thesis, will just be addressed as atoms) on the growth front of the new phase have not been taken into account. Therefore kinetics also need to be considered to describe the growth dynamics on a microscopic atomic level and define the rates at which various growth processes occur. The basic underlying theories for crystal growth were developed

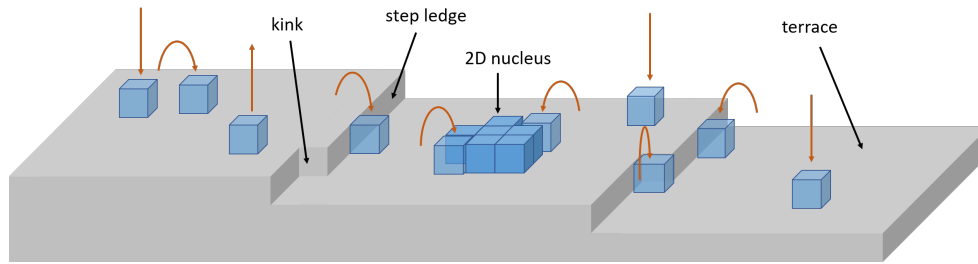


Figure 2.4: Schematic drawing to illustrate the surface kinetic processes during crystal growth, including impingement, evaporation, and surface migration of atoms on the surface, as well as atoms attaching to step and kink sites either from upper or lower terraces and formation of 2D nuclei on the terraces.

further from Gibbs thermodynamic aspects [30] by Kossel [31] and Stranski [32] in 1927-1928 by introducing the concept of mean separation work to describe the attachment and detachment of the individual atoms at crystal surface and further generalized to the famous **terrace-ledge-kink (TLK)** model, which described how growths proceed under small driving forces. They demonstrated that some sites, like steps and kinks as shown in Figure 2.4, if present, are more energetically favorable for atoms to attach as such incorporation results in a fewer number of unsaturated dangling bonds and lower surface free energy. On the other hand, for smooth step-less surfaces where attachment sites are rare, crystal growth may occur via a two-dimensional nucleation stage and continuous as atoms attach to the edges of the two-dimensional nuclei Figure 2.4. As the driven force increases further, the growth becomes more kinetics-controlled. Then the physics of crystal growth depends largely on the microscopic nature of surfaces and various kinetic processes may be involved.

2.3.2 Surface kinetics

The fundamental aspects of surface kinetics involve the microscopic processes of impingement, evaporation, and surface migration of atoms on the crystal surface, as shown in Figure 2.4. An atom absorbed on the crystal surface becomes an *adatom* and is not immediately attached to the crystal lattice but has a certain lifetime to meander along the surface before being incorporated or re-evaporated. The lifetime of the adatom τ_{ad} can be expressed in terms of the activation energy for evaporation, E_{ad} , as

$$\tau_{ad} \text{ [evaporation]} \sim \exp(E_{ad}/k_B T). \quad (2.2)$$

However, if the crystal grows under a very high driving force, the adatom may never be desorbed from the surface again. Its lifetime in the precursor stage will be restricted to the attachment to a preferred site on the surface and its collision with the other adatoms, i.e, the atomic flux J_{ad} :

$$\tau_{ad} \text{ [surface diffusion]} \sim 1/J_{ad}. \quad (2.3)$$

During its lifetime on the surface, the distance the adatom migrates to find a suitable site for attachment is then

$$l_d = \sqrt{D_s \tau_{ad}} \quad (2.4)$$

which is called the surface diffusion length and D_s is the surface diffusivity and can be expressed as

$$D_s \sim \exp(-E_{sd}/k_B T) \quad (2.5)$$

where E_{sd} is the energy barrier which adatom needs to overcome in order to diffuse along the surface due to its coupling with the underlying crystal lattice. The nature of crystalline surfaces is important for surface dynamics and surface steps can influence the kinetic processes take place on the surface in many ways. The atoms composing the step can diffuse along the step ledge or detach from somewhere on the step and attach somewhere else. When there are a few steps that are close together with an average separation shorter than the adatom diffusion length, these steps can interact with each other via the diffusion field of the adatoms [33]. Moreover, adatoms can be incorporated in a surface step from the upper and lower terraces either symmetrically or asymmetrically. For certain materials and growth conditions, asymmetry in step attachment is significant and shows a strong effect on the mass transport as well as the morphological transformations on the surface. As shown in Figure 2.5(a), when an adatom diffusing on the lower terrace collides with the step, it can be easily attached to the step as it will be immediately bounded by quite a few more neighboring crystal atoms at the step after attachment as compared as being an atom on the terrace. On the other hand, when an adatom approaches the step from the upper terrace, it needs to jump over the step and pass a configuration where it finds fewer neighboring atoms. The adatom on the upper terrace, therefore, needs to overcome an energy barrier which is greater than the diffusion barrier on the terrace E_{sd} and this an additional energy barrier E_{es} is known as the *Ehrlich-Schwoebel barrier* [34, 35]. The positive Ehrlich-Schwoebel barrier results in a net flow of uphill mass transport [36]. There also exist many other processes which lead to downhill surface currents. For example, the *knock-out effect* (Figure 2.5(b)) describes the circumstance of a freshly deposited atom displacing and occupying the the original step-edge site of the atom it landed upon as observed in molecular dynamics simulations [37]. All of these kinetic processes have been widely used in the analysis of morphological developments on the surface.

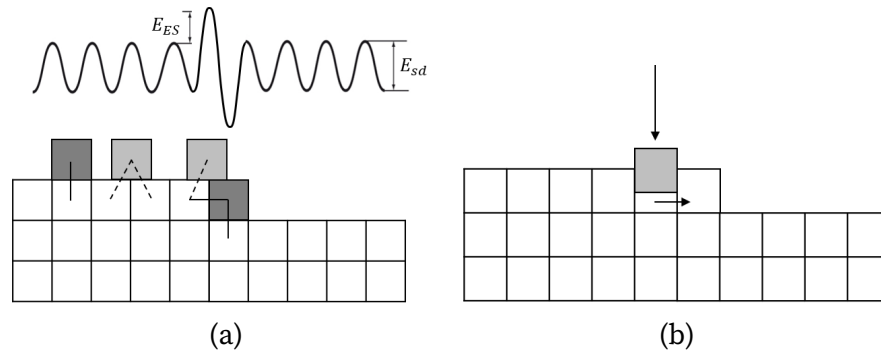


Figure 2.5: Schematic illustration for (a) the Ehrlich–Schwoebel effect with the adatom potential energy profile and (b) the knock-out effect. The atoms represented in cubes. The light gray atoms in (a) are moving along the surface with potential bonds with nearest neighbors depicted by dashed lines and the dark gray atoms are attached to the surface with bounds represented by solid lines to the nearest neighbors. The light gray atom in (b) is being freshly deposited towards the surface.

2.3.3 Crystal morphology

The morphology of single crystals is determined by the crystal structure, the crystal growth conditions, and the growth process. The shape of a crystal at thermodynamic equilibrium should be unique under given temperature and pressure conditions. As first considered by Gibbs (1874-1878) [30] and then by Curie (1885)[38], the equilibrium crystal shape takes a form such that the total surface free energy is minimized. For isotropic droplets of liquid, a true spherical shape is expected to form; while for crystal solids with anisotropic properties, facets will develop and the exact shape can be determined by the celebrated Wulff’s construction [39]. It was recognized by Stranski [32] that for the growth under a small driving force to occur, a small crystal cluster (or a 2D nuclei in the case of a 2D crystal formed on one of the faces of a 3D crystal) of a critical size must be formed first for atoms to be continuously attached to the steps sites at its edges Figure 2.4. The critical size is characterized by the dynamic equilibrium of the small crystal with its ambient phase, as determined by the mean work separation. This idea has been further adapted to study the morphological features of spiral growth around crystal defects by Burton, Cabrera, and Frank (BCF) [40]. However, when the crystals are formed under conditions of a high driving force, the system is very far away from equilibrium and the crystal will not necessarily attain their equilibrium shape but takes on a very different morphology. For crystalline materials grown by molecular beam epitaxy (MBE) for example, which is a growth technique that has high control over the growth activity

and will be explained in more detailed in [section 4.1](#), the crystal morphology is mainly determined by the kinetic processes during the growth, which can be directly influenced by applying different growth conditions.

2.4 Epitaxial growth

Epitaxy, termed after the Greek *epi*, meaning ‘upon’, and *taxis*, meaning ‘order’, is a well-controlled crystal growth such that the newly formed crystalline solids have a well-defined crystallographic orientation with respect to the substrate crystal structure.

2.4.1 Pseudomorphic epitaxy

When the material composition of the epilayer is exactly the same as that of the substrate even if differing in doping, it is called *homoepitaxy*. However, in most cases, *heteroepitaxy* is desired where structures with epilayers of different chemical composition and structural parameters than those of the substrate are deposited, enabling many more applications with various material combinations. A heterostructure is *pseudomorphic* when the epilayers are coherently strained with the substrate by adopting the in-plane lattice constant of the substrate. In a pseudomorphic cubic heterostructure, the strain in the two lateral directions is equal and such a biaxial strain results in a tetragonal distortion of the epilayer. If the lattice constant of the epilayer is smaller than that of the substrate, i.e, $a_l < a_s$, the lateral strain in the epilayer is tensile and a smaller lattice constant results in the vertical direction. On the other hand, for epilayers with $a_l > a_s$, the epilayer is strained compressively in the lateral direction, resulting in a larger vertical lattice constant. The resultant vertical lattice constant of the epilayer a_l^\perp can be deduced from the Poisson ratio of the epilayer material ν as

$$a_l^\perp = a_l \frac{1 + \nu}{1 - \nu} - a_l^\parallel \frac{2\nu}{1 - \nu} \quad (2.6)$$

where a_l is the lattice constant of the epilayer when free-standing and a_l^\parallel is the in-plane lattice constant which equals that of the substrate a_s for the pseudomorphic structure. The lattice constant and the Poisson ratio for a ternary III-V semiconductor compounds can usually be interpolated by *Vegard’s law*:

$$a_{A_x B_{1-x}}(x) = x a_A + (1 - x) a_B \quad (2.7)$$

$$\nu_{A_x B_{1-x}}(x) = x \nu_A + (1 - x) \nu_B \quad (2.8)$$

where A and B are the two end binary materials, i.e, when $x = 1$ and $x = 0$ respectively.

2.4.2 Generation of misfit dislocations

The elastic strain energy of the coherent film scales with the film thickness h . When the film thickness is less than the critical thickness h_c , it is energetically favorable for the film to strain elastically to reduce the misfit (also called lattice mismatch) f between the two lattices, which is defined as:

$$f = \frac{a_l - a_s}{a_s} \quad (2.9)$$

When the film thickness reaches the critical value of h_c , the misfit strain is expected to be relaxed by accommodating **misfit dislocations (MDs)**. Such relaxed epilayers are termed *metamorphic*. The critical thickness depends on the misfit between the two crystals and their elastic constants. As the misfit increases, this critical thickness decreases and eventually vanishes.

Two main approaches are usually considered for predicting the critical thickness and modeling the formation of **MDs**. One is the energy minimization formalism originally proposed by van der Merwe [41, 42] which calculates the mismatch-induced strain energy needed to compensate the core energy of the introduced strain-relieving **MD**. The other one is the force balance model adopted by Matthews and Blakeslee [43] which involves the balancing between the line tension of a pre-existing **threading dislocation (TD)** (which threads through the layer structure and hence the name) and the Peach-Koehler force on the threading arm to glide along the hetero-interface to generate **MDs** (Figure 2.6). It has been verified that, with correct formalism, the results from the two theories are actually qualitatively identical and should always yield the same numerical number values of critical thickness. [44, 45]. Though discrepancies were observed between the critical thicknesses calculated from theory (equilibrium case) and the experimental ones (kinetic case) in early studies, particularly on low-mismatched systems, [46] with more reliable characterization techniques and in large mismatch systems, relaxation were always observed near the theoretical critical thickness. [44]

The strain relaxation process and the mechanism for the formation of **MDs** are found to also depend on the growth modes and the growth stages in different epitaxial films. The two early models above have considered the layer-by-layer growth mode during which the strain distribution is uniform in the overgrown film. The layer-by-layer growth

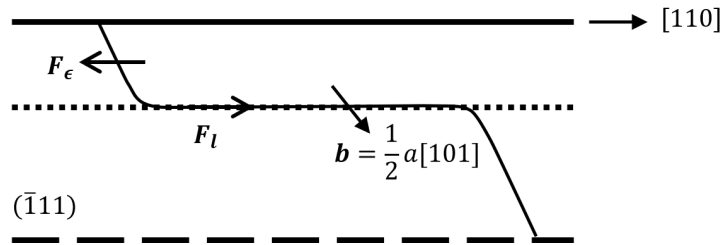


Figure 2.6: The generation of a **MD** segment at the epilayer interface from a **TD** that is initially extended from the lower layer to the upper layer. The thick continuous and thick dashed lines represent the intersection of the $(\bar{1}11)$ slip plane with the top surface of the upper layer and the bottom surface of the lower layer respectively. The thin dotted line is the intersection of the $(\bar{1}11)$ slip plane with the interface of the two layers. The thin continuous line is the dislocation line with its burgers vector F_ϵ is the force exerted by the misfit strain and F_l is the tension in the dislocation line. [Adapted from [47] with permission]

mode, also named the *Frank-van der Merwe mode*, usually takes place when the lattice mismatch of the system is low. One mechanism for the generation of strain-relieving **MDs** under such growth mode is the model proposed by Matthews and Blakeslee [43] as already mentioned above (Figure 2.6). However usually the **threading dislocation density (TDD)** from the substrate is very low and the **MDs** generated in this way cannot accommodate all the misfit strain. In addition to that, they also postulated a mechanism for the formation of **MD** segments from the nucleation of surface dislocation half loops. These half loops, nucleated at the top surface of the epilayer, glide and expand on the four inclined $\{111\}$ slip planes toward the hetero-interface under the driving force of the misfit strain, forming orthogonal arrays of 60° **MDs** lying along $\langle 110 \rangle$ directions, as shown in Figure 2.7. The Burgers vector of such a 60° dislocation is equal to any one of $\pm \frac{a}{2}[101]$, $\pm \frac{a}{2}[10\bar{1}]$, $\pm \frac{a}{2}[011]$ and $\pm \frac{a}{2}[01\bar{1}]$, being inclined at 60° with respect to the dislocation line and hence the name. The nucleation and propagation of the 60° half loops were experimentally observed and investigated in many material systems, for example $\text{Ge}_{1-x}\text{Si}_x/\text{Si}$ [48], GaAs/Si [49] and $\text{InGaAs}/\text{GaAs}$ [50], as well as tensilely strained Si/GaP systems [50]. Models have also been developed to calculate the strain relaxation as a function of the epilayer thickness in terms of energy considerations for the nucleation and expansion of the surface half loops. [49, 50]

When the lattice mismatch gets larger, the growth would proceed by the growth modes which involve the formation of three-dimensional islands. For the *Stanski-Krastankov mode*, the growth starts with a wetting layer of a few monolayers in thickness followed by

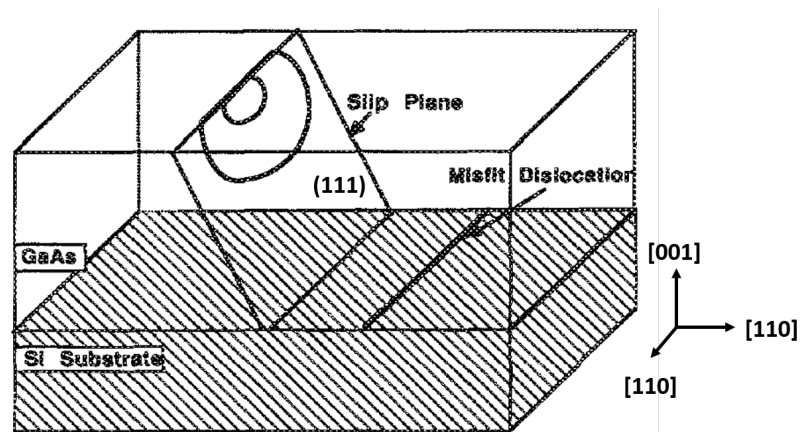


Figure 2.7: The schematic drawing of the nucleation and glide of 60° dislocation half loops on the 111 plane and the generation of 60° misfit segment at the interface between the GaAs layer and the Si substrate. [Adapted from [49] with permission]

islands formation on the surface, then after the islands are large enough to coalesce, the growth continues with layer-by-layer growth mode; while in the case of *Volmer-Weber growth mode*, the growth starts with 3D island formation directly with no wetting layers and is followed by the layer-by-layer growth once the islands coalesce. Strain relaxation in such island-forming systems show different characteristics than the planer systems modeled by the two equilibrium theories above. As opposed to the 2D growth mode, the strain distributions in island growth are inhomogeneous, as observed in highly strained $\text{In}_x\text{Ga}_{1-x}\text{As}$ islands on GaAs. [51] Moreover, the critical thickness for a 3D growth was found to be larger than that for a 2D case. Coherent dislocation-free GaAs islands with 6nm height, more than four times the predicted planer critical thickness, were achieved on a Si substrate. [52] Similarly in a Ge/Si system, elastic deformation was observed around the islands which delayed the formation of MDs. [53]

A unique mechanism of introducing MDs was proposed [54] to dominate the relaxation process during the initial island growth stage and the schematic diagram for this mechanism is shown in Figure 2.8. Since the stress field is highest at the island edges and less material rearrangement is required at the edge of the island than in the center, new MDs spontaneously nucleate at the leading edges of the islands when the stress reaches a critical value. Then the stress field near the island edges quickly drops, promoting the lateral growth of the islands. As the islands continue growing, the stress field near the island edges increases again until another MD is nucleated. In Stranski-Krastanov Ge/Si systems ($\sim 4\%$ mismatch), the islands were observed to first appear as small coherent

ones and sharing a uniform size limited by the strain [55]. A cyclic growth pattern on the island shapes was detected under in-situ transmission electron microscopy (TEM) imaging, with each cycle corresponding to an abrupt lateral growth phase due to the introduction of a new MD at the island edge. [56] In non-wetting Volmer-Weber growth systems, the periodic generation of MDs at the periphery of the islands was also observed in GaSb/GaAs [57, 58] (~ 8% mismatch), InAs/GaP [54] (~ 11% mismatch) and InSb/GaAs (~ 14% mismatch)[59] systems. The islands grow strain-relaxed in a InAs/GaP (~ 11% mismatch) system in which the mismatch is even larger than that allowed to grow a coherent epilayer in one monolayer thickness. [54] Unlike Ge/Si systems, these relaxed InAs islands diverse largely in their shapes and sizes as well as the amounts of MD formed in them in the early stages of island development. They first appear hemispherical then facet when the islands reach a critical size to minimize surface energy. Similarly, it was found that the aspect ratio of the InAs islands decreased as the number of MDs generated in the island increased [54].

The MDs generated at the island edge were identified by most groups to be of 90° pure edge-type. [54, 57, 58] However, since islands of III-V materials are bounded by {111} crystallographic planes, some groups [60, 61] also observed generation of 60° MDs at the island edges, though very rarely. Unlike the 60° MDs which are mixed-type dislocations, 90° MDs are pure edge dislocations that lie at the (001) hetero-interface with Burgers vectors being either $\pm\frac{a}{2}[110]$ or $\pm\frac{a}{2}[\bar{1}\bar{1}0]$ and are hence twice more efficient in relieving the strain energy. Since the (001) plane is not a closed-packed slip plane in the fcc lattice, the 90° dislocations are sessile. Moreover, the 90° MDs are also termed Lomer dislocations as identified under TEM to have two of the inclined {111} atomic planes simultaneously terminate at the core, while the 60° dislocation cores have only one of the {111} half-planes. Hence the 90° Lomer dislocations can also be pictured as a combined pair of two interfacial 60° misfit dislocation segments as in the case of a Lomer-Cottrell locking. Actually, as will be discussed later, the reaction of two complementary 60° half-loops can result into 90° Lomer dislocations at the interface except with extra four TD arms.

When the size of the islands reaches a certain value, the residual strain in the islands may not be large enough to overcome the energy barrier for the generation of more 90° MDs. Therefore the islands are not necessarily fully relaxed before they coalesce and strain relaxation may continue well beyond the initial stage of island growth. After the 2D planer growth has started, the strain-relieving MDs can no longer spontaneously appear at the hetero-interface and the mechanism of a glissile MD introduction is required. The mechanism for the nucleation of 60° dislocation half loops is believed to take over the responsibility to relieve the residual strain during the planer growth stage in high lattice-mismatch systems. Such nucleation of dislocation half loops was also observed

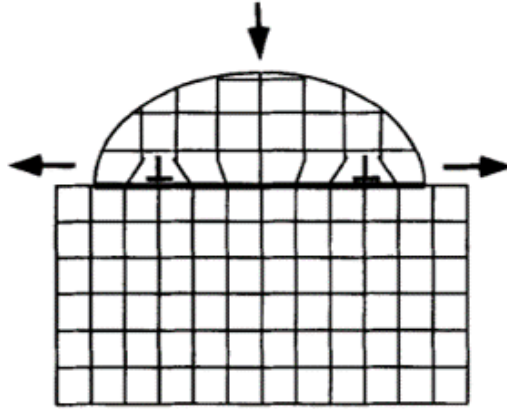


Figure 2.8: Schematic diagram showing the strain relaxation of an island on the surface by the introduction of MDs at its edges. [Adapted from [54] with permission]

to happen during the initial stage of island growth, as some islands were found to also contain 60° dislocations with two TD segments and these islands appeared to be rounder. [57, 62] However, such defective islands were much fewer than the ones that only contain regular arrays of pure 90° MDs and the half-loop mechanism hence was suspected to become more important after island coalescence.

More 90° MDs may still form at the hetero-interface during the planer growth stage, as proposed in a co-operative mechanism of the nucleation of two 60° glissile dislocation half loops. [63, 64] The introduction of the MD at the hetero-interface through gliding of the first surface half-loop was found to reduce the energy barrier for the nucleation of a second surface half loop, with the complementary screw component and the same edge component. Then as the second surface half-loop propagated to the hetero-interface, the two 60° dislocation pairs would react and form a sessile 90° MD, since the core energy of a 90° dislocations is much lower than that of 60° one. However, the threading segments being locked up in a sessile configuration may lead to more strain-relieving dislocation half loops, resulting in increased TDDs in the epilayer.

2.4.3 Sources of threading dislocations in III-Vs

The generation and propagation of dislocations are essential for the relaxation of strains in lattice-mismatched heteroepitaxial growths, however the threading kind among them propagate through the material structures and may severely deteriorate the device per-

formance if they reach the active region. In order to suppress the formation of TDs, it is important to study the origin of them in the first place. Here we present a brief review and discussion on the possible sources of TDs reported in the literature, especially for the high lattice-mismatched systems where the situation gets more complicated with more than one growth stage.

Substrates are evidently one of the sources for TDs. Yet usually the TDDs are very low ($< 1 \times 10^5 \text{ cm}^{-2}$) in high-quality substrates, so the majority of TDs in lattice-mismatched hetero-structures are generated during the process of strain relaxation.

TDs of edge, screw, and mixed types have been observed in many heteroepitaxial material systems. Yet in lattice-mismatched systems consisted of solely III-V materials grown in (001) crystallographic directions, the 60° mixed-type TDs were found to dominate. As discussed earlier, 90° MDs are pure edge dislocations with their Burgers vectors confined at the (001) epilayer interface perpendicular to the growth direction while the slip systems of 60° mixed-type dislocations lie in $\{111\}$ planes, allowing them to thread through the layer structures. Therefore, for high lattice-mismatched systems, by optimizing the growth during the island formation stage to promote the formation of 90° dislocations over the 60° ones, fewer 60° TDs may be generated in the epilayer. The study of the so-called interfacial misfit (IMF) dislocation array growth mode will be presented in section 5.3. The formation of the MD types were found to depend on the growth temperature. For example, more defective islands with 60° MDs and in rounder shapes were found in GaSb/GaAs systems grown at 520°C than the ones grown at 420°C or 470°C . [57] It was also found that more ordered 90° MD networks could be achieved in certain material systems, for example, GaSb/GaAs, over many others [62, 65]. In addition, controversy remains over whether surface steps are responsible for generating 60° dislocations [57, 66]

Ideally, the more strain is relaxed by 90° MDs during the initial island growth stage, the fewer 60° half-loops will be generated to relieve the residual strain in the later planar growth stage, resulting in a lower density of TDs. The residual elastic strain in the epilayer is correlated with the spacing of the MDs. [49, 54] GaSb islands grown on GaAs substrates have been observed to be already nearly fully relaxed, with quasi-perfect 90° MD networks spaced every 13 or 14 $\{110\}$ planes corresponding to an average spacing of about 56 \AA [57, 58]. However, TDDs up to $1 \times 10^8 \text{ cm}^{-2}$ have been widely reported to reach the surface of thick GaSb epilayers on GaAs substrates [67–70], suggesting that there might be some other mechanisms involved in introducing TDs.

There has been considerable debate on whether the coalescence of islands in the transition between the initial 3D island growth stage and the 2D planar growth stage

is correlated with the introduction of more 60° dislocations. Many believed that the threading 60° dislocations were mainly originated from the misalignment of the 90° MD network during the coalescence of the 3D islands. This possibility was first suggested by Eaglesman et al. in 1988 [71] who observed the interfacial MD networks at a GaAs/Si interface to consist of clusters of 90° MDs separated by smaller groups of 60° ones. Similar observations were also found in GaSb/GaAs systems where threading components were traced back to the interface at the sites joining 90° dislocations with different spacings, which are suspected to be a result of different island sizes [57, 65]. On the contrary, the origin of TD was observed to be poorly correlated to the coalescence sites of burred AlSb islands on the Si substrate using electron tomographic reconstruction. [60]. In addition, the area density of TDs was found to stay constant as the GaSb islands kept growing and merging on the GaAs surface [58]. Wang et al. [72] investigated the GaSb/GaAs interface and identified several types of 90° dislocation network imperfections as the main sources of threading 60° dislocations, though it is still unclear whether the imperfections in the dislocation network are associated with the coalescence of islands.

Lastly, post-growth thermal annealing may also influence the TDD in the epilayer. It has been found that thermal annealing after the growth can transform the dislocation system into a more equilibrium configuration with improved crystalline quality [57, 65] and the energy minimization allowed the 90° MDs at the interface to be redistributed into a more uniform spacing [54, 73]. The relative fraction of the 90° MDs also increased after annealing due to the interaction of 60° MDs at the interface [61] and the 60° TDs decreased as a result of their annihilation inside the layer. [74] However, depending on the annealing conditions, some other processes which increase the number of TDs may also be encouraged, such as dislocation multiplication. [44]

Even though the sources and the generation mechanisms of TDs are still not fully understood, the literature reports point to many possible optimization directions in the epitaxial growth of high lattice-matched material systems.

Chapter 3

Electronic properties of semiconductors

3.1 Semiconductors: some basic concepts

3.1.1 Band theory

The electronic behavior of a crystalline solid is usually explained by its band structure. The band structure is a collection of energy bands formed from all eigenvalues $E_n(\mathbf{k})$ of the Schrödinger's equation for an electron in the crystal:

$$\hat{H}\psi(\mathbf{r}, \mathbf{k}) = \left[-\frac{\hbar^2}{2m^*}\nabla^2 + V(\mathbf{r})\right]\psi(\mathbf{r}, \mathbf{k}) = E(\mathbf{k})\psi(\mathbf{r}, \mathbf{k}) \quad (3.1)$$

where $\psi(\mathbf{r}, \mathbf{k})$ is the electron wavefunction with a wave vector \mathbf{k} at a given spatial coordinate \mathbf{r} . Bloch showed that if an electron moves in a periodic potential energy $V(\mathbf{r})$ such as in the crystal lattice, where $U(\mathbf{r} + \mathbf{R}) = U(\mathbf{r})$, then the solutions to the Schrödinger equation take the form of a plane wave modulated by a periodic function with the same periodicity as the periodic potential:

$$\psi(\mathbf{r}) = \exp(i\mathbf{k} \cdot \mathbf{r})u(\mathbf{r}). \quad (3.2)$$

This is known as *Bloch's theorem*, which underlies the concept of electronic band structures. From the Bloch theorem, for a given band index n , the energy $E_n(\mathbf{k})$ is periodic in the reciprocal lattice, that is, $E_n(\mathbf{k}) = E_n(\mathbf{k} + \mathbf{G})$, where \mathbf{G} is given by [Equation 2.1](#). Therefore, it is sufficient to plot the band structures reduced in the reciprocal space to the first Brillouin zone ([Figure 3.1\(b\)](#)), which is the primitive Wigner-Seitz cell in the reciprocal lattice, as discussed previously.

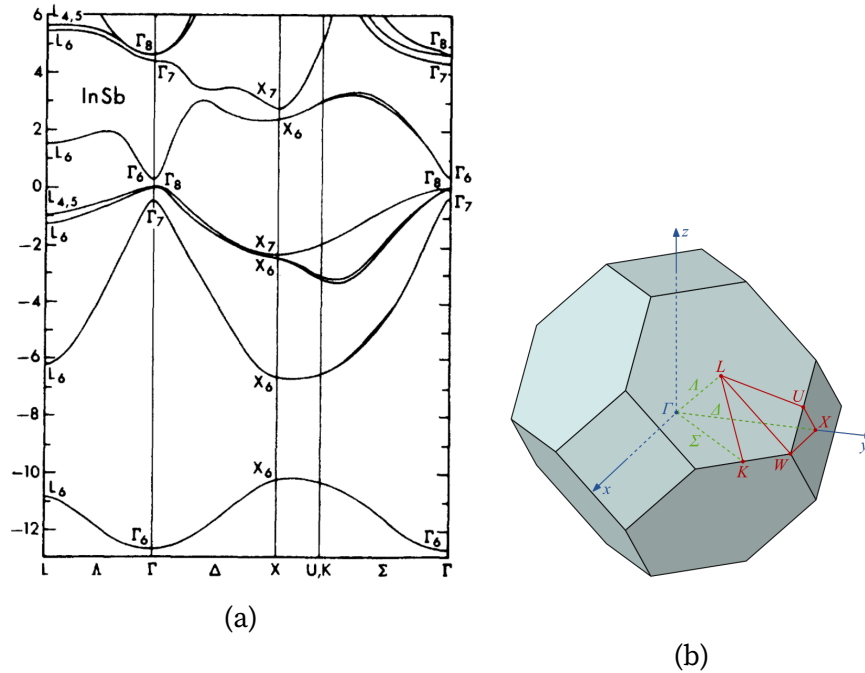


Figure 3.1: (a) The band structure of InSb calculated using the pseudo-potential method. (Adapted from Chelikowsky and Cohen [75] with permission). The band indices are represented by the number in the subscript. (b) The first Brillouin zone of a **face-centered cubic (fcc)** lattice showing the corresponding representations for the high symmetry lines and points in (a).

The band structures of solids have been calculated theoretically using a variety of numerical methods, such as the orthogonalized plane-wave method, pseudo-potential technique, and the $\mathbf{k} \cdot \mathbf{p}$ method. Figure 3.1a shows the results of the energy-band structures of InSb calculated using the pseudo-potential method. Notice that there is a forbidden energy range in which no allowed states can exist in the plot of the energy bands in Figure 3.1(a). The energy bands above this energy gap are unfilled and the lower ones are filled bands. The gap between the energy of the lowest upper band, the conduction band E_c , and that of the highest lower band, the valence band E_v , is called the bandgap E_g , which is one of the most crucial parameters in semiconductor physics. In conductors, the conduction band overlaps with the valence band and in insulators, there is a large energy gap. If the gap is small enough such that electrons can be excited into the conduction band then these materials are called semiconductors and their conductivity depends on the availability of vacant electronic states. The E-k relationship near the

bottom of the conduction band and top of the valence band are quite isotropic and may be approximated by a quadratic equation:

$$E(k) = \frac{\hbar^2 k^2}{2m^*}, \quad (3.3)$$

where m^* is the effective mass of the carrier in the conduction band or the valence band. However, the parabolic approximation is not appropriate for semiconductors with narrower band gaps, such as InSb, where the eight-band Kane model is most commonly used [76].

Another important parameter in the band theory is the Fermi level, which for the case of metals corresponds to the top of the available electron energy levels at absolute zero temperature. At higher temperatures, a fraction of the states above the Fermi level will get occupied as characterized by the Fermi-Dirac distribution, and the Fermi level is the energy of the state with 50% occupation probability at thermodynamic equilibrium. In a semiconductor or an insulator, the Fermi level lies inside the band gap but it can be shifted by presence of impurities. With the small gap of semiconductors, a small percentage of doping can dramatically increase their conductivity and this is the unique and one of the most important properties of semiconductors. The donor-type impurities, also termed n-type dopants, have an energy level closer to E_c in the energy gap of the semiconductor and hence can donate electrons to E_c . On the other hand, when acceptors, also known as p-type dopants, are introduced to semiconductors, they can accept electrons as their energy levels lie in the proximity of E_v , generating holes in the valence band.

3.1.2 Heterostructure

When crystals with different band structures are brought together, further complexity is added. The alignment of the conduction and valence bands as determined by the electron affinity of each material can drastically change the electrical properties of such *heterostructures*, which hence can be engineered to have a wide range of applications, such as diodes, lasers, and photodetectors. To understand how band structures change with position in the heterostructures in real space, band diagrams are used which plot the key energy band edges with the Fermi level as a function of spatial dimension. These band diagrams are extremely useful to visualize the *band bending* at the interface of different materials, understand the distribution of charge within the structure, and explain the operation of many semiconductor devices.

Ternary alloys have been widely used in the design of heterostructures as they enable many more possibilities in the band alignment compared to binary compounds.

Figure 5.1 shows the variation of bandgap with lattice constant for binary and ternary III-V materials. The bandgap of a ternary alloy $A_{1-x}B_x$ has been shown to depend on the composition x as:

$$E_g(A_{1-x}B_x) = (1-x)E_g(A) + xE_g(B) - x(1-x)c. \quad (3.4)$$

where c is the bowing parameter which accounts for the deviation from a linear interpolation between the bandgaps of the two binaries A and B.

3.1.3 Two-dimensional electron gas

Through proper band engineering, heterostructures with electrons confined in a two-dimensional sheet can be achieved. The electrons are confined by a potential $V(z)$ in the z -direction but are free to move in the two-dimensional x - y plane, hence the name **two-dimensional electron gas (2DEG)**. The heterostructure containing a thin narrow gap material such as InSb between materials with wider gaps such as $Al_xIn_{1-x}Sb$ creates a region with low potential energy locally at the InSb layer known as a **quantum well (QW)** where a 2DEG can exist. Since the InSb QW layer is so thin in the growth direction z (smaller than the carrier Fermi wavelength (subsection 3.1.5), the energy spectrum in the conduction band split into discrete energy levels, known as *subbands*. The **density of states (DOS)** $g(E)$, defined as the number of available carrier states per unit energy per unit volume, for a 3D bulk material, by assuming a simple parabolic energy dispersion, is continuous and energy-dependent:

$$g_{3D}(E) = \frac{1}{2\pi^2\hbar^3} (2m^*)^{3/2} (E - E_c)^{1/2} \quad (3.5)$$

where $E - E_c$ is the energy relative to the minimum of the conduction band. When the carriers are confined in a quasi-2D plane, the DOS remains the same within each subband and increases in a step-wise fashion for the whole conduction band:

$$g_{2D}(E) = \sum_{n_z} \frac{m^*}{\pi\hbar^2} \theta(E - E_{n_z}) \quad (3.6)$$

where the discontinuity is described by the step function $\theta(E - E_{n_z})$. When the 2-D quantum well is further confined into a one-dimensional quantum wire, the DOS for each subband has an energy dependence of $E^{\frac{1}{2}}$:

$$g_{1D}(E) = \frac{1}{\pi\hbar} \sqrt{\frac{m^*}{2(E - E_c)}}. \quad (3.7)$$

Finally, the quasi-0D DOS is represented by a delta function for structures like quantum dots and the DOS for the first subband is:

$$g_{0D}(E) = 2\delta(E - E_c). \quad (3.8)$$

The DOS for all electron gas dimensionalities are drawn in Figure 3.2.

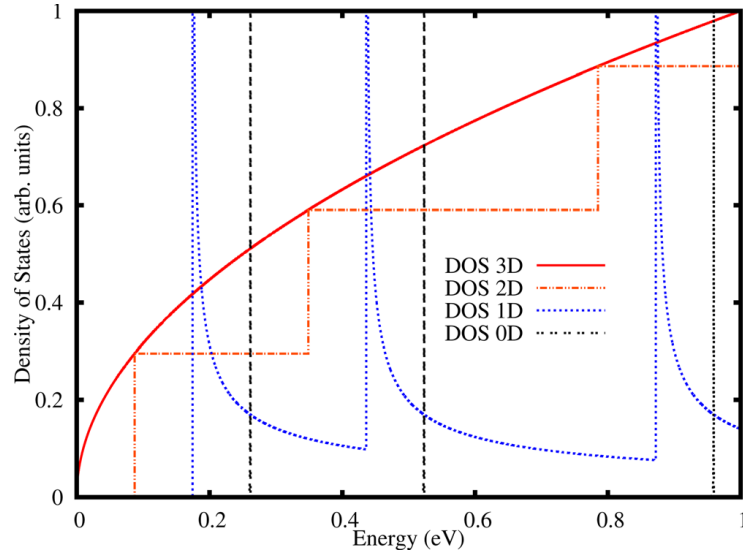


Figure 3.2: Density of states for 3D, 2D, 1D and 0D systems. [Adapted from [77] with permission]

3.1.4 Modulation doping

Various doping schemes are used in heterostructure designs for different applications. Modulation doping is especially important for high mobility 2DEG heterostructures. Back in earlier times when dopants were introduced directly in the 2DEG materials, electron mobility was largely limited by the scattering due to the ionized impurities. By incorporating the dopants away in the barrier layer yet reasonably close to the 2DEG, the so-called modulation-doped 2DEG heterostructures can achieve very high mobility as a result of reduced distance-dependent Coulomb scattering from the donors. The technique of δ -doping offers further advantages over the bulk doping by limiting the dopants in a 2D plane in the structure. Modulation doping causes band bending and therefore the doping density, spacer thickness between the 2DEG and the doping layer

as well as the band offset at the 2DEG/barrier interface need to be carefully considered for the design of the heterostructure. The active region consisting of the InSb/Al_xIn_{1-x}Sb QW and the modulation doping in the studied material systems were simulated using the commercial software nextnano++ [78], a Schrödinger-Poisson solver for systems up to 3D, which offers an insight into the optimization directions of the heterostructure design.

3.1.5 Length scales in quantum transport

In solid-state systems, quantum mechanical effects arise when the dimension of the device L is comparable to the Fermi wavelength λ_F of the charge carriers, which in a 2DEG is given as

$$\lambda_F = \frac{2\pi}{k_F} = \sqrt{\frac{2\pi}{n_{2D}}} \quad (3.9)$$

where k_F is the Fermi wave vector and n_{2D} is the 2D carrier density. The electron density in metals is very high, resulting in a very short λ_F and the device size needs to be in a few nanometers to see quantum effect. On the other hand, due to the low electron density in semiconductors, λ_F of electrons and hence the achievable device dimensions can be in the order of several tens of nanometers.

To understand the transport regimes of a quantum device, two length scales regarding the motion of the carriers are usually considered. The first is the carrier mean free path l , which is to the average distance the carriers travel before their momentum is randomized due to scattering by disorders in the systems:

$$l = v_F \tau \quad (3.10)$$

where v_F is the Fermi velocity and τ is the carrier scattering time. The mean free path of the carriers determines whether the device is in a ballistic ($l \gg L$) or diffusive ($l \ll L$) transport regime. The other length scale of importance is the dephasing length l_ϕ which refers to the average distance electrons travel in the device before their phase is disrupted through scattering:

$$l_\phi = \sqrt{D\tau_\phi} \quad (3.11)$$

It determines whether the transport is coherent ($l_\phi \gg L$) or incoherent ($l_\phi \ll L$).

Weak localization

Weak localization describes the quantum-mechanical effect of coherent backscattering which superposes to the Drude conduction and leads to an increase in the net resistivity in disordered electronic systems at low temperatures. Electrons propagating in a disordered medium experience a large number of scattering events and the probability of them being backscattered is given by the sum of the quantum-mechanical amplitudes of all paths:

$$P_{\text{backscatter}} = \left| \sum_{\text{path } L} A_L \right|^2 = \sum_{\text{path } L} |A_L|^2 + \sum_{\text{path } i,j} A_i A_j^* \quad (3.12)$$

Most of the interference terms in the second sum involve different paths whose phases are uncorrelated and hence are expected to be canceled. The only terms which do not cancel result from electrons traveling **clockwise (CW)** and **counter-clockwise (CCW)** around the same loops resulting in the same phase and constructive interference:

$$P_{\text{backscatter}} = \sum_{\text{path } L} |A_L|^2 + 2 \sum_{\text{loop } i} |A_i|^2 \quad (3.13)$$

Therefore, the quantum interference effectively causes electrons to be more likely backscattered in circular paths, increasing the total resistivity.

However, for the systems with strong spin-orbit coupling, the spin of the electrons rotates in the opposite direction as they move **CW** and **CCW** around the loop, resulting in a destructive interference of the partial wave functions along the two paths:

$$P_{\text{backscatter}} = \sum_{\text{path } L} |A_L|^2 - 2 \sum_{\text{loop } i} |A_i|^2 \quad (3.14)$$

As a result, the resistivity decreases and this effect is called the *Weak anti-localization* effect.

3.2 Magnetotransport

Magnetotransport measurements are of crucial importance for studying the electronic transport properties of the heterostructures. The quality of **2DEG** is typically characterized by two key parameters, the sheet carrier density and the carrier mobility, which can be acquired from the behaviors of the carriers under the influence of electric and

magnetic fields. By understanding the transport mechanisms, optimization in the growth of the crystalline materials and improvements in the design of the heterostructures can be carried out further.

3.2.1 Classical Hall effect

Within the classical diffusive regime, the carrier transport can be accurately described by the Drude model. In the Drude assumptions, electrons move nearly freely though the stationary crystal lattice and experience a force of $\mathbf{F}_E = -e\mathbf{E}$ under the influence of an electric field, which accelerates the electrons and result in a net current flow with the current density being

$$\mathbf{j} = -nev_d = \frac{ne^2\tau\mathbf{E}}{m^*} = \sigma\mathbf{E} \quad (3.15)$$

where

$$\mathbf{v}_d = \frac{-e\mathbf{E}\tau}{m^*} \quad (3.16)$$

is the net drift velocity and τ is the mean time between the scattering events which randomize the electron drift velocity. From [Equation 3.15](#), the conductivity σ can be described by

$$\sigma = \frac{ne^2\tau}{m^*} = ne\mu \quad (3.17)$$

where the mobility of the electrons is given as

$$\mu = \frac{e\tau}{m^*} \quad (3.18)$$

and is a measure of the response of the electrons to the electric field.

When a magnetic field is also applied, the electrons feel an additional Lorentz force and experience a total force of

$$\mathbf{F} = -e(\mathbf{E} + \mathbf{v}_d \times \mathbf{B}) \quad (3.19)$$

For thin quasi-2D materials with a current flowing through in the $+x$ direction and a magnetic field applied in the $+z$ direction, as shown in [Figure 3.3](#), then electrons traveling under the electric field in the $-x$ direction will be deflected by the Lorentz force to the left in the orthogonal $-y$ direction, causing accumulation of electrons at one side of the material, which in turn gives rise to a transverse electric field opposing to the Lorentz

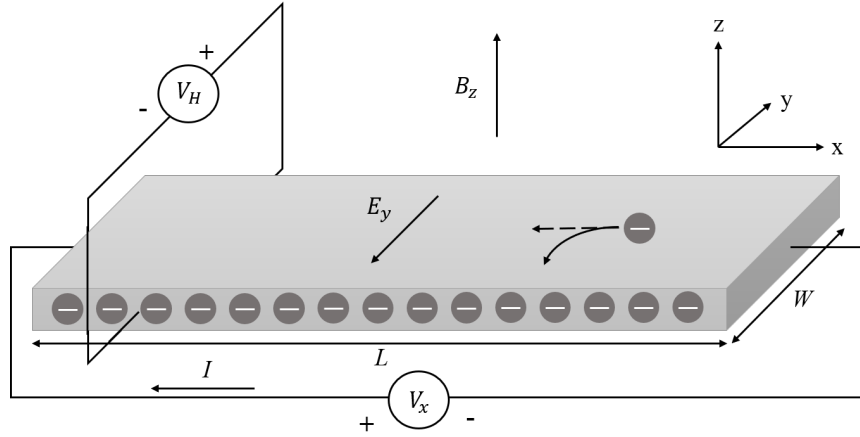


Figure 3.3: The basic setup for classical Hall effect.

force and repelling the oncoming electrons until an equilibrium state is reached such that $-eE_x = -ev_d B_z$. The transverse voltage can thus be measured with a magnitude given as

$$V_H = \frac{B_z I_x}{en_s} \quad (3.20)$$

This voltage was first discovered by Hall and this effect is known as the Hall effect. The carrier density of the sample can then be determined from the Hall voltage V_H or transverse resistivity ρ_{xy} as follows:

$$n_s = \frac{B_z I_x}{eV_H} = \frac{B}{e\rho_{xy}} \quad (3.21)$$

and the charge of the majority carrier can be determined from the polarity of V_H . Lastly, the mobility of the carriers can be calculated from the longitudinal resistivity ρ_{xx} using [Equation 3.17](#):

$$\mu = \frac{\sigma}{n_s e} = \frac{1}{n_s e \rho_{xx}}. \quad (3.22)$$

In reality, the measured Hall mobility differs from the drift mobility μ and their relationship is given by

$$\mu_H = r_H \mu \quad (3.23)$$

where r_H is the Hall factor defined as

$$r_H = \frac{\langle \tau^2 \rangle}{\langle \tau \rangle^2} \quad (3.24)$$

and is dependent on the mean scattering time of electrons between collisions caused by the scattering mechanism in the material.

3.2.2 Landau Quantization

Landau quantization refers to the quantization of the cyclotron orbits of charged particles in a uniform magnetic field. Upon the introduction of a magnetic field, the translational invariant effective mass Hamiltonian in its gauge invariant form in the quantum mechanical descriptions can be written as

$$\hat{H} = \frac{\Pi^2}{(2m^*)} = \frac{(\mathbf{p} - e\mathbf{A}(\mathbf{r}))^2}{(2m^*)} \quad (3.25)$$

where $\Pi = \mathbf{p} - e\mathbf{A}(\mathbf{r})$ is the canonical momentum operator and $\mathbf{A}(\mathbf{r})$ is the magnetic vector potential such that $\nabla \times \mathbf{A}(\mathbf{r}) = \mathbf{B}$. If we choose the Landau gauge $\mathbf{A}(\mathbf{r}) = (0, xB, 0)$, then the Hamiltonian for an electron traveling in the xy plane in a 2D material is given by

$$\hat{H} = \frac{p_x^2}{(2m^*)} + \frac{(p_y - eBx)^2}{(2m^*)} \quad (3.26)$$

Since the momentum operator p_y is absent by the choice of the gauge, by using a plane-wave ansatz for a free particle with no potential $\psi_{n,k}(x, y) = \psi_n(x)e^{ik_y y}$, the Hamiltonian for $\psi_n(x)$ becomes

$$\hat{H} = \frac{p_x^2}{(2m^*)} + \frac{e^2 B^2}{2m^*} \left(x - \frac{\hbar k_y}{eB}\right)^2 = \frac{p_x^2}{(2m^*)} + \frac{1}{2} m^* \omega_c^2 (x - x_0)^2 \quad (3.27)$$

which resembles that of a one-dimensional harmonic oscillator with an orbit center at $x_0 = \frac{\hbar k_y}{eB}$ and ω_c being the cyclotron frequency dependent on the strength of the magnetic field:

$$\omega_c = \frac{eB}{m^*} = \frac{\hbar}{m^* l_B^2} \quad (3.28)$$

where $l_B = \sqrt{\hbar e B}$ is the magnetic length or the radius of the lowest orbit. As a result, the solutions to the Schrödinger equation for the motion in x-y plane are given by quantized energy states:

$$E_n = \hbar \omega_c \left(n + \frac{1}{2}\right), n = 0, 1, 2, 3... \quad (3.29)$$

which are called *Landau levels*. When Zeeman splitting is taken into account, the spin degeneracy is lifted and each energy level will further split into a spin up and a spin-down

level separated by $\Delta E_Z = g\mu_B B$, where g is the g-factor of the material and μ_B is the Bohr magneton. Since Equation 3.29 is k -independent, states with the same n but different orbit center and k are degenerate. The magnetic flux threading the area in between the two neighboring states is found to be constant and is defined as one flux quantum:

$$\phi_0 = \frac{h}{e} \quad (3.30)$$

As a result the number of flux quanta in the sample can be associated with the number of orthogonal electron states. Thus the *filling factor*, the number of filled Landau levels, is given as

$$\nu = \frac{n_s}{n_\phi} = \frac{n_s}{\left(\frac{B}{\phi_0}\right)} = \frac{hn_s}{eB} \quad (3.31)$$

where $n_\phi = \frac{B}{\phi_0}$ is the flux quantum density in the sample.

3.2.3 Shubnikov de-Haas oscillations

The *Shubnikov-de Haas (SdH) oscillations* is a direct manifestation of the Landau quantization observed at sufficiently high magnetic fields and low temperatures. The DOS of a 2DEG is constant for each subband in the absence of a magnetic field (Figure 3.2), as discussed in subsection 3.1.3. As the magnetic field becomes strong enough such that the Landau level spacing, $\hbar\omega_c$, is greater than the thermal energy, $k_B T$, and the electron performs at least one complete cyclotron orbit without scattering, the DOS starts to form discrete delta peaks at the Landau levels as a result of Landau quantization. However, in reality, there are no perfectly clean samples and disorder, whose localized energy states could now lie in between the Landau levels (Figure 3.5(a)), broaden the DOS peaks as shown in Figure 3.4, where the broadening of the Landau levels are represented by a Gaussian form.

According to Equation 3.29 and Equation 3.31, as the magnetic field increases, the Landau levels become more widely spread and the degeneracy of each level (n_s/ν) becomes higher. Therefore, as each energy level passes through the Fermi level with increasing magnetic field, the electron states become depopulated and the effective sweeping of density of states results in the oscillation in the longitudinal resistivity ρ_{xx} . When the Fermi level lies at the center of a Landau level (Figure 3.4(a)), there is a maximum number of available *extended bulk states* for electrons to scatter into and out of, and hence ρ_{xx} is at the maximum value. As the next lower level moves towards the Fermi level with increasing magnetic field, ρ_{xx} decreases as the scattering events are reduced due to the

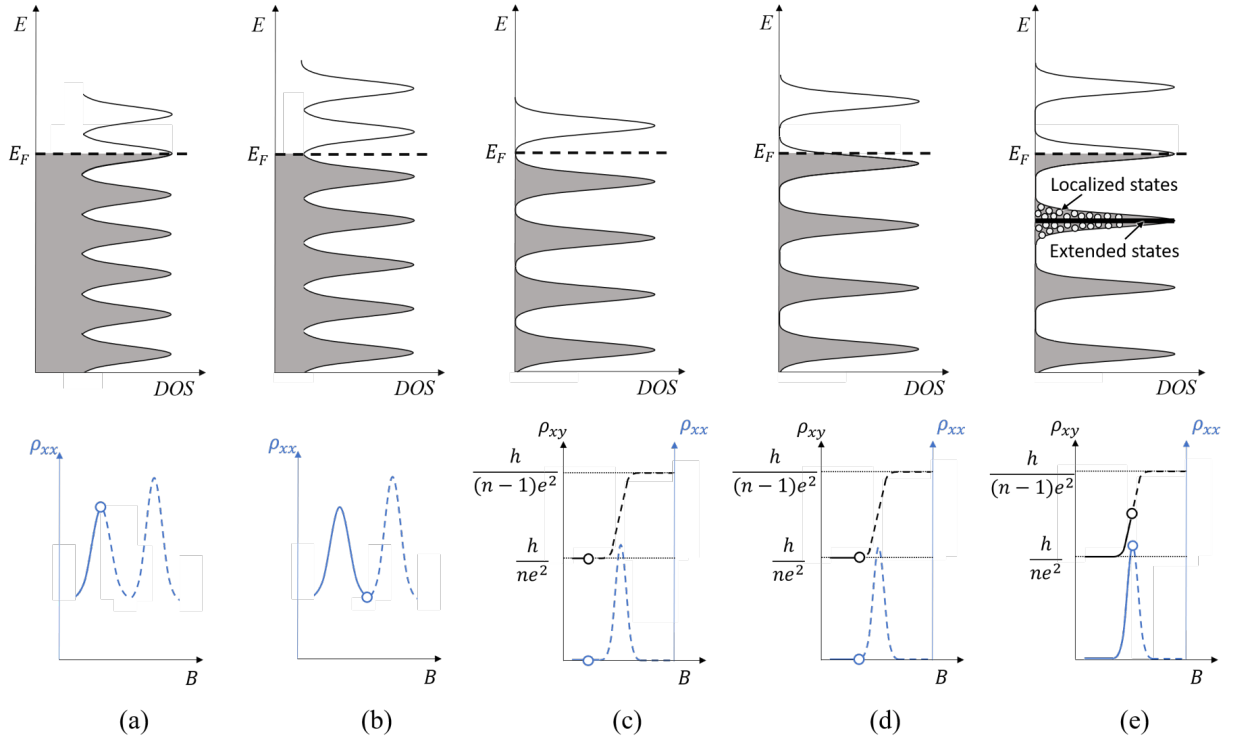


Figure 3.4: The evolution of the 2DEG density of states (top) and the corresponding ρ_{xy} and ρ_{xx} curves (bottom) as the magnetic field increases from (a) to (e).

fewer available states and is at minimum when the Fermi level lies exactly in between two Landau levels (Figure 3.4(b)). From the analysis of the periodicity of the SdH oscillations in $\frac{1}{B}$ and with Equation 3.31, the carrier density of the sample can be extracted:

$$n_{2D} = g_s \frac{e}{h} \left(\frac{1}{B_{i+1}} - \frac{1}{B_i} \right)^{-1} \quad (3.32)$$

where B_{i+1} and B_i correspond to the two successive minima (or maxima) in ρ_{xx} and g_s is the spin degeneracy.

The longitudinal resistivity ρ_{xx} does not necessarily vanish for SdH oscillations, the phenomena of ρ_{xx} reaching zero will be discussed with the behavior of transverse resistivity ρ_{xy} as the magnetic field increases further in the integer quantum Hall regime.

3.2.4 Integer quantum Hall effect

The quantum Hall effect, the quantum mechanical version of the classical Hall effect, explains the phenomena of quantized transverse Hall resistivity ρ_{xy} which exhibited step-like behavior as a function of the magnetic field. By rearranging Equation 3.21 and replacing n_s given by Equation 3.31, the transverse resistance or resistivity can be expressed as

$$\rho_{xy} = R_{xy} = \frac{B}{en_s} = \frac{h}{\nu e^2} = \frac{R_H}{\nu} \quad (3.33)$$

which is simply a constant, known as the resistance quantum R_H , divided by the filling factor. The filling factors are not necessarily integers and quantized ρ_{xy} with fractional ν can be observed with samples of very high quality. Nevertheless, here we focus on the **integer quantum Hall effect (IQHE)**, where ν takes values of integers as a direct result of Landau quantization.

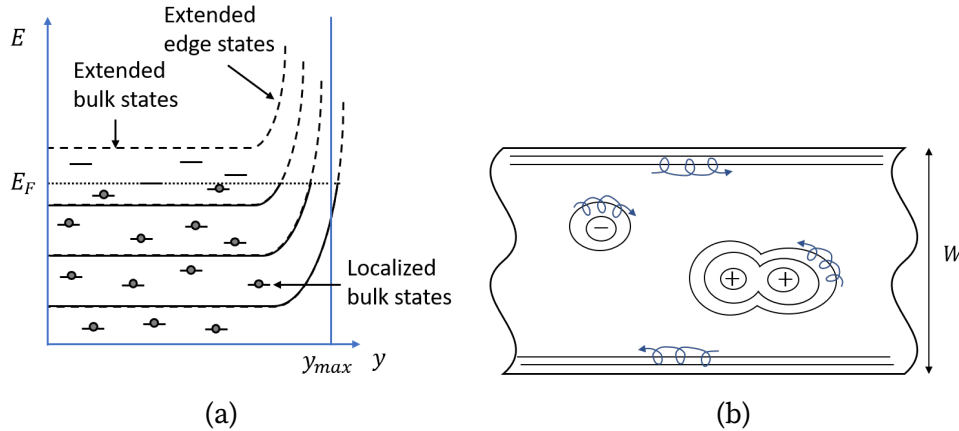


Figure 3.5: (a) Graphic illustration of the energy level bending higher at the edge of the sample. The extended bulk and edge states as well as the localized bulk states which lie in the gaps of the extended bulk states are also included in the drawing. (b) The electrostatic potential landscape of the sample as well as the chirality of the edge states and the impurity states. The equipotential lines at the edge of the samples are open and hence the edge states are extended states. The charged impurity states are localized as their equipotential lines are closed.

In **IQHE** measurements, as the magnetic field increases, the transverse resistivity ρ_{xy} plateaus and the minima of the oscillating longitudinal resistivity ρ_{xx} reach zero for a wide range of B centered around $B = \frac{hn_s}{\nu e}$, $\nu = 1, 2, 3, \dots$. Such behaviors of ρ_{xy} and ρ_{xx}

can be explained by the evolution of the density states as a function of further increase in magnetic field as shown in [Figure 3.4\(c\)-\(e\)](#). When the Fermi level is in the middle between the n th and the $(n+1)$ th Landau levels as shown in [Figure 3.4 \(c\)](#), then n Landau levels are completely filled and the $(n+1)$ th one is unoccupied. The filling factor is exactly $\nu = n$ and hence the Hall resistivity takes the quantized value of $\frac{h}{e^2 n}$. Though no bulk states are available at this condition for the current flowing in the sample, the continuity of the sample conductance is still maintained, and it is enabled by the *extended edge states*. Since the electrons at the edge of the sample will only need to complete half of their cyclotron orbits, they repeat their motions at twice the frequency than the bulk electrons which complete their whole orbits. Therefore the energy of the edge states is higher than the bulk states ([Figure 3.5\(a\)](#)), which can also be considered as a result of quantum confinement. Therefore when the Fermi level lies in between the states, the edge states ensure the continuing current flow. Moreover as shown in [Figure 3.5 \(b\)](#), the chirality is the same for all edge states at the same sample edge where the gradient of the confinement potential does not change its direction. Consequently, even if an electron is scattered from one edge state to another at the same edge it does not change its direction of motion. The electron cannot be backscattered unless it is scattered to the opposite edge with inverse chirality, which is impossible as no extended bulk states are available. As a result, the sample is effectively a bulk insulator with perfectly conducting (non-dissipative) edges and this explains the zero ρ_{xx} .

In fact, with a perfect sample where disorders are absent, the Fermi level will never stay in the gap between the Landau levels. Due to the high degeneracy of bulk states and the trivially small number of edge states, when the last electron is removed from the $(n+1)$ th Landau level with increasing magnetic field, the Fermi energy would jump almost immediately to the n th level. However, the samples in reality are full of disorders and it is exactly these disorder states as already elaborated in [subsection 3.2.3](#) that allow the Fermi level to lie in between the Landau levels ([Figure 3.4 \(e\)](#) and [Figure 3.5 \(a\)](#)).

As the magnetic field continues to increase in [Figure 3.4 \(d\)](#), the extended bulk states at Landau level n are still occupied by electrons while the disorder states in the bulk are depopulated by the Fermi level. However, these disorder states are *localized* – the electrons can only move along closed equipotential lines around the disorders in the center – and therefore do not affect the global transport characteristics ([Figure 3.5 \(b\)](#)). As a result, the Hall resistance does not even depend on the geometry of the sample! It also explains why ρ_{xy} simply remains unaltered and the ρ_{xx} stays at zero even when the filling factor is varied around $\nu = n$ by sweeping the magnetic field over a certain range. Larger plateaus hence are expected at higher fields when the spacing between the Landau levels become larger.

When the magnetic field increases further such that the Fermi level is near the center of the n th Landau level, i.e, the n th Landau level is approximately half-filled (Figure 3.4(e)), the extended bulk states in the center of the DOS peaks now dominate the transport and significantly increase the scattering events. The edge states can now also be back-scattered through the abundant bulk states. Therefore in this case ρ_{xy} is transiting from the quantized $R_H = \frac{h}{e^2 n}$ value to the next one of $R_H = \frac{h}{e^2(n-1)}$ and ρ_{xx} reaches its local maxima.

3.3 Majorana devices

3.3.1 Majorana bound states and topological quantum computing

Majorana fermions are unique fermions that are their own antiparticles, as first derived by Ettore Majorana in 1937 based on the Dirac equation [79]. While the exotic properties of Majorana fermions have drawn much attention in the high-energy physics community, the excitations with similar properties are expected to emerge in condensed matter systems as quasi-particle zero-energy Majorana bound states (MBS) or Majorana zero modes (MZM). Majorana quasi-particles however are *anyons*, not fermions. The very special thing about anyons is that if two anyons are exchanged and then exchanged back, the system does not necessarily end up in the same state where it starts. Such *non-abelian statistics* is very important as it gives rise to the topological properties of the system and basically endows it with non-local protection. Because of the topological protection, quantum computing could be performed in a so-called *braiding* process. As the anyons are interchanged, their timelines are twisted into braids, which are very robust to decoherence. Even though the environment may alter the local quantum states of the individual particles, the global information encoded in the number of such twists will not be affected. Essentially, the MZM interchanges become the quantum gates and thanks to the adiabatic theorem, such interchanges can be done literally by just moving the anyons around in 2D or 3D networks.

3.3.2 Systems hosting Majorana modes

By rearranging the conventional operators for the creation and annihilation of electrons in terms of their real and imaginary parts:

$$c^\dagger = \gamma_1 + i\gamma_2, \quad (3.34)$$

$$c = \gamma_1 - i\gamma_2, \quad (3.35)$$

the Majorana operators can be expressed in terms of the creation and annihilation operators of electrons as

$$\gamma_1 = \gamma_1^\dagger = \frac{1}{2}(c^\dagger + c), \quad (3.36)$$

$$\gamma_2 = \gamma_2^\dagger = \frac{1}{2i}(c^\dagger - c), \quad (3.37)$$

which represent equal superpositions of an electron and a hole. Hence Majorana particles can be considered as ‘half’ an electron. Such mixing of electron and hole creation operators also emerge in the formation of Cooper pairs underlying the [Bardeen-Cooper-Schrieffer \(BCS\)](#) theory of superconductivity. This suggests that a superconductor would be a natural place to find Majorana quasi-particles. In fact, because of the electron-hole symmetry inherent to superconductors, the [Bogoliubov-de Gennes \(BdG\)](#) equation describing quasi-particle excitations in superconducting systems remarkably resembles the Majorana equation.

However, zero-energy excitations are not permitted by [BdG](#) Hamiltonian for ordinary superconductors which are characterized by an order parameter with s-wave symmetry. Robust energy levels pinned to zero can exist in p-wave superconductors, which unfortunately barely exist in nature. Moreover, for non-trivial emergent excitations of Majorana modes, they need to be localized and well-separated and therefore the system must either be spinless, or spinful but with broken time-reversal symmetry. Such a system is called a *topological superconductor* – the superconductor needs to undergo a *topological transition* such that one of the degenerate phases is driven trivial by closing and reopening the superconducting gap as the *topological invariant* defined by Pfaffian invariant is changed, and the presence of a non-zero superconducting gap provides *topological protection* for the Majorana zero modes. Many theoretical models have been proposed for such topological superconductors that host stable Majorana modes. For example, it has been predicted that Majorana modes can emerge at the edge modes propagating along the boundary or occur at the vortex cores of a two-dimensional chiral $p_x + ip_y$

superconductor [80]. Among all the novel proposals, the simplest and most intuitive is probably the one constructed by Kitaev[81], which is essentially a toy lattice model for an effective one-dimensional spinless p-wave superconductor such that Majorana modes emerge at its ends.

These theoretical models however had been drawing very little interest in experimental implementations, due to the rare existence of such systems, until a major breakthrough was made by Fu and Kane [82] who proposed that the topological phase can be engineered by inducing s-wave superconductivity on the surface of a topological insulator. Following this conceptual realization, many ‘recipes’ on how to ‘cook’ effective p-wave superconductivity from conventional s-wave superconductors started to emerge. The exploit of the proximity effect was extended further from topological insulators to semiconductor heterostructures by Sau et al. [83] and Alicea [84]. Finally, Lutchyn et al. [4] and Oreg et al. [5] demonstrated a further simplified blueprint employing one-dimensional InAs or InSb semiconducting nanowires with strong spin-orbit coupling and a large g factor, which triggered a race for Majorana bound states in laboratories around the world. [10–14, 16, 85, 86].

3.3.3 Ingredients for the Rashba nanowire model

The four important ingredients that outline the Rashba nanowire model proposed by Lutchyn et al. [4] and Oreg et al. [5] for experimentally engineering a 1D spinless p-wave superconductor are (1) a 1-D semiconductor wire, (2) strong spin-orbit interaction, (3) superconductivity, (4) magnetic field.

First of all, we need a 1D semiconductor nanowire, then the Rashba spin-orbit coupling leads to an effective magnetic field B_{SO} perpendicular to the axis of the wire, as shown in Figure 3.6(a). The Rashba field lifts the spin degeneracy of the one-dimensional parabolic band except at $k = 0$ and separates the two spin branches with opposite spins relative to each other along the momentum axis, each by an amount $k_{SO} \propto \alpha$, while shifts them both down in energy by an amount $E_{SO} \propto \alpha^2$, where α is the spin-orbit coupling strength (Figure 3.6(b)).

Then if a magnetic field B is applied perpendicular to the Rashba field (Figure 3.6(a) in which B is applied parallel to the nanowire axis), it mixes both spins together with the spin-orbit interaction such that spin conservation is broken. The Magnetic field breaks the Kramer’s degeneracy so now the spin double degeneracy at $k = 0$ is also lifted and a Zeeman gap of $2E_Z \propto g\mu_B B$ is formed at $k = 0$ where g is the Landé g-factor and μ_B is the Bohr magneton (Figure 3.6(c)).

Now if the nanowire is coupled to an ordinary s-wave superconductor, the proximity effect will induce a superconducting gap Δ in the semiconductor wire, which appears at the crossings of the electron and hole branches. With the existing magnetic field and spin-orbit coupling, gaps will open at both the intraband and the interband crossings in the proximitized wire (Figure 3.6(d)).

The magnetic field tends to destroy the s-wave superconductivity by mixing up the spins of the Cooper pairs couples. Therefore the Zeeman splitting and the superconducting gap compete at $k = 0$ and when the magnetic field is increased to the critical value B_c such that the critical Zeeman splitting is given as

$$E_Z^c = \sqrt{\mu^2 + \Delta^2} \quad (3.38)$$

where μ is the chemical potential, the gap at $k = 0$ vanishes (Figure 3.6(e)), indicating that the proximitized wire is going through the topological phase transition at the moment. With further increased magnetic field, the gap reopens when $E_Z > E_Z^c = \sqrt{\mu^2 + \Delta^2}$, i.e., the Zeeman splitting finally exceeds the superconducting gap (Figure 3.6(f)). Now the wire has transited from an s-wave into a p-wave superconductor. It is also spin-less since the Zeeman field has already broken the time-reversal invariance. As a result, due to the confinement by this gap in the bulk and boundaries of the wire itself, Majorana zero modes appear at the wire ends (denoted as stars in Figure 3.6(a)). In reality, for a wire of finite length L , the oscillating MZM's wavefunction decays exponentially into the bulk of the wire.

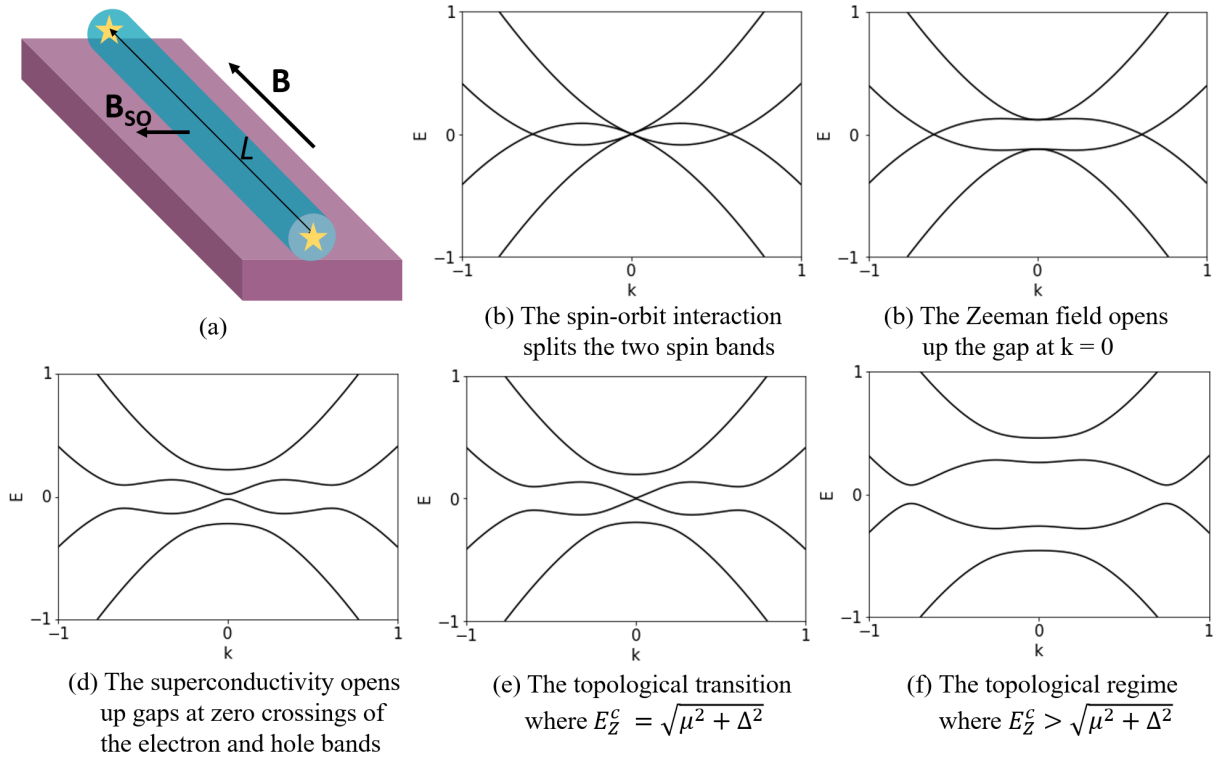


Figure 3.6: (a) Experiment setup for the Rashba nanowire model. (b-f) The energy spectrum of a Rashba nanowire generated using the kwant Python package [87], demonstrating the process of its topological phase transition controlled by the four ingredients given in the model.

Chapter 4

Experimental setup

4.1 Molecular beam epitaxy

Among epitaxial growth techniques, [molecular beam epitaxy \(MBE\)](#) offers significantly more precise growth control. As a result, it is exceptional in reproducibly growing high-crystalline-quality, low-impurity-level nanostructures with precise thicknesses and abrupt hetero-interfaces. [MBE](#) is particularly maturely developed for III-V compound semiconductors and is the most desirable technique to develop high-quality InSb [quantum well \(QW\)](#) heterostructures for this project. All the advantages of [MBE](#) are enabled by a highly complex system that requires mindful operation and meticulous maintenance.

4.1.1 GEN10™ MBE system

The Veeco GEN10™ [MBE](#) system at the University of Waterloo is configured for the growth of III-V compound semiconductors and it consists of a total of four modules: a [load lock \(LL\)](#), a [cluster tool \(CT\)](#), a [preparation module \(PM\)](#) and a [growth module \(GM\)](#). Each module is equipped with its own pumping system and is isolated from the others by an [ultra-high vacuum \(UHV\)](#) gate valve.

Load-lock chamber

The low-volume [LL](#) with a small access entry door allows wafers mounted on the substrate holders to be rapidly loaded into or unloaded out of the [MBE](#) system without affecting

the UHV environment in the other chambers. It has a vertically movable storage stage which may hold up to seven 3" diameter substrates. Once the substrate is loaded into the LL, the module is heated up to 200 °C with internal quartz lamps and the moisture and other contamination are pumped out by a turbo pump.

Cluster tool

When the pressure inside the LL is stabilized at $\sim 10^{-8}$ Torr after the outgassing process, the substrates can be transferred into the CT by an automated robot arm mounted in the center of the CT. Other than providing the wafer transfer and distribution service, the CT also serves as a storage chamber with two wafer storage stages, each with eight shelves. The pressure in the CT is maintained in the 10^{-11} Torr range by an ion pump.

Preparation module

Before being transferred in the GM for growth, the substrate is first transferred into to the PM where they can be outgassed to a much higher temperature (up to 800 °C). Depending on the type of the substrate, additional plasma cleaning using Ar or H atoms can be applied to further decontaminate the substrate surface. The GaAs substrates used in this project all went through thermal outgassing at 400 °C for at least one hour in the PM. The pressure inside the PM is maintained at $\sim 10^{-9}$ Torr by a large turbo pump.

Growth module

After proper PM treatment, the substrate is ready to be transferred into the GM for MBE growth. A schematic diagram of the GEN10™ MBE GM is shown in Figure 4.1. The background pressure of the GM is maintained under the UHV environment in the 10^{-11} Torr range (more in subsection 4.1.2). The two main zones inside the GM are the zone where the material beams are generated (more in subsection 4.1.3) and the zone where the epitaxial growth takes place on the substrate surface. The substrate mounted on the wafer holder (more in subsection 4.1.4) is held by a substrate manipulator (Figure 4.1) equipped with a motor and a rotation belt which enable the rotation of the substrate at a chosen rate to ensure a uniform epilayer layer thickness and composition across the entire wafer during the growth. Though substrate rotation is preferred for most growths, it is sometimes intentionally stopped during certain processes. For example, for some growths in this project that involves δ - doping layers, the substrate rotation

was stopped at a desirable azimuth such that a gradient δ -doping density was achieved across the wafer. Then with one single growth, multiple samples of different doping densities can be cleaved at different positions of the wafer, making the optimization of doping density in the growth structure much faster. The manipulator also has a radiative heater that heats up the substrate to the target temperature during the growth by a [proportional-integral-derivative \(PID\)](#) controller and a thermocouple positioned on the back of the substrate. The thermocouple is not in contact with substrate, because of the need to rotate the latter. More accurate substrate temperature measurement tools are installed on [MBE](#) systems, which will be discussed in [section 4.2](#), together with many other monitoring tools installed around the [GM](#) for *in-situ* characterization of the growth process.

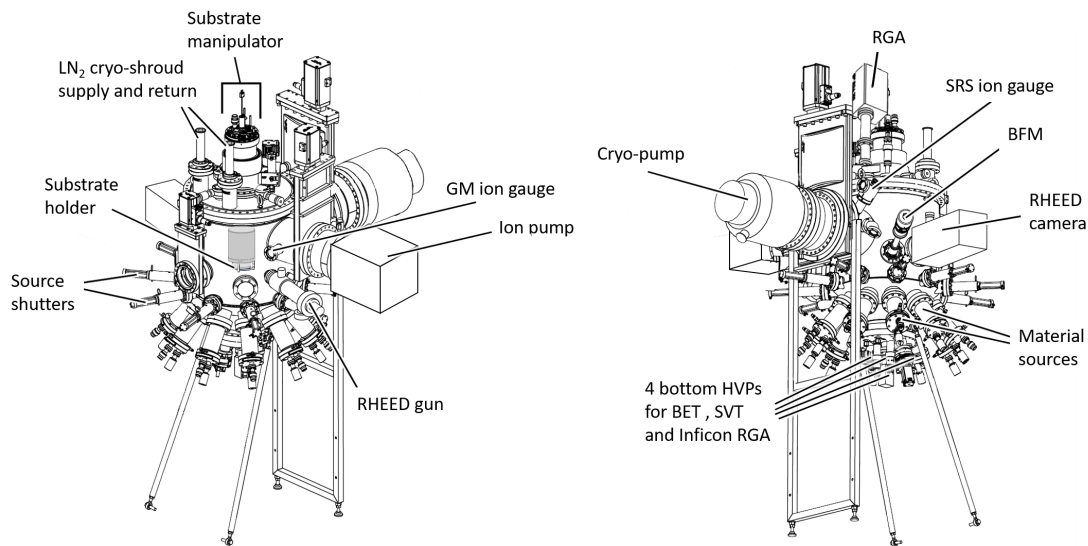


Figure 4.1: The schematics of the front and back views of the [GM](#) of the GEN10™ [MBE](#) system at the University of Waterloo. The part of the substrate manipulator that is inside the [GM](#) is represented in a gray shade. This diagram is modified based on the [GM](#) figure in the system manual provided by Veeco Instruments Inc. [[88](#)].

4.1.2 Ultra-high vacuum environment

Unlike most deposition techniques which require a [high vacuum \(HV\)](#) environment (with a total pressure of the residual gas in the reactor in the range of 10^{-3} – 10^{-9} Torr),

the background pressure in an **MBE** growth chamber is usually maintained at a pressure level of 10^{-11} Torr, which is classified as **UHV**. It ensures the high quality of the films grown by **MBE**.

The mean free path of the gas molecules is usually considered as one of the parameters characterizing the vacuum level, which is defined as the average distance of a molecule will travel before a scattering process. To ensure the beam nature of the mass flow in an **MBE** reactor, the mean free path needs to be larger than the distance between the material sources and the substrate. This, however, can be already achieved with an **HV** environment. In fact, another parameter directly related to the vacuum level, the concentration of the residue gases in the reactor, is the key reason for the **UHV** required by **MBE**. Due to the relatively low growth rates ($\sim 1 \mu\text{m/h}$) typical for **MBE**, the unintentional impurity levels embedded in the epilayer during the growth pose a much more rigorous limit on the background pressure in the **MBE** reactor. For the GEN10™ **MBE** system used in this project, the **UHV** environment in the growth module is achieved through a CT10 cryo-pump, an ion-pump and a liquid nitrogen cryo-shroud surrounding the manipulator and the effusion cell ports (Figure 4.1).

The pressure level in the **GM** and in the other chambers in the GEN10™ system are continuously monitored by ion gauges (Figure 4.1). An ion gauge consists primarily of three electrodes. A heated filament acts as the cathode which emits electrons thermionically. The emitted electrons are accelerated into a cylindrical wire cage at a higher voltage acting as the anode. The residual gas molecules inside the gauge are ionized through electron impact ionization as the kinetic energy of the accelerated electrons is higher than the ionization energy of the gas molecules they interacted with. These ionized particles are captured by a thin wire collector in the center of the wire cage negatively biased with respect to the grid. As a result, the measured collector current is proportional to the number of molecules in the gauge volume, which provides a measure for the pressure.

Other than the ion gauge, the **GM** is also equipped with a **residual gas analyzer (RGA)** located at the top of the chamber to analyze the residual gas species contributing to the background pressure (Figure 4.1). The **RGA** used for the GEN10™ system is a quadrupole mass spectrometer consisting of an ionizer, a quadrupole mass filter, and an ion detector. The ionizer operates similarly to the one in the ion gauge, except that the wire collector in the center of the grid is replaced with a focus plate to draw the ions from the anode grid into the filter section. An electron repeller covering the grid is also added to redirect the electrons back into the grid to increase ionization efficiency. The quadrupole mass-filter is composed of four cylindrical rod electrodes which can be tuned to filter the entered ions according to their mass-to-charge ratio by varying the RF and DC voltages

applied to the rods. The positive ions that are successfully transmitted through the quadrupole are focused towards the detector by an exit aperture. The ion current can be measured directly by a Faraday Cup detector or by an electron multiplier detector for partial pressures lower than 10^{-9} Torr.

4.1.3 Material beams

The atomic beams are generated from the ultra-high-purity material sources loaded into UHV compatible crucibles in the effusion cells, which face the wafer mounted in the manipulator (Figure 4.1). There are a total of ten effusion cells installed on the GEN10™ MBE system consisting of six group III cells (including two aluminum, two gallium, and two indium cells), two group V cells (arsenic and antimony) and two dopant cells. Currently, the two dopant cells are filled with silicon and beryllium, acting as n-type and p-type dopants respectively. Tellurium as n-type and carbon as p-type dopants were also used in the past. For the n-type doping used in this project, Si was used for most growths. Te was only used for a few inverted structures but it was replaced with Si in the system as Te has a long memory effect which affects other projects which involve the growth of high-mobility structures.

After loaded into the crucible as solid pallets, the elements in the group III cells are melted such that a stable evaporation flux can be maintained during the growth. Sufficient sublimation can happen at reasonably low temperatures for group V elements and the Sb and As are kept in the solid form in their bulk zones of the cells. Mono-atomic beams are produced by the group III cells, while group V elements sublime molecules. For some growths, smaller molecules are preferred and the As_4 or Sb_4 tetramers are cracked into two As_2 or two Sb_2 dimers with cracking zones. As_2 and Sb_2 are used for all the growths involved in this project, with a cracking zone temperature at 900 °C and 950 °C respectively.

Stable beams of group III elements with desired fluxes are achieved by heating the cells to the target temperature controlled by high-performance PID controllers and thermocouple feedback. The atomic flux coming out of the effusion cell is related to the vapor pressure of the group III material at equilibrium by a factor proportional to $1/\sqrt{T}$ where T is the effusion cell temperature. Since the equilibrium vapor pressure can be expressed as a Boltzmann exponential in $1/T$, an empirical relation between the effusion cell temperature, T , and the atomic flux, ϕ , impinging on the substrate per unit

time, per unit area can be written as:

$$\phi = \frac{\alpha}{\sqrt{T}} \exp\left(-\frac{\beta}{T}\right) \quad (4.1)$$

where α and β are constants that can be obtained from calibration growths.

Other than monitoring the pressure level inside the chamber (subsection 4.1.2), ion gauges are also commonly used to measure the material beam fluxes ϕ in MBE systems. We have a retractable ion gauge – beam flux monitor (BFM) – for the purpose of flux measurement (Figure 4.1). The BFM can be extended under the structure to measure the flux coming from the material cells which would reach the substrate if under a normal growth process. The collector current measured by the BFM is proportional to the number of particles entering the gauge with an area A per second and the time t they spent within a distance of L inside the gauge:

$$I \propto n \cdot t = \phi A \cdot \frac{L}{v} \quad (4.2)$$

where v is the velocity of the beam particles, which is related to the temperature of the effusion cell they are emitted from: $v \propto \sqrt{T}$. Since A and L are both constants determined by the geometry of the gauge, the beam equivalent pressure (BEP) can be expressed with a calibration constant η as

$$I = \frac{\phi}{\eta \sqrt{T}} \quad (4.3)$$

Group V cells on the other hand are kept at constant bulk and cracker temperatures during the growths and their fluxes are regulated by needle valves. Each cell port is equipped with a shutter enabling near-instant switches of the fluxes for layer interfaces with atomic precision. The *sticking coefficient* is the fraction of atoms or molecules reaching the substrate that incorporate into the growing layer. Under most growth conditions, the sticking coefficient for group III atoms is near unity while group V molecules stick only as much as needed to ensure stoichiometric growth. Therefore, group V flux is usually supplied with *overpressure* to prevent group III droplet formation and the excess amount of group V simply re-evaporates from the substrate. The V/III ratio required for stoichiometric growth usually increases with increasing substrate temperature. The sticking coefficient of Sb is much higher comparing to As, especially at lower growth temperatures. Much higher overpressure can be used for As for most growth conditions, however a rough morphology with square-like defects can be observed on the surface

with too high Sb pressure. For all the growths conducted in this project, the V/III ratio was kept greater than 1:1. As a result, it is the group III flux which determines the growth rate, R :

$$R = \frac{(a_l^{\parallel})^2 a_l^{\perp}}{Z} \cdot s \cdot \phi = \frac{(a_l^{\parallel})^2 a_l^{\perp}}{4} \cdot \phi \quad (4.4)$$

where a_l^{\parallel} and a_l^{\perp} are the in-plane and perpendicular lattice constants of the epilayer ([subsection 2.4.1](#)). Z is the number of atoms per unit cell, which is 4 for a III-V crystal and s is the sticking coefficient which can be assumed to be 1 for group III atoms.

The growth rate of a layer grown at cell flux of ϕ for a known time interval can be calculated by measuring its thickness using [high-resolution x-ray diffractometry \(HD-XRD\)](#). Then the calibration constants α , β and η can be determined by combining [Equation 4.4](#) with [Equation 4.1](#) and [Equation 4.3](#). With the calibration constants ascertained, the growth rate and composition for each layer in any material structure can be conveniently calibrated by measuring the [BFM BEP](#) before and after the growth.

4.1.4 Substrate mounting

3-inch [UHV](#) compatible molybdenum substrate holders are used to accommodate high-quality single-crystalline substrates for epitaxial growth in the GEN10™ [MBE](#) system. By using molybdenum retainer plates of difference sizes and molybdenum securing rings on the 3-inch holder, substrates in a wide range of sizes from as small as 1 cm×1 cm up to full 3 inches can be introduced into the system. In this project, either a [quarter of a two-inch \(Q2"\)](#), a [quarter of a three-inch \(Q3"\)](#), a full 2-inch, or a full 3" substrate were used. The cleaving and holder-mounting of the substrates as well as introducing the substrates into the system all take place in a class 100 Clean-Ceiling™ portable laminar flow cabinet, with the [LL](#) door inside it to minimize the combination introduced into the system during the process.

The molybdenum substrate retainer plates are usually found to contribute to a significant thermal gradient of about 5–10 °C from the center to the edge of the substrate. In cases when the uniformity of substrate temperature is critical, the normal substrate mounting configuration is modified into a setup with a sapphire plate. As shown in [Figure 4.2\(a\)](#), the normal substrate mounting for a [Q3"](#) uses a retainer plate with an opening slightly smaller than [Q3"](#) as the bottom plate and a retainer plate with an opening slightly larger than [Q3"](#) with 4 small tabs as the top plate to sandwich the [Q3"](#) substrate

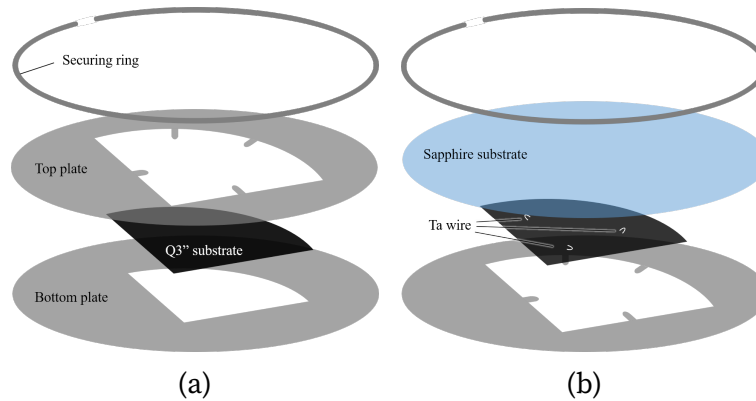


Figure 4.2: Schematic overview of the stacking sequence of the cleaved substrate, retainer plates, and securing ring on the full 3" substrate holder for (a) the normal mounting and (b) the sapphire plate mounting configuration.

in between. In the sapphire plate setup (Figure 4.2(b)), the top plate with 4 small tabs is used as the bottom plate and the top plate is changed to a full 3-inch sapphire wafer. In addition, three tantalum wires are placed between the Q3" substrate and the sapphire plate to ensure minimum thermal contact between them. As a result, the Q3" substrate mounted in this configuration is essentially suspended in the holder by only 4 small tabs and much better thermal uniformity can be achieved during the growth.

The sapphire plate mounting setup also allows the edge of the wafer to be completely exposed except for the 4 small tabs of the bottom retainer plate. As a result of mechanical polishing, commercial substrates all have a surface bowing at the edge, as illustrated in Figure 4.3, which leads to effective vicinal surfaces with different offcut angles within about 1 mm from the edge of the substrates. Therefore, by suspending a 2-inch substrate on the 3-inch substrate holder using the sapphire plate mounting, we were able to study the surface morphology of AlInSb metaphoric buffers and InSb QW heterostructures at different edge locations of the wafer as a function of the effective substrate offcut angle and offcut azimuth. (Figure 4.3(b)).

4.2 *In-situ* monitoring

Being conducted in a UHV environment, one of the strengths of MBE is that it may be controlled *in situ* by many diagnostic methods. These powerful real-time monitoring

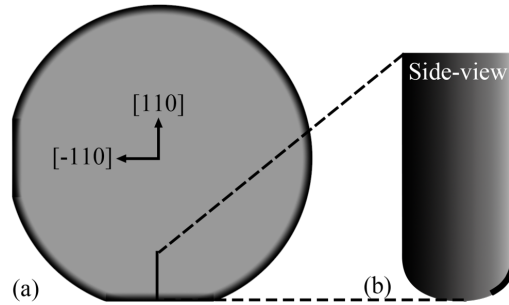


Figure 4.3: (a) The wafer polishing-induced surface bowing at the edge of the substrate. (b) Cross-section along the solid line in (a). Surface morphology at positions close to the edge on the front polished side of the wafer (region indicated by a black curve) are studied as a function of substrate offcut angle.

tools significantly eliminate the guesswork in the growth process and enable reproducible growth of sophisticated material structures.

4.2.1 Reflection high-energy electron diffraction (RHEED)

As one of the most important *in-situ* diagnostic tools for MBE, reflection high-energy electron diffraction (RHEED) is a powerful tool for real-time monitoring of the surface morphology and reconstruction of the growing epilayer as well as the growth dynamics at the surface. The RHEED setup for the GEN10™ system is shown in Figure 4.1. A high-energy electron beam is emitted by an electron gun mounted on one side of the chamber and directed towards the substrate at a glancing incident angle. Due to the low incident angle, the interaction of the electrons with the wafer is only restricted to the few atomic layers on the surface and characteristic diffraction patterns can be detected on the phosphorescent screen and recorded by a charge-coupled device (CCD) camera on the other side of the chamber. For the GEN10™ system, the *k*SA 400 software for RHEED analysis is also coupled to four external triggers which enable quasi-stationary image acquisition at chosen azimuth angles synchronized with substrate rotation.

In the kinematic theory of diffraction, constructive interference occurs when the scattering wave vector is a vector of the reciprocal lattice:

$$\mathbf{k}' - \mathbf{k}_0 = \Delta\mathbf{k} = \mathbf{G} \quad (4.5)$$

For elastically scattered electrons such that $|\mathbf{k}'| = |\mathbf{k}_0|$, the diffraction condition can be geometrically constructed using the *Ewald sphere* in reciprocal space, as shown in

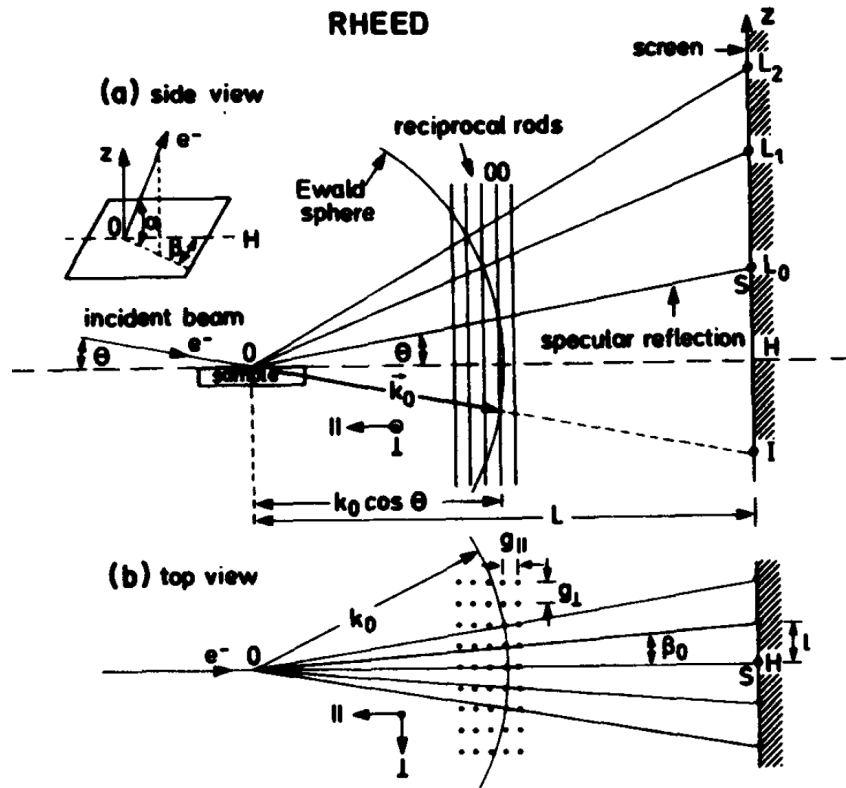


Figure 4.4: Schematics of both the (a) side view and (b) top view of the RHEED diffraction geometry and the Ewald sphere construction [adapted from [89] with permission].

Figure 4.4. The Ewald sphere is defined by a radius $|k_0|$ around the origin of k_0 . The diffraction occurs for all k' connecting to a reciprocal lattice point that lie on the surface of the Ewald sphere. Since the electrons only interact with the atoms on a two-dimensional surface, the third dimension perpendicular to the surface is missing in real space. As a result, the reciprocal lattice is transformed into a set of infinite rods along the third dimension (Figure 4.4). Due to the fact that the radius of the Ewald sphere is usually much larger than the spacing between the reciprocal lattice rods and both the Ewald sphere and rods have finite thickness, the intersection of the sphere and rods usually results in a streaky, rather than a spotty, diffraction pattern.

RHEED can be used to monitor the growth mode and surface roughness of the growing epilayer based on the characteristics of the diffraction patterns. Under the layer-by-layer growth mode and when the surface roughness is small, only the topmost atomic layers are probed by RHEED, resulting in a streaky diffraction pattern as discussed

above. Under the 3D island growth mode or when the surface is considerably rough, the diffraction pattern is produced in transmission through the surface bumps, exhibiting a spotty feature analogous to those seen in [transmission electron microscopy \(TEM\)](#). The crystalline quality of the growing material can also be monitored by the [RHEED](#) diffraction pattern. If the surface of the growing crystal is evolving from single-crystalline to polycrystalline, the diffraction of clear dots and streaks will transform into diffuse *Laude* rings. If the surface is amorphous, then only a constant diffuse background is observed. A distinct evolution from a diffusive [RHEED](#) diffraction pattern to a streaky surface pattern is used as a guide during the thermal oxide removal process for the GaAs substrate in this project, which was carried out under a high As flux at a substrate temperature of 630 °C.

Surface atoms are typically arranged differently than the bulk atoms and since [RHEED](#) is a surface-sensitive tool, its diffraction pattern provides valuable information on the reconstruction of the crystal surface. The spacing between the streaks of the [RHEED](#) pattern is inversely proportional to the periodicity the rearranged surface atoms in real space. *Wood's notation* is usually used to denote the surface atomic arrangement and a $(m \times n)$ reconstruction describes a mesh of surface unit cells that is m and n multiples of the bulk unit translation vectors in the two perpendicular directions such as $[\bar{1}10]$ and $[110]$ for an [face-centered cubic \(fcc\)](#) (001) surface respectively. If the unit cell of surface structure is centered, i.e, it has an additional atom in the center of the mesh then a notation of $c(m \times n)$ or $(m\frac{\sqrt{2}}{2} \times n\frac{\sqrt{2}}{2})R45^\circ$ is used. The surface reconstruction of a material is largely influenced by the properties of unreconstructed surface and growth conditions. Phase diagrams of different materials can be determined by varying the V/III ratios and the substrate temperatures during the growth, which are useful for the calibration of substrate temperatures as well as providing a useful feedback on the growth quality.

Transitions points in [RHEED](#) surface diffraction pattern are often used for the calibration of the minimum group V overpressures necessary to sustain group V stabilized surface reconstruction, which is referred to as a group V/III flux ratio of 1:1. For the calibration of minimum As flux, this [RHEED](#) transition point is $(2 \times 4)/(4 \times 2)$ corresponding to the As-rich/III-rich regimes. A (3×1) surface pattern can be observed near the transition between the two regimes, which is also sometimes referred to as the As-stable regime. For the minimum Sb flux calibration, the [RHEED](#) Sb-rich/III-rich transition point of $(1 \times 3)/(4 \times 3)$ is used and a (2×3) Sb-stable reconstruction is observed near the transition point. For the calibrations of minimum group V overpressures carried out in this project, the minimum As and Sb overpressures are assumed for the minimum flux which gives a persisting V-stable [RHEED](#) pattern for at least a few minutes without flipping to the III-rich pattern.

For the material structures studied in this thesis (Figure 5.2, Figure 7.1 and Figure 7.7 and more details in the corresponding chapters), the GaAs smoothing buffer has always been grown in the optimal (2×4) As-rich regime. For the growth of AlSb and GaSb layers, typical Sb-rich (1×3) RHEED surface diffraction pattern was observed, similar to Figure 4.5(b). When growing the AlInSb layers and InSb layer, several RHEED surface diffraction patterns have been observed depending on the substrate temperature and group V/III flux ratio during the growth. For AlInSb grown at 420 °C and InSb grown at 380 °C under a group V/III flux ratio of ~1.2, an asymmetric-(1×3) (a(1×3)) pattern, also known as pseudo-(1×3)), is observed (Figure 4.5(a)), corresponding to growth under flux ratios greater than 1 at higher substrate temperatures. As the substrate temperature decreases while the group V/III flux ratio increases during the growth of AlInSb and InSb layer, a more symmetric (1×3) corresponding to a more Sb-rich growth regime was observed (Figure 4.5(b)). As the substrate temperature decreases and/or the group V/III flux ratio increases further, RHEED changes to a mixed (1×3) and centered-(4×4) (c(4×)) pattern. The c(4×4) pattern, which can also be written as $(2\sqrt{2} \times 2\sqrt{2})R45^\circ$, corresponds to the Sb-rich growth regime at low substrate temperatures and was observed on the InSb surface when the substrate temperatures were further decreased (Figure 4.5(d)).

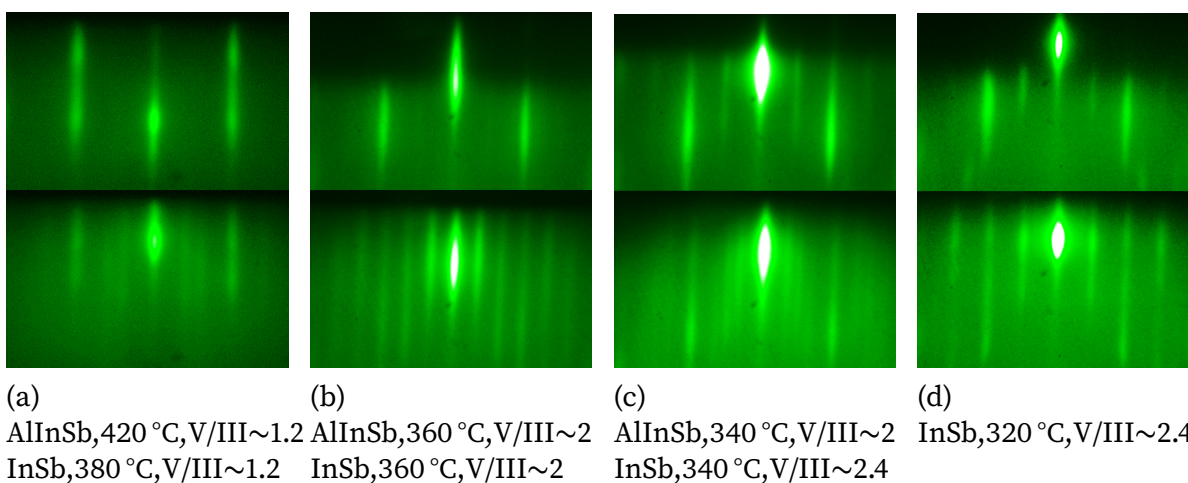


Figure 4.5: RHEED diffraction patterns acquired during growth of the AlInSb and InSb layers at different substrate temperatures and group V/III flux ratios as specified in (a)-(d).

The intensity oscillations of the RHEED features can also be used to directly determine the growth rate of the epilayer for growth grown in a layer-by-layer mode [90]. When monitored overtime, the intensity of a chosen RHEED diffraction spot, usually the

brightest specular spot, oscillates with the maxima of the intensity corresponding to fully finished layers and the minima corresponding to approximately half-finished layers with maximal surface disorder. However, usefulness of this approach is highly limited since the wafer needs to be stationary and the flux gradient makes the resulting oscillation frequency sensitively dependent on the exact electron beam positioning. In this project, **RHEED** is mainly used for the characterization of the roughness, growth mode, and the reconstruction of the surface.

4.2.2 Desorption mass spectrometry (DMS)

Other than the SRS **RGA** installed on the top of the **GM** to monitor the background residual gases in the chamber (subsection 4.1.2), we have another quadrupole based **RGA**, an Inficon Transceptor MPH, mounted at the bottom of the **GM** and used for **desorption mass spectrometry (DMS)** (Figure 4.1). A cylindrical nozzle is installed at the port with its tip pointing at the substrate to monitor the re-evaporated particles from the substrate during the growth, enabling real-time monitoring of the growth dynamics. It is especially useful in determining the group V/III ratio during the growth.

A typical Inficon **RGA** trace of Sb **partial pressure (PP)** measurement for the deposition of an III-Sb layer is shown in Figure 4.6. Both group III (in this case Al) and Sb shutters were closed for stage (i) and a background Sb **PP**, PP_{bg} , of $\sim 4.1 \times 10^{12}$ Torr was measured. Then the Sb shutter was opened at the beginning of stage (ii) and at the same time the Sb valve opening was quickly ramped from 120 mil to 200 mil. The Sb **PP** showed a rapid increase and soon stabilized at $\sim 6.2 \times 10^{11}$ Torr. Since no growth is happening at this point, this signal represents total re-emission of supplied Sb. In stage (iii), the Al shutter was opened and the growth of the AlSb layer was started, resulting in a sudden drop in the Sb **PP** due to the incorporation of Sb molecules on the substrate surface forming AlSb. In the meantime, the Sb valve opening was slowly reduced from 200 mil to 120 mil, which is clearly reflected as the slow **PP** ramp-down throughout stage (iii). The Sb valve was maintained at 120 mil for the rest of the growth and the Sb **PP** stayed relatively constant at $\sim 3.5 \times 10^{11}$ Torr throughout stage (iv). In stage (v), the growth of AlSb was stopped by closing the Al shutter, leading to an abrupt step up in the Sb **PP** to around 5.0×10^{11} Torr. The Sb shutter was then closed in stage (vi) leading to the huge drop in Sb **PP**. The whole Sb **PP** trace exhibited a slightly increasing trend, which is more noticeable during stage (v), probably due to the effect of the building up of the Sb population in the **RGA** port. The difference in the Sb **PP** during and after the growth serves a real-time quantitative measure for the V/III ratio used during the growth. In this case, the V/III ratio during the growth of the AlSb layer is equal to $(PP_{after} - PP_{bg}) / [(PP_{after} - PP_{bg}) - (PP_{during} - PP_{bg})] =$

$(5.0 - 0.4)e^{11} / [(5.0 - 0.4)e^{11} - (3.5 - 0.4)e^{11}] \approx 3.1$. A similar Sb PP difference during and after the growth was measured for each III-layer in the InSb QW heterostructures grown at similar growth conditions, which was used to confirm the same group V/III condition used during the growth.

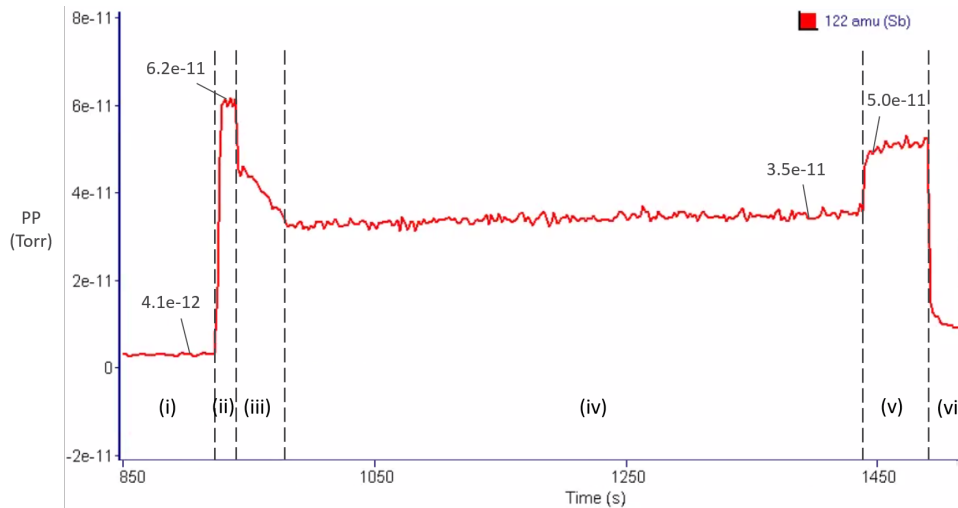


Figure 4.6: The partial pressure of Sb measured by Inficon RGA during a typical deposition process of an AlSb layer.

4.2.3 Substrate temperature monitoring

The substrate temperature strongly influences the growth dynamics and hence it is of critical importance to have good control of the substrate temperature during the growth. The manipulator thermocouple is essential for the PID control feedback. However, without physically touching the substrate, it can only provide a rough estimate of the substrate temperature. In our GEN10™ MBE system, it measures a temperature roughly 100–150 °C higher than the actual substrate temperature. Many more accurate temperature monitoring tools are usually installed on MBE systems. For the GEN10™ MBE system used in this project, accurate temperature monitoring covering a wide range of temperatures and substrate selections are enabled by three complementary methods as discussed below.

Reflectance corrected pyrometry

Pyrometry is widely used for the measurement of substrate temperature in MBE systems. It relies on the black body radiation of the substrate, which is expressed by Planck's law. Pyrometry works for many substrates, either semi-insulating or doped, as long as the sensing wavelength is carefully chosen to avoid the spectral region in which the substrate is transparent. For wide-bandgap substrates like GaAs and InP, Si sensor-based pyrometers are typically used. However, the black-body emission at substrate temperatures below 450 °C becomes too low for a usable signal-to-noise ratio. A considerably higher signal can be acquired at low temperatures for narrow bandgap substrates such as InAs and GaSb with InGaAs-based pyrometers. However, stray thermal radiation from other sources in the system such as effusion cells and heated view ports (HVP)s – a characteristic source of error for pyrometry – becomes even more severe at low substrate temperatures. For the same reason, pyrometers do not work well for smaller cleaved substrates either.

Another drawback of pyrometry arises from the light interference in semiconductor thin films which results in changes in the emissivity as the epilayer grows thicker or switching to other materials. To overcome this problem, the SVT pyrometry we have on the GEN10™ MBE system (Figure 4.1) is a reflectance compensated pyrometry and the material emissivity is corrected by the reflectance change at the pyrometry wavelength of 950nm. In most circumstances, the substrate temperature in the GEN10™ system is measured using other more reliable temperature measurement tools (see below), and the SVT instrument is mostly used for reflectance measurements where the two independent optical reflectometer signals at 950 nm and 470 nm are analyzed to provide real-time information of epilayer thickness and growth rate.

Band-edge thermometry (BET)

Band-edge thermometry (BET) is a much more reliable temperature measurement technique utilizing the intrinsic temperature dependence of semiconductor bandgaps. The bandgaps of most semiconductors are found to decrease with increasing temperature. From a light source, in our case the substrate manipulator or with an additional halogen lamp at low manipulator power settings, photons with wavelengths corresponding to energies larger than the semiconductor energy bandgap will be absorbed while those below the bandgap energy will be transmitted, resulting in a sharp absorption band edge in the transmission spectrum. As a result, accurate measurement of the substrate temperature can be made by measuring the position of this absorption edge with a

suitable spectrometer. For the GEN10™ system, an InGaAs array spectrometer is coupled to the GM bottom HVP (Figure 4.1) via a low-attenuation infrared optical fiber and a bi-convex lens.

BET is independent of background radiation in the system, material emissivity, or substrate size. It also measures temperature reliably in the low-temperature range. Though it does not work as well for doped substrates or substrates with indirect bandgaps, with good calibrations and cross calibrations with pyrometry, BET in the GEN10™ system provides reliable temperature measurements for most larger bandgap substrates. However, for substrates with small bandgaps such as GaSb or InAs, the adsorption edge falls outside of the detectable wavelength range 900–1700 nm of our InGaAs array detector. Instead of using a rather bulky and expensive Fourier spectrometer which covers a spectral range >1700 nm, we implemented a modified pyrometry technique: **integrated spectral pyrometry (ISP)** based on the BET setup we already have, which solves the temperature measurement problem for small bandgap materials.

Integrated spectral pyrometry (ISP)

ISP is essentially a modified pyrometry technique, for which the thermal radiation of the grown structure is integrated over the whole spectral range where it is fully opaque to the manipulator heater, unlike the conventional pyrometry which only relies on measurements at a single wavelength. The ISP employs the BET setup and it is calibrated with the BET measurement using a Q2" small-bandgap InAs substrate indium-mounted on a full 3" large-bandgap GaAs semi-insulating substrate. As shown in Figure 4.7, the GaAs substrate is mostly covered by a Molybdenum plate, except for a very small gap at the corner of the pie-shaped opening. The bi-convex focusing lens limits the radiation collection within a spot of approximately 10 mm in diameter, which is shifted between the exposed GaAs region for BET measurements and the center of the InAs substrate for pyrometry measurements during the calibration process. The ISP signals are collected by integrating the spectrometer response over the entire 900–1700 nm range. Both the ISP signals, I_{InAs} and the BET temperatures, T_{BET} (°C) were measured at a series of temperature setpoints and fitted with an Arrhenius-type exponential relation to obtain constants C_1 and C_2 :

$$I_{\text{InAs}}(T_{\text{BET}}) = C_1 \exp\left(-\frac{C_2}{T_{\text{BET}} + 273}\right) \quad (4.6)$$

Then any **ISP** temperatures can be determined from the acquired **ISP** signals after subtracting the measured background scattered radiation from all other sources $\sum_j I_j$:

$$I_{\text{InAs}}(T_{\text{ISP}}) = I_{\text{all}}(T_{\text{ISP}}) - \sum_j I_j = C_1 \exp\left(-\frac{C_2}{T_{\text{ISP}} + 273}\right) \quad (4.7)$$

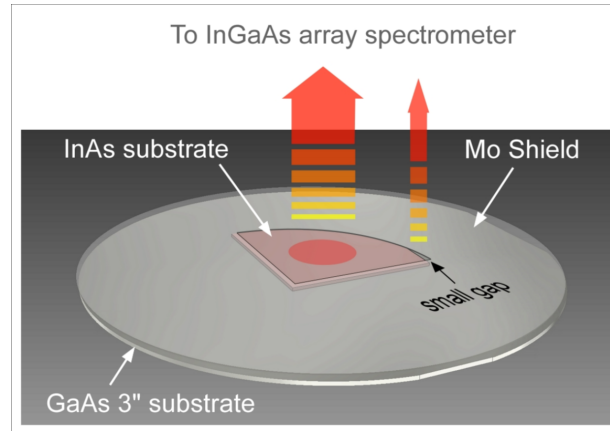


Figure 4.7: Schematic illustration for the substrate mounting configuration used for the calibration of **ISP** with the GaAs substrate exposed in only a small opening enclosed by the Mo plate and the InAs substrate.

Temperature measurement for InSb QW heterostructure growth

The substrate temperature measurement for InSb **QW** heterostructures is a very special case. This is because the growth starts with a large-bandgap GaAs substrate, yet as the metamorphic buffer of low-bandgap $\text{Al}_x\text{In}_{1-x}\text{Sb}$ with low x value grows thicker, the wafer gradually becomes opaque for whole spectrometer range. Therefore, both **BET** and **ISP** are measured throughout the growth and the substrate temperature is taken from either one of them depending on the growth stage. A typical substrate temperature measurement trace for the InSb **QW** structure growth is shown in [Figure 4.8](#). In stage (i), the native oxide was desorbed at a substrate temperature of 630 °C. Stage (ii) consists of the growths of a GaAs smoothing layer at 580–620 °C, an AlSb nucleation buffer at 500 °C, and a GaSb cap layer at 475 °C. In both stage (i) and (ii), the substrate temperature was accurately measured by **BET**, while a much higher **ISP** signal was acquired due to transmission of the substrate manipulator radiation through the GaAs wafer. During

stage (iii), as the $\text{Al}_{0.12}\text{In}_{0.88}\text{Sb}$ metamorphic buffer grows thicker and the wafer turns more opaque in the bandgap spectral range, **BET** reading became noisier and eventually become undetectable at around $t \sim 13000\text{s}$. T_{ISP} is still much higher than the actual substrate temperature at this point as appreciable radiation from the manipulator still managed to transmit through the wafer. As the growth of the metamorphic buffer continues, T_{ISP} keeps dropping as the radiation transmission reduces. Eventually at around $t \sim 25000\text{s}$, T_{ISP} starts to stabilize at around 420°C , which was equal to the last readable **BET** signal. The up and down steps in T_{ISP} are resulted from the opening and closing of Al and In shutters during the growth and during ramping of cells respectively. Such steps can be eliminated by compensating the stray intensity changes associated with shutter opening and closing. At last in stage (iv), the substrate temperature was lowered by 40°C according to the substrate manipulator thermocouple T_c for the $\text{InSb}/\text{Al}_{0.12}\text{In}_{0.88}\text{Sb}$ QW region with Te δ -doping. A similar drop in T_{ISP} was observed and the constant **ISP** reading at this point suggests negligible effect of radiation transmission from the manipulator, confirming a reliable **ISP** measurement.

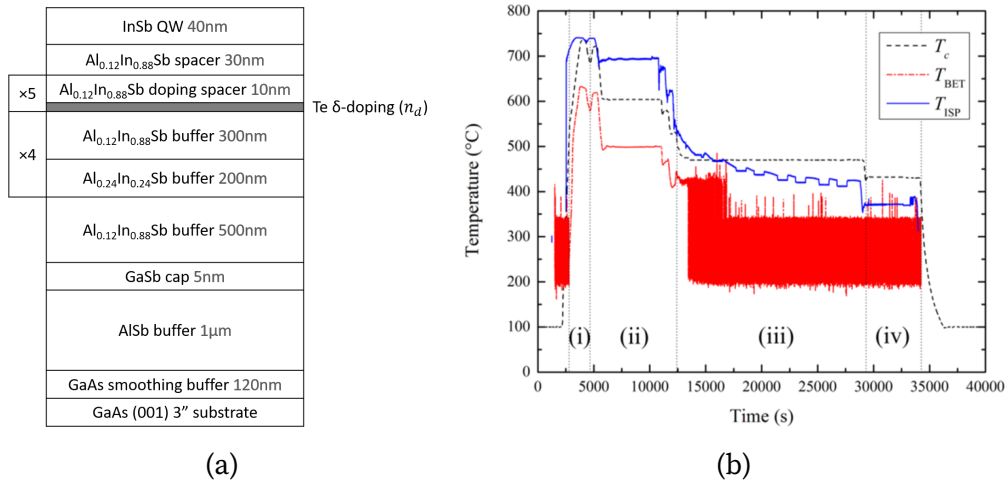


Figure 4.8: (a) The schematic overview of a typical InSb QW heterostructure and (b) the plot of the substrate temperature measured by the thermocouple (T_c), **BET**, and **ISP** during the growth with the four growth stages indicated in (a).

The **ISP** calibration was only performed with an InAs wafer, yet the similarity in the emissivity of $\text{Al}_x\text{In}_{1-x}\text{Sb}$ with InAs results in a very small error. Though more accurate measurement can be achieved by multiplying **ISP** reading by the emissivity ratio for the two materials, the reproducibility of the substrate temperature measurement is more important than the absolute temperature in most **MBE** growth.

4.3 *Ex-situ* characterization

After being taken out of the [MBE](#) system, the grown wafers can be further characterized with *ex-situ* analytical techniques to acquire information on the properties of the material structures in many aspects.

4.3.1 Nomarski differential interference contrast (DIC) microscope

A Nomarski [differential interference contrast \(DIC\)](#) microscope in the QNC-MBE lab is used for a quick and convenient inspection of wafer surface morphology over large areas. The light source in the microscope is polarized then separated by a Wollaston prism into two mutually coherent but orthogonally polarized beams. The two beams are focused on the sample surface where they are sheared (spatially displaced) and hence experience different optical path lengths. After being reflected from the surface, the two beams are recombined by a second Wollaston prism leading to interference due to their phase difference. The resultant contrast gives an image with a shadowed-like three-dimensional appearance corresponding to the actual topography of the sample surface. The much higher sensitivity of Nomarski microscopes to the vertical displacements of surface features than the conventional optical microscopes makes them an essential characterization tool in an [MBE](#) lab.

The Nomarski microscope used in this project is a Nikon Corporation Optiphot 66 equipped with a SPOT digital camera which has a lateral resolution of about 200nm and high vertical sensitivity on the order of about 1nm.

4.3.2 Atomic force microscopy (AFM)

[Atomic force microscopy \(AFM\)](#) is a powerful surface analysis technique that can be used for investigating in even smaller surface features that optical microscopes fail to resolve. During operation, a sharp tip connected to the end of a cantilever is scanned over the surface of the sample. The change in the force between the tip and sample deflect the cantilever according to fluctuations in the surface topography. A laser beam is reflected off the cantilever to a detector, which offers a feedback loop for [AFM](#) controlling the force and tip position. The cantilever deflection is measured by the changes in the laser reflection direction, enabling direct imaging of the sample surface with a high vertical resolution in the order of Angstroms. With the use of a conductive probe tip and a voltage

bias applied between the tip and the sample holder, a conductive AFM (C-AFM) can be operated. By simultaneously measuring the surface topography and the tunneling current as a function of the tip contact position on the surface, the resistivity map of the sample surface can be studied when compared with its topology image.

A Veeco Nanoscope MultiMode AFM and a Bruker FastScan/Icon AFM in tapping mode were used to study the surface morphology and dislocations for the material structures grown in this project, both offering high-quality topology images revealing atomic steps.

4.3.3 Scanning electron microscopy - electron channeling contrast imaging (SEM-ECCI)

In order to study the nano-scale features of materials and devices, electron microscopes with much higher resolving power than optical microscopes are compulsory and among which scanning electron microscopy (SEM) is probably one of the most widely used ones. SEM uses a focused beam of high-energy electrons to raster the sample. The incident electrons lose their energy in various mechanisms as they interact with the sample, producing a variety of signals which can be detected by different types of detectors. SEM is most commonly used to study the surface topology via secondary electrons. Back-scattered electrons (BSEs) are also widely detected to study the chemical composition. Though the direct observation of crystal defects is usually thought to be studied by TEM, it has been demonstrated that SEM operated in the electron channeling contrast imaging (ECCI) mode with highly parallel electron beams of high current density enables a convenient, non-destructive and direct observation of crystal defects over a large area on the surface of bulk samples. [91] In this technique, the primary beam that enters the crystalline sample undergoes multiple scattering events by the crystal lattice and are eventually back-scattered to leave the entry surface to be detected by an electron back-scatter diffraction (EBSD) detector. The intensity of the BSEs depends on the orientation of the 'channels' defined by the crystal lattice with respect to the direction of the primary beam and as a result the local variations in the crystal lattice give rise to the contrast in the BSE yield corresponding to the local crystal defects and strain field.

In this project, SEM-ECCI was performed with a Zeiss Supra 55VP Field Emission SEM in the back-scattering geometry, where the sample was placed horizontally at approximately 90° to the highly parallel impinging electron beam with the BSEs detected by an angle-selective backscatter (AsB) detector integrated into the pole piece of the GEMINI objective lens. The ECCI mode in this study was operated with the largest

aperture in a high beam-current mode, at a high accelerating voltage of 12 kV, and a short working distance of 1.5 mm for imaging.

4.3.4 Scanning transmission electron microscopy (STEM)

TEM is another commonly used electron microscope. Unlike **SEM** which sweeps the electron beam across the sample surface and detects the reflected electrons, **TEM** collects the electrons transmitted through a much thinner sample, analogous to a slide projector except the light source is replaced by an electron source. As a result, **TEM** provides detailed information on the internal structure of the sample, such as crystal structure, morphology and strain field, grain boundaries and defects at a sub-nanometer resolution. However, the thinning process required to prepare samples suitable for **TEM** imaging requires additional equipment and is technically challenging. **Scanning transmission electron microscopy (STEM)** is a type of **TEM** that combines the principles used by both **TEM** and **SEM** such that the transmitted signal is collected as the electron beam is rastered across the sample. When using a **high-angle angular dark-field (HAADF)** detector, an annular dark-field image is generated by the incoherently scattered electrons at a very high angle, which is highly sensitive to the atomic number of the atoms in the sample, resulting in directly interpretable Z-contrast imaging as well as crystal defect detection from the structural differences.

The samples studied in this thesis were prepared for cross-sectional **STEM** using a focused ion beam, and the dislocation generation and filtering progress throughout the material structures were investigated with a Zeiss Libra 200MC **TEM** in the **HAADF** mode.

4.3.5 Defect selective etching (DSE)

Defect selective etching (DSE) has been a widely studied technique for revealing and characterizing the defects in the crystals. With an optimized etching recipe, it allows for a simple, and low-cost assessment for a broad range of defect types. Two primary modes of selective-etching for defects in semiconductors are typically used. One is the orthodox chemical etching where valence electrons are exchanged between the etched surface and the etchant through chemical reactions. The etchant is selected such that the etch rate is faster in certain crystallographic directions. The other one is an electrochemical etching, where an external voltage source was used to supply the charge carriers to rupture the surface bonds. With either mode of etching, the outcrops of defects on the

surface are revealed as **etch pit (EP)** and imaged with instruments such as Normaski **DIC** microscope or **SEM**.

In this project, orthodox chemical **DSE** was performed with the **diluted sirtl-like mixture with light (DSL)** ($\text{CrO}_3 - \text{HF} - \text{H}_2\text{O}$) etching method [92] on AlInSb buffers. A $\text{D}_{1:2}\text{S}_{1/5}$ solution was applied for 30 s at room temperature under halogen lamp illumination. The subscript notation for the etching solution is adopted from Weyher and van de Ven in Ref. [93], where $\text{D}_{1:2}$ means that a one volume part of HF/ CrO_3 Sirtl-like basic mixture is diluted with two volume parts of water, and $\text{S}_{a/b}$ means that the Sirtl-like basic mixture consists of a and b volume parts of HF (48 wt. %) and CrO_3 (33 wt. %) aqueous solutions, respectively. The surface **EPs** after selective etching was examined and counted using Nomarski **DIC** microscopy. A procedure of two-step etching followed by **DIC** microscopy examination was used to confirm the correlation between the dislocations and the **EPs**.

4.3.6 Secondary ion mass spectrometry (SIMS)

Secondary ion mass spectrometry (SIMS) is a widely used technique to analyze the trace elements in solid materials, especially semiconductors. **SIMS** uses an ion gun to generate a primary ion beam which is then accelerated and focused by an ion column to sputter the sample under high vacuum. As the primary ion beam interacts with the sample, a fraction of the sample particles are ionized and emitted from the surface, producing secondary ions depending on the ions composing the primary beam. These secondary ions are then collected and analyzed according to their mass/charge ratios by a mass spectrometer (subsection 4.1.2).

SIMS is considered the most sensitive technique for elemental detection. Since it can provide elemental depth profiles with very low concentrations, the grown materials in this project were sent to EAG Laboratories, a commercial material testing company, for **SIMS** measurements to study the Si segregation effect in the structure.

4.3.7 High-resolution x-ray diffractometry (HD-XRD)

HD-XRD is a non-destructive technique widely used to study the structural properties of high-quality crystalline materials, including the epilayer composition, thickness, strain relaxation, tilt, curvature, and defect densities.

The Jordan Valley QC3 diffractometer in the QNC-MBE lab consists of an X-ray source, an X-ray tube, a sample stage, a detector and a goniometer. The X-ray tube conditions

the divergent X-rays to a highly parallel Cu- K_α beam with a wavelength of $\lambda_x = 1.54056\text{\AA}$. The detector has an adjustable slit for the option of using a high-resolution triple-axis analyzer crystal. The goniometer provides independent rotational motions for both the sample stage and the detector stage. The rotation and translation axes available in this machine are shown in [Figure 4.9](#). The sample stage has three rotation axes, allowing different scanning modes. The rotation around the ω -axis changes the incident angle of the X-ray on the sample. χ allows the sample to be tilted in the direction perpendicular to the diffraction plane. ϕ rotates the sample in the sample plane. The sample stage also has three translation axes (x, y, z) such that different spots on the sample can be scanned, enabling a whole wafer mapping. Lastly, the detector can be rocked to different 2θ angles.

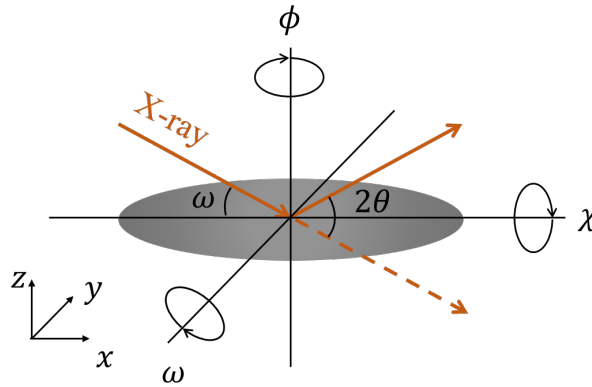


Figure 4.9: Rotation and translation axes enabled by the Jordan Valley QC3 diffractometer

For an X-ray beam incident at an angle θ on a set of parallel lattice planes, the condition for constructive interference is determined by Bragg's law as

$$2d \sin \theta = n\lambda_x \quad (4.8)$$

where d is the spacing between adjacent lattice planes. For III-V pseudomorphic or metamorphic epilayers, a crystal structure with a tetragonal unit cell can be assumed, then the inter-planar spacing can be expressed in terms of the Miller indices (refer to [section 2.1](#)) as:

$$\frac{1}{d_{hkl}^2} = \frac{h^2 + k^2}{a_{\parallel}^2} + \frac{l^2}{a_{\perp}^2} \quad (4.9)$$

where a_{\parallel} is the in-plane lattice parameter, and a_{\perp} is the lattice parameter perpendicular to the lattice plane.

In a double-axis scan, the detector is unable to discriminate between different diffraction angles 2θ over a small range which are therefore all measured simultaneously. The use of the triple-axis crystal allows the position of the detector to be defined more precisely. As a result, a much narrower range of 2θ is measured in a triple-axis configuration.

A symmetric scan is taken when $\omega = \frac{1}{2}2\theta$, such that the diffraction vector s is normal to the surface of the sample. Then the vertical lattice parameter a_{\perp} can be measured. The symmetric diffraction planes are very convenient to measure and generally produce intense peaks which high resolution and accuracy. However for relaxed alloy epilayers, both composition and relaxation can influence a_{\perp} . In order to correctly determine the composition and relaxation, the lateral lattice a_{\parallel} also needs to be determined. The diffraction planes which are not parallel to the sample surface can be measured by tilting the sample in asymmetric scans. In the case when $\omega < \frac{1}{2}2\theta$, it is called the grazing incidence geometry and the grazing exit means that $\omega > \frac{1}{2}2\theta$.

Rocking curve

A rocking curve is scanned when the sample is rotated about the incident x-ray to vary ω while the detector is fixed at twice the Bragg angle 2θ . The scanning trace in reciprocal space can be pictured as an arc centered on the origin within the accessible space defined by the diffractometer (Figure 4.10). Since only one d_{hkl} is probed, a rocking curve works the best for lattice-matched epilayers whose Bragg angle is about the same as that of the substrate. The peak position is essentially determined by the Bragg angle and the ω offset angle: $\omega = \frac{1}{2}2\theta + \theta_t$, therefore both the tilt in the crystallographic planes and the change of Bragg angle due to strain in the epilayer can shift the rocking curve peak positions in a double-axis setup. With more defined Bragg angles using a triple-axis crystal, the information of the layer tilt, curvature, and mosaic spread can be accurately measured by eliminating the effect from the layer strain. In addition, a perfect crystal has an intrinsic width of the diffraction peak for the scanned crystallographic planes, while defects in real crystals broaden the peak beyond its intrinsic width. Therefore, triple-axis rocking curve scans provide a good estimate of the defect densities in the material.

Coupled scan

An ω - 2θ coupled scan is the most common type of scan performed, in which the sample and the detector are rocked together with the detector at twice the speed to ensure that

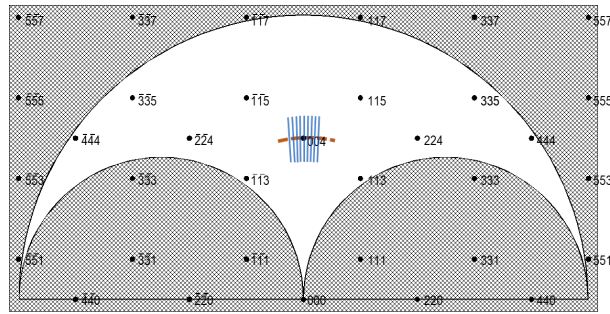


Figure 4.10: A schematic of the Ewald sphere in the reciprocal space defined by the diffraction conditions for a (001) orientated single-crystal material. The light area represents the area from which a diffraction spot is physically possible for the machine and the hatched regions are not accessible due to the limited range of the diffractometer in use. The orange dash line represents a rocking curve. The blue solid lines together constitute an **reciprocal space map (RSM)** with each one of the lines representing a coupled scan.

ω always equals to 2θ . In the reciprocal space, a coupled scan can be represented by a straight line pointing away from the origin (Figure 4.10). Therefore all the possible d_{hkl} of the same hkl planes are measured and coupled scans can be used to determine the presented epilayers in the structure. The thickness of the epilayers can be determined from the width of their Bragg peaks and the width of the interference fringes. Moreover, by analyzing the positions of the Bragg peaks, the strain and composition corresponding of different epilayers can be calculated. For layers with relaxation, symmetric scans need to be coupled with asymmetric scans together to accurately acquire both the composition and the relaxation degree of layers. With the use of a triple-axis crystal, high-resolution Bragg peaks can be achieved with a more accurate measure of d_{hkl} .

Reciprocal space map (RSM)

The peak positions in a single coupled scan are affected by many aspects of the layers, including the tilt, strain/relaxation, and composition. Therefore, a series of coupled scans usually need to be performed to separate these contributing factors. For more complicated material structures, an **RSM** is usually acquired, which is typically done by collecting multiple coupled scans with varying the relative ω angle. As a result, the scanning region with an **RSM** can be visualized as the area covered by all the straight lines across the ω arc in the reciprocal space (Figure 4.10). By mapping out the reciprocal space directly, tilt and mosaic spread can be easily separated from other lattice-related features

such as strain and composition by a symmetric RSM, while composition, relaxation as well as tilt and defect information of different layers can all be independently reflected in an asymmetric RSM. With careful interpretations, symmetric and asymmetric RSMs together can provide a very comprehensive analysis of the material structure.

Exemplar symmetric (004) and asymmetric (115) RSMs of an InSb QW heterostructure grown on GaAs (001) substrate are shown in Figure 4.11, with the material of the main peaks labeled. The $\text{Al}_{0.1}\text{In}_{0.9}\text{Sb}$ and InSb peaks in the (004) RSMs taken at both $\phi = 0^\circ$ (Figure 4.11(a)) and $\phi = 90^\circ$ (Figure 4.11(b)) are off the straight line connecting from the origin to the substrate peak, indicating that the layers are slightly tilted in both [110] and $[\bar{1}\bar{1}0]$ crystallographic directions. The tilt component in either $\langle 110 \rangle$ crystallographic direction can be directly deduced from the (004) RSM plotted in reciprocal lattice units such as $1/\text{\AA}$ as:

$$\tan(\theta_t) = \frac{\Delta q_y^{004}}{\frac{4}{a_s} - |\Delta q_z^{004}|} \quad (4.10)$$

where a_s is the lattice constant of the substrate, while Δq_z^{004} and Δq_y^{004} are the peak splittings in [001] and either one of $\langle 110 \rangle$ directions respectively. If the (004) RSM is plotted in terms of the unit-less h, k, l Miller indices such as in Figure 4.11, θ_t can be expressed as:

$$\tan(\theta_t) = \frac{\Delta h^{004}}{l_l^{004}} \quad (4.11)$$

where l_l is the l value of the layer peak.

The $\text{Al}_{0.1}\text{In}_{0.9}\text{Sb}$ peaks in the grazing incident (115) RSMs taken at both $\phi = 0^\circ$ (Figure 4.11(c)) and $\phi = 90^\circ$ (Figure 4.11(d)) fall very close to the (115) line in the reciprocal space, indicating that the $\text{Al}_{0.1}\text{In}_{0.9}\text{Sb}$ layers in the structure are nearly fully relaxed. On the other hand, the InSb peaks in both (115) asymmetric RSM lie almost exactly on the vertical line in the [001] direction going through the center of the $\text{Al}_{0.1}\text{In}_{0.9}\text{Sb}$ peaks, suggesting that the InSb layer in the structure is nearly fully strained to the $\text{Al}_{0.1}\text{In}_{0.9}\text{Sb}$ parallel lattice constant.

After subtracting the tilt, the lattice mismatch in the [001] growth direction can be calculated from the (004) RSM in $1/\text{\AA}$ units as:

$$\frac{a_l^\perp - a_s}{a_s} = \frac{-\Delta q_z^{004}}{\frac{4}{a_s} + |\Delta q_z^{004}|} \quad (4.12)$$

and the parallel lattice mismatch in the [110] or $[\bar{1}\bar{1}0]$ directions can be determined from

the (115) **RSM** in $1/\text{\AA}$ units as:

$$\frac{a_l^{\parallel} - a_s}{a_s} = \frac{-\Delta q_y^{115}}{\frac{\sqrt{2}}{a_s} + \left| \Delta q_y^{115} \right|} \quad (4.13)$$

For **RSM** plotted in the h, k, l units, the lattice mismatch in the perpendicular and parallel directions are written as:

$$\frac{a_l^{\perp} - a_s}{a_s} = \frac{l_s^{004} - l_l^{004}}{l_l} \quad (4.14)$$

$$\frac{a_l^{\parallel} - a_s}{a_s} = \frac{h_s^{115} - h_l^{115}}{h_l} \quad (4.15)$$

From the perpendicular and parallel lattice constants of the layer a_l^{\perp} and a_l^{\parallel} , the lattice constant a_l and the composition x of the relaxed layer can be determined from two independent equations of a_l expressed in terms x . One is Vegard's law for a_l as a function of x and the other is a_l expressed in terms of a_l^{\perp} and a_l^{\parallel} :

$$a_l = \frac{-(a_l^{\perp}(\nu - 1) - 2\nu a_l^{\parallel})}{1 + \nu} \quad (4.16)$$

where the Poisson ratio ν is again dependent on the composition through Vegard's law. Lastly, the percent relaxation of the layer can be calculated as

$$R\% = \frac{a_l^{\parallel} - a_s}{a_l - a_s} \cdot 100\% \quad (4.17)$$

The Al composition x and the relaxation degree $R\%$ for the $\text{Al}_x\text{In}_{1-x}\text{Sb}$ layers in the InSb heterostructures were determined by fitting the peak positions with PeakSplit, a **HD-XRD** data analysis software provided by the Jordan Valley company. Similar a_{\perp} and a_{\parallel} and close to 100% of relaxation were found for the $\text{Al}_x\text{In}_{1-x}\text{Sb}$ layers in all the InSb heterostructures studied in this project. This is exactly what to be expected as the $\text{Al}_x\text{In}_{1-x}\text{Sb}$ layers include a metaphoric buffer of a few μm s in thickness to bring the lattice constant of the material structure from that of the GaAs substrate to that close to the InSb **QW** (**chapter 5**). The **HD-XRD RSM** analysis has also confirmed that the InSb **QW** in the heterostructures is close to being fully strained by the $\text{Al}_x\text{In}_{1-x}\text{Sb}$ barrier material without signatures of relaxation as intended.

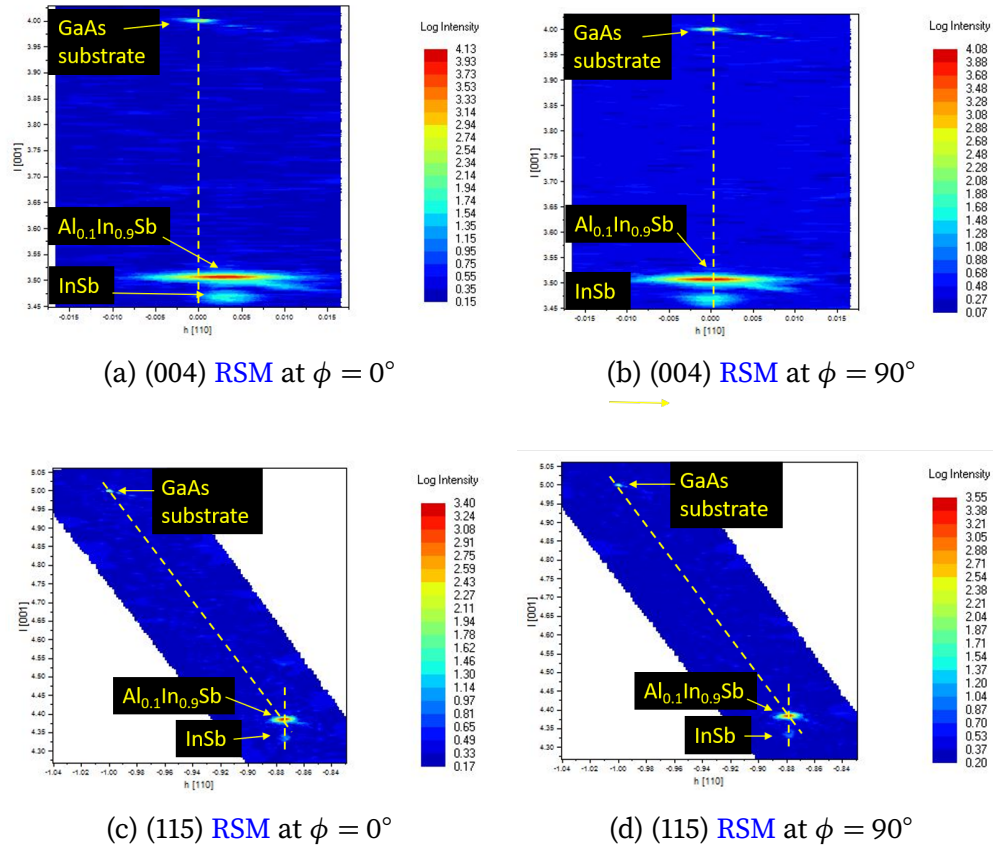


Figure 4.11: Symmetric and asymmetric RSMs of a typical InSb heterostructure studied in this thesis with the main layer peaks labeled.

4.4 Transport characterization

4.4.1 Hall measurements

To characterize the quantum-mechanical transport properties of our InSb QW heterostructures, the wafers are fabricated for low-temperature Hall measurements. The device fabrication (see [Appendix A](#)) and transport measurements in this thesis were performed by Emma (Annelise) Bergeron, Ph.D. candidate with the help from Dr. Francois Sfigakis in our collaborator Professor Jonathan Baugh's research group. Fabricated samples were measured in a Janis liquid Helium Cryostat with a variable temperature controller which allows measurements to be performed in a temperature range from

290 K down to 1.4 K. The system is equipped with a superconducting magnet which can generate a perfectly aligned magnetic field of a variable range from -6 T to 6 T. For the measurements of the [Shubnikov-de Haas \(SdH\)](#) oscillations and the quantum Hall effect, the longitudinal and transverse voltages were measured using standard 4-point constant-current AC lock-in techniques at low frequency (10 Hz) for a magnetic field range of 0 to 5 T. An AC signal of 1V is provided by the output of an SR830 lock-in amplifier and sent through a 1 M Ω resistor in series with the sample, yielding a very small constant current of 1 μ A through the sample with reduced Joule heating effect.

The ability to modulate the carrier density of a 2DEG in the structure with a top gate is of high significance in many applications including the pursuing of Majorana devices with 1D channels in our case. For gated devices, as the carrier density in the 2DEG becomes completely depleted by an increasing negative top gate voltage, the sample will become much more resistive than the 1 M Ω resistor in series. To prevent potential damaging of the device from the high voltage drop across the sample, the experimental set-up for the gate measurements in the pinch-off regime was changed from a constant current configuration to one with constant voltage by replacing the 1 M Ω resistor with a voltage divider as illustrated in [Figure 4.12](#). More details on the measurement set-ups can be found in Bergeron's M.Sc thesis [94].

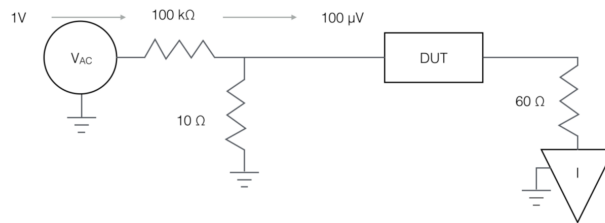


Figure 4.12: Circuit diagram of the 1/10 000 voltage divider used in the gate measurements in the pin-off regime. The resistance of the shunt resistor (10 Ω in this case) must be much less than the resistance of the sample R_{DUT} .

The carrier density and mobility of the InSb [QW](#) samples are attained from the longitudinal and transverse resistivities (using [Equation 3.21](#), [Equation 3.32](#) and [Equation 3.22](#)) measured in either one of two geometries, van der Pauw or Hall bar, as shown in [Figure 4.13](#), each with its own advantages.

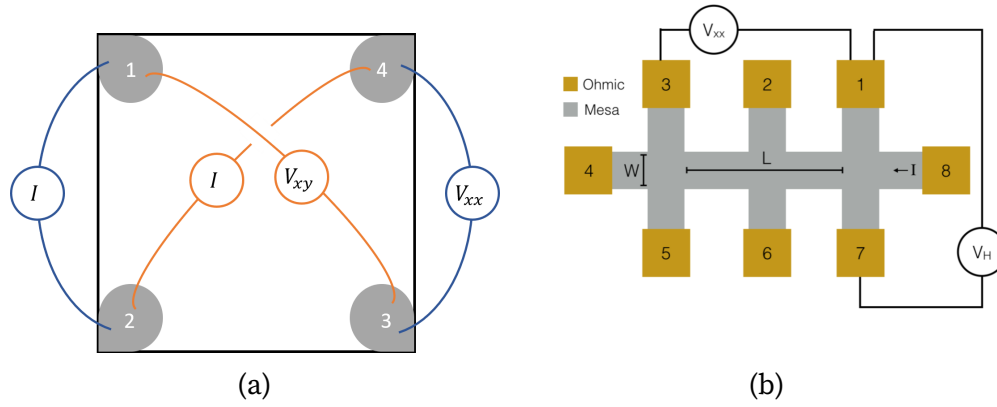


Figure 4.13: Schematic diagram of the (a) van der Pauw and (b) Hall bar geometries used in this study.

Van der Pauw

The [van der Pauw \(vdP\)](#) technique [95] is a simple yet powerful way to make Hall measurements and characterize the samples' basic transport properties. Van der Pauw has demonstrated that the resistivity of the sample measured using this method is independent of the shape of the sample as long as the sample is homogeneous, isotropic, and approximately two-dimensional, while the contacts are placed at the sample edges. Symmetric samples are desirable to reduce errors in the calculations. As shown in [Figure 4.13](#) (a), the InSb QW samples in this study are cleaved into square shapes and contacts to the InSb 2DEG were made by soldering pure Indium at the four corners. The simple sample preparation of the van der Pauw geometry provides quick feedback for optimization of the [MBE](#) growth of InSb heterostructures.

In contrast to the linear four-terminal measurements, the voltage probes and current probes in the van der Pauw configuration are not in line. The averaged longitudinal resistivity of the sample can be found from the 4-terminal resistances measured vertically $R_{12,34}$ (blue lines in [Figure 4.13](#)(a)) and horizontally $R_{14,32}$ across the wafer:

$$\rho_{xx} = \frac{\pi}{\ln(2)} \frac{R_{14,32} + R_{12,34}}{2} f\left(\frac{R_{14,32}}{R_{12,34}}\right) \quad (4.18)$$

where the function $f(x)$ is a correction term defined as

$$\frac{x-1}{x+1} = \frac{f(x)}{\ln(2)} \cosh^{-1}\left(\frac{1}{2} \exp\left(\frac{\ln(2)}{f(x)}\right)\right) \quad (4.19)$$

to account for the differences between the resistances measured in horizontal and vertical directions. In the case where $R_{12,34} = R_{14,32} = R$, then ρ_{xx} reduces to

$$\rho_{xx} = \frac{\pi}{\ln(2)}R \quad (4.20)$$

By placing the current and voltage probes perpendicular to each other across the wafer, as shown by the orange lines in [Figure 4.13\(a\)](#), the Hall resistivity can be determined from the diagonal $R_{13,24}$ and anti-diagonal $R_{24,13}$ resistances measured with and with no magnetic field:

$$\rho_{xy}(B) = \frac{R_{13,24}(B) - R_{13,24}(0) + R_{24,13}(B) - R_{24,13}(0)}{2} \quad (4.21)$$

Hall bar

Hall bar device fabrications are much more complicated and time-consuming than the preparation of van der Pauw samples, however, they can be turned into more complicated devices to enable more interesting studies and applications by including top gates or semiconductor-superconducting junctions. As shown in [Figure 4.13\(b\)](#), the hall bar geometry provides Ohmic contacts at two ends for the current source and drain (4 and 8) as well as Ohmic contacts along both sides for voltage measurements across both the length and width of the device (1-3 and 5-7).

For long and narrow Hall bars with length L and width W , the transverse resistivity can be determined from a Hall voltage V_{xy} measured across the width of the Hall bar using contacts 3 and 5, 2 and 6, or 1 and 7:

$$\rho_{xy} = \frac{V_{xy}}{I} \quad (4.22)$$

and the longitudinal resistivity is given by

$$\rho_{xx} = \frac{V_{xx}}{I} \frac{W}{L} \quad (4.23)$$

where V_{xx} is the longitudinal resistivity measured between any two contacts on one side of the Hall bar. The Hall bar geometry was designed with six instead of four lateral Ohmic contacts to check the uniformity of the sample by allowing six combinations of longitudinal voltage measurements and three transverse voltage measurements. In the case of a uniform geometry, $V_{12} = V_{23}$ and $V_{12} + V_{23} = V_{13}$ are expected and similarly for the contacts on the other side of the Hall bar for the longitudinal voltage measurements while $V_{17} = V_{26} = V_{35}$ should be measured for the three transverse voltages.

Chapter 5

Minimizing the defect densities

5.1 Challenges and buffer designs

The achievement of high-quality InSb quantum wells is especially challenging due to the lack of a III-V semi-insulating substrate or barrier materials lattice-matched to InSb, as shown in [Figure 5.1](#). CdTe could be a potential choice for substrate and barrier material as it shows a zinc blende crystal structure and has a nearly identical lattice constant to that of InSb as well as a large band gap energy. In fact, the initial attempt was made by using CdTe as a barrier. [\[96\]](#) However, CdTe is a II-VI material and hence would result in many growth difficulties [\[97\]](#) including defects, cross-doping, [\[98\]](#) and chemical reactions [\[99\]](#) at the interface which significantly limits the electron mobility in the well. [\[98, 100–103\]](#) Moreover, cadmium tends to show a long memory effect and is detrimental to be introduced even just as in the substrate to III-V vacuum chambers that are after high-mobility structures.

In recent years many efforts have been devoted to the development of metamorphic buffers which enables the growth of InSb [quantum well \(QW\)](#)s on substrates with dissimilar lattice constants [\[17, 104–106\]](#). Commercially available GaAs substrates have been the most popular choice, due to their high quality and reasonable price. GaAs substrates are also among the ones with the most maturely developed epitaxial growth techniques, which provide advantages for the growth reproducibility of the material structures. However, the large lattice-mismatch between GaAs and InSb ($\sim 14.6\%$) leads to structural defects, such as [misfit dislocation \(MD\)](#)s, [threading dislocation \(TD\)](#)s, and [micro-twins \(MT\)](#)s, which deteriorate the electrical and optical performance of InSb-based devices [\[17–21, 23\]](#). To obtain high-quality InSb [QW](#) active regions on GaAs substrates, well-

designed metamorphic buffers must be grown such that the lattice constant changes from that of the substrate to that of the layer of interest, the defects that propagate towards the active region are minimized and smooth surface morphology is achieved.

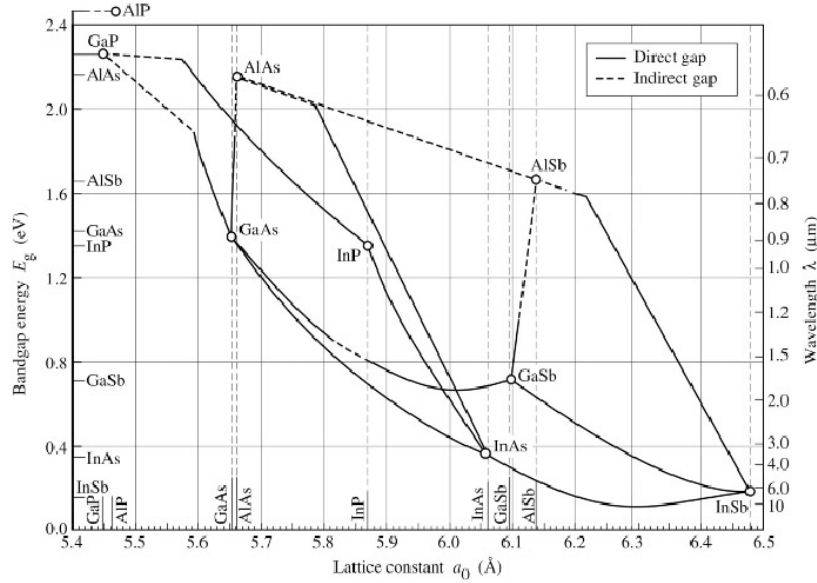


Figure 5.1: Bandgap energy versus lattice constant of various III-V semiconductors at room temperature (Reprint from Schubert (adopted from Tien, 1988)[107])

To partially release the large misfit strain far away from the active region in the system, the buffer sequence usually starts with AlSb or GaSb, both of which having a lattice constant about midway between GaAs and InSb. It has been demonstrated that quantum confinement in InSb wells could be achieved by using $\text{Al}_x\text{In}_{1-x}\text{Sb}$ as barrier layers in the early 1990s [108] and since then many studies on the design of AlInSb structures as the second-stage metamorphic buffer layers has been carried out, including thick single-layer buffers [106, 109], superlattices [110, 111], interlayer buffers [105, 112], step-graded buffers [113] and linear-graded buffers [114].

Herein we report on the optimization of metamorphic buffers consisted of two parts: a first intermediate buffer and a second-stage buffer. The detailed schematic representation of the buffer structures used in this thesis is shown in Figure 5.2. The native oxide was desorbed thermally by annealing the substrate at 630°C for 5 min under As_2 flux. A 120 nm GaAs layer was subsequently deposited at 580°C and 2Å/s to smooth out the surface and bury residual contaminants present on the substrate surface after the oxide desorption. AlSb (with a thickness $t_a = 100$ nm or 1 μm) or GaSb (600 nm-thick),

both of which have an intermediate lattice constant between GaAs and InSb, was then deposited to serve as the nucleation layer and the first intermediate buffer layer. A thin (5 nm) GaSb cap was deposited on top of the AlSb buffer to protect the AlSb surface from oxidation when necessary. Subsequently, on top of the first intermediate buffer, a single-composition t_s -thick $\text{Al}_x\text{In}_{1-x}\text{Sb}$ layer or an interlayer buffer was grown as the second-stage buffer. The interlayer structure, similar to the design proposed by Mishima et al. [105], is consisted of a 500 nm lower $\text{Al}_x\text{In}_{1-x}\text{Sb}$ buffer, 200 nm $\text{Al}_x\text{In}_{1-x}\text{Sb}$ interlayers separated by 300 nm $\text{Al}_y\text{In}_{1-y}\text{Sb}$ matrix spacer layers, and lastly an $\text{Al}_x\text{In}_{1-x}\text{Sb}$ upper buffer of thickness t_u . The total number of interlayers used in this study, N , is varied from 1 to 4 to study the dislocation filtering effect.

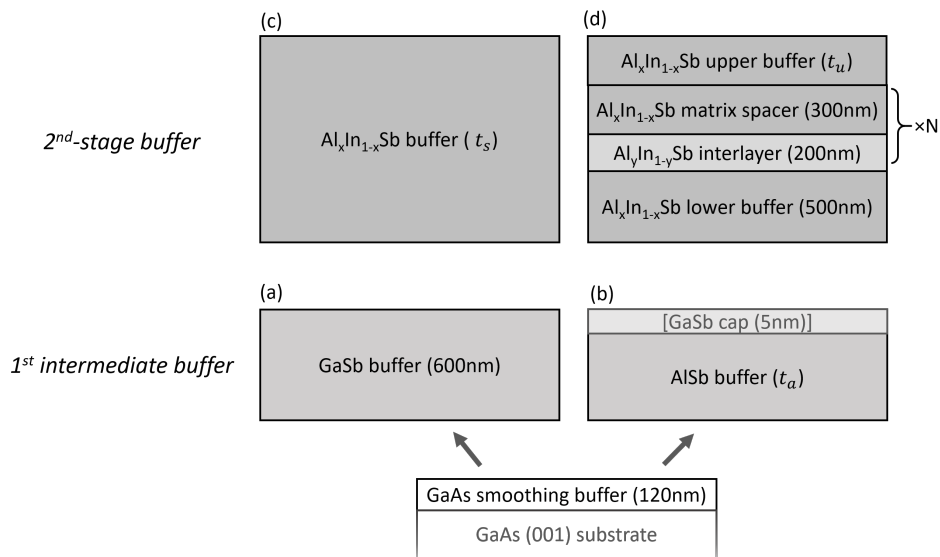


Figure 5.2: Schematics of the buffer structures consisted of a first intermediate buffer of either kind (a) or (b) and a second-stage buffer of design (c) or (d).

5.2 Defect characterization

In order to properly evaluate the crystalline quality and optimize the structural design and growth parameters of the metaphoric buffers, convenient and accurate characterization techniques that allow rapid identification and analysis of individual defects are required. [transmission electron microscopy \(TEM\)](#) and [high-resolution x-ray diffractometry \(HD-XRD\)](#) have often been the technique of choice for the characterization of structural

defects in semiconductor materials. Cross-sectional TEM enables the visualization of defect distribution across an entire thickness of heterostructures, providing important information on the mechanisms of dislocation generation and reduction, but it is not suitable for quantitative evaluation of threading dislocation density (TDD). Analysis of HD-XRD peaks provides an estimate of the overall threading dislocation density (TDD) in the samples but does not reveal the individual defects or their distribution throughout the epitaxial structure. [115] On the other hand, plan-view TEM can reveal individual TDs very clearly. However, TEM is a destructive technique. The sample preparation is also very demanding and time consuming. Here we present a comparative study on three alternative techniques that can reveal and count individual TDs and discuss their merits and limitations in the characterization of Sb-based metamorphic buffers grown on GaAs (001) substrate, the quality of which is of critical importance to the quality of the InSb QWs grown on them. The metamorphic buffer used to demonstrate the various features of these TDD characterizing techniques is consisting of a first intermediate buffer of AlSb (Figure 5.2 (a)) of a thickness $t_a = 1\mu m$ with a GaSb cap and a second-stage buffer containing interlayers (Figure 5.2(d)) with the composition of the matrix buffer $x = 0.12$, the composition of the interlayer $y = 0.24$, no upper buffer ($t_u = 0$), and the total number of interlayers (N) varied between 0, 1 and 3. Note that the structure denoted as N = 0 here in this section, the $Al_{0.12}In_{0.88}Sb$ lower matrix layer is not included, i.e., the buffer ends with the GaSb cap.

5.2.1 Atomic force microscopy (AFM)

The surfaces of all buffer structures (with N = 0, 1, and 3) are covered by pyramid-like hillocks with clear atomic-height terraces on the sidewalls, as revealed under atomic force microscopy (AFM) (Figure 5.3). These hillocks, with typical height varying from 1 up to 40 nm, are formed as a result of spiral growth around the outcrops of TDs with a screw component (which will be discussed in more detail in chapter 6), dominant in this material system. Careful inspection of the hillocks sidewalls reveals the emergence of additional pinned atomic step (PAS)s on some terraces, which are also clear signatures of TD outcrops (Figure 5.4). The TDDs quoted in Figure 5.3 are calculated by counting both hillocks and PASs on the surface and averaged from several AFM scans. The clear atomic step spirals revealed by AFM provide additional information on the Burgers vector direction. Indeed, TDs with opposite Burger vector directions result in a clockwise or anticlockwise winding of spirals (Figure 6.3). Typically, a pair of dislocations very close to each other are unresolvable by TEM, but can be readily detected using AFM. The signs (like or opposite) of the dislocation pair can be identified by examining the appearance

of the atomic steps at the intersection of the dislocation pair, [40] which usually appear on the apex of a large hillock. Besides TDs, MTs which have been identified in the past with cross-sectional TEM, [17, 116] have been revealed as distinctive dash-like features under AFM [Figure 5.4(c)]. More MTs are observed along $[1\bar{1}0]$ than the $[110]$ direction. We found that the formation of MTs can be largely promoted when the Sb overpressure significantly higher than a group V/III flux ratio of 2 is used. Elimination of MTs can be achieved with offcut substrates as discussed further in section 6.4.

As helpful as AFM could be for evaluating metamorphic buffers, it is not without limitations. One issue is that detection of all dislocation outcrops relies on the presence of clear atomic terraces on the surface which requires optimized step flow growth conditions. Additionally, since the distinct morphological features of TD outcrops are in the scale of nanometers, only high-resolution AFM scans, 1×1 or 2×2 μm^2 , are suitable for resolving them. However, just three TDs are observed on the 1×1 μm^2 AFM image of the $N = 3$ buffer (Figure 5.4(c)), and a large number of such scans need to be taken to obtain an averaged TDD that is statistically meaningful. Such a limited inspection area makes dislocation counting challenging for samples having TDDs below $1 \times 10^8 \text{ cm}^{-2}$, unless facilitated with a mapping capability, available on higher-end AFM instruments, where a matrix of scans can be acquired automatically. The single high-resolution AFM scan is ideal for high TDD samples, for example, the $N = 0$ buffer which shows a TDD of around $3 \times 10^9 \text{ cm}^{-2}$. Based on our observations, we estimate that AFM is well suited as a TD counting tool for samples with TDD in the range of $1 \times 10^8 - 1 \times 10^{10} \text{ cm}^{-2}$.

5.2.2 Scanning electron microscopy - electron channeling contrast imaging (SEM-ECCI)

TD outcrops are easily identified on the surfaces of the $N = 0, 1,$ and 3 buffers by using scanning electron microscopy (SEM) in electron channeling contrast imaging (ECCI) mode. They appear as spots with sharp dark-bright contrasts, two of which are indicated with thin arrows in Fig. Figure 5.5(c). Such contrast is a result of the changes in the intensity of back-scattered electrons (BSE) (section 4.3). Small distortions in local strain field and crystallographic configurations close to the sample surface lead to variations in the electron channeling probability, and thus the local BSE yield. Atomic steps, though very indistinct, are also visible in the ECCI images (Figure 5.5(c)) due to the lattice distortion at the terrace ledges. The winding directions of the spiral steps are barely resolved by ECCI, but TDs with opposite Burgers vector directions can be distinguished, thanks to the clearly resolved dark-bright contrast reversal, as indicated with the two

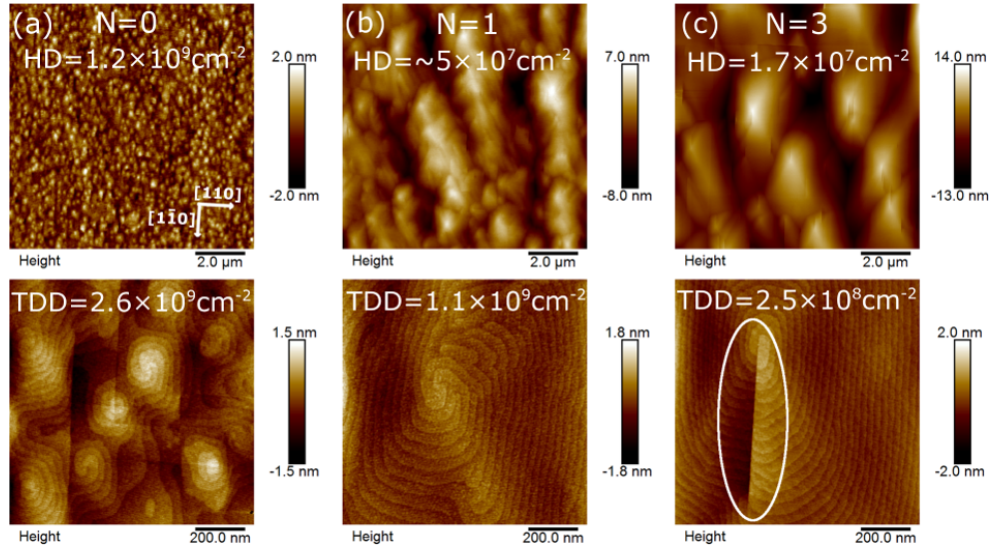


Figure 5.3: AFM images of buffers with a different number of interlayers (N) on GaAs (001) substrates as well as their surface hillock density (HD)s and TDDs. The white ellipse in (c) shows a signature of MTs observed on all buffers.

circles and associated arrows in Figure 5.5(b). Besides TDs, MTs are also revealed with ECCI, as bright (Figure 5.5(a)) or dark (Figure 5.5(b) and (c)) dashes on the surface.

The TDD values counted with ECCI images (quoted in Figure 5.5) for the $N = 1$ and $N = 3$ buffers agree with those obtained using AFM. However, the TDD of the $N = 0$ buffer measured with ECCI is lower than that measured with AFM by more than a factor of two. SEM has a relatively low tolerance for surface roughness in dislocation studies, and the predominant surface feature of bright ridges observed on the $N = 0$ sample may be obscuring many TD outcrops. Since the bright ridges in ECCI images have a similar width to the hillocks in AFM images, we postulate that their characteristic contrast originates from the elongation of surface hillocks in the $[1\bar{1}0]$ direction. Another contributing factor to the lower than expected TD count for $N=0$ may be the limited ECCI resolution for a high density of TD outcrops. In fact, the TDD value of $1.3 \times 10^9 \text{ cm}^{-2}$ for the $N = 1$ buffer in Figure 5.5(b) approaches the upper limit of SEM-ECCI resolution for revealing all TD outcrops. Since there is a clear tendency for the formation of TD clusters, and the dark-bright features of TD outcrops have an average diameter of around 50 nm, the presence of closely spaced TDs may lead to significant under-counting at such TDD levels. This observation, together with a much wider field of view compared to AFM, sets SEM-ECCI applicability limits for a reliable TDD measurement in the range of approximately

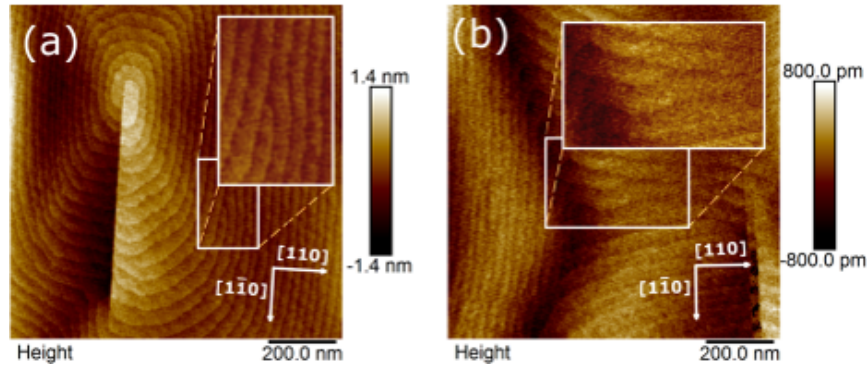


Figure 5.4: AFM images of $1 \times 1 \mu\text{m}^2$ of the N=3 buffer showing the step insertions on the hillock sidewalls in both (a) [110] and (b) $[1\bar{1}0]$ directions.

$1 \times 10^6 - 1 \times 10^9 \text{ cm}^{-2}$.

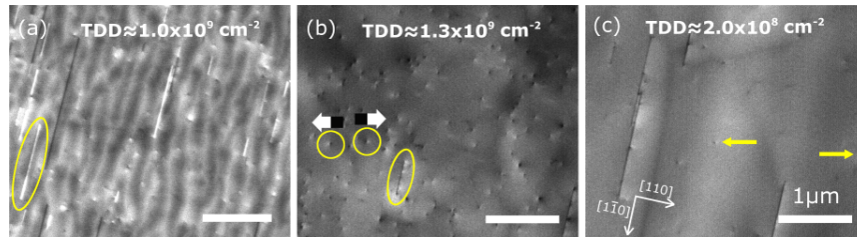


Figure 5.5: SEM-ECCI images revealing the TDs (examples pointed by two thin arrows in (c)) and MTs defects (examples indicated by two ellipses) on the (a) N = 0, (b) N = 1, and (c) N = 3 buffers, with their TDDs quoted. Two TDs with opposite signs are indicated by two circles with thick black-white arrows above representing the opposite directions of the dark-light contrasts.

5.2.3 Defect selective etching (DSE)

Square-shaped etch pit (EP)s were observed by Nomarski contrast optical microscopy on the surface of the N = 3 buffer after the defect selective etching (DSE) treatment using the diluted sirtl-like mixture with light (DSL) method (more details in chapter 4), as shown in Figure 5.6. No dash-shaped contrasts were observed, indicating that the DSL- DSE process employed is not capable of revealing MTs. A comparison of the same areas etched for 15 s [Figure 5.6(a)] and then an additional 15 s [Figure 5.6(b)] shows an enlargement

of the initial EPs and creation of very few new EPs on the sample after the additional etching cycle, indicating a strong correlation between TDs and the EPs. Nevertheless, the calculated etch pit density (EPD) of the N = 3 buffer is more than 1 order of magnitude smaller than the TDD obtained from the AFM and SEM-ECCI measurements on the same sample. A close agreement between the TDD measured from SEM-ECCI and molten KOH selective etching on a GaP/Si sample with $TDD=1 \times 10^7 \text{ cm}^{-2}$ was found by Yaung et al., [117] where the same areas of EPs and SEM-ECCI image were compared. EPs appeared at the locations identical to the spots of SEM-ECCI dark-bright contrast, except that one out of seven expected EPs was missing. However, for samples of $TDD > 1 \times 10^7 \text{ cm}^{-2}$, a much larger discrepancy was reported by the same group. [118] These reports, together with the large variation in pit sizes and significant number of EP overlapping observed even in our lowest TDD sample ($2 \sim 2.5 \times 10^8 \text{ cm}^{-2}$ as measured by AFM and SEM-ECCI) observed in Figure 5.6, indicate that DSE is indeed not a reliable technique for samples with TDD larger than $1 \times 10^7 \text{ cm}^{-2}$. In principle, detection of all TDs in layers with high TDDs without undesirable overlapping may be possible with very fine control of the etching process and resorting to SEM or AFM for subsequent imaging. However, this would significantly diminish the advantage of this technique for fast feedback. Reducing the EPs' lateral size would restrict their depth and facet definition, jeopardizing other important advantages of the DSE method demonstrated for lower EPDs. These include (1) information on the nature of a dislocation, which can be gained through measurement of the etched facet angles and (2) locating the TD origin through a study of the EP base morphology and its depth below the surface. [119, 120]

5.3 Interfacial misfit (IMF) growth mode

5.3.1 A literature review

Recently a new growth technique has been reported to significantly reduce the TDD in Sb-based hetero-epitaxial layers, particularly in the material system of thick GaSb epilayers grown on GaAs substrate, through the realization of interfacial misfit (IMF) dislocation arrays. Similar to AlSb, due to the large lattice mismatch ($\sim 7.78\%$) between GaAs and GaSb, the critical thickness is predicted to be only a couple of monolayers. For most applications, much thicker GaSb epilayers are required and the growth begins as islands which later merge to form a uniform layer and the growth continues in a layer-by-layer manner. Both 60° and 90° MDs usually exist at the GaAs/GaSb interface. As discussed earlier in subsection 2.4.1, the dominating strain relief mechanism is believed

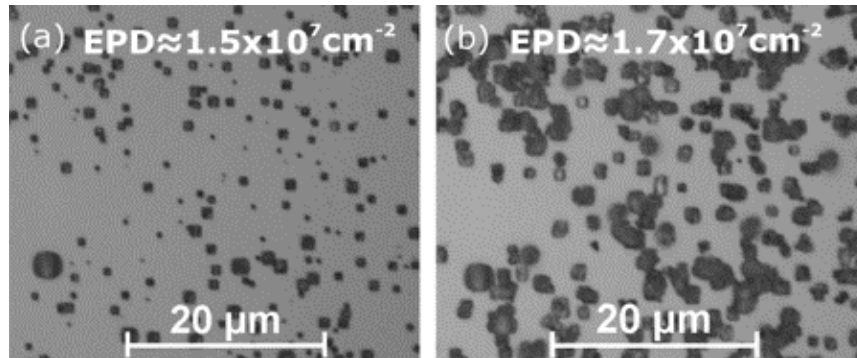


Figure 5.6: Nomarski **differential interference contrast (DIC)** optical images of the $N = 3$ buffer surface after subsequent **DSL** etching for (a) 15s and (b) additional 15s. The second etching results primarily in the enlargement of the existing pits. Several new pits can also be detected. The quoted threading **EPD** in the image is measured from the square-shaped etch pits.

to be accomplished by the laterally propagating 90° **MDs**, while the 60° ones were demonstrated to prevail in contributing to **TDs** propagating upwards in the epilayer, typically on the order of 10^9 cm^{-2} . However, it has been claimed that by properly utilizing the **IMF** growth mode with particular growth conditions, the formation of 90° misfit dislocations can be actively encouraged over the formation of 60° ones, lowering the **TDD** to 10^5 cm^{-2} . [62] Even more so, the group who first reported this growth mode showed that no pseudo-morphic growth will take place even before reaching the critical thickness. When optimal growth conditions are reached, the lattice-mismatch in the system is large enough such that the strain can be instantly relieved at the interface by forming preferred 90° **MDs**. [62, 121] Therefore the **IMF** growth mode has been considered as a desirable ‘buffer-free’ alternative for devices made out of this material system.

Different approaches to achieve the **IMF** mode has been demonstrated by different groups. Nevertheless, it has been widely agreed that the Ga-As bonds on the surface prohibit the formation of 90° **MDs**. On the other hand, the cleaner the Ga-Sb bonds are formed everywhere at the interface, the more ideal **IMF** dislocation arrays are generated [67, 68, 70]. The two main approaches for preparing the Ga-Sb surface are usually used from the literature. The first method starts with As-deportation followed by an Sb soak. The other approach employs an As-to-Sb anion exchange technique. For the As-desorption method, the As cell is valved off at a sufficiently high substrate temperature after the growth of the GaAs buffer to create a Ga-rich surface. A (4×2) **reflection high-energy electron diffraction (RHEED)** pattern should be observed at this stage. Then the

Sb flux is introduced to create a strain-relieving GaSb monolayer with IMF dislocation arrays readily prepared, before starting the GaSb growth. As for the cooling process from the growth temperature of GaAs to that of GaSb, some researchers claimed that Sb flux should only be introduced when the GaSb growth temperature was reached [67]. Yet some stressed that Sb needs to be opened at a high substrate temperature once the Ga-rich surface is obtained and cool down under Sb overpressure [69]. On the contrary, some groups found that the best results were achieved with Sb shutter opening at a high substrate temperature first then closing during cool down and re-opening before the GaSb growth [122]. For the As-to-Sb anion exchange process, the Sb flux is introduced before closing the As valve at reasonably high substrate temperatures for the Ga-As bonds on the surface to slowly change to Ga-Sb bonds [122]. With either surface preparation approaches, a (2×8) RHEED pattern should be observed before the GaSb growth, which has been reported to be more advantageous than the (1×3) surface in forming 90° MDs. [67, 69, 70, 121, 122] In addition, several research groups have suggested that the insertion of an AlSb interfacial monolayer were able to provide better relief of strain and improve the IMF formation at the GaSb/GaAs interface. [123, 124]

Other than the various surface preparation procedures using by different groups, the growth temperatures and V/III ratio of GaSb for the realization IMF mode also diverse among the literature reports. The optimal growth temperature reported ranges from as low as 310 °C [125] to as high as 530 °C [126]. As for the temperature effect on the GaSb surface morphology, the root-mean-square (RMS) roughness was reported by Brown et al. to increase with decreasing growth temperature [127] while Tan et al. found a smoother surface at lower substrate temperatures due to the formation of smaller islands during the initial island growth stage.[70]

The effect of group V/III flux ratio has not been thoroughly studied and only one group reported that V/III being 1.4 showed superior results than V/III at 1 or 1.8 for GaSb IMF dislocation formation using metal-organic chemical vapor deposition (MOCVD). Most groups did not mention the V/III ratio used for the GaSb deposition. For those who mentioned, the ratio was usually kept somewhere between 1 to 3 [69, 126, 128].

5.3.2 The observed RHEED patterns

All of the IMF GaSb buffer growths in this thesis were started with thermal oxide desorption at 630 °C under As overpressure, followed by the growth of a 1200 nm GaAs smoothing buffer, which was started at 580 °C and slowly ramped to 620 °C through the first half of the buffer and continued at 620 °C for the rest of the growth.

Before growing the GaSb buffer, we attempted both the As-desorption and the anion exchange methods to prepare a single monolayer of Sb with Ga-Sb bonds on the GaAs surface. For the As-to-Sb anion exchange to take place, the substrate temperature was lower to around 590 °C after the growth of the GaAs buffer under As overpressure, then the As flux was replaced with an Sb flux and wafer was soaked under the Sb flux at 590 °C for 5 min. For the method of As-desorption, the As cracker valve and shutter were both closed at 590 °C to evaporate As on the surface and leave a Ga-rich surface. The wafer was annealed for 20 min at this temperature to ensure a complete As evaporation. In contrast to many literature reports where (4×2) GaAs surface reconstruction could be sustained till 440 °C, we observed that the surface reconstruction would no longer be stabilized at (4×2) when the substrate temperature was lower than 590 °C. When the substrate temperature was cooled down to a [band-edge thermometry \(BET\)](#) temperature of 580 °C, we started to see a mixture of (3×1) and (4×2) [RHEED](#) pattern ([Figure 5.7](#)). The [RHEED](#) pattern changed to (3×6) when the substrate temperature was cooled down to around 520 °C. When the substrate was lowered further to 450 °C, a (2×6) pattern was observed. A mixed (2×6) and (3×6) can be observed during the cooling from 520 °C to 450 °C.

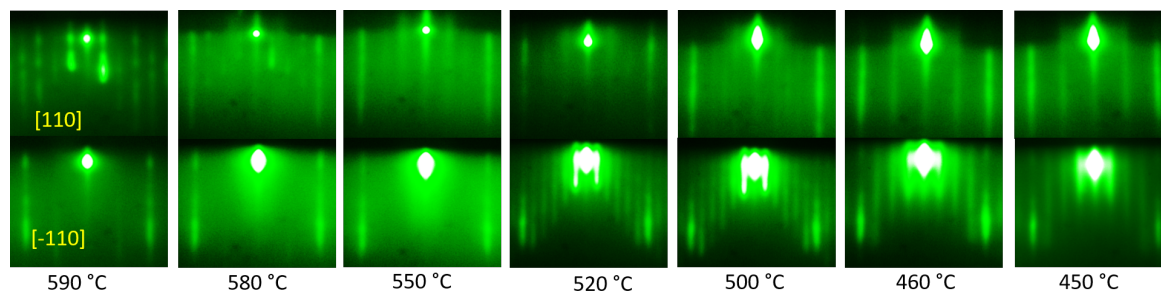


Figure 5.7: [RHEED](#) pattern observed on GaAs surface at different substrate temperatures as cooling down from 590 °C to 450 °C under no fluxes

For the As-to-Sb anion exchange technique, the wafer was cooled down under the Sb flux to the target growth temperature of GaSb. For the As-desorption method, after the Ga-rich surface was obtained, the substrate was ramped to different temperatures to study the effect of Sb soak temperature on the [IMF](#) growth mode. As described by Huang et al. [62], when the Ga-rich surface is exposed to an antimony flux at right conditions, a regular array of 90° [MDs](#) can readily be prepared on the surface, with most of the strain energy already relieved without tetragonal distortion. Under the Sb flux which is equivalent to a $V/III \sim 1.5$ for GaSb grown at 2 Å/s, we observed the favored (2×8) Sb-induced surface reconstruction in a substrate temperature range of

440–500 °C (Figure 5.8(c)). If the same Sb soak was initiated above 580 °C, we observed a (2×4) Sb-induced reconstruction (Figure 5.8(b)), which agrees with the observation by Jia et al., who found the (2×4) reconstruction under Sb flux when the substrate temperature is higher than 560 °C [122]. As the Sb flux was increased to be greater than that for a V/III ratio ~ 3 for GaSb grown at 2Å/s, the surface reconstruction became the more Sb-rich (2×8) even at substrate temperatures higher than 580 °C (Figure 5.8(a)). A (1×3) Sb-induced pattern has been demonstrated to indicate a mixture of Ga-As and Ga-Sb bonds on the surface due to incomplete As-desorption. [122] The (1×3) reconstruction was observed once by us at ~ 450 °C after introducing the Sb flux. However, as we ramped up the substrate temperature to 480 °C under Sb flux, the (1×3) pattern changed to (2×8) and then remained as (2×8) after ramping back down to 450 °C. We suspect that a more complete As-Sb exchange was achieved as the substrate temperature was ramped from 450 °C to 480 °C. We also noticed that even though (2×4) was usually observed at high substrate temperatures, it could also be observed when cooling down an Sb-induced surface under no Sb flux to lower substrate temperatures such as 440 °C. We attribute this to the cooling time being longer than Sb lifetime on the surface and Sb lifetime is expected to be shorter at higher substrate temperatures.

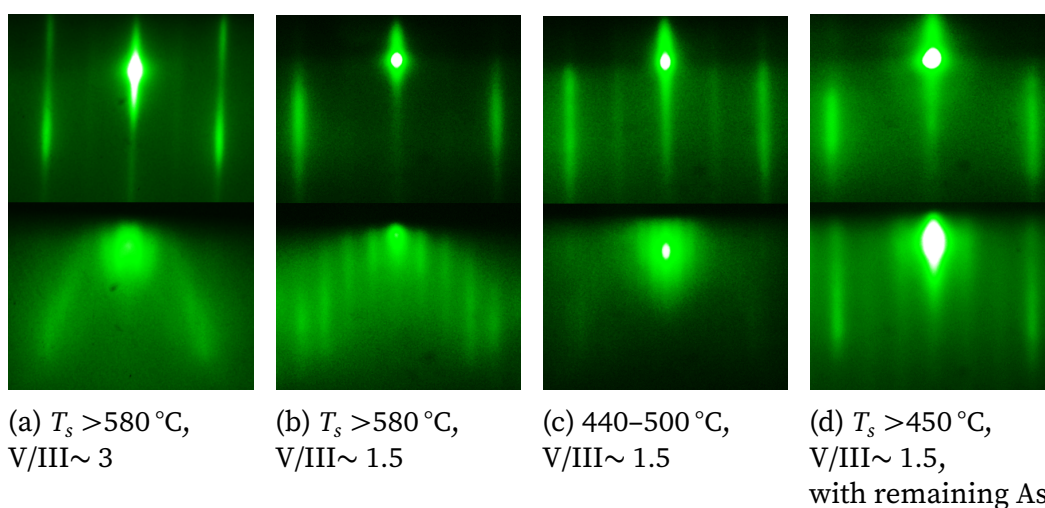


Figure 5.8: The RHEED patterns of the Sb-terminated GaAs surface under different conditions as specified.

Table 5.1: A summary of the GaSb IMF buffer growths with different surface preparation methods, various substrate temperatures to initiate the Sb soak, diverse growth conditions, and other applied growth techniques. "A-E" and "A-D" stand for the "anion exchange" and "As desorption" surface preparation methods receptively. "PG-A" and "I-A" stand for other applied growth techniques of "post-growth annealing" and "inserted annealing", respectively.

Growth	Surface prep.	Sb soak T_s (°C)	Growth T_s (°C)	Sb/III	Other tech.	TDD (cm ⁻²)
G0630	A-E	450→480	500	~1.5		~8.1 × 10 ⁸
G0631	A-D	590	440→500	~1.5		~8.4 × 10 ⁸
G0671	A-D	500	510	~1.5		~8.1 × 10 ⁸
G0672	A-D	500	450	~1.5		~8.8 × 10 ⁸
G0673	A-D	500	450→510	~1.5		~8.4 × 10 ⁸
G0674	A-D	500	510	~1.5	AlSb ML	~6.7 × 10 ⁸
G0682	A-D	500	400	~1.5		~1.2 × 10 ⁹
G0694	A-D	500	400	~1.5	PG-A	~8.1 × 10 ⁸
G0777	A-E	590	510	~4→2		~7.9 × 10 ⁸
G0779	A-E	590	510	~4→2	I-A	~7.8 × 10 ⁸

5.3.3 Factors affecting the growth mode

To optimize the IMF growth mode for GaSb buffers, the effects of several growth parameters are studied. This study does not cover a full investigation of dislocation generation and propagation mechanisms, which requires TEM imaging. Instead, since we are mostly interested in the effectiveness of the IMF mode on TDD reduction, SEM-ECCI was used to characterize the TDD reaching the surface for GaSb buffers grown under different conditions and by applying different growth techniques. The details of all the growths and the resulting TDDs are summarized in Table 5.1.

First of all, we found that for growths that were carried out under the same conditions otherwise, using different substrate temperatures to initiate the Sb soak barely had any effect in the outcome surface morphology or the TDD measured at the layer surface (*e.g.*, G0631 vs. G0673 in Table 5.1). Moreover, we also found no perceptible difference between the growths using the As-to-Sb anion exchange method and the one with the As-desorption method for the surface preparation (*e.g.*, G0630 vs. G0671 in Table 5.1). In view that different procedures of Sb soak were followed by different groups as presented in subsection 5.3.1, the exact procedure for preparing the Sb-rich surface with Ga-Sb

bounds is probably not so critical, as long as the Ga-As bonds on the surface are well replaced with Ga-Sb bonds, as indicated by the (2×8) RHEED pattern.

Substrate temperature

A wide range of substrate temperatures has been used in the literature for the IMF growth mode, therefore we carried out a study on the dependence of the GaSb IMF buffers on the substrate temperature. The 600 nm-thick GaSb buffers in this series were all started with an As desorption at 590 °C followed by an Sb soak which was always performed at ~500 °C for about 2 min. For the GaSb buffers grown at substrate temperatures lower than 500 °C, the Sb valve was closed during the cool down from 500 °C to the target growth temperature to prevent too much Sb accumulation on the surface. The Sb flux was reintroduced for about 10s when the desired temperature was reached and a stable (2×8) RHEED pattern was observed before starting the GaSb growth. As shown in Figure 5.9(a), (b), and (c), the TDD on the GaSb buffer surface decreases as the substrate temperature increases from 400 °C (G0682) to 450 °C (G0672) and finally to 510 °C (G0671). This result however is in contrast to that reported by Mansoori et al. [69], who found an exactly opposite trend. The TDD measured using plan-view TEM decreased from $\sim 5.9 \times 10^8 \text{ cm}^{-2}$ for the GaSb buffer grown at 540 °C to $\sim 1.3 \times 10^8 \text{ cm}^{-2}$ for the one grown at 420 °C. The exact TDD values between our results and theirs can not be compared directly, since their GaSb buffers are 2 μm-thick, which are more than three times thicker than our GaSb buffers. A decrease in TDD may be expected for our GaSb IMF buffers if they grow to the same thickness. The SEM-ECCI also offers the advantage over TEM of revealing the surface morphological dependence on the substrate temperature. As shown in Figure 5.9(a), (b), and (c), the hillocks on the surface become larger and their shapes evolve from more pyramid-like with square bases into more dome-like with round bases. Such morphological transformation will be discussed in more detail in chapter 6. We also tried to grow the GaSb buffer with a lower starting substrate temperature at 450 °C then gradually ramped up the substrate temperature and kept at 510 °C for the rest of the growth, similar to the procedure suggested by Lehner et al., [114]. However on the contrary to their results, as shown in Figure 5.9(f), the GaSb buffer which started with a lower substrate temperature (G0673) exhibits no less but slightly higher TDD than the GaSb buffer grown under a constant substrate temperature of 510 °C (G0671).

The RHEED pattern during the island formation stage for GaSb growths carried out at different substrate temperatures was recorded which provides some insights into the TDD trend with substrate temperature. As shown in Figure 5.9(a), (b), and (c), as the substrate temperature decreases, the islands formed during the nucleation stage

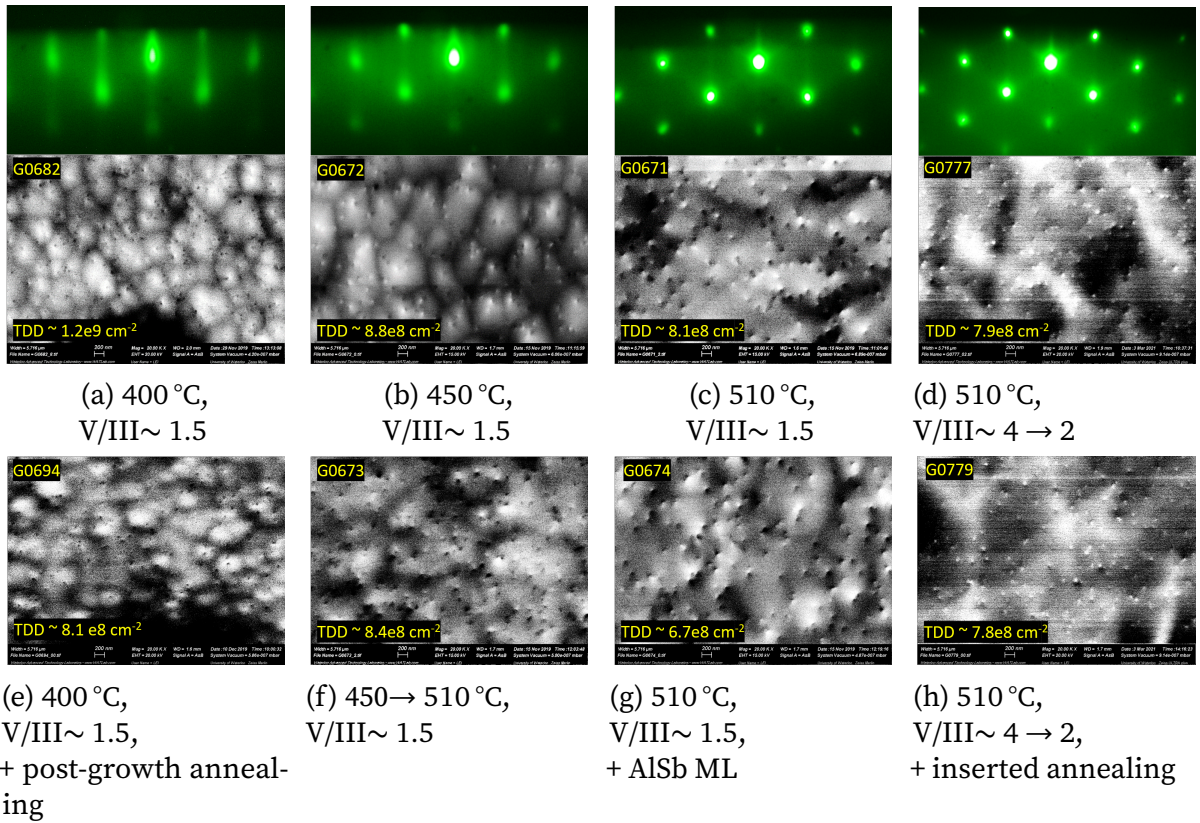


Figure 5.9: The SEM-ECCI images of the GaSb IMF buffers grown at different growth conditions and additional treatments as specified as well as the RHEED patterns during the island formation stage for the GaSb IMF buffer growths in (a)-(d). The RHEED patterns for (e)-(h) are similar to their corresponding ones above, i.e., (a)-(d) respectively. The growth number and the counted TDD for each growth is indicated in its SEM-ECCI image.

become smaller, as indicated by the enhanced streakiness of the RHEED pattern. Larger islands that formed at higher substrate temperatures showed signs of faster relaxation according to RHEED, suggesting the generation of 90° MDs which are more efficient in strain relieving than 60° MDs (subsection 2.4.3). In addition, if indeed TDs are correlated with island coalescence, as discussed in subsection 2.4.3, then for growths carried out at higher substrate temperatures, there will be fewer island coalescence sites due to the larger islands formed on the surface, lowering the chances of misalignment in dislocation networks and hence reducing the TDD.

V/III ratio

Though the effect of V/III ratio has not been widely studied for the IMF growth of GaSb thick buffer on GaAs substrate, it has been demonstrated by G. Balakrishnan et al. [129] that the growth mode for GaSb quantum dots (QDs) on GaAs substrates can be selected by the V/III ratio. According to this group, at a V/III ratio of 1, highly-strained QDs were grown in the Stranski-Krastanov mode, while strain-relaxed IMF QDs were achieved at a V/III ratio of 10, as demonstrated by TEM imaging. The Stranski-Krastanov mode and the IMF mode were also distinguished at real-time of the growth by RHEED, which showed a 'chevron' pattern for Stranski-Krastanov QDs and a pattern corresponding to relaxed islands (typical examples in Figure 5.9(c) and (d)) for IMF QDs. Here we examine the applicability of increased V/III ratio on further TDD reduction in thick GaSb buffers grown on GaAs surfaces. To compare with the growth (G0671) of GaSb buffer grown under a constant V/III ratio of 1.5 (Figure 5.9(c)), we carried out another growth (G0777) with a V/III ratio of 4 for the first island formation stage (~10 nm) and a V/III ratio of 2 for the rest of the GaSb buffer growth. Unfortunately, as shown in Figure 5.9(d), the largely increased V/III ratio for the initial island growth and the slightly increased V/III ratio for the rest layer growth altogether did not make a significant improvement in the TDD reduction as revealed by the SEM-ECCI images. The counting of the TDDs for the two growths yields a highly similar value of $\sim 8 \times 10^8 \text{ cm}^{-2}$. Moreover, the RHEED pattern for the two growths also appeared to be very similar (Figure 5.9(c) and (d)). In fact the RHEED pattern for the growth with a V/III ratio of 1.5 already showed signatures of highly relaxed islands.

Thermal annealing

The effect of two thermal annealing processes were studied. For the first process, the annealing was performed in the middle of the GaSb growth between the initial island growth stage and the layer-by-layer growth stage. About 10nm of GaSb was deposited during the island growth stage at $\sim 510^\circ\text{C}$ and a V/III ratio of 4. Then the growth was paused for a 30 min annealing at 520°C . After the annealing, the rest of the GaSb growth was resumed at 510°C and a V/III ratio of 2. This inserted annealing process was designed to address the postulation in many works on the generation of 60° TDs at the island coalescence sites (subsection 2.4.3) by 'correcting' the misalignment of the IMF network. The SEM-ECCI image of the growth with the inserted annealing step (G0779) is shown in Figure 5.9(h) while that of the growth grown under the same growth conditions without the annealing step (G0777) is shown in Figure 5.9(d). Unfortunately, as shown

in Figure 5.9, the inserted extra annealing step did not provide a remarkable reduction of the TDD in the GaSb buffer. A similar TDD of $\sim 7.8 \times 10^8 \text{ cm}^{-2}$ was counted for the growth with annealing comparing to $\sim 7.9 \times 10^8 \text{ cm}^{-2}$ for the growth without annealing and the difference of $\sim 0.1 \times 10^8 \text{ cm}^{-2}$ is within the error of TDD calculation from the area selection and the counting of the TD outcrops.

The other thermal annealing process we studied was performed after the growth of the GaSb layer. One quarter of the GaSb buffer grown at 400 °C with an protective As cap was transferred back into the growth module (GM) after a quick cleaving. After evaporation of the amorphous As cap, the RHEED pattern recovered to the streaky (1×3) pattern, and the quarter wafer was then annealed at 500 °C for 1 h. As shown in Figure 5.9 (e), even though the surface morphology remained unchanged after the post-growth annealing, the TDD on the surface has been reduced considerably from $\sim 1.2 \times 10^9 \text{ cm}^{-2}$ (G0682) to $\sim 8.1 \times 10^8 \text{ cm}^{-2}$ (G0694), which is similar to the GaSb layer grown directly at 510 °C (G0671). We suspect that the post-growth thermal annealing encouraged the dislocation annihilation process by rearranging the thermally active atoms towards a more ordered state, leading to decreased TDD in the system (subsection 2.4.3). For the inserted annealing process, the substrate temperature may not be high enough to encourage such thermally activated rearrangement as it was only elevated by 10 °C from the growth temperature. On the other hand, the results of the two annealing processes also suggest that most of the TDs in the GaSb may not have been generated during the island growth stage but rather in the lay-by-layer growth stage. Moreover, there may exist other mechanisms contributing to the generation of TDD in such material structures which need to be considered.

Interfacial AlSb monolayer

It was reported that insertion of an AlSb monolayer at the interface on an Sb-rich GaAs surface has the potential to ensure a more localized strain distribution at the interface forming more uniform 90° Lomer dislocation arrays and hence reduce the TDDs in the epitaxial layers. [124] Following their development, we attempted a GaSb buffer growth at 510 °C with an AlSb monolayer at the interface (G0674). As shown by the SEM-ECCI image in Figure 5.9(g), the TDD on the surface has been indeed reduced further to $\sim 6.7 \times 10^8 \text{ cm}^{-2}$, which is so far the lowest TDD we achieved with the 600 nm GaSb IMF buffers. However, it is still one order of magnitude higher than the reported TDD of $6 \times 10^7 \text{ cm}^{-2}$ by Wang et al. [124].

5.3.4 Effectiveness of the technique

The **TDD** we achieved with our GaSb **IMF** buffers are all noticeably higher than that reported by many other groups. **TDD** in the order of $1 \times 10^5 \text{ cm}^{-2}$ was only reported by the group who first demonstrated this **IMF** technique [62]. The rest of the groups mostly reported a **TDD** slightly lower than $1 \times 10^8 \text{ cm}^{-2}$, which however is still considerably lower than the lowest **TDD** we achieved ($\sim 6.7 \times 10^8 \text{ cm}^{-2}$). One of the reasons for this discrepancy may be related to the fact that our GaSb **IMF** buffers are considerably thinner than the ones reported by many other groups and **TDD** can usually be reduced significantly within the first few μm s of such metamorphic buffers. Another possible reason is that we are the only group that uses **SEM-ECCI** for the characterization of **TDD**, which we believe to be the most accurate method for determining the exact **TDD** for such buffers, as discussed in section 5.2. In our studies, the **TDDs** measured using **SEM-ECCI** were also compared with those measured and averaged over several **AFM** scans and similar results were yielded. **HD-XRD** used by many groups does not provide a direct measurement and needs very careful interpretation. **AFM** and plan-view **TEM** allow smaller inspection areas than that **SEM-ECCI** can offer. Hence unless the measured **TDD** is averaged over quite a few images, they can be less accurate as the distribution of the **TD** outcrops on the surfaces are highly non-uniform, for example as shown in Figure 5.9(g). Lastly, the mechanism for the **IMF** growth mode is not fully understood. From the fact that various procedures were carried out by different groups and the contradictory results we observed, there may not be a strict boundary between the **IMF** and the non-**IMF** mode. The formation of perfect **IMF** arrays at the interface and the **TDD** reduction might be rather a result of optimized growth conditions and therefore can not be easily transferred between different **molecular beam epitaxy (MBE)** systems. Our results suggest that to further improve the **IMF** growth technique with our system, even higher substrate temperatures such as 540°C during the GaSb growth may lead to further reduced **TDD**.

All the GaSb **IMF** buffers of 600nm exhibited much lower **TDDs** (by more than a factor of 3) than the AlSb buffer of a higher thickness ($1 \mu\text{m}$), which showed a **TDD** of $2.6 \times 10^9 \text{ cm}^{-2}$ as measured by **AFM** (Figure 5.3 (a)). However, the substantial reduction in **TDD** of the GaSb buffer comparing to the AlSb buffer did not seem to sustain after the growth of the AlInSb buffer and the InSb **QW**. As shown in Figure 5.10, similar **TDDs** were measured for the growth with a 100nm AlSb buffer and the one with a 600nm GaSb buffer. The GaSb buffer was grown at 400°C and capped by an As amorphous layer. Then the growth of the AlInSb buffer and the InSb **QW** was deposited after the re-evaporation of the As protective cap. Though we cannot rule out the possible **TDD** contribution by the

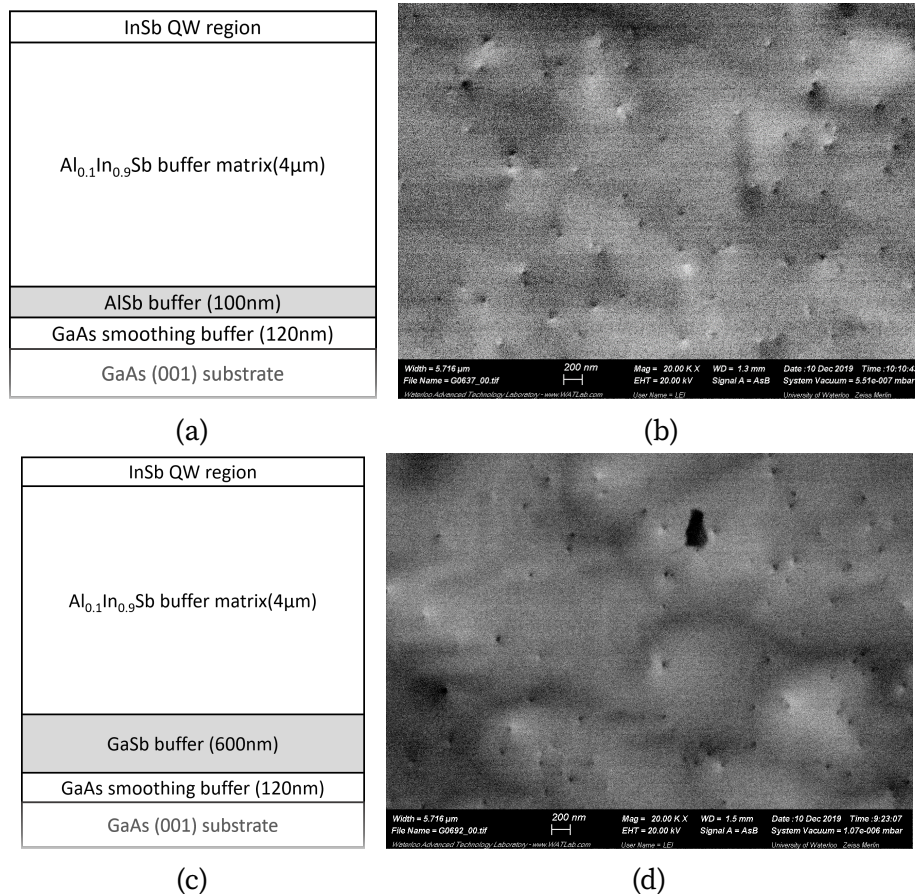


Figure 5.10: The schematics of the InSb QW structures for (a) G0637 with a 100nm AlSb buffer and (c) G0792 with a 600nm GaSb buffer instead. The two structures share the same QW region and the only difference between them is the first intermediate buffer as highlighted in light gray. The characterization of TDD using SEM-ECCI for the structures in (a) and (c) are shown in (b) and (d) respectively.

extra step of As cap desorption, the similar surface morphologies and TDD value of the two growth shown in Figure 5.10 suggests that the thick AlInSb second-stage buffer may play a more important role than the first intermediate buffer in the structure. Therefore we decided not to continue improving the first intermediate buffer and instead focus on the optimizations on the second-stage buffer.

5.4 Dislocation filtering by Interlayers

$\text{Al}_x\text{In}_{1-x}\text{Sb}/\text{Al}_y\text{In}_{1-y}\text{Sb}$ interlayer buffers have been demonstrated by Mishima et al. to be more effective than superlattices [112] and thick single-layer buffers [105] in eliminating propagating defects. On the contrary, Lehner et al. [104] reported a doubling of TDD after replacing the single-layer buffer with the interlayer structure. Here we present the results of our studies on the effectiveness of dislocation filtering by the interlayers and discuss the possible reasons for the discrepancy in the conclusions from different groups.

The buffer structure with a second-stage buffer with three interlayers and a first intermediate buffer of AlSb were studied using cross-sectional scanning transmission electron microscopy (STEM), as shown in Figure 5.11. The first AlSb buffer was grown at 500 °C and 2Å/s followed by a GaSb cap deposited at 475 °C and 1Å/s. The interlayer region, which is consisted of 200nm $\text{Al}_{0.24}\text{In}_{0.76}\text{Sb}$ interlayers surrounded by $\text{Al}_{0.12}\text{In}_{0.88}\text{Sb}$ matrix buffer layers, was grown at 420°C. The interlayers were grown at 2.84Å/s and the matrix buffer layers were grown at 2.5Å/s. As illustrated in Figure 5.11, a high density of TDs (white lines in the STEM image) is generated at GaAs/AlSb and AlSb(GaSb)/ $\text{Al}_{0.12}\text{In}_{0.88}\text{Sb}$ interfaces due to the large lattice mismatch. However, the $\text{Al}_{0.12}\text{In}_{0.88}\text{Sb}/\text{Al}_{0.24}\text{In}_{0.76}\text{Sb}$ direct and inverse interfaces in the interlayer buffer region filtrate the threading components very effectively. Similar TD generation and filtering phenomena have been observed previously with cross-sectional TEM [105, 112]. The 200nm thickness of the interlayers (the thinner layer in the interlayer region) is approximately six times larger than the critical thickness h_c for this material [105]. According to Matthews and Blakeslee [130], when the epilayer is above its critical thickness, the misfit strain at the interface can glide the threading component of the dislocations out of the layer while leaving the strain-relieving misfit component confined at the interface. This leads to an efficient dislocation filtering by the AlInSb interlayer system, as explained in ref[105] and references therein.

As already shown earlier by the AFM analysis in subsection 5.2.1, the application of three interlayers to AlSb buffers reduced the overall TDD by a factor of 10. Here we further demonstrate the effectiveness of the interlayer structure by comparing it to a single-composition buffer of the same thickness. Figure 5.12(a) and (b) show schematics of the two InSb QW structures (G0637 and G0704) grown at the same growth conditions and sharing the same QW region and first intermediate buffer but with different second-stage buffers. A single-composition $\text{Al}_{0.1}\text{In}_{0.9}\text{Sb}$ buffer was used for G0637 and an $\text{Al}_{0.1}\text{In}_{0.9}\text{Sb}/\text{Al}_{0.2}\text{In}_{0.8}\text{Sb}$ interlayer buffer was used for G0704. The details of the QW growth will be discussed in chapter 7. As shown in SEM-ECCI Figure 5.12(c) and (d), a

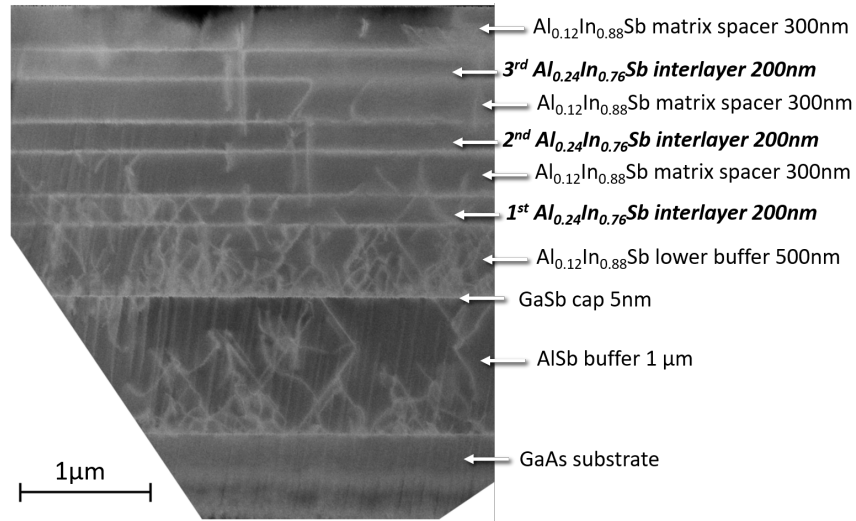


Figure 5.11: The cross-sectional STEM image of the buffer structure with 3 interlayers ($N = 3$). Each layer of the buffer is indicated to the right of the image. The dislocations are identified as the white lines, many of which are observed to stop at the interlayer interfaces.

much lower density of TD outcrops is observed on the surface of G0704 with an interlayer buffer than that of G0637 with a single-composition buffer. The TDD for G0637 is counted to be around $4.5 \times 10^8 \text{ cm}^{-2}$ while the TDD for G0704 is around $1.5 \times 10^8 \text{ cm}^{-2}$, resulting in an effectiveness TDD reduction by a factor of ~ 3 with the application of four interlayers.

Both of our cross-sectional TEM and SEM-ECCI studies have demonstrated a very impelling TDD filtering effect by interlayers. The ratio between the Al percent in the interlayer and that in the buffer matrix layer is exactly 2 for both buffer structures used for the cross-sectional TEM ($y = 0.24$ and $x = 0.12$) and the SEM-ECCI ($y = 0.2$ and $x = 0.1$) analysis. A similar ratio was used by Mishima et al. [105] while a ratio of 3 ($y = 0.3$ and $x = 0.1$) was used with an additional 5 nm InSb layer ($x = 0$) inserted at the interlayer interfaces in the structure reported by Lehner et al. [104]. The effectiveness of TDD reduction was found to first increase then decrease with increasing difference in the Al composition between the matrix layer and the interlayers [131]. Therefore the contradictory results on the effectiveness of interlayers might be a consequence of the different choice of the Al percentage ratio at the interface between the interlayers and the matrix buffer layers. If the ratio is too large, the TDDs being generated may be higher than that being filtered.

For a TDD of $\sim 1 \times 10^8 \text{ cm}^{-2}$ with our current interlayer buffer structures, defect-free

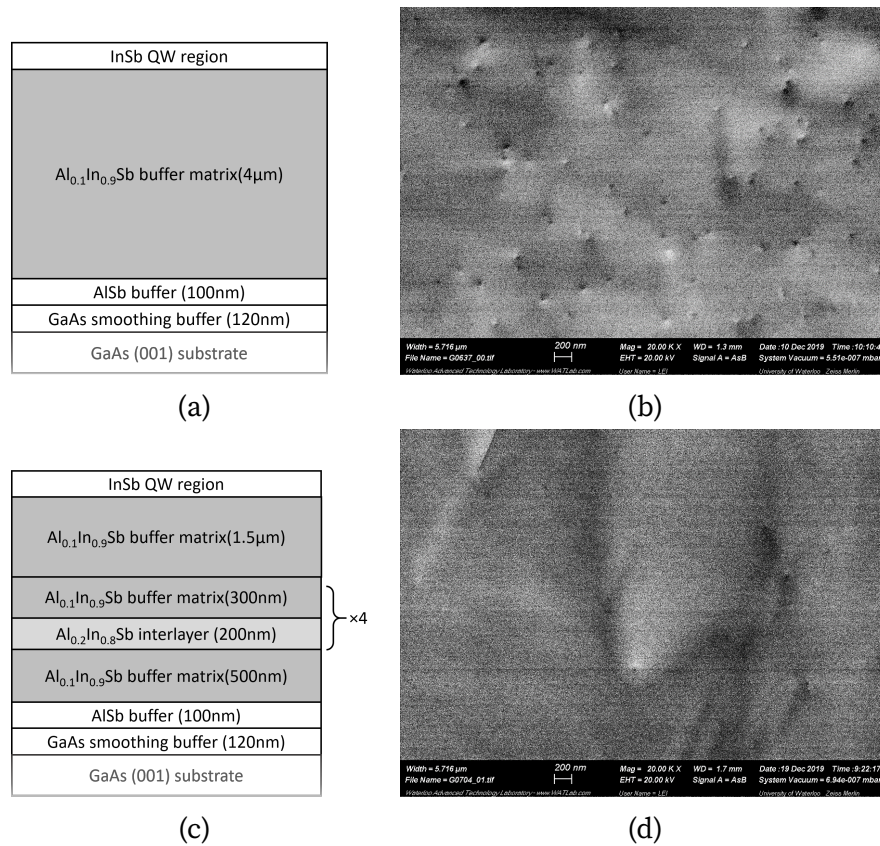


Figure 5.12: The schematics of the InSb QW structures for (a) G0637 with a single-composition buffer and (c) G0704 with an interlayer buffer. The two structures share the same QW region and the only difference between them is the second-stage buffer as highlighted in gray. The characterization of TDD using SEM-ECCI for the structures in (a) and (c) are shown in (b) and (d) respectively. Note that the ECCI image in (a) is the same as the one shown earlier in Figure 5.10(b) and is simply presented here again for easier comparison with (d).

areas of up to a few μm^2 can be located (Figure 5.12(d)) on the InSb QW heterostructure surface. With appropriate alignment marks, these areas can be readily used for subsequent fabrication of 1D InSb nanostructure devices suitable for Majorana experiments.

5.5 Conclusions

The **TDD** at different stages of the metamorphic buffer and the InSb **QW** region were characterized by three different techniques and the results were compared with each other. **AFM** was used to identify the **TD** outcrops on the surface by inspecting the distinct surface features such as hillocks and additional **PASs** on the hillock sidewalls. However, such **PASs** are detectable only with small area scans, which makes **AFM** particularly suitable for samples with high **TDD** values in the range of 10^8 – 10^{10} cm^{-2} . **TDs** were revealed as distinctive spots with sharp dark-bright contrast under **SEM-ECCI**, making their identification much easier compared to **AFM**. For metamorphic buffers with one and three $\text{Al}_{0.12}\text{In}_{0.88}\text{Sb}/\text{Al}_{0.24}\text{In}_{0.76}\text{Sb}$ interlayers, similar **TDD** values were measured by **ECCI** and **AFM**. However for the AlSb first intermediate buffer with very high **HD** and **TDD** on the surface, the **TDD** measured by **ECCI** was more than two times lower than the **AFM** measurement due to the high sensitivity of **ECCI** to surface roughness and the resolution limit of **ECCI** on **TD** outcrops. Notwithstanding this limitation, the small size and sharp contrast for the **ECCI** signatures of **TD** outcrops allow clear **TD** detection at relatively large inspection areas, making **SEM-ECCI** ideal for a broad range of **TDD** measurement (10^6 – 10^9 cm^{-2}). The identification of **TD** outcrops on the surface was also performed using a two-step **DSE** process. However, the need for relatively large pit sizes (~ 1 μm) for easy detection with Nomarski **DIC** optical microscope sets the upper limit of **TDD** allowed by the **DSE** method to be less than 10^7 cm^{-2} . As a result, a large discrepancy between **EPD** and **TDD** was obtained for the metamorphic buffers with **TDD** $> 10^8$ cm^{-2} studied in this thesis. Though the **DSE** technique can be extended to much higher dislocation densities with further etching recipe optimization and switching to higher resolution inspection methods such as **SEM** or **AFM**, it is more suitable for low **TDD** samples. For low **TDD** samples, quick characterization can be achieved with Nomarski microscope and **DSE** can be more advantageous than **SEM-ECCI**.

To further reduce the **TDD** reaching the InSb **QW** active region, we implemented the **IMF** growth mode proposed by Huang et al. [62] on our first intermediate GaSb buffers. However, the results are not very satisfying. Even though a lower **TDD** was observed for the **IMF** GaSb buffers than for the AlSb buffers, the lowest **TDD** we achieved ($\sim 7 \times 10^8$ cm^{-2}) is still higher than the values reported by many other groups ($< 1 \times 10^8$ cm^{-2}). Such discrepancy may be related to the lower thickness of our GaSb **IMF** buffers, since increased **TD** annihilation process in thicker layers is expected to further reduce **TDD**. The disagreement in **TDD** may also be a result of the different characterization technique used. We are the only group that uses **SEM-ECCI**, which we believe to be the much more accurate in determining the exact **TDD** in GaSb/GaAs

systems, comparing to HD-XRD, AFM, and plan-view TEM used by the other groups.

We attempted to improve our IMF growth techniques by varying the growth conditions. We found that further increase in the group V/III ratio of higher than 1.5 does not have a significant influence on the TDD in the GaSb buffer. On the other hand, a trend of increasing TDD was found with decreasing substrate temperature during the growth, which is, however, opposite to the literature report [69, 114]. An inserted annealing step between the island growth stage and the layer-by-layer growth stage of the GaSb buffer does not show any effect on the TDD in the structure. However, post-growth annealing at a substrate temperature elevated by 100 °C for 1 hr has successfully reduced the TDD to the same level measured for the buffer grown directly at the annealing temperature. Insertion of an AlSb monolayer at the GaAs/GaSb interface has also been shown to further reduce the TDD slightly, yet the reduction was not as effective as that demonstrated in Ref.[124].

The underlying mechanism for the IMF growth mode is still not fully understand. As a result, various IMF growth procedures were carried out by different groups and contradictions were found in the reported results. Our results indicate that, without further understanding of the IMF growth mode, it is hard to transfer this growth technique between different MBE systems and reproduce the same level of TDD reduction. Moreover, even though the IMF GaSb buffer is more than three times more effective in reducing the TDD than the AlSb buffer, the TDD levels after the growth of an AlInSb second-stage buffer on the two types of first intermediate buffers are similar. This result suggests that optimization of the thick AlInSb second-stage buffer may be more important than that of the first intermediate buffer for the development of the InSb QW structures.

Cross-sectional STEM has revealed effective dislocation filtering by the $\text{Al}_{0.12}\text{In}_{0.88}\text{Sb}$ / $\text{Al}_{0.24}\text{In}_{0.76}\text{Sb}$ interlayer structure first proposed by Mishima et al. [105] as the second-stage buffer in our metamorphic buffer structure. However, the difference in the Al composition between the interlayer and the buffer matrix layer needs to be chosen carefully. If such difference is too large, the interfaces in the interlayer structure may be responsible for generating more TDs than filtering them.

By replacing the single-composition $\text{Al}_{0.1}\text{In}_{0.9}\text{Sb}$ second-stage buffer with an $\text{Al}_{0.1}\text{In}_{0.9}\text{Sb}$ / $\text{Al}_{0.2}\text{In}_{0.8}\text{Sb}$ interlayer structure, the TDD on the surface of InSb QW structure was reduced by a factor of three to $\sim 1.5 \times 10^8 \text{ cm}^{-2}$. For such a TDD level, defect-free surface areas of up to a few μm^2 can be easily located on the surface of our InSb QW heterostructures, making these structures already suitable for the top-down fabrication of InSb nanowire devices.

Chapter 6

Improving the surface morphology

6.1 Threading dislocation mediated surface morphology

Threading dislocations (TDs) can have a significant effect on the growth kinetics. When the threading dislocation density (TDD) in the epitaxial layer is high, the development of the surface morphology is driven by the presence of steps at the surface associated with the screw component of the TDs. The basic idea behind this process originates from the paper published by Burton, Cabrera, and Frank (BCF) [40] in 1951, which is hereafter denoted as the BCF theory. When a mixed-type TD terminates at the epilayer surface, a component of its Burgers vector perpendicular to the growth direction yields a step on the surface which provides a preferred step edge site for atoms to attach. Since the step is pinned at the dislocation line, the step winds up until the curvature at the center reaches a critical value of $1/\rho_c$, as predicted in the BCF theory. Then the whole spiral pattern grows with a stationary shape as the step advances during growth, as illustrated in Figure 6.1(a). A single TD with a screw component can hence send out successive turns of steps and provides an inexhaustible source of step edge sites for incoming growth atoms. When the density of such dislocations is high, the surface morphology can be dramatically influenced as the spiral growth dominates the surface kinetics. The BCF paper also predicted the outcome morphology due to the interactions between the spiral hillocks centered on different dislocations. No hillocks will be formed if a pair of dislocations of opposite signs are closer than the critical terrace width of the hillock spiral steps. Yet if they are separated far away enough from each other, steps with closed loops and flat terraces shared by the two hillocks will be sent out from their bases after they meet (Figure 6.1(b)). In this case, the locus of intersections is a straight line dividing

the two hillock into two areas with the steps in each area fed by the center dislocation belonged to the area. For a pair of dislocations with like signs that are far apart, the locus of intersections is an s-shaped curve, bisecting the two hillocks each fed with steps from both spiral centers (Figure 6.1(c)). On the other hand, if the dislocations are closer than the critical terrace width of their spiral steps, then the resultant hillock will take a shape similar to the one formed from a single dislocation, except that each consecutive steps now originates from different dislocations in the center and the hillock will be bigger in size due to the resultant larger growth rate. Figure 6.1(d) shows a group of dislocations of the same sign arranged closely in a line as an example.

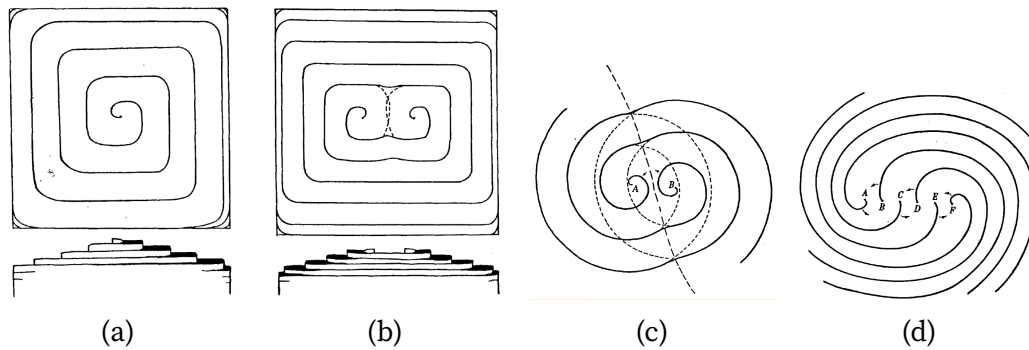


Figure 6.1: Schematic illustration of the surface spirals as a result of (a) one single dislocation with a screw component; (b) a pair of dislocations of opposite signs; (c) a pair of dislocations of similar signs and (d) a group of dislocations of similar signs, as predicted by the BCF theory (adapted from the BCF paper, 1951 [40])

6.2 Surface hillocks on antimonides/GaAs and their disadvantages

Atomic force microscopy (AFM) scans revealed a large number of hillocks with atomic height terraces on all Sb-based material structures grown on GaAs substrates studied in this thesis due to their high TDDs. Figure 6.2 shows the morphology of spiral hillocks on AlSb, GaSb, and $\text{Al}_{0.12}\text{In}_{0.88}\text{Sb}$ surfaces. The AlSb layer and GaSb layer presented in Figure 6.2(a) and (b) were both grown directly on GaAs substrates at 500 °C except that the AlSb layer was covered by a thin 5 nm GaSb cap to prevent oxidation. The $\text{Al}_{0.12}\text{In}_{0.88}\text{Sb}$ layer in Figure 6.2(c) was grown at 420 °C on top of an AlSb intermediate buffer. The

thickness of the three buffer layers are comparable, being 1 μm , 600 nm, and 1 μm for the AlSb, GaSb, and $\text{Al}_{0.12}\text{In}_{0.88}\text{Sb}$ layers, respectively. Yet the shapes, sizes, and terrace width of the hillocks are all different on the surfaces of different materials. On the other hand, these hillocks are all elongated in the $[1\bar{1}0]$ direction, reflecting atom diffusivity anisotropy along different crystalline directions.

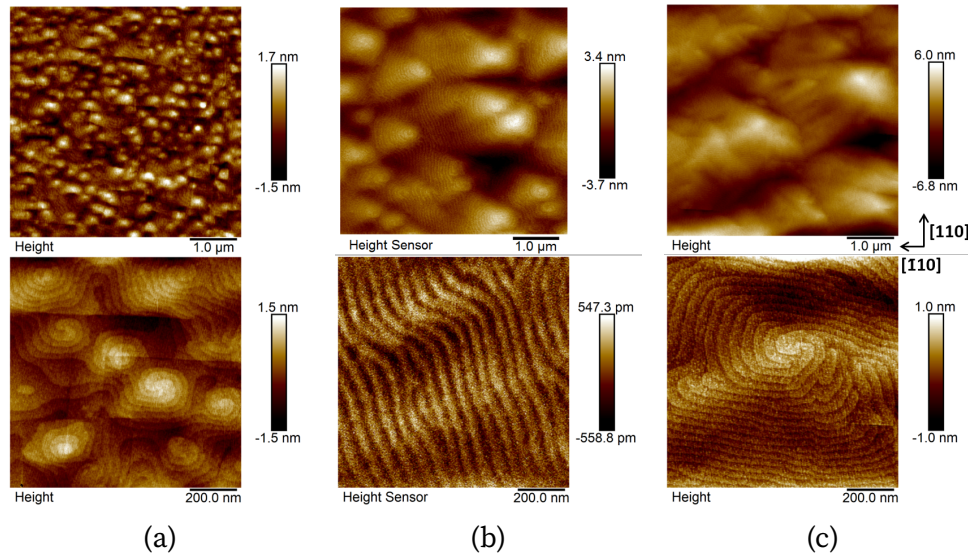


Figure 6.2: 5×5 and $1 \times 1 \mu\text{m}^2$ AFM images showing the morphological features of spiral hillocks on (a) AlSb of 1 μm thick on GaAs substrate; (b) GaSb of 600 nm thick on GaAs substrate; and (c) $\text{Al}_{0.12}\text{In}_{0.88}\text{Sb}$ of 1 μm thick grown on top of a 1 μm AlSb layer on GaAs substrate

Since the distribution of TDs emerging the surface is highly non-uniform, different morphological features as a result of hillock interactions are observed and they agree well with the predictions in the BCF theory. A $1 \times 1 \mu\text{m}^2$ AFM image of an AlSb surface is shown in Figure 6.3 with the spiral steps of several hillocks highlighted. In the center of the image, a hillock resulted from a right-handed TD is traced out in a yellow dashed line. Another hillock two-terrace-width away formed around a left-handed TD is highlighted by a white dashed line. The interaction of these two hillocks results in closed loops with flat terraces after the two hillocks meet, similar to the BCF's prediction shown in Figure 6.1(b). In the upper right corner of the image, the interaction of a pair of dislocations of like signs are also highlighted in yellow and white dashed lines. Moreover, a big hillock formed around a group of dislocations of similar signs can be seen in the bottom of the image. The spiral steps originated from different dislocations are highlighted in different

colors, exhibiting a shape similar to the one predicted by BCF shown in Figure 6.1(d).

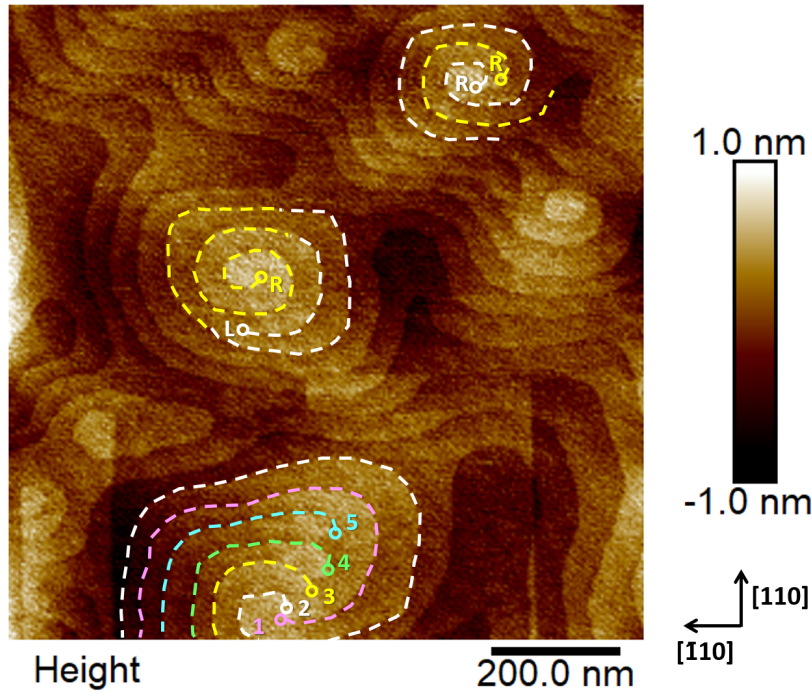


Figure 6.3: $1 \times 1 \mu\text{m}^2$ AFM image showing different forms of hillocks due to their interactions with each other on an AlSb surface. The spiral steps of some hillocks are highlighted for easy comparison to the predictions in Figure 6.1.

At first sight, the comparatively flat surface features of hillocks, according to the AFM height scales in Figure 6.2, together with their relatively low density, should not pose a serious challenge to top-down nanowire device fabrication. However, the mesh of two orthogonal and well-defined atomic steps may cause undesirable phase separations and/or alloy ordering effects in ternary materials. Indeed, different facet angles were observed on the hillock sidewalls in $[\bar{1}10]$ and $[110]$ directions. This may lead to different probabilities for the attachment of Al and In atoms on these steps, which in turn could cause fluctuations in the composition of AlInSb barriers, giving rise to related fluctuations in confining potentials and local strains. Such fluctuations would have deleterious effects on the electronic mean free path and the uniformity of the chemical potential, both of which are undesirable from the quantum device performance point of view. In fact, the adverse influence of hillocks due to dissimilar chemistry for different ledge directions has been noted in the InGaN family of materials [132, 133].

The low-temperature mobility measured with InSb [quantum well \(QW\)](#) structures have always been far from ideal compared to the behavior of InSb bulk materials (which has the highest mobility of any III-V semiconductor at room temperature), and it has been suggested lately that the reason might be related to surface hillocks, with the boundaries of which acting as scattering centers. [24] Therefore, from the perspective of quantum device performance and formation of robust bound Majoranas, suppression of hillock formation is as important as further reduction in [TD](#) and [micro-twins \(MT\)](#) densities.

6.3 Influence of growth conditions

To better understand the growth dynamics of highly lattice-mismatched Sb-based metamorphic materials on GaAs substrate, we studied the hillock-decorated surface morphology of AlSb, GaSb, and AlInSb at different growth conditions.

[Figure 6.4](#) shows the surface morphology of the first intermediate AlSb buffers of 1 μm thick on GaAs (001) substrate at different substrate temperatures and with different techniques for the removal of substrate native oxides. 5 nm GaSb protective caps were grown at 475 $^{\circ}\text{C}$ on top of all the AlSb buffers to prevent them from oxidation. Normally the substrate native oxides were thermally evaporated at a high substrate temperature of 630 $^{\circ}\text{C}$ under As flux and a 1200 nm GaAs smoothing buffer was deposited before the growth of the AlSb buffer, as in the case of the AlSb buffers presented in [Figure 6.4\(a\)](#) and [\(b\)](#). However, the As cell was used up in the middle of the campaign and we were forced to clean the substrate oxides through a chemical process with small In fluxes [134] at a much lower substrate temperature and no GaAs smoothing buffers were deposited for the AlSb growths in [Figure 6.4\(c\)](#) and [\(d\)](#). The other growth parameters including the growth rate (2 $\text{\AA}/\text{s}$) and the V/III flux ratio (~ 1) were kept the same for all the AlSb buffers in [Figure 6.4](#). The growths of AlSb buffer using the [In-assisted oxide desorption \(IOD\)](#) and without the GaAs smoothing buffer ([Figure 6.4\(c\)](#)) showed a different surface morphology than the one using [thermal oxide desorption \(TOD\)](#) and with a GaAs smoothing buffer ([Figure 6.4\(b\)](#)) despite the same growth conditions used. Since it is still unclear how the oxide desorption procedure and the substrate smoothing buffer affect the surface morphology, growths are only compared among the ones that went through the same surface preparation procedures. The terrace width on the hillock sidewalls becomes wider as the substrate temperature increases for the growths using [TOD](#) ([Figure 6.4\(a\)](#) and [\(b\)](#)) while this trend is less obvious with the growth using [IOD](#) ([Figure 6.4\(c\)](#) and [\(d\)](#)). However, for both sets of data, a weak trend of increasing hillock lateral size with higher substrate temperature is observed.

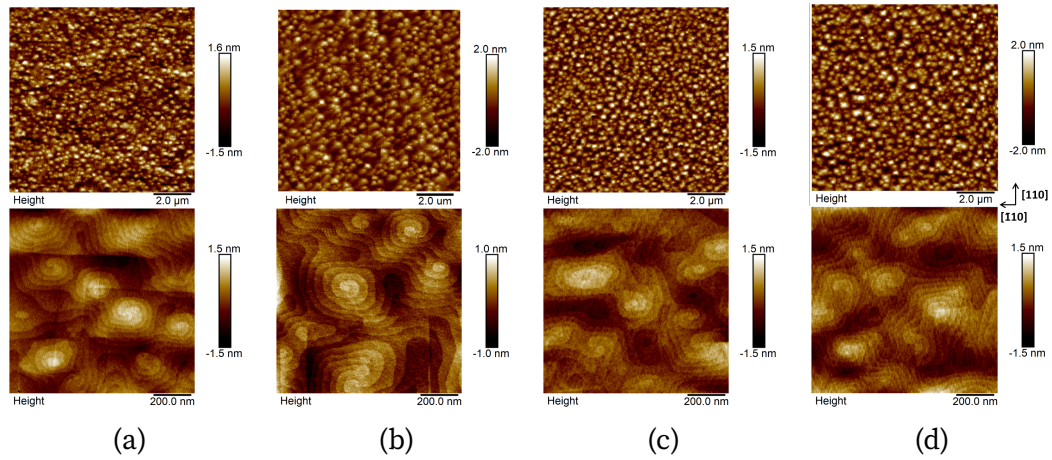


Figure 6.4: AFM height scans of $10 \times 10 \mu\text{m}^2$ (up) and $1 \times 1 \mu\text{m}^2$ (down) in size showing the surface morphology of AlSb buffers grown at (a) 500 °C and (b) 550 °C using thermal oxide desorption; (c) 550 °C and (d) 600 °C using Indium assisted oxide desorption.

The surface morphology of 600 nm-thick GaSb and 3 μm -thick $\text{Al}_{0.1}\text{In}_{0.9}\text{Sb}$ buffers grown at different substrate temperatures are shown in Figure 6.5 and Figure 6.6 respectively. The growths of GaSb and $\text{Al}_{0.1}\text{In}_{0.9}\text{Sb}$ buffers were all proceeded by TOD and GaAs smoothing buffers. The GaSb buffers in this study are 600 nm thick and were grown directly after the GaAs smoothing buffer. All the $\text{Al}_{0.1}\text{In}_{0.9}\text{Sb}$ buffers have a thickness of 3 μm and were grown on top of a 100 nm AlSb intermediate buffer. The growth of the $\text{Al}_{0.1}\text{In}_{0.9}\text{Sb}$ buffers was also followed by an InSb QW region grown at a slightly lower substrate temperature than that used for the $\text{Al}_{0.1}\text{In}_{0.9}\text{Sb}$ buffer in the structure. The InSb QW region contained the same $\text{Al}_{0.1}\text{In}_{0.9}\text{Sb}$ material as the barrier, a 30 nm InSb QWs and a Si δ -doping layer. The growth of the 30 nm InSb QW was 70 nm below the surface and appeared as small hillocks due to its small thickness on the large $\text{Al}_{0.1}\text{In}_{0.9}\text{Sb}$ hillocks, as shown in Figure 6.6. The morphology of the $\text{Al}_{0.1}\text{In}_{0.9}\text{Sb}$ hillocks was essentially preserved after the growth of the InSb QW region and hence can be studied directly with these samples. Due to the small sizes, the hillocks on the AlSb and GaSb buffers can not be revealed clearly under Nomarski microscope and hence were examined by AFM. On the other hand, the hillocks of the thick $\text{Al}_{0.1}\text{In}_{0.9}\text{Sb}$ buffers are large enough to be easily studied using Nomarski microscope. As shown in Figure 6.5 and Figure 6.6, both the GaSb and $\text{Al}_{0.1}\text{In}_{0.9}\text{Sb}$ buffers demonstrated a strong trend of increasing hillock terrace width and at the same time widening hillock lateral size as the substrate temperature increases.

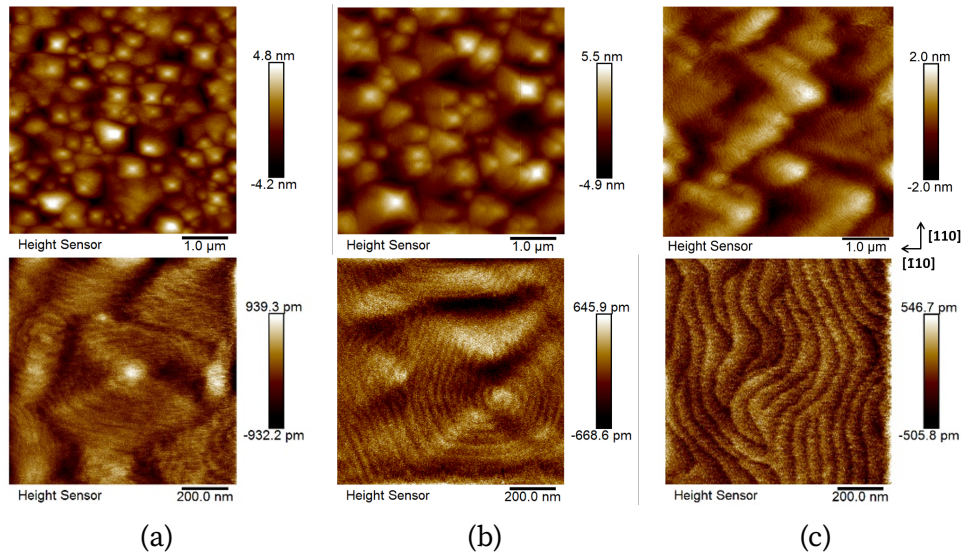


Figure 6.5: AFM height scans of $5 \times 5 \mu\text{m}^2$ (up) and $1 \times 1 \mu\text{m}^2$ (down) in size showing the surface morphology of GaSb buffers grown at (a) 400 °C, (b) 450 °C and (c) 510 °C.

The critical width of the hillock spiral steps was formulated by the BCF theory as a function of supersaturation, which is a thermodynamic result following the same derivation of the critical radius of a 2D nucleus under equilibrium conditions. The growth process considered was under relatively low supersaturation and low growth rates due to atoms being continuously desorbed from the surface. However, as discussed in chapter 4 the growth process inside an molecular beam epitaxy (MBE) chamber proceeds under conditions of high driving force and is far away from thermodynamic equilibrium. The crystal morphology usually does not resemble its equilibrium shape, therefore the terrace width of the hillocks developed on the Sb-based materials shown above cannot be fully explained by the BCF formalism and instead should be studied by considering the kinetic processes on the surface.

As mentioned in chapter 4, the growths of all the III-V materials in this study were carried out under the conditions of supplying the group V atoms in a flux higher than the V/III ratio of 1:1. The growth rates are strictly determined by the flux of group III atoms and therefore the surface morphology is a direct result of the migration of the group III atoms on the surface. Since no group III atoms are expected to desorb during the growth, the lifetime of the group III atoms on the surface in the precursor stage can be considered the same for the growths conducted at different substrate temperatures as long as the growth rate and V/III ratio were kept the same (Equation 2.3). On the other hand, the

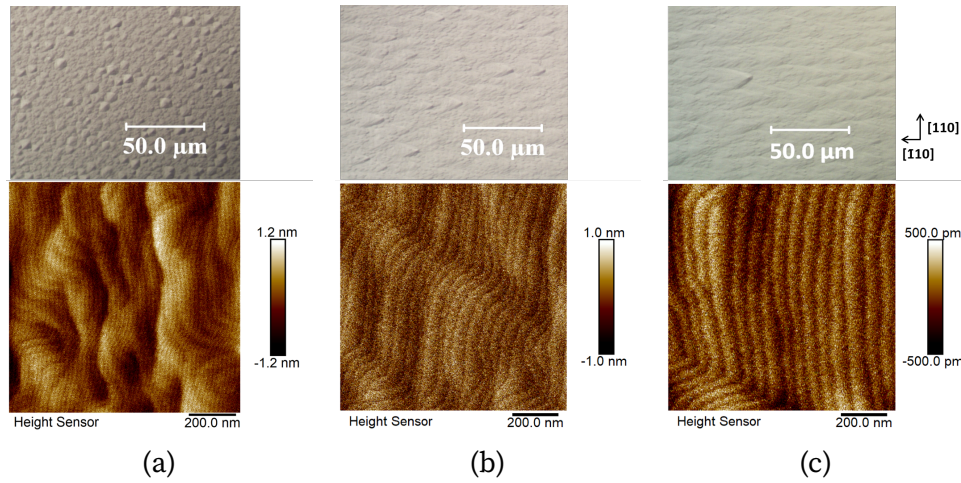


Figure 6.6: Nomarski and $1 \times 1 \mu\text{m}^2$ AFM images showing the surface morphology of $\text{Al}_{0.1}\text{In}_{0.9}\text{Sb}$ buffers grown at (a) 350°C , (b) 380°C and (c) 420°C .

diffusivity of the group III atoms are expected to increase with substrate temperature (Equation 2.5). As a result, the diffusion length of the group III atoms becomes larger as the substrate temperature increases (Equation 2.4). Very likely the trend of hillock terraces widening with increasing substrate temperature observed for AlSb, GaSb, and $\text{Al}_{0.1}\text{In}_{0.9}\text{Sb}$ is related to the change in the adatom diffusion length.

Very consistent terrace width on the hillock sidewalls can be observed on the AlSb (Figure 6.4) and GaSb (Figure 6.5) buffers as well as the $\text{Al}_{0.1}\text{In}_{0.9}\text{Sb}$ buffer grown at 420°C (Figure 6.6(c)). This suggests that a stable growth mode was achieved locally on the hillock sidewalls. Indeed, as shown in the bottom $1 \times 1 \mu\text{m}^2$ AFM images in Figure 6.7, the terrace widths on the hillock sidewalls remain constant as the thickness of the $\text{Al}_{0.12}\text{In}_{0.88}\text{Sb}$ buffer increases from $2 \mu\text{m}$ to $12 \mu\text{m}$. Though the spiral nature of the steps can still be observed on the top of the hillock near the dislocation center (Figure 6.6 (c)), once the hillocks have developed and grown bigger, the adatom diffusion is influenced primarily by the local surface slope, not by the spiral nature of the entire hillock. Many models for numerical simulations have been developed to explain the dynamics of epitaxial growths including slope selection, facet formation, and surface roughing based on kinetic continuum equations [135–139]. Though formulated in a different context, we hypothesize that such models can also be adapted to explain the stable terrace width achieved on the hillock sidewalls. On a stepped surface, different attachment kinetics at the step edges lead to diffusion biases that manifest themselves in either an uphill or downhill surface currents (section 2.3). For example, a positive Ehrlich–Schwoebel (ES) barrier (section 2.3) can

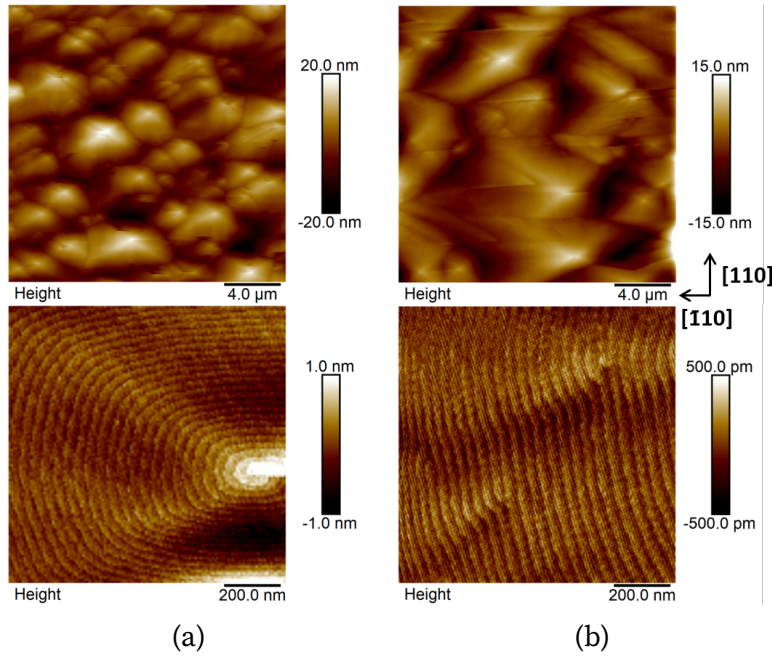


Figure 6.7: $20 \times 20 \mu\text{m}^2$ (up) and $1 \times 1 \mu\text{m}^2$ (down) AFM images of (a) $2 \mu\text{m}$ -thick and (b) $12 \mu\text{m}$ -thick $\text{Al}_{0.12}\text{In}_{0.88}\text{Sb}$ buffers grown at 420°C under the same growth conditions on AlSb nucleation buffers on GaAs (001) substrates.

lead to a net uphill current. In the extreme case for the positive Ehrlich–Schwoebel (ES) barrier, no adatom on a vicinal surface can overcome the barrier to jump downward. If the diffusion length in this case is longer than the terrace width of the steps, a stable growth in a step-flow growth mode can be achieved locally on the hillock sidewalls. The ES barrier can also be negative in some circumstances, which will lead to a net downhill currents. Other effects such as the knock-out effect (section 2.3) may also contribute to a downhill current. On the other hand, steps may also interact with each other elastically and via the diffusion field of adatoms [33], which can further influence the surface currents [33]. We suspect that the uniform terrace width we observed on the hillock sidewalls is related to the balancing between the uphill and downhill currents influenced by all the above and possibly other kinetic processes.

On the other hand, the $\text{Al}_{0.1}\text{In}_{0.9}\text{Sb}$ buffer grown at lower substrate temperatures showed evidence of instability in retaining a selected critical slope on the hillock sidewalls. The $\text{Al}_{0.1}\text{In}_{0.9}\text{Sb}$ buffer grown at 380°C started to show variation in terrace widths on the hillock sidewalls while the terrace width showed even greater divergence and

appear wavier for the $\text{Al}_{0.1}\text{In}_{0.9}\text{Sb}$ buffer grown at 350 °C (Figure 6.6(b) and (c)). Since there were two group III atoms involved in the growth, the instability in the hillock sidewall slopes might be a result of their diffusivity responding differently in the range of change in the substrate temperature. Moreover, as the terrace width becomes smaller, the interaction between the steps becomes stronger, which, together with the different diffusivities of the adatoms, may lead to instabilities such as step meandering and step bunching (Figure 6.6(a)).

We also attempted to influence the hillock terrace width on the AlSb surface by varying its growth rates and using different V/III ratios. However, unlike the clear trend of terrace width widening with increasing substrate temperature, no significant trend was observed as the growth rate was decreased from 2 Å/s to 1 Å/s or as the III-V ratio was reduced from 2 to 1 for AlSb buffers grown at 550 °C. A more visible effect on the hillock terrace width may be observed if a larger change in these growth conditions is made. Since a much weaker dependence on temperature was also observed for the AlSb buffers compared to the GaSb and $\text{Al}_{0.1}\text{In}_{0.9}\text{Sb}$ buffers, a stronger morphological influence by the growth rate and the V/III ratio may be observed with other III-Sb materials.

6.4 Effect of substrate offcut

As the buffer grows thicker, one may expect that the hillocks will retain their size as each of hillocks grows stably with the characteristic facet angle. However, as shown in Figure 6.7, the hillocks on the surface of the 12 µm-thick $\text{Al}_{0.12}\text{In}_{0.88}\text{Sb}$ buffer are significantly larger than the ones on the 2 µm-thick $\text{Al}_{0.12}\text{In}_{0.88}\text{Sb}$ buffer. The hillocks did not retain their sizes during the 10 µm buffer growth. One possible explanation for this observation is the reduced TDD on the surface due to the TD annihilation process as the layer grows thicker, leading to hillocks smaller in number and larger in size. However such TD annihilation activity becomes very rare as the dislocation densities are reduced below a certain limit and the layer has grown beyond certain thickness. We found that the 12 µm $\text{Al}_{0.12}\text{In}_{0.88}\text{Sb}$ buffer shares a very similar TDD with the 2 µm $\text{Al}_{0.12}\text{In}_{0.88}\text{Sb}$ buffer. Therefore the decrease in TDD becomes marginal as the layer thickness increases above 2 µm. Another more plausible explanation is that the hillocks have different growth rates. As shown in Figure 6.3, hillocks that developed around a larger group of dislocations appear larger as they grow faster. Therefore, such hillocks will grow larger and slowly 'devour' the smaller hillocks as the layer continues to grow thicker. Indeed, AFM analysis shows that the application of three interlayers to AlSb buffers reduces the surface hillock density by a factor of 70, while the overall TDD is reduced by only a factor of 10

(Figure 5.3). As shown in Figure 5.4, instead of forming hillocks, TD outcrops observed on the sidewalls of large hillocks simply appear as additional pinned atomic steps (PASs). This provides the most direct hint that the inclination angles of the hillock sidewalls are the optimum substrate offcut to achieve a hillock-free surface.

Suppression of dislocation-related surface hillocks on vicinal surfaces has been reported in other material systems and using different growth techniques. Metal-organic chemical vapor deposition (MOCVD) grown hillock-free GaN on the vicinal sapphire surface was reported by Heying et al. [140]. Yet such hillock-free GaN templates with fairly long and wide dislocation-pinned steps were subsequently used for GaN growth by MBE and showed a large density of hillocks. The observations were explained by the authors using a simple model based on the BCF theory [40], and very different surface diffusivities for MOCVD and MBE processes. The authors also postulated that when the step width of the spiral approaches the width of the natural steps on the vicinal surface, the hillock formation will be suppressed. Similar conclusions were reached by Cui and Li [141] for GaN grown on vicinal 6H-SiC(0001) substrates.

To verify our postulation based on the observation on the hillock sidewalls and examine the applicability of the proposed mechanism from the literature, we conducted a comprehensive study on the surface morphology of Sb-based materials on (001) GaAs substrates as a function of substrate offcut angle by employing the polishing-induced gradual change of surface orientation at the edge of the substrate, as demonstrated in subsection 4.1.4.

Figure 6.8 shows the AFM images of the 1 μm AlSb layer grown at 550 $^{\circ}\text{C}$ and 1 $\text{\AA}/\text{s}$ taken at several locations progressively closer to the wafer edge (Figure 4.3). The effective offcut angle of the substrate with respect to (001) orientation was determined directly from the AFM images as:

$$\theta_{\text{offcut}} = \tan^{-1}((h_{\text{ML}} \times \sum_n (\pm 1))/d_{\text{total}}), \quad (6.1)$$

where d_{total} is the distance over which the total number of atomic steps, n , was counted in the direction of the steepest surface slope. \pm are for up and down steps respectively. It is found that as the effective substrate offcut angle increases from 0° to around 0.8° , the surface morphology of the AlSb layer progresses from a hillock decorated surface to one dominated by parallel steps. Interestingly, when the offcut angle is further increased the surface becomes rough again, this time as a result of step bunching effect and the formation of surface depressions. Under as described growth conditions, the smoothest AlSb layer surface morphology obtained for GaAs (001) substrate with offcut angles towards the $[1\bar{1}0]$ direction is between 0.8° and 1.3° . We must stress here the importance

of the particular growth conditions, since the average step width of the hillock spirals is expected to change if the surface diffusivity changes, as demonstrated in [section 6.3](#). Only the primary flat of the [quarter of a three-inch \(Q3"\)](#) wafer was exposed during the growth. Since the minor flat of the wafer was covered by the Q3" inserts, the morphological transformation as a function of substrate offcut in the [110] direction was not studied for the AlSb growth. However, AlSb layer has also been grown under the same growth conditions on a GaAs (001) substrate with 2°-offcut towards [110] direction. As shown in [Figure 6.8\(b\)](#), the growth exhibited an even rougher surface morphology than [Figure 6.8\(a\)\(v\)](#) as expected. This result also helps to largely rule out the possibility that the observed surface roughening at high substrate offcut angles is related to inferior surface epi-ready preparation when approaching the wafer edge.

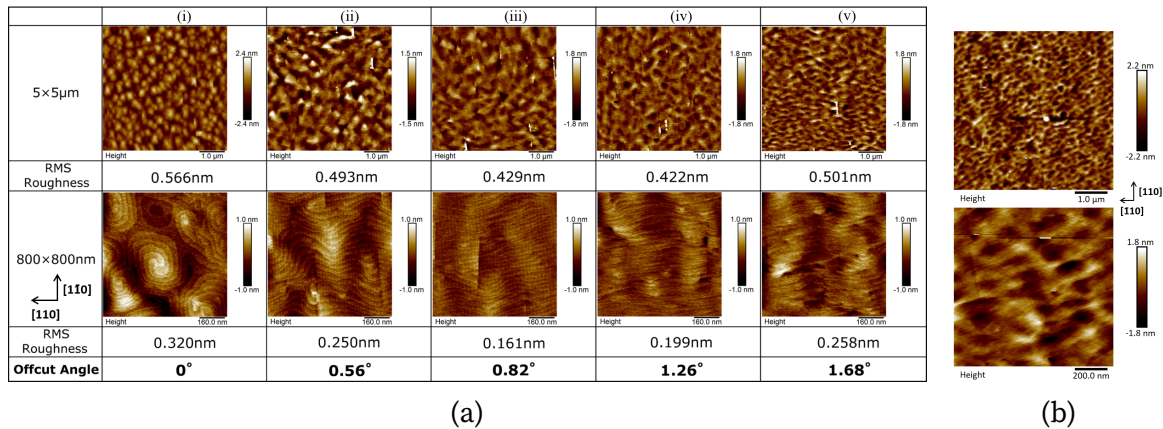


Figure 6.8: 5×5 and 1×1 μm² AFM images showing (a) the transition of the surface morphology of the AlSb layer on GaAs (001) substrate with offcut angle increasing from 0° to 1.68° in [110] direction at the very edge of the wafer, and (b) the surface morphology of AlSb layer grown directly on GaAs (001) substrate with 2°-offcut towards [110] direction.

The surface morphology of the AlInSb buffer was studied as a function of the substrate offcut angle at all directions by performing the growth on a 2" GaAs (001) substrate mounted in the suspended configuration with a sapphire plate ([subsection 4.1.4](#)). As shown in [Figure 6.9](#), as the effective offcut increases towards the very edge of the wafer in [110] direction, the hillock-dominated surface morphology gradually transitions into a smooth and hillock-free morphology, and eventually to a rough surface with step-bunching and depressed regions, similarly to that observed for AlSb. The optimal offcut angle for Al_{0.12}In_{0.88}Sb in the [110] (equivalent to [110] due to crystal symmetry) direction, calculated using the 1×1 μm² AFM images, is 0.4~0.5°, which is much smaller than that

for AlSb, ($0.8\sim 1.3^\circ$). Similar morphological transformation of the AlInSb surface was also found in the $[110]$ direction and the optimal offcut angle is calculated to be around $0.7\sim 0.8^\circ$ in this direction. The sidewall facet angles of the hillocks in the center of the wafer were also calculated by counting the number of atomic steps on hillock sidewalls in the $1\times 1\ \mu\text{m}^2$ AFM scans. The hillock facet angles found in the center of the wafer are $0.4\sim 0.5^\circ$ towards $[\bar{1}10]$ direction and $0.7\sim 0.8^\circ$ towards $[110]$ direction, which agree well with the optimal offcut angles found at the edge of wafer for both directions. This result further validates our earlier hypothesis.

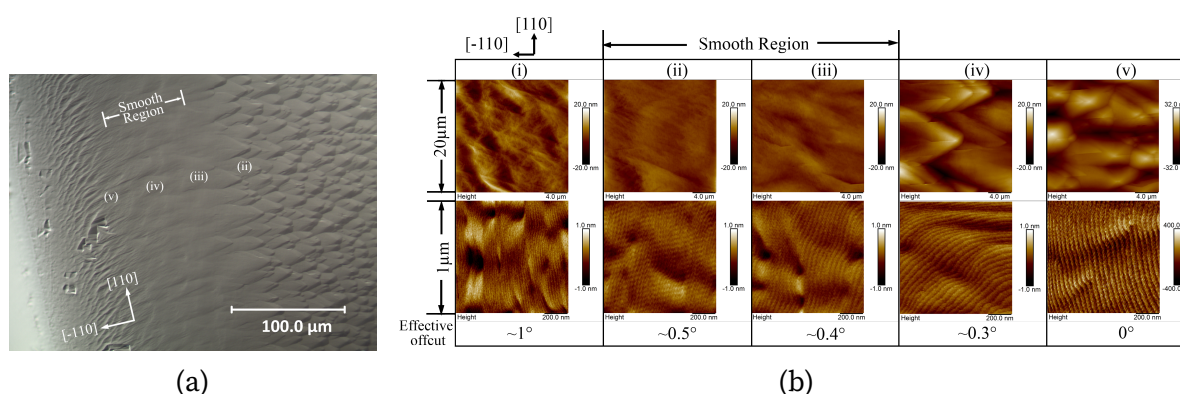


Figure 6.9: (a) Nomarski and (b) AFM images of $20\times 20\ \mu\text{m}^2$ and $1\times 1\ \mu\text{m}^2$ in size showing the transition of the $\text{Al}_{0.12}\text{In}_{0.88}\text{Sb}$ surface morphology as a function of the effective substrate offcut angle at the edge of the wafer. The approximate AFM scan positions in (b) are indicated by label (ii)-(v) in (a) correspondingly. The effective offcut are calculated using the $1\times 1\ \mu\text{m}^2$ AFM images. The insert in (b) panel (v) is a magnified view to show the step-bunching effect.

Some variation of atomic fluxes and temperatures across a wafer is expected and should be considered as a factor when comparing morphology between different wafer locations. From an independent study, we know that the Al and In fluxes for our MBE system, averaged over the manipulator rotation cycle, change by less than 0.5% and 2% respectively from the centre to the edge of a 3" substrate, while smaller than 5°C temperature variation is expected for indium-free mounted GaAs substrates at temperatures below 600°C . However, a qualitative change in hillock terrace width was only observed under a rather significant change in growth conditions (section 6.3). In view that all the AFM images in Figure 6.8 were obtained within a $\sim 1\ \text{mm}$ long surface strip at the wafer edge, we can safely conclude that inhomogeneity in fluxes and temperatures are not expected to affect the surface morphology for the small area investigated. Thus,

GaAs (001) substrates with an offcut angle of $0.4\sim 0.5^\circ$ towards $[\bar{1}10]$ direction or $0.7\sim 0.8^\circ$ towards $[110]$ direction can be considered as optimal for growing hillock-free $\text{Al}_{0.12}\text{In}_{0.88}\text{Sb}$ metamorphic buffers.

Here we discuss the hillock morphological transitions as a function of substrate offcut, with a graphical illustration in [Figure 6.10](#). On the substrate with no offcut, surface adatoms preferentially attach to the atomic steps pinned at **TD** outcrops and wind up to form pyramid-like hillocks on the surface. These hillocks would grow indefinitely with small hillocks annihilating on the sidewalls of larger hillocks. When substrate offcut is non-zero but less than the natural hillock facet angle, because of the crystalline symmetries, the hillocks appear tilted on the surface, as if part of the hillocks is ‘buried’ by the effective extra surface steps originated from the substrate offcut. When the offcut of the substrate equals exactly to the natural hillock facet angle, the local equilibrium of surface currents achieved on the hillock sidewalls is now realized globally. Furthermore, we observed that such hillock-free growth can also be achieved with a very narrow range of substrate offcut slightly larger than the natural hillock facet angle. In this narrow range of offcut angles, step-flow growth takes place by following the native steps on the substrates and no hillocks can develop. However, when the offcut of the substrate increases further, the growth mode transitions from step-flow to step-bunching. Such step bunching instability may be a result of the **ES** barrier turning from positive to negative [[33](#), [142](#)] due to increased elastic interaction between steps and non-linear step-step interaction due to largely overlapped diffusion field of adatoms [[33](#)] as the steps become too close to each other. Moreover, it has been suggested that surface depressions may form at **TD** outcrops due to the balance of dislocation-associated strain energy density by surface tension. [[143](#)] This effect might also promote the surface roughening process and the surface depressions we observe on the $1\times 1\mu\text{m}^2$ **AFM** image in [Figure 6.9](#) panel (v) might be related to it.

With **InSb QW** overgrown on the $\text{Al}_{0.12}\text{In}_{0.88}\text{Sb}$ metamorphic buffer, the surface morphology is essentially preserved — a large density of hillocks covering the surface ([Figure 6.11\(a\)](#)). However, now two groups of hillocks with different sizes can be easily distinguished. The large hillocks originate from the very thick $\text{Al}_{0.12}\text{In}_{0.88}\text{Sb}$ buffer. The small hillocks with slightly steeper sidewalls, which emerge on the top and the sidewalls of the large **AlInSb** hillocks, are formed from the **InSb QW** layer at **TD** outcrops. The two groups of the hillocks provide us an insight into the structure of **InSb** quantum wells grown on typical metamorphic buffers. As shown in the insertion of [Figure 6.11\(a\)](#), the quantum well is thicker at the **InSb** hillocks and thinner elsewhere, which may result in undesirable localization effects. On the other hand, the emergence of such little **InSb** hillocks shows that the natural facet angle for **InSb** is slightly larger than that for **AlInSb**

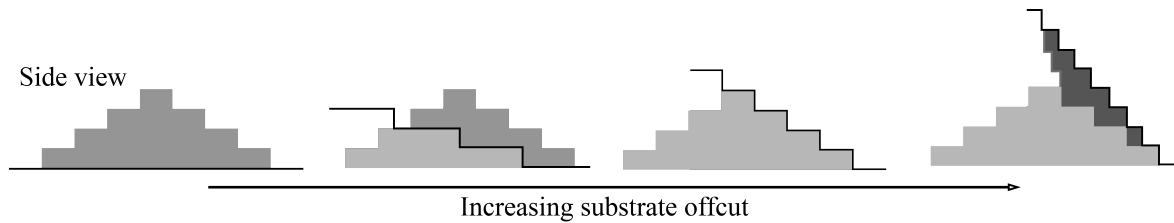


Figure 6.10: Graphic illustration of the growth mechanism that results in a morphological transition with increasing substrate offcut angle. The black curves are surfaces parallel to the substrate. The medium gray regions represent the hillocks formed on the surface. The light gray and dark gray regions are the ‘suppressed parts’ and the ‘over-suppressed parts’ of the hillocks, respectively. Hillock-free and smooth surface can be achieved when the substrate offcut angle agrees with the hillock sidewall angle.

and a larger substrate offcut is needed for the complete suppression of InSb hillocks. Indeed, at the edge of the InSb QW wafer towards $[\bar{1}10]$ direction, we observed a new morphological transition region where the large AlInSb hillocks are already suppressed while the small InSb hillocks persist. Our calculation of the atomic step density on the $1 \times 1 \mu\text{m}^2$ AFM scans confirmed that the effective substrate offcut angle for this region is around $0.4 \sim 0.5^\circ$, which is the optimum substrate offcut for $\text{Al}_{0.12}\text{In}_{0.88}\text{Sb}$. A hillock-free and atomically smooth InSb surface is found at a slightly steeper substrate offcut angle of around $0.5 \sim 0.6^\circ$.

We subsequently regrew the same InSb QW structure on GaAs (001) substrates with a specified offcut of $0.55 \pm 0.02^\circ$ towards $[\bar{1}10]$ direction. A hillock-free and atomically smooth surface morphology is observed on the entire 2-inch wafer (Figure 6.13(a) and (b)). By comparing to the same QW structure grown on the on-orientation GaAs (001) substrate in the smooth region at the edge of the wafer, the offcut wafer shows a comparable but even smoother morphology, probably due to the higher substrate quality and more uniform growth conditions at the center of the wafer. Importantly, we no longer observe any MTs on the surface. MTs are more disruptive crystallographic defects than TDs. Though being of a low density, they could have a much larger influence on the electric mobility of the InSb QW. The suppression of MTs with offcut substrates has been reported [144] and the reason for that is still under investigation. In the $1 \times 1 \mu\text{m}^2$ AFM scans (Figure 6.13(b)), we observed a near-parallel step-flow growth mode and the substrate offcut was calculated to be indeed around $0.5 \sim 0.6^\circ$. At the edge of the wafer when the offcut just starts to increase to around $0.7 \sim 0.8^\circ$, the offcut-induced rough surface morphology with step-bunching and depressions is again observed (Figure 6.13(c)),

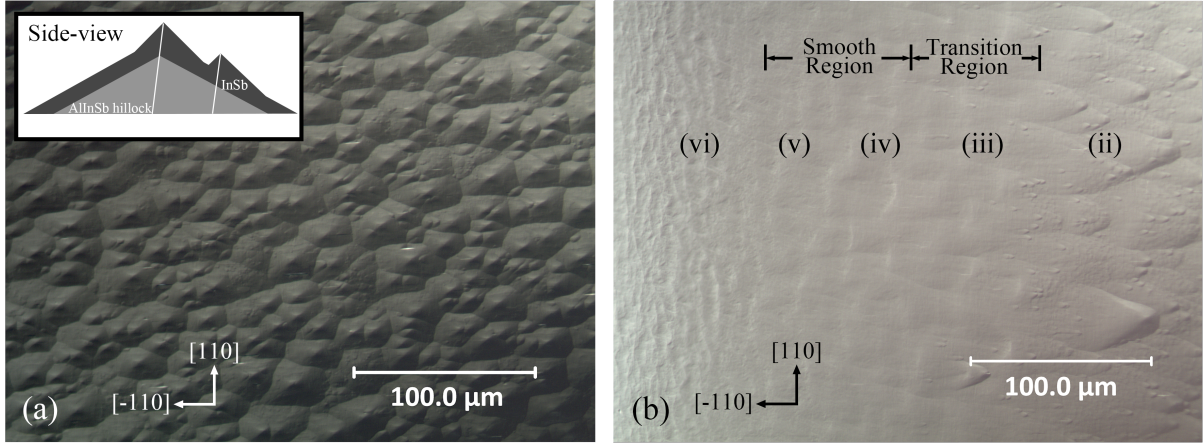


Figure 6.11: The Surface morphology of the InSb QW under Nomarski at (a) the center and (b) the edge of the wafer. The insert in (a) shows a dramatic illustration of the side-view of the InSb QW structure. Label (ii)-(vi) in (b) corresponds to the approximate positions of the AFM scans in Figure 6.12.

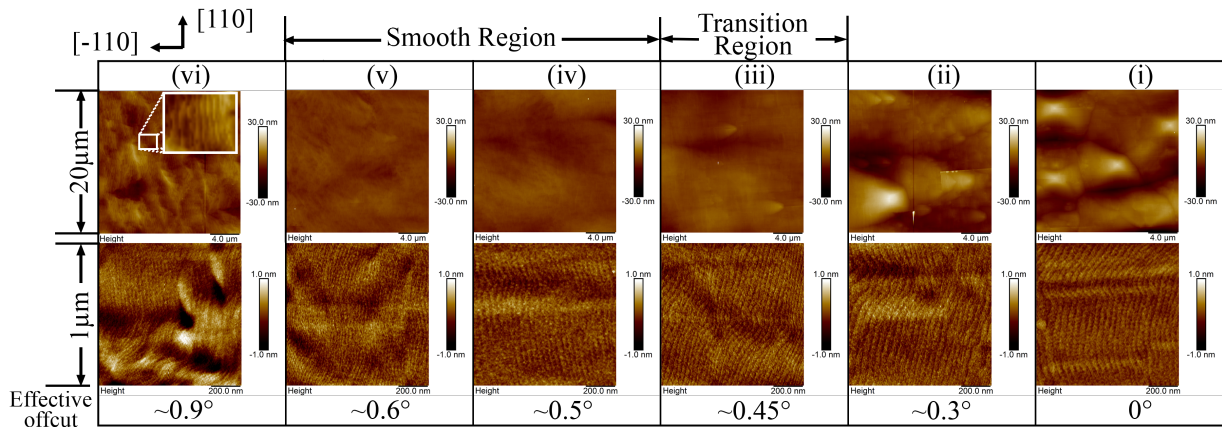


Figure 6.12: $20 \times 20 \mu\text{m}^2$ and $1 \times 1 \mu\text{m}^2$ AFM images showing the transition of the InSb surface morphology as a function of effective substrate offcut angle. The insert in the panel (vi) is a magnified view to show the step-bunching effect. The approximate AFM scan positions are indicated by label (ii)-(vi) in Figure 6.11(a) correspondingly.

consistent with the morphology observed further near the edge on the on-orientation substrate.

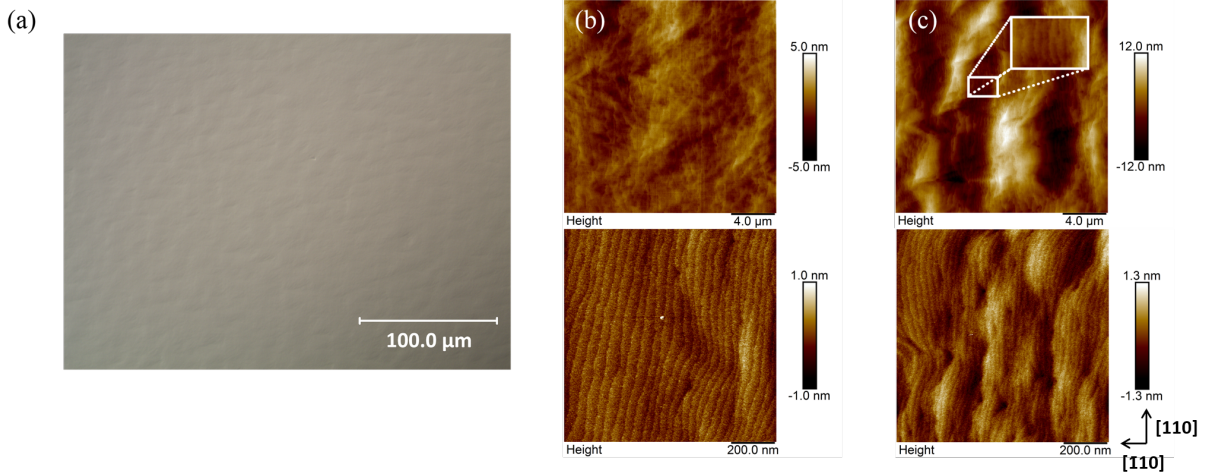


Figure 6.13: The surface morphology of InSb QW grown on the GaAs offcut substrate observed with (a) Nomarski microscope at the center of the wafer and $20 \times 20 \mu\text{m}^2$ and $1 \times 1 \mu\text{m}^2$ AFM scans both (b) at the center and (c) at the edge of the wafer. The insert in (c) is a magnified view to show the step-bunching effect, similar to that in Figure 6.9(b) panel (v) and Figure 6.12 panel (vi).

6.5 Conclusions

Due to the high TDD resulted from the large lattice mismatch in the material systems, hillock-decorated surface morphologies of III-Sb layers grown on GaAs (001) substrates were observed, as predicted by the BCF theory [40]. The different morphological features of hillocks resulted from various hillock interactions were studied closely using AFM and the observations agree well with BCF's predictions [40].

The effect of growth conditions on the surface morphologies of different III-Sb materials grown on GaAs (001) substrates were studied. A clear trend of widening terrace width of the hillock spiral steps with increasing substrate temperature was observed for AlSb, GaSb, and $\text{Al}_{0.1}\text{In}_{0.9}\text{Sb}$ buffers. We speculate that the widening in the hillock terrace width is a direct result of increased surface diffusion length of group III atoms at higher

substrate temperatures. While the $\text{Al}_{0.1}\text{In}_{0.9}\text{Sb}$ buffers grown at 380 °C and 350 °C exhibited slight variations in the terrace widths on the hillock sidewalls, consistent terrace widths were observed across the wafer for all the GaSb and AlSb buffers as well as the $\text{Al}_{0.1}\text{In}_{0.9}\text{Sb}$ buffer grown at 420 °C. Moreover, the hillock terrace width of the $\text{Al}_{0.1}\text{In}_{0.9}\text{Sb}$ buffer grown at 420 °C remained constant over a further 10 μm growth, suggesting stable growth kinetics on the hillock sidewalls. We hypothesize that the stable hillock sidewall slope is related to the balanced uphill and downhill surface currents. Such surface currents are mainly influenced by the surface diffusion length of the group III atoms, the attachment kinetics at the steps, and the interaction between the steps on the hillock sidewalls.

We have also studied the influence of substrate offcut angle on the surface morphology of AlSb and AlInSb metamorphic buffers, and InSb QW structures grown on GaAs (001) substrates. Similar surface morphological transitions with substrate offcut angles were observed for all the $\text{Al}_x\text{In}_{1-x}\text{Sb}$ layers ($x = 1, 0.12, \text{ and } 0$) studied. As the effective substrate offcut increases towards the very edge of the wafer due to mechanical polishing, the surface morphology evolves from one which is hillock-dominated to a hillock-free morphology and then transitions into step-bunching and surface depressions. A toy model was discussed to demonstrate the offcut-dependent morphological transitions. We confirmed the postulation that hillock-free morphology can be achieved for the substrate offcut angle equal to the facet angle of hillocks. The natural facet angles of hillocks are different for different materials and they also depend on the growth conditions. With our growth conditions, the optimum substrate offcut was found to be around $0.4 \sim 0.5^\circ$ in $[\bar{1}10]$ direction and $0.7 \sim 0.8^\circ$ in $[110]$ for $\text{Al}_{0.12}\text{In}_{0.88}\text{Sb}$. The optimum substrate offcut angle for AlSb in $[\bar{1}10]$ direction lays between 0.8° and 1.3° . The optimum substrate offcut in $[\bar{1}10]$ direction for InSb is $0.5 \sim 0.6^\circ$, which is only slightly larger than that for $\text{Al}_{0.12}\text{In}_{0.88}\text{Sb}$. The suppression of hillocks is important since these hillocks are potentially detrimental to the InSb QW performance by acting as scattering centers and causing fluctuations in the InSb QW thickness as well as the AlInSb barriers composition. Substrate offcut is found to be effective in suppressing the formation of MTs as well. On GaAs (001) substrates with the offcut angle optimized for InSb, we have successfully grown hillock-free, MT-free, and atomically smooth InSb QWs.

Chapter 7

Magneto-transport Analysis

High-performance [high-electron-mobility transistors \(HEMTs\)](#) hosting InSb [two-dimensional electron gas \(2DEGs\)](#) are especially appealing in the modern semiconductor industry, given the many unique properties of InSb. However, the InSb [2DEGs](#) engineered so far all share a common problem of suffering much lower mobilities than bulk InSb which has the highest mobility of any binary III-V semiconductors. InSb [HEMTs](#) are far less studied in experiments compared to GaAs and InAs [HEMTs](#). Their fabrication processes are also much less developed. In a standard [HEMT](#) structure, the modulation doping is usually placed above the [2DEG](#) in the structure or symmetrically on both sides. In the application of realizing topological quantum computing with [Majorana bound states \(MBS\)](#), a near-surface InSb [quantum well \(QW\)](#) is required to enable the superconducting proximity effect. In this case, an inverted [HEMT](#) needs to be developed such that the modulation doping is located below the [2DEG](#) in case of screening the top gate or the superconductor material. However inverted InSb [HEMTs](#) are even less explored. In this thesis, the magneto-transport properties of InSb [QW](#) heterostructures with the active region in both the standard and the inverted fashion are studied.

7.1 InSb QW standard structure

InSb [QW](#) standard structures, which are more widely studied, are employed to investigate the effect of growth parameters on the transport properties of InSb [QW](#) heterostructures, proving a solid foundation for the development of InSb [QW](#) inverted structures. [Table 7.1](#) below summarizes all the growths of InSb [QW](#) standard heterostructures discussed in

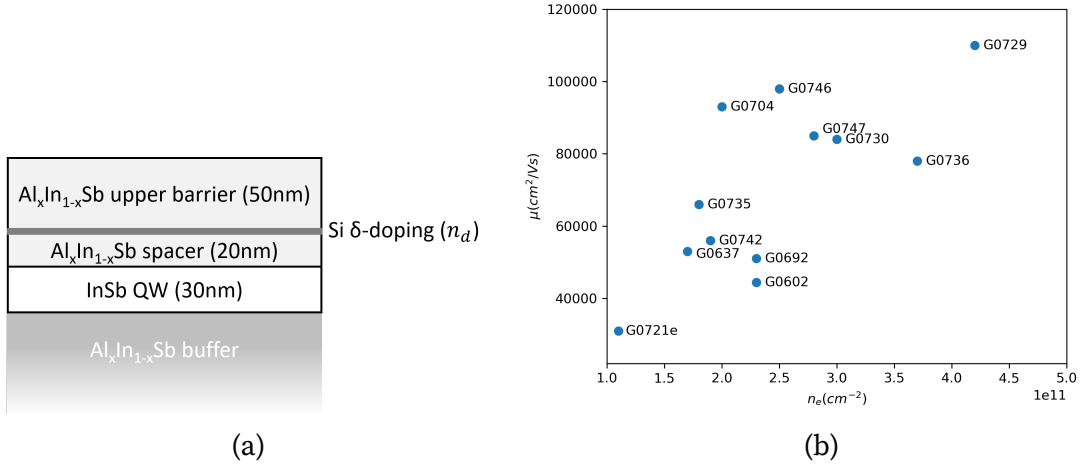


Figure 7.1: (a) Schematic overview of the active region for InSb QW standard structures with a single Si δ -doping layer and (b) The mobility as a function of carrier density at 1.4 K for the InSb QW standard structures listed in Table 7.1 except for G0721c.

this thesis. To quickly compare the performance of the standard InSb QW structures of interest, the mobility of involved samples listed in Table 7.1 are plotted versus the carrier density as shown in Figure 7.1 (b).

7.1.1 Doping profile

As a prerequisite to study and improve the transport properties of InSb QW heterostructure, the doping profile needs to be optimized to achieve a desirable single conducting InSb 2DEG channel in the structure. We adopted a simple buffer structure with a 100nm AlSb first intermediate buffer and a single 4 μ m Al_xIn_{1-x}Sb second-stage buffer layer (Figure 5.2(b) and (c)), to minimize any possible contributing factors from more complicated buffer structures. After finishing the growth of the Al_xIn_{1-x}Sb buffer, the growth of the active region for the standard structure immediately started with an InSb QW layer of 30 nm thick, followed by a 20 nm Al_xIn_{1-x}Sb spacer layer. Then the Si δ -doping layer with a sheet doping density of n_d was deposited under the same Sb flux to minimize the possibility of Si atoms acting as p-type dopants by replacing the Sb atoms on the surface. Lastly, the QW region was finished by a 50 nm Al_xIn_{1-x}Sb layer acting as an upper barrier for the InSb QW. The schematic of the standard structure active region is shown in Figure 7.1 (a). The sheet doping density n_d for the Si δ -doping layer, the Al

Table 7.1: A summary of the growths of InSb QW standard heterostructures with varying Al compositions x and doping densities n_d , different buffer structures as well as diverse growth conditions, which include the substrate temperature T_s and the group V/III ratio. The number before and after the ‘/’ are for the $\text{Al}_x\text{In}_{1-x}\text{Sb}$ metamorphic buffer and the InSb QW active region respectively. Buffer structures labeled by ‘G’ ‘A’ ‘S’ ‘I’ refer to GaSb, AlSb, single composition, and interlayer AlInSb buffers as shown in Figure 5.2(a)-(d) respectively. The measurement geometry (either Hall bar (HB) or van der Pauw (vdP)) as well as the measured low magnetic field electron mobilities μ and charge carrier densities n_e are included in the table for all the conducting wafers, except for G0597, the mobility and density were not measured (as denoted by not available (N/A)). G0617 was non-conducting (N.C.). The ‘c’ and ‘e’ following the growth number indicate the sample cleaved from the center and the edge respectively. If not specified, a central piece was measured.

Growth	x	n_d (cm^{-2})	buffer	T_s ($^\circ\text{C}$)	V/III	geometry	μ (cm^2/Vs)	n_e (cm^{-2})
G0597	0.08	2×10^{12}	A+S	420/380	1.5	HB	N/A	N/A
G0602	0.1	2×10^{12}	A+S	420/380	1.5	HB	44 450	2.3×10^{11}
G0617	0.1	1×10^{12}	A+S	420/380	1.5	HB	N.C.	N.C.
G0637	0.1	1.5×10^{12}	A+S	420/380	1.5	vdP	53 000	1.7×10^{11}
G0692	0.1	1.5×10^{12}	G+S	420/380	1.5	vdP	51 000	2.3×10^{11}
G0704	0.1	1.5×10^{12}	A+I	420/380	1.5	vdP	93 000	2.0×10^{11}
G0721c	0.1	1.5×10^{12}	A+S	420/380	1.5	vdP	3000	3.4×10^{11}
G0721e	0.1	1.5×10^{12}	A+S	420/380	1.5	vdP	31 000	1.1×10^{11}
G0729	0.1	1.5×10^{12}	A+S	350/330	1.5	vdP	110 000	4.2×10^{11}
G0730	0.1	1.5×10^{12}	A+S	380/350	1.5	vdP	84 000	3.0×10^{11}
G0735	0.1	1.5×10^{12}	A+S	380/350	2	vdP	66 000	1.8×10^{11}
G0736	0.1	1.2×10^{12}	A+S	380/350	1.5	vdP	78 000	3.7×10^{11}
G0742	0.1	1.5×10^{12}	A+S	380/350	2	vdP	59 000	1.9×10^{11}
G0746	0.12/0.09	1.5×10^{12}	A+S	380/350	2	vdP	98 000	2.5×10^{11}
G0747	0.11	1.5×10^{12}	A+S	380/350	2	vdP	85 000	2.8×10^{11}

percentage x in the $\text{Al}_x\text{In}_{1-x}\text{Sb}$ barrier material, and buffer structures were varied until a satisfactory single conducting channel in the hetero-structure from the InSb 2DEG was achieved.

As shown in Figure 7.2 (a), the magneto-transport data of G0597 with an Al percentage in the buffer and barrier of $x = 0.08$ and a doping density of $2 \times 10^{12} \text{ cm}^{-2}$ exhibited very weak and broad Shubnikov-de Haas (SdH) oscillations on top of a large background resistance at high magnetic fields and a Hall trace with no clear plateaus and a hump-like feature at low fields. Such transport data have been often observed with InSb QWs by other groups [114, 145] and are explained by the existence of parasitic channels other than the InSb 2DEG in the structure. The dependence of the longitudinal resistivity on magnetic field at small magnetic fields of G0597 is shown in Figure 7.2(b). The small dip of resistivity near zero field is attributed to a weak anti-localization effect, due to the destructive quantum interference in disordered 2D systems with strong spin-orbit interaction (subsection 3.1.5). This effect loses its strength quickly in the presence of a magnetic field and the resistivity increases as the quantum interference becomes constructive with increasing magnetic field. Then the resistivity decreases again with further increased magnetic field, which is likely related to the slower falling of the weak localization effect comparing to the weak anti-localization effect in this case. Lastly, we attribute the further increasing of the resistivity in the high magnetic field end in Figure 7.2(b) to a normal Lorentz effect which is expected to be proportional to $1 + (\mu B)^2$. Unfortunately, the InSb 2DEG is of low density and the transport is highly influenced by parallel conduction as shown by the broad SdH oscillations at high magnetic fields (Figure 7.2(a)).

Discrepancies were observed between our measured transport properties and that predicted by the nextnano++ simulations, including the ideal doping density and the carrier concentration in the QW. Such mismatch may be related to the loss of charge to the surface states, the change in the doping efficiency of Si at different growth conditions and many other factors in reality. Extra care is needed to fine tune the fitting parameters in the simulation to better reflect the reality. However, it still serves as a very useful guide for possible improvement directions in our structural design. According to nextnano++ simulations, when the sample is over-doped, the conduction band edge at the δ -doping layer will also drop below the Fermi level, contributing to the conduction as a parasitic channel. However, reducing the doping density will result in an even lower carrier density in the InSb QW. On the other hand, increasing the Al concentration x of the $\text{Al}_x\text{In}_{1-x}\text{Sb}$ layers will have two advantages: (1) lead to a higher barrier for the QW allowing the 2DEG carrier density to be increased and (2) reduce the risk of parallel conduction by lifting the ground state of the Si δ -doped layer above the Fermi level. As shown in

Figure 7.2 (c), G0602, which is a repeat of the G0597 hetero-structure except with the Al percentage increased to $x = 0.1$ in the $\text{Al}_x\text{In}_{1-x}\text{Sb}$ buffer and barrier layers, exhibited more oscillations in the same range of magnetic field than G0597, implying a higher carrier density as predicted. However, there is still significant parallel conduction in the structure, as indicated by the rising background of the SdH oscillations and the elbow feature of the Hall trace near 1 T. As a result, low mobility of $44\,000\text{ cm}^2/\text{Vs}$ was measured.

More growths with lower doping density were carried out while the Al percentage and other parameters were kept constant. As listed in Table 7.1, G0617 with a Si δ -doping density of $1 \times 10^{12}\text{ cm}^{-2}$ was N.C., but G0637, which is midway in the δ -doping density between G0602 and G0617, shows strong periodic oscillations in the SdH data with no significant rising background and evident quantum Hall plateaus with no characteristic elbow at low field, indicating very limited parallel conduction (Figure 7.2(d)). As denoted in Table 7.1, G0637 was measured in the vdP geometry unlike the other two samples, and the ‘dip’ feature in the quantum Hall data unique to the G0637 in Figure 7.2(d) is a known artifact of the vdP geometry. Starting from this growth of standard InSb QW structures, we decided to switch to the vdP geometry with simple In soldering at the four corners for a much quicker feedback loop for characterizing transport properties associated with growth parameters. We have acquired the desirable doping profile for a single conducting 2DEG channel in G0637, which has mobility of $5.3 \times 10^4\text{ cm}^2/\text{Vs}$ and an electron density of $1.66 \times 10^{11}\text{ cm}^{-2}$. G0637 hence was set as a reference for future studies on the factors limiting the mobility and influencing the transport properties of InSb QW heterostructures.

7.1.2 Effect of buffer structures

The effect of buffer structures on the transport properties were studied by varying both the first intermediate buffers and the second-stage buffer in the hetero-structure. The growths involved in this section were all measured in vdP geometry, the same as our control structure, G0637. Other than offering a much faster feedback loop, the simple preparation procedure of the vdP geometry also significantly minimizes the potential influences of inconsistent fabrication steps on measurement results.

The 100nm AlSb first intermediate buffer in G0637 was replaced by a 600nm GaSb layer in G0692, as illustrated in Figure 5.10 (a) and (c). The magneto-transport measurement of G0692 yielded a charge carrier density of $2.27 \times 10^{11}\text{ cm}^{-2}$ and electron mobility of $51\,000\text{ cm}^2/\text{Vs}$. With similar mobility, G0692 has a higher carrier density than G0637.

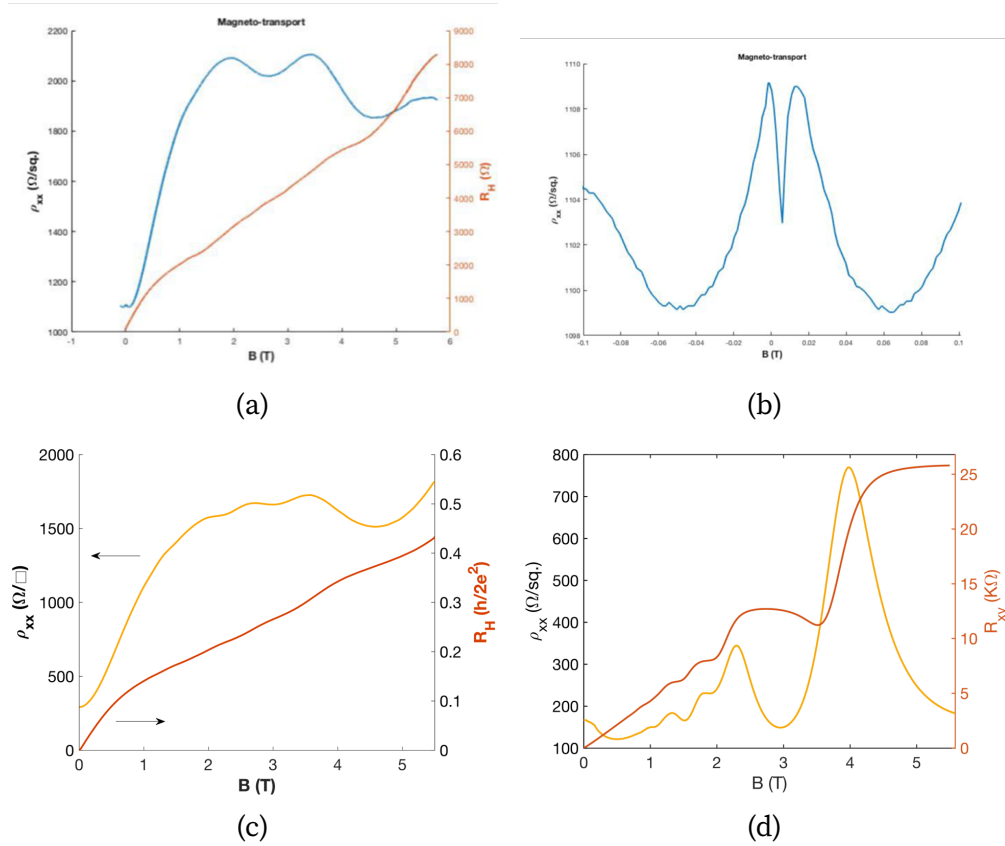


Figure 7.2: The Longitudinal (ρ_{xx} , left axis) and transverse (ρ_{xy} , right axis) resistivity as a function of magnetic field B at $T = 1.4$ K for (a) G0597, (c) G0602 and (d) G0637. (b) The weak anti-localization effect measured at $B = 0$ T in G0597 which was also observed with the other standard InSb QW structures.

As presented earlier in Figure 5.10, despite the threading dislocation density (TDD) on the GaSb buffer surface being less than that on the AlSb buffer surface, the TDD levels reaching the InSb QW region are comparable for G0692 and G0637. However, due to the substantial parallel conduction in G0692, we can not inspect the effect of the GaSb interfacial misfit (IMF) buffer on the InSb 2DEG performance at this point. Though the GaSb buffer was the only nominal change of parameter in G0692 comparing to G0637, it may not be directly correlated with the parallel conduction in the structure, as will be discussed later.

The effect of the interlayer buffers on the transport properties of the InSb QW hetero-

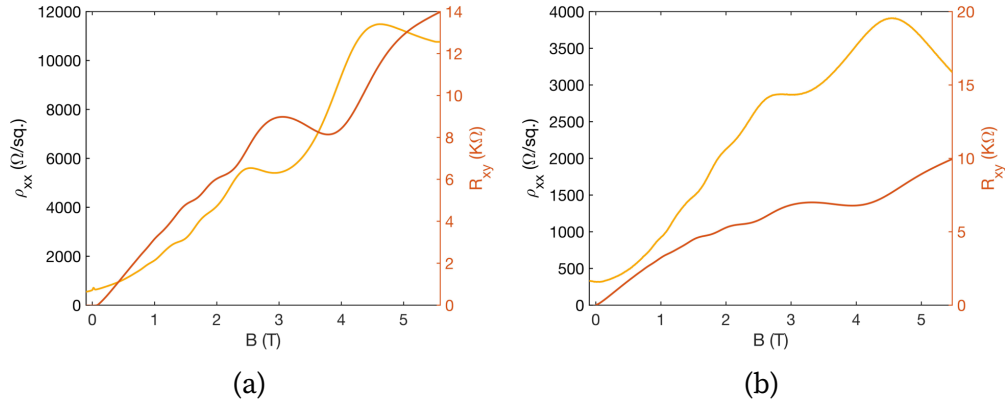


Figure 7.3: The Longitudinal (ρ_{xx} , left axis) and transverse (ρ_{xy} , right axis) resistivity as a function of magnetic field B at T = 1.4K for (a) G0692 and (b) G0704, both showing parallel conduction.

structures was studied by replacing the simple $\text{Al}_{0.1}\text{In}_{0.9}\text{Sb}$ buffer in G0637 by four repetitions of $\text{Al}_{0.1}\text{In}_{0.9}\text{Sb}/\text{Al}_{0.2}\text{In}_{0.8}\text{Sb}$ interlayers in G0704. The magneto-transport measurement of G0704 yielded a charge carrier density and electron mobility of $2.04 \times 10^{11} \text{ cm}^{-2}$ and $93\,000 \text{ cm}^2/\text{Vs}$ respectively. With only a slightly larger electron density comparing to G0637, G0704 almost doubled the mobility of G0637. We attribute the transport improvement to the TDD reduction by the interlayers, as demonstrated earlier in [section 5.4](#) and [Figure 5.12](#).

However, signs of parallel conduction are again observed for G0704, as shown in the Hall and [SdH](#) plots in [Figure 7.3](#) (b). In contrast to the report by Lehner et al. [[114](#)] who suggested that the interlayer buffers showed advantages in reducing the parallel conduction in the structure, we found that the parallel conduction in G0704 is much more severe than in G0637. Since we were able to achieve InSb [QW](#) structures with no parallel conduction with the simple single-composition $\text{Al}_x\text{In}_{1-x}\text{Sb}$ buffer, like many other groups [[24](#), [109](#), [145](#), [146](#)], it implies that the parallel conduction in the structure might not be directly related to the design of the buffer structures but some other growth parameters.

The parallel conduction in both G0692 and G0704 which share the same active region as G0637 made us question the source of the parasitic channel as well as the reproducibility of the growth. Therefore in the subsequent growth G0721, we attempted to reproduce G0637 (which was grown on a [quarter of a three-inch \(Q3"\)](#) substrate) on a full 3" substrate. Unfortunately, both a piece cleaved in the center and at the edge of G0721 exhibited

much worse 2DEG quality than G0637 based on their mobility and density measurements as shown in Table 7.1. The substrate temperatures measured by band-edge thermometry (BET) were nearly the same for G0637 and G0721, however, the manipulator temperature was about 10 °C higher for G0721 than for G0637 in order to get the same BET temperature. The difference in the setup between 3" and Q3" holders affect the heating environment during the growth, which may impose changes in the effective growth parameters during the growth. Very different mobilities (by an order of magnitude) were also measured between the center and the edge piece, which are 3000 cm²/Vs and 31 000 cm²/Vs respectively. Gradients in both fluxes and substrate temperatures are expected from the center to the edge of a full 3" wafer but are usually less than 2% and 5 °C respectively. Based on these facts, we suspect that the growth conditions we applied for the standard InSb QW growths we have discussed so far (G0597-G0721 in Table 7.1) may settle very close to the boundary of the optimum or even stoichiometric growth regime. As a result, even though all these growths were grown under the same nominal growth conditions, slight deviations to the condition during the growth may lead to irreproducibility in wafer quality and development of parasitic channels in the structure.

7.1.3 Variations in growth conditions

Here we study the effect of growth conditions on the transport properties of standard InSb QW heterostructures and investigate whether sub-optimal growth conditions were the culprit in introducing parallel conduction. The substrate temperatures and group V/III ratios were varied for G0729, G0730, and G0735 as listed in Table 7.1. All of these growths were also measured in the vdP geometry to minimize the possible complications in the fabrication procedure and for a better comparison with G0637.

The substrate temperature during the growth of the Al_{0.1}In_{0.9}Sb metamorphic buffer was reduced from 420 °C in G0637 to 350 °C in G0729 and 380 °C in G0730. The InSb QW active regions were all grown at slightly lower substrate temperatures used for the Al_{0.1}In_{0.9}Sb buffer in the individual structures, which are ~380 °C, ~330 °C, and ~350 °C as measured by integrated spectral pyrometry (ISP), for G0637, G0729, and G0730, respectively. As shown in Figure 7.4 (a) and (b), signs of parallel conduction are observed for both G0729 and G0730 grown at lower substrate temperatures than G0637. As the substrate temperature during the growth continues to decrease in the order of G0637, G0730, and G0729, both the mobility and carrier concentration of the sample increase. The rising trend in the carrier density may be related to the increasing electron doping efficiency of Si atoms with decreasing substrate temperature during the growth of the active region. Such temperature dependence of Si doping efficiency in (Al)InSb layers

has been reported earlier [147, 148]. Substrate temperature has been shown to affect the TDD (chapter 5) as well as the surface morphology (chapter 6) of the material structure, both of which are considered as factors contributing to the scattering. However, due to the parallel conduction in the structure, it is hard to study the effect of substrate temperature on the transport performance of the QW.

Nevertheless, the current results indicate that a slight drop in the substrate temperature in the repeated growth might make the sample over-doped causing parallel conduction. Based on our measured carrier density change with substrate temperature, a 10 °C drop in substrate temperature can result in an increase in the carrier density up to about $0.4 \times 10^{11} \text{ cm}^{-2}$, which can effectively bring the carried density measured in a single-channel structure (such as G0637) close to that in an over-doped sample (such as G0602) (Table 7.1). This may also explain the different transport properties measured between the center and edge piece of G0721 as well as that between G0721 and G0637. It is therefore essential to accurately monitor the substrate temperature for reproducible growths of InSb QW heterostructures, especially for the growth of the active region. However, reliable substrate temperature measurement is particularly challenging for the active region, as described in subsection 4.2.3. The ISP technique when coupled with BET instrument allows us to measure the substrate temperature of thick narrow-gap material grown on wide-gap substrates more reliably than most groups, however, an error larger than $\pm 5 \text{ }^\circ\text{C}$ in the measured temperature may still be possible. Therefore more effort is needed to further improve the substrate temperature measurement during the active region growth.

To study the effect of Sb overpressure, the group V/III ratio was increased from 1.5 to 2 in G0735 while the other growth parameters were kept the same with G0730. Surprisingly, as shown in Figure 7.4 (c), the transport data of G0735 shows distinct quantum Hall plateaus and the SdH oscillations going to zero resistance, indicating the absence of parallel conduction in the structure. The increase in V/III ratio appeared to be exactly what was needed to solve the plague of parallel conduction since the growth of G0637. The carrier density and mobility of G0735 are measured to be $1.8 \times 10^{11} \text{ cm}^{-2}$ and $66\,000 \text{ cm}^2/\text{Vs}$, respectively, both very similar to G0637. The increase in Sb flux removed the parallel conduction in the structure without reducing the carrier density in the InSb QW. In an independent study on the resistivity of III-Sb buffers, we observed a clear trend of increasing buffer resistivity with higher effective Sb overpressure supplied during the growth. Though the reason for this trend is still unknown, we suspect that the higher Sb flux in G0735 compensated for the undesirable extra free carriers in the rest of the material structure. It is still unclear if the increase in the Sb flux also plays a role during the deposition of the δ -doping layer.

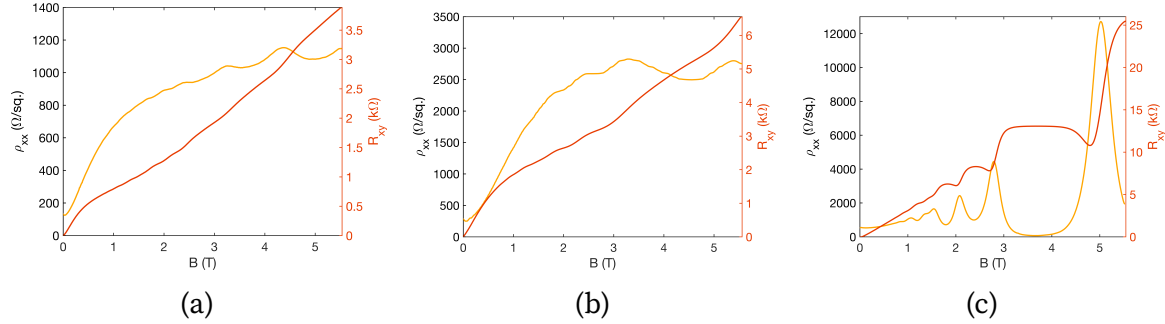


Figure 7.4: The longitudinal (ρ_{xx} , left axis) and transverse (ρ_{xy} , right axis) resistivity as a function of magnetic field B at $T = 1.4\text{K}$ for (a) G0729, (b) G0730 and (c) G0735.

To confirm the effectiveness of increased group V/III ratio on removing the parallel conduction in the structure and test the growth reproducibility, G0735 was repeated with exactly the same recipe. As shown in Figure 7.5 (a), parallel conductance appears again in the repeated growth G0742, preventing the minima in the SdH oscillations from reaching zero resistivity. The carrier density of G0742 $1.9 \times 10^{11} \text{ cm}^{-2}$ is only slightly higher than the carrier density of G0735 where $n_e = 1.8 \times 10^{11} \text{ cm}^{-2}$, and the mobility measured for G0742 ($55\,800 \text{ cm}^2/\text{Vs}$) is again comparable to G0735 ($66\,000 \text{ cm}^2/\text{Vs}$) considering the adverse effects of the slight parallel conduction in the sample. Therefore the growth can be considered to be reasonably well reproduced. The total carrier density n_{tot} for G0742 was determined by fitting to the high field Hall resistance bisecting the plateaus: $n_{tot} = 2.18 \times 10^{11} \text{ cm}^{-2}$, as shown in Figure 7.5(b). From the periodicity in the minima of the SdH oscillations when plotted versus inverse magnetic field, the 2DEG density was determined as $n_2 = 2e/h\Delta(1/B) = 1.92 \times 10^{11} \text{ cm}^{-2}$ (Equation 3.32), which is in good agreement with the carrier density $n_e = 1.86 \times 10^{11} \text{ cm}^{-2}$ used in Table 7.1, which is calculated from the slope of the low field Hall resistance using Equation 3.21 (Figure 7.5(b)) From n_{tot} and n_{2DEG} , the density of the parallel conducting channel n_p was then determined by $n_p = n_{tot} - n_{2DEG} = \sim 0.3 \times 10^{11} \text{ cm}^{-2}$. As expected, the parasitic channel in the structure is only contributing a small number of carriers. However, the re-appearance of the parallel conduction is still troublesome and further investigations on this matter will be discussed in the next section.

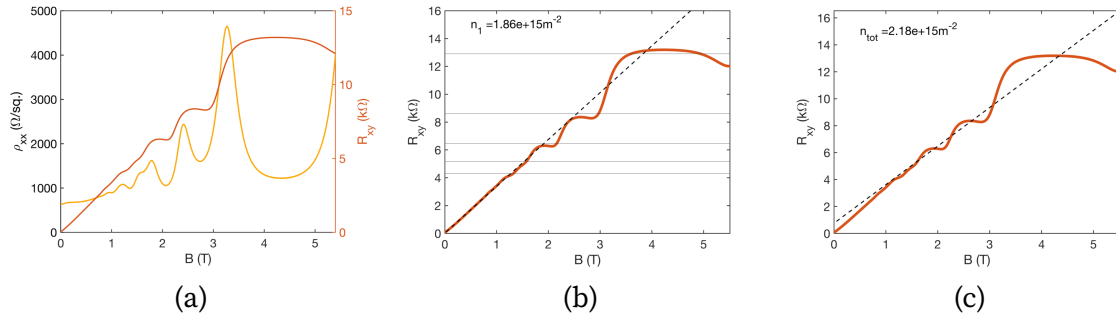


Figure 7.5: (a) The Longitudinal (ρ_{xx} , left axis) and transverse (ρ_{xy} , right axis) resistivity as a function of magnetic field B at $T = 1.4\text{K}$ for G0742. The fitting to the slope of the Hall resistance (b) in the low field range for determination of the 2DEG carrier density and (c) in the high field range for determination of the total carrier density.

7.1.4 Issues with parallel conduction and growth reproducibility

As we have already seen in subsection 7.1.1, when the structure is over-doped, the doping layer can act as the source of parallel conduction. From our previous results, signs of parallel conduction can be observed with only a slightly higher carrier density in the 2DEG, suggesting that our current doping profile may be close to the limit of over-doping. Therefore G0736 was grown which shares the same structure and growth conditions with G0730 except that it has a slightly lower doping density of $1.2 \times 10^{12} \text{ cm}^{-2}$ in the Si δ -doping layer. Surprisingly, G0736 suffered severe parallel conduction and exhibited an even higher electron density and lower mobility than G0730 (Figure 7.6 (a)). Since G0736 was grown subsequently after G0735, this result further supports the conclusion that the increase in Sb overpressure is crucial for eliminating the parallel conduction in the structure.

By applying the high-resolution x-ray diffractometry (HD-XRD) reciprocal space map (RSM) analysis described in subsection 4.3.7 on our InSb QW structures, we found that the Al composition x determined from the $\text{Al}_{0.1}\text{In}_{0.9}\text{Sb}$ peak can vary by $\pm 0.1\%$ among different growths. A weak trend of higher x values corresponding to minor parallel conduction was observed. The growth of the $4 \mu\text{m}$ AlInSb buffer takes more than 5 hours, thus any flux fluctuations due to cell instability may lead to the change in the exact composition of the alloy. Such composition change can result in variations in the effective confinement provided by the barrier or the buffer layer. Therefore we designed two structures to verify the correlation between the parallel conduction and the Al composition in the barrier layer as well as in the buffer layers. G0747 has a higher

Al composition ($x = 0.11$) for all the $\text{Al}_x\text{In}_{1-x}\text{Sb}$ layers in the structure comparing to the Al composition of $x = 0.1$ for the previous growths. On the other hand, G0746 has a higher Al composition in the barrier ($x = 0.12$) while a lower Al composition ($x = 0.09$) in the buffer. Both G0746 and G0747 were grown at the same growth conditions as G0742. As shown in Figure 7.6(b) and (c), parallel conduction and very similar transport behaviors are observed for G0746 and G0747 which also have similar mobilities and densities (Table 7.1). Therefore a small change in the Al composition in either the buffer or the barrier layer has minimal effect on the transport properties and is unlikely to be the reason for parallel conduction appearing in the repeated growths.

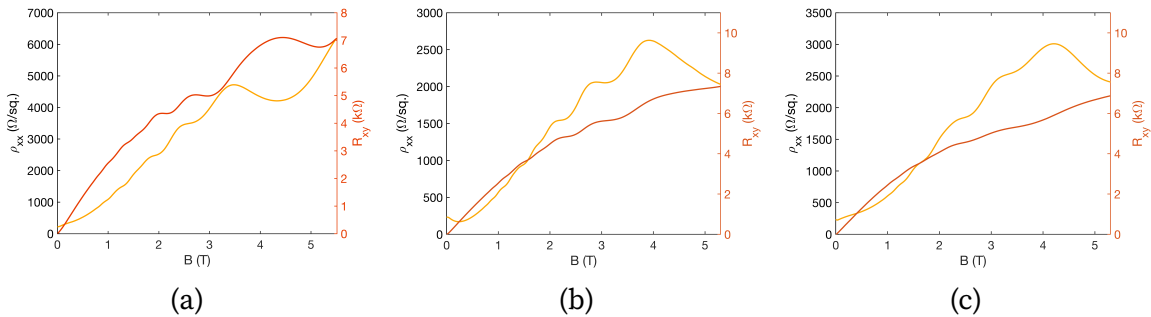


Figure 7.6: The Longitudinal (ρ_{xx} , left axis) and transverse (ρ_{xy} , right axis) resistivity as a function of magnetic field B at $T = 1.4\text{K}$ for (a) G0736, (b) G0746 and (c) G0747, all showing parallel conduction.

The difficulty in the growth reproducibility of InSb QW heterostructures seems to be a rather common problem. In the Ph.D. Thesis by Lehner from ETH Zürich [114], different buffer structures were designed to improve the transport properties as well as reduce the parallel conduction in the structure, yet larger deviations in the reproducibility are found with more complicated buffers and a sample is hard to be repeated ‘even when grown consecutively on the same day’. Even though we have conducted a comprehensive study on the source of parallel conduction appearing in the repeated growths, it remains fairly inconclusive on what exactly caused this irreproducibility. Due to the COVID-19 shutdown followed by molecular beam epitaxy (MBE) system maintenance after lab reopening, the study on the source of parallel conduction in repeated growths and the issues in growth reproducibility was forced to stop.

Nevertheless, we have drawn some speculations based on the current results, which may be helpful for future growths of such structures. First of all, we noticed a trend of increasing parallel conduction with the same doping density over time, suggesting

that there might be a drift in the chamber environment due to the residues from other growths (or something else) over time which may change the effective carrier density in the material structure. However, we speculate that with re-optimized doping profile, the growth can be highly reproducible within a certain time frame (such as G0729 vs. G0730, G0735 vs. G0742, and G0746 vs. G0747). Additionally, we affirmed that the appearance of parallel conduction was not a result of layer composition change due to the instabilities of the cells. On the other hand, a slight drift in the substrate temperature during the growth may have a substantial influence on the doping efficiency, resulting in irreproducible transport properties as well as the over-doping induced parallel condition. Therefore accurate substrate temperature monitoring is essential for the growth of InSb QW heterostructures. We also found that the parallel conduction in the structure can be significantly reduced when grown under a slightly higher Sb/III ratio of 2 than 1.5. The increase in Sb flux during the growth may have effect in eliminating the extra charge carriers in the structure, though the mechanism of which remains unknown.

7.2 InSb QW inverted structure

The development of high-quality inverted InSb QW structures, especially surface InSb QWs, is essential for the top-down fabrication of Majorana devices. However inverted InSb HEMTs are much less explored. There is only one published work to date from ETH Zürich [149] and the reported inverted InSb QW structures were parallel conducting. Surface QWs are much harder to achieve than the structures with a thick top barrier as they suffer severe scattering from surface disorders. The ETH group found that the quality of the InSb 2DEG reduced drastically as the QW was moved closer to the surface. [114] Surface QWs are also more challenging for device fabrication due to their high susceptibility to surface treatment and handling. In this thesis, inverted near-surface InSb QW structures are achieved in two approaches. The first approach is to populate the InSb QW with remote δ -doping layers placed below the well and the second approach uses a generously bulk-doped layer serving as a back gate to modulate the carrier density in the InSb QW.

7.2.1 Structures with modulation doping

The structures employing modulation doping all contain a total of five Te δ -doping layers below the QW. The schematic of the active region is shown in Figure 7.7(a). The active

region for all the growths except G0381 was grown on the same buffer structure, which consists of a 1 nm AlSb buffer with a 5nm GaSb cap (Figure 5.2(b)) and an interlayer 2nd-stage buffer (Figure 5.2(d)) with 4 repetitions of $\text{Al}_{0.12}\text{In}_{0.88}\text{Sb}/\text{Al}_{0.24}\text{In}_{0.88}\text{Sb}$ interlayers. G0381 has an extra 10 μm $\text{Al}_{0.12}\text{In}_{0.88}\text{Sb}$ buffer layer on top of the buffer structure used for the other growths. A 10 nm InSb or $\text{Al}_{0.12}\text{In}_{0.88}\text{Sb}$ cap was grown on top of the 30nm InSb QW. When an InSb cap was used, the inverted structures are actually surface QW structures with a 40 nm InSb QW right at the surface. The active region was grown at a substrate temperature of around 380 °C and a flux ratio of Sb/III of about 1.5. In order to optimize the doping density more efficiently, the substrate rotation was stopped at a desirable azimuth such that a gradient in the doping density with a factor of ~ 2 across the wafer was achieved along the [110] direction for each δ -doping layer. Then multiple samples cleaved at different positions along the [110] direction can be obtained with one single growth and the doping density can be considered reasonably constant along the $[\bar{1}10]$ direction which is considered as the high mobility direction for InSb 2DEGs. All the growths in Table 7.2 were grown with a gradient doping density except for G0414, which was grown with substrate rotation and has a uniform doping density.

Table 7.2: A summary of the InSb surface QW growths using the modulation doping approach with their corresponding low magnetic field electron mobilities μ and charge carrier densities n_e . The materials used for the cap layer are listed. The doping densities n_d was estimated based on the location of the cleaved sample on the wafer. The term ‘hi’ ‘mid’ or ‘low’ behind the growth numbers are used to indicate that the sample is cleaved from a high, mid or low doping area, respectively. All growth except G0414 has a gradient doping density for each δ -doping layer. ‘eqw’ is short for etched quantum well. The material used for the cap layer is also listed. For G0414eqw, the InSb cap was etched away as represented with an additional pair of round brackets.

Sample	Cap	n_d (cm ⁻²)	μ (cm ² /Vs)	n_e (cm ⁻²)
G0381mid	InSb	1×10^{12}	9400	3.4×10^{12}
G0383mid	InSb	1×10^{12}	11 000	2.8×10^{12}
G0387mid	$\text{Al}_{0.12}\text{In}_{0.88}\text{Sb}$	3×10^{11}	18 000	9.9×10^{11}
G0387low	$\text{Al}_{0.12}\text{In}_{0.88}\text{Sb}$	2.3×10^{11}	6200	6.5×10^{11}
G0390hi	$\text{Al}_{0.12}\text{In}_{0.88}\text{Sb}$	1.2×10^{11}	N.C.	N.C.
G0396hi	$\text{Al}_{0.12}\text{In}_{0.88}\text{Sb}$	1.8×10^{11}	N.C.	N.C.
G0401hi	InSb	2.3×10^{11}	2700	4.4×10^{11}
G0414	InSb	2.6×10^{11}	16 000	8.0×10^{11}
G0414eqw	(InSb)	2.6×10^{11}	1900	4.0×10^{11}

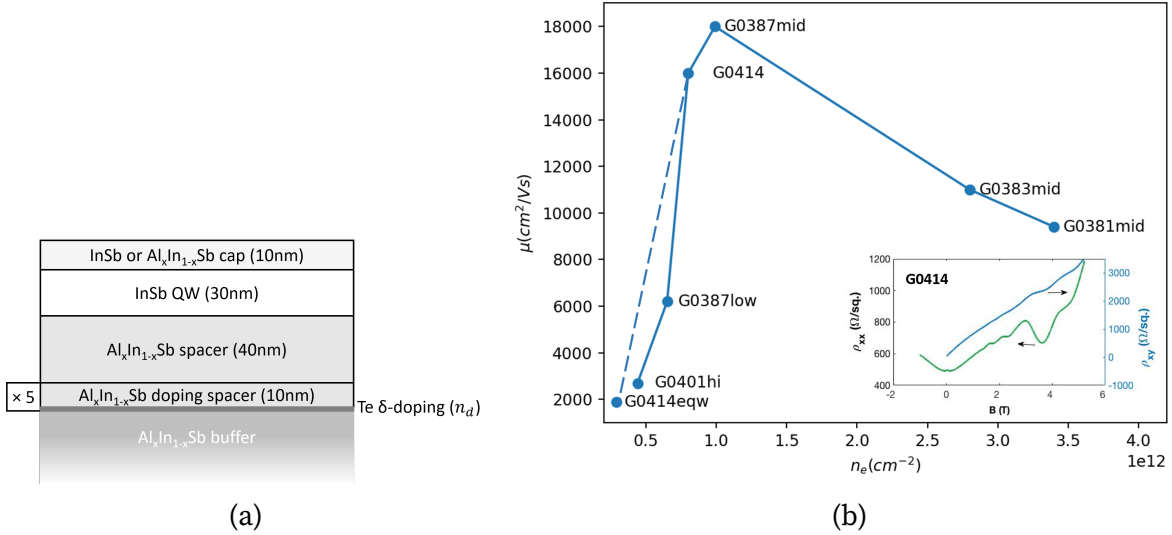
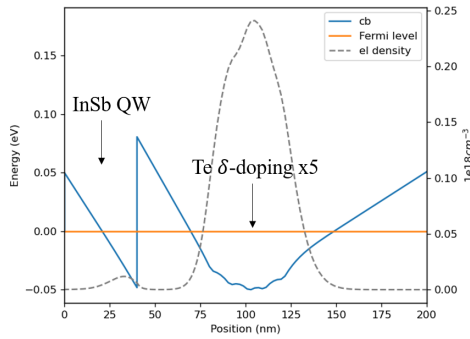


Figure 7.7: (a) Schematic overview of the InSb QW active region for the inverted structures with five Te δ -doping layers. (b) The mobility as a function of carrier density at 1.4 K for all the conductive inverted InSb QW structures are listed in Table 7.2. The inset at the bottom right corner is a plot of the longitudinal resistivity ρ_{xx} (left axis) and the transverse resistivity ρ_{xy} (right axis) as a function of magnetic field B at T = 1.4 K for G0414, which serves as a representative of the magneto-transport data for all the samples in this plot. Additional data can be found in Appendix B.

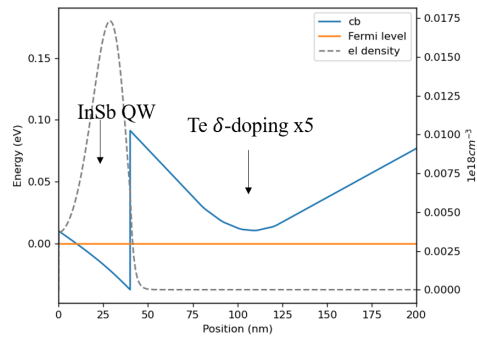
A plot of mobility versus carrier density for all the conductive InSb surface QW samples listed in Table 7.2 is shown in Figure 7.7(b). All these conductive samples in the plot exhibited parallel conduction, as shown in the inset of Figure 7.7(b) for the magnetotransport measurement of G0414 as an example. Since the quality of a 2DEG can be generally judged by the mobility as a function of the carrier density, it can be seen that the sample quality has been improved significantly as the carrier density was increased until $\sim 1 \times 10^{12} \text{ cm}^{-2}$. While a further increase in the carrier density leads to a decline in the sample quality. The only difference between G0381 and G0383 is the extra $10 \mu\text{m Al}_{0.12}\text{In}_{0.88}\text{Sb}$ buffer layer in G0381. The carrier density and mobility of the two growths are reasonably comparable, except that a slight increase in the carrier density is observed in the repeated growth, G0383. Such an increase in the carrier density has also been observed in the repeated growth of the standard InSb QW structures (section 7.1). We hypothesize that the decrease in mobility with increasing carrier density from G0387mid to G0381mid is a result of increased density of the low-mobility carriers

in the parallel-conducting δ -doping plane as the doping density increases. The sharp decrease in mobility from G0387mid to G0401hi below the carrier density of $\sim 1 \times 10^{12} \text{ cm}^{-2}$ is probably due to the reduced Thomas-Fermi screening from the diminishing of the carrier densities in the QW with further decreased doping density. As the doping density decreases further for G0390 and G0396, the QW structures become non-conductive, as shown in Table 7.2. We were not able to find an ideal doping regime with the inverted InSb surface QWs as with the standard structures, such that the InSb 2DEG is the only conductive channel in the structure. Moreover, instead of the weak anti-localization effect observed in the standard InSb QW samples, weak localization was observed in InSb surface QWs, appearing as a small peak around zero magnetic field in the inset of Figure 7.7(b). This suggests a diffusive transport that may be dominated by the disordered surface. The weak localization peak was also observed to manifest with more negative top gate voltage. Since the InSb surface QW in our structure is fairly wide (40 nm), a parasitic channel might be created at the surface where the conduction band bends lower towards the surface due to the populated surface states. This hypothesis may explain the increase in the weak localization with negative gate voltage as well as the source of parallel conduction in the structure. Therefore, a sample from growth G0414 was wet-etched to contain only 30nm of the InSb QW at the surface and is labeled as G0414eqw (where 'eqw' stands for etched quantum well) in Table 7.2. Unfortunately, the sample still shows severe parallel conduction. The InSb 2DEG quality has also been declined significantly (Figure 7.7(b)) which may be a result of the worsened surface condition by wet-etching. Nevertheless, our InSb surface QWs are so far the first true surface QW structure demonstrated for such material systems. The best ones among our samples, such as G0414 with mobility of $16000 \text{ cm}^2/\text{Vs}$ and a carrier density of $8.0 \times 10^{11} \text{ cm}^{-2}$, exhibit even more promising quality than the near-surface InSb QW with a 5 nm AlInSb top barrier in the previously published work [149].

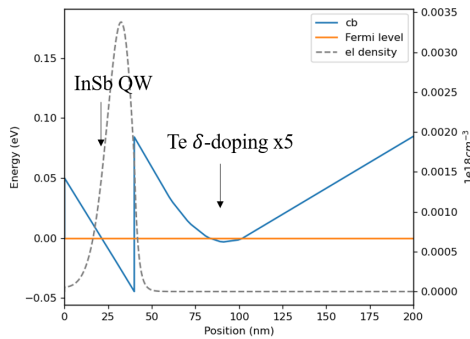
The possible causes and potential improvement directions for the parallel conduction issue in the inverted InSb QW structures were studied by modeling the active regions using nextnano++. The conduction band non-parabolicity of narrow-gap InSb is taken into account by the effective-mass approximation. Because of the very small electron effective mass for InSb, the Bohr radius of the Si donors is very large such that the wavefunctions of the electrons will heavily overlap and form a continuous energy band. Therefore full ionization is assumed for Si doping in our nextnano++ simulation. As shown in the simulation result for G0414 at a temperature of $T = 1\text{K}$ in Figure 7.8 (a), the transport of the inverted structure is dominated by the doped region consisted of five δ -doping layers below the surface QW with very little carriers confined inside the InSb QW. As a result, decreasing the doping density would deplete the QW first before lifting



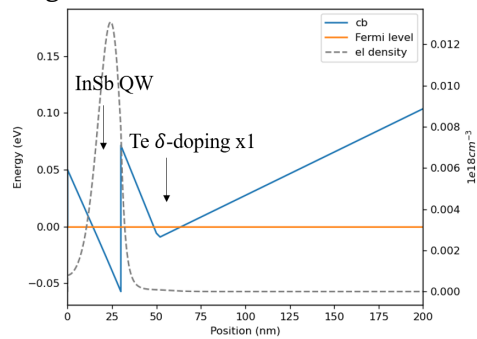
(a) G0414



(b) modified G0414 with surface pinning decreased to 0.01 eV



(c) modified G0414 with spacer thickness decreased to 20nm



(d) modified G0414 with spacer thickness decreased to 20nm and the number of δ -doping layers reduced to 1

Figure 7.8: nextnano++ simulation results of (a) G0414 and (b-d) the possible modifications in the G0414 structure with the doping densities adjusted accordingly to achieve single-channel conduction at the InSb QW in the structure. The conduction band edge is represented by a solid blue line and the Fermi level is fixed at 0eV as shown by an orange solid line. The distribution of the electron densities in the structure is depicted by a gray dashed line.

the conduction band edge of the doping layers above the Fermi level.

This simulation result, however, is largely determined by the boundaries conditions. The metamorphic buffer below the active region is not entirely modeled. The boundary condition for the simulation edge deeper in the structure towards the substrate side is set such that a constant potential is reached beyond around 200nm below the doped region. The Fermi level pinning due to the surface states at the surface is modeled by

a Schottky contact, serving as the boundary condition at $z = 0$. Surface pinning has a strong effect on the conduction band profile for inverted InSb QW structures. The Schottky barrier height was set at 0.05 eV in Figure 7.8 (a) which generates a comparable result with our measurement with a total carrier concentration of around $1 \times 10^{12} \text{ cm}^{-2}$. Increasing of this fitting parameter lifts the QW further above the Fermi level and a higher doping density is required to populate the well, worsening the parallel conduction in the structure. By lowering the surface pinning, the doping density needed to populate the QW decreases and a single-conducting channel in the structure at the InSb QW may be achieved, as shown in Figure 7.8 (b) with a Schottky barrier height at 0.01 eV, a doping density of $4 \times 10^{10} \text{ cm}^{-2}$ for each δ -doping layer and a very low sheet carrier density of around $4 \times 10^{10} \text{ cm}^{-2}$ in the QW. The lowering of the surface pinning may be achieved by deliberate surface treatments or by depositing another thin Schottky-barrier-free layer at the surface which at the same time will not affect the interface transparency in the prospective superconductor-normal (S-N) devices.

Moreover, nextnano++ simulation suggests that the thinner the AlInSb spacer between the doping layers and the QW is, the less doping is needed to populate the QW. By reducing the spacer thickness from 40nm to 20nm, the parallel conduction from the doped region can be removed with a doping density of $5.8 \times 10^{10} \text{ cm}^{-2}$ for each δ -doping layer without lowering the surface pinning, as shown in Figure 7.8 (c). However, this will result in a really low electron density in the QW for this structure, which is only around $6 \times 10^9 \text{ cm}^{-2}$ for the structure shown in Figure 7.8 (c). We further suspect that the total of five δ -doping layers is problematic as it makes the doped region much wider with smaller confinement, leading to lower energy levels available in the doped region. Reducing the total number of δ -doping layers from five to one effectively improves the electron density in the 2DEG, as shown in Figure 7.8 (d) for the structure containing a single δ -doping layer with a doping density of $4 \times 10^{11} \text{ cm}^{-2}$ and a slightly higher sheet carrier density of around $2 \times 10^{10} \text{ cm}^{-2}$ in the QW. However to achieve InSb surface QW structures with decent carrier densities and without parallel conduction, lowering the Schottky barrier at the surface is still indispensable.

7.2.2 Structures with back gates

Our InSb QW inverted structures with remote δ -doping layers are either parallel-conducting or non-conducting. Nextnano++ simulation suggests that there are several possible remedies to lift the parallel conduction, however without careful tuning of all the fitting parameters, it only serves as a rough guide and does not guarantee that the simulated result can be realized in experiments. We suspect that it is such difficulty

Table 7.3: A summary of the growths of InSb QW back-gated structures with varying Si-doping densities n_d for the back-gate layer, Al composition x in the $\text{Al}_x\text{In}_{1-x}\text{Sb}$ barrier layer and thickness of the $\text{Al}_x\text{In}_{1-x}\text{Sb}$ spacer, as well as the corresponding 2DEG isolation to the back gate $R_{2deg-bg}$ in the structure.

Sample	x	t_{bs} (μm)	n_d (cm^{-3})	$R_{2deg-bg}$ (Ω)
G0787	0.1	0.5	2×10^{19}	very little
G0797	0.12	1	5×10^{18}	30
G0817	0.12	1	5×10^{17}	114

that there are still zero publications on InSb QW inverted structures without parallel conduction. To work around this problem, we decided to use back-gating, instead of modulation doping to populate the InSb QW in the structure.

Back gates in the structures are usually achieved by employing doped substrates which require careful calibrations on the substrate temperature measurements. Instead, we used a Si-doped AlInSb layer on top of our current AlInSb metamorphic buffer to serve as the back gate, which is easier to be incorporated into our current growth procedure. The schematic illustration of the active region with the back gate layer is shown in Figure 7.9), which was directly deposited on the thick simple $\text{Al}_x\text{In}_{1-x}\text{Sb}$ buffer on GaAs substrate. The whole active region was grown at a flux ratio of Sb/III at 2 and a substrate temperature of 340 °C to reduce the segregation of Si.

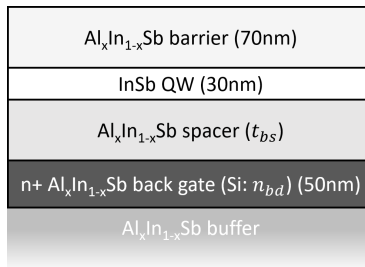


Figure 7.9: The schematics of the back-gated InSb QW structures

A back gate doping test sample was grown first which consisted of an $\text{Al}_{0.1}\text{In}_{0.9}\text{Sb}$ buffer layer of 620 nm total thickness on GaAs substrate. A portion of 50 nm thick and 70 nm below the surface in the AlInSb buffer was degenerately doped with Si with a bulk doping density of $2 \times 10^{19} \text{ cm}^{-3}$. The wafer was mounted in a sapphire wafer configuration (subsection 4.1.4) for improved uniformity in the substrate temperature across the wafer.

The back-gate layer was found to be highly conductive with a sheet resistance of 48 k Ω /sq. Unfortunately, when such a back-gate layer was inserted 500nm below the InSb QW (G0787 in Table 7.3), the InSb 2DEG was found to be severely shorted to the back gate, with a very small resistance measured between the QW and the back gate. For better isolation of the InSb 2DEG from the back gate, the thickness of the spacer layer between the QW and the back gate t_{bs} was increased from 500 nm to 1 μ m for both G0797 and G0817. The barrier height was also increased for G0797 and G0817 by increasing the Al composition x in the $\text{Al}_x\text{In}_{1-x}\text{Sb}$ layers throughout the structure from 10% to 12%. The doping density in the Si-doped back-gate layer n_{bd} was reduced from $2 \times 10^{19} \text{ cm}^{-3}$ to $5 \times 10^{18} \text{ cm}^{-3}$ in G0797 and further to $5 \times 10^{18} \text{ cm}^{-3}$ in G0817. Though a trend of increasing isolation between the InSb 2DEG and the back gate is observed with decreasing doping density, the InSb 2DEG is still badly shorted to the back gate.

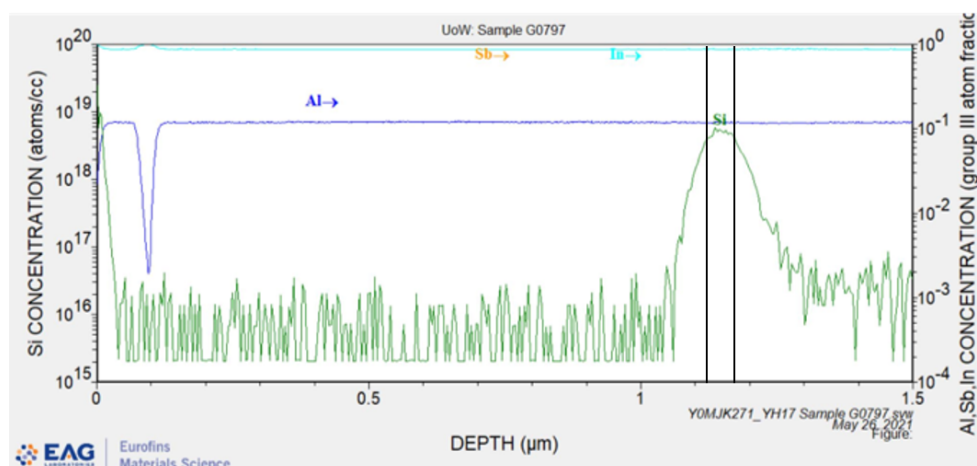


Figure 7.10: The secondary ion mass spectrometry (SIMS) spectra measured for G0797.

The cause of the leakage from the back gate failed to be explained by nextnano++ simulations, which shows a more than sufficient AlInSb barrier persisting between the QW and back gate layer with varying doping density. To check whether the observed short was due to Si segregation in the structure during the growth, a SIMS profile was acquired from the surface all the way to 1.5 μ m below the surface of G0797. As shown in Figure 7.10, no sign of excessive segregation of Si can be observed. The background noise signal for Si is at the level of $\sim 1 \times 10^{16} \text{ atoms/cc}$. The slight widening of the Si peak on both sides could be a result of Si diffusion and/or SIMS crater base roughening during the sputtering process deep into the structure.

As the next steps, we plan to decrease further the Si doping density in the back gate

layer in the current structure to see if it can solve the leakage problem. Additionally, it was found in our previous experiments that a 4 μm $\text{Al}_x\text{In}_{1-x}\text{Sb}$ buffer was able to provide much better mesa-to-mesa isolation than the same buffer of 3 μm -thick. Therefore we will also attempt to grow on a doped n^+ GaAs substrate with a full 4 μm $\text{Al}_x\text{In}_{1-x}\text{Sb}$ buffer to isolate the InSb QW from the back gate. The isolation may be further improved by employing a 4 μm linearly graded $\text{Al}_x\text{In}_{1-x}\text{Sb}$ buffer with $x = 0$ near the back gate.

7.2.3 Top gate-ability

Top gates are essential for the top-down definition of 1D structures from InSb surface QWs for the applications of Majorana devices. An ideal gate dielectric is required for a working top gate by creating a fully insulating barrier with minimal gate hysteresis from charge buildup or surface states. Successful gate-tunable InSb/AlInSb QW structures have been demonstrated with Al_2O_3 and HfO_2 as suitable gate dielectrics [145, 150]. HfO_2 has been further demonstrated to be more advantageous over Al_2O_3 by having a higher dielectric constant and being able to be deposited at lower temperatures. [145] In this thesis, HfO_2 was deposited at 150 $^\circ\text{C}$ by atomic layer deposition (ALD) on our gated InSb surface QW samples to study the effectiveness of HfO_2 on gating the carrier densities in the structure.

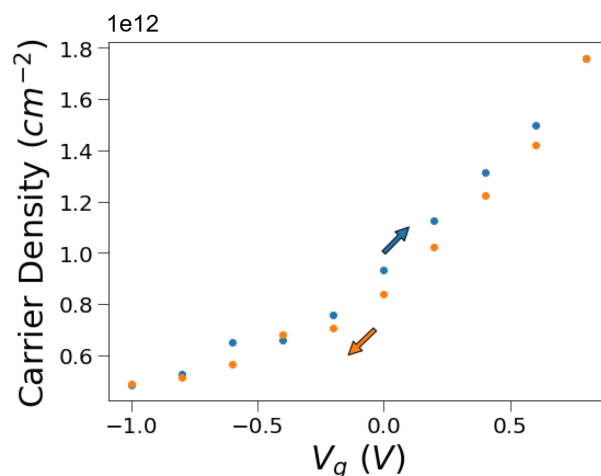


Figure 7.11: Carrier density of G0414 as a function of top gate voltage sweeping from -1 V to +0.8 V and back that show minimal hysteresis in the gating [Adapted from the E. Bergeron's MSc thesis [94]].

Uniform HfO_2 film was achieved and negligible leakage current was measured from the gate to the InSb QW. The carrier density modulated by the top gate voltage is shown in Figure 7.11. The carrier density was varied by a factor of three as the top gate voltage was changed in a range of -1 V to +0.8 V and a nonlinear dependence was observed. Top gate voltage sweeps from negative to positive and backward indicated minimal hysteresis as shown in Figure 7.11. However, the carrier density plateaued near $5 \times 10^{11} \text{ cm}^{-2}$ rendering pinch-off (i.e. zero carrier density) being unachievable. Considering the severe parallel conduction in the structure, we suspect that the remaining carrier density mostly results from the parallel conducting δ -doping layers.

7.3 Conclusions

In this chapter, the magneto-transport properties of both the standard and inverted InSb QW structures are studied. Inverted InSb QW structures and especially near-surface InSb QW structures are required for Majorana experiments. The studies on the better developed standard InSb QW structures serve as a basis for the development of inverted structures. For the standard structures with a Si δ -doping above the InSb QW, over-doped samples showed severe parallel conduction with a high carrier density and low mobility, while the under-doped sample was non-conducting. The doping profile was optimized by varying the Al composition in the barrier and the Si δ -doping density until a single-channel conducting 2DEG in the structure is achieved as indicated by the plot of the transport data showing SdH oscillations going to zero resistance and clear quantum Hall plateaus.

Both the effect of the first intermediate buffer and the second-stage buffer on the transport properties of the standard InSb QW structures are investigated. However, parallel conduction re-appeared in the growths with different buffer structures, despite the same active region used. Due to the parallel conduction, we cannot speculate on the effect of the GaSb IMF buffer on the QW performance. On the other hand, despite the parallel conduction, the InSb QW structure with the single composition buffer replaced by an interlayer structure showed significantly improved 2DEG performance by doubling the mobility with only a little increase in the carrier density.

InSb QW heterostructures are known to be often plagued with parallel conduction and suffer from a lack of reproducibility. In this thesis, a comprehensive study on the reproducibility and parallel conduction issues was performed by varying a broad range of growth parameters.

The mobility and carrier concentration of the standard InSb QW structures were found to increase with decreasing substrate temperature during the growth. The increase in the carrier concentration is likely a result of increased doping efficiency as the substrate temperature was decreased. From the transport data, the increase in the doping efficiency caused by a 10 °C drop in the substrate temperature can lead to an increase in the carrier density by $0.4 \times 10^{11} \text{ cm}^{-2}$, which may be enough to make the sample over-doped and become parallel conducting. This result also stresses the importance of reliable substrate temperature measurement for the growth of InSb QW heterostructures. Moreover, we found that an increase in the group V/III flux ratio from 1.5 to 2 is surprisingly helpful for solving the plague of parallel conduction in standard InSb QW structures, though the mechanism is still unclear.

By changing the Al compositions in the buffer layer and the barrier layers, we affirmed that the appearance of parallel conduction was not a result of insufficient barrier height due to the instabilities of the atomic fluxes. Since a trend of increasing parallel conduction was observed over time with our samples grown under the same conditions and with the same doping density, we further speculate that the parallel conduction and irreproducibility may also be a result of a drift in the chamber environment over time which effectively changes the optimal doping density for the structure. Nevertheless, the growth of InSb QW structures can be highly reproducible within a certain time frame once the doping profile is re-optimized.

The highest mobility we have achieved with the standard InSb QW structures without parallel conduction is $66\,000 \text{ cm}^2/\text{Vs}$ with a carrier density of $1.8 \times 10^{11} \text{ cm}^{-2}$. The mobility can be easily doubled by employing an interlayer buffer. However, the carrier density in the InSb 2DEG is still quite low with our current doping profile. Though mobility is not the major concern for the Majorana experiments, the mobility of the standard InSb QW structures can be further improved by optimizing the doping profile to allow for a higher 2DEG carrier density without parallel conduction.

Inverted InSb QW structures with five Te δ -doping layers beneath the QW are developed in this thesis. The InSb QWs were placed near or right at the surface and hence were strongly affected by scattering from the surface disorders. Weak localization was observed, in contrast to the weak anti-localization effect in standard structures, suggesting a diffusive transport. However, the InSb surface QW structures, being the first reported case of such structures, showed a promising performance with a mobility of $16\,000 \text{ cm}^2/\text{Vs}$ and a carrier density of $8.0 \times 10^{11} \text{ cm}^{-2}$. Unfortunately, the structures can not be tuned by the doping density to eliminate the parallel conduction without depopulating the InSb QW at the same time. nextnano++ simulations suggested that the parallel conduction in the doping layer may be removed by reducing the Fermi level

pinning at the surface, decreasing the spacer layer thickness, and reducing the number of δ -doping layers.

Inverted InSb QW structures with a Si-doped AlInSb back gate layer have also been developed. However, so far the InSb QW in these structures all suffered severe leakage from the back gate. SIMS measurements demonstrated no signs of Si segregation in the structure, which has ruled out the possibility of leakage due to the effect of Si segregation during the growth. We plan to decrease further the doping densities in the back-gate layer and increase the thickness of the spacer between the QW and the back gate as the next steps to solve the leakage problem.

HfO₂ was deposited to serve as the gate dielectric layer to study the top gateability of the InSb surface QW structures with Te modulation doping. Negligible leakage was found from the top gate to the InSb QW and minimal hysteresis was observed as the carrier density was varied by a factor of three by the top gate. However, the parallel conduction in the structure prevents the full depletion of the carrier density.

Chapter 8

Summary and outlook

8.1 Summary

In this thesis, InSb [quantum well \(QW\)](#) heterostructures have been developed on GaAs substrates using [molecular beam epitaxy \(MBE\)](#) for experimental realization of [Majorana bound states \(MBS\)](#) as a first step towards topological quantum computing. The optimization of the material structures was carried out for both the metamorphic buffers and the active regions to reduce the defect densities, smooth the surface morphology and improve the transport properties for the InSb [QWs](#). Metamorphic buffers consisted of a first intermediate buffer of either AlSb or GaSb and a second-stage buffer of either $\text{Al}_x\text{In}_{1-x}\text{Sb}$ with a single composition or an $\text{Al}_x\text{In}_{1-x}\text{Sb}/\text{Al}_y\text{In}_{1-y}\text{Sb}$ interlayer structure are developed to bring the lattice constant of the material from that of the GaAs substrate to the InSb [QW](#). The InSb [QW](#) active region was designed to have either a standard or an inverted [high-electron-mobility transistor \(HEMT\)](#) structure. Magnetic-transport measurements were made for samples fabricated in both [van der Pauw \(vdP\)](#) and hall bar geometries.

Defects in the metamorphic buffer and InSb [QW](#) heterostructures studied in this thesis are characterized by [atomic force microscopy \(AFM\)](#), [scanning electron microscopy \(SEM\)-electron channeling contrast imaging \(ECCI\)](#), [defect selective etching \(DSE\)](#), and cross-sectional [scanning transmission electron microscopy \(STEM\)](#). Both [threading dislocations \(TDs\)](#) and [micro-twinns \(MTs\)](#) have been observed using [AFM](#), [SEM-ECCI](#) in the III-Sb/GaAs systems. Cross-sectional [STEM](#) allows direct visualization of the generation and propagation process of defects, while the other techniques are more suitable for quantitative analysis of [threading dislocation density \(TDD\)](#) by directly

revealing the dislocation outcrops on the surface. From our observations, SEM-ECCI can be used for a broad range of TDD measurements (10^6 – 10^9 cm⁻²), which makes it the best technique for characterizing the TDD for most of our samples. By using SEM-ECCI together with AFM, TDDs from 10^{10} cm⁻² to 10^8 cm⁻² are determined at different stages of our buffer structures.

The optimization of the growth mode of interfacial misfit (IMF) formation for the GaSb first intermediate buffer was carried out. However, higher TDD values and opposite dependence of the substrate temperatures were observed compared to the literature reports. We conclude that without understanding the underlying mechanism, the IMF growth mode cannot be easily transferred between MBE systems. Moreover, the more effective TDD reduction of the IMF GaSb buffer than the AlSb buffer became insignificant after the growth of the second-stage buffer. On the other hand, effective dislocation filtering by Al_{0.12}In_{0.88}Sb/Al_{0.24}In_{0.76}Sb interlayers was observed with cross-sectional STEM. The use of four repetitions of Al_{0.1}In_{0.9}Sb/Al_{0.2}In_{0.8}Sb interlayers instead of a simple composition buffer was found to reduce the TDD in the InSb QW structures by a factor of three as measured by SEM-ECCI. For a TDD of $\sim 1 \times 10^8$ cm⁻² with the interlayer second-stage buffer, defect-free surface areas of up to a few μm^2 can be easily located on the surface of our InSb QW heterostructures, which is already suitable for the top-down fabrication of InSb nanowire devices.

Hillock-decorated surface morphologies as a result of high TDD were observed on the III-Sb material structures grown on GaAs (001) substrates using Nomarski microscope and AFM. A clear trend of widening terrace width of the hillock spiral steps with increasing substrate temperature was observed for AlSb, GaSb, and Al_{0.1}In_{0.9}Sb buffers, consistent with the expected changes in the adatom diffusion length. The constant hillock terrace width observed across the wafers and independent on the layer thickness was hypothesized to be related to the balancing of uphill and downhill surface currents on the hillock sidewalls, which are influenced by kinetic processes including the adatom diffusion length, the step energy barriers, and the interactions between steps.

The surface morphologies of AlSb and AlInSb metamorphic buffers as well as the InSb QW regions were studied as a function of substrate offcut angle by employing the polishing-induced surface bowing at the wafer edge. As the effective substrate offcut increases, a similar morphological transition has been observed for all the material structures studied and discussed with a toy model. The optimal substrate offcut angle for a hillock-free surface was found to be equal to the facet angle of hillock sidewalls, which is dependent on the growth conditions and the material compositions. Such offcut angles were also found to suppress the formation of MTs. On GaAs (001) substrates with a 0.55° offcut towards $[\bar{1}10]$ direction, we have successfully grown hillock-free, MT-free

and atomically smooth InSb QW heterostructures.

Standard InSb QW structures with negligible parallel conduction were achieved by optimizing the doping profile. The structure with an interlayer second-stage buffer showed further improved mobility due to reduced TDD in the structure. However, parallel conduction and reproducibility problems were found to accompany the growth of the InSb QW heterostructures, therefore a comprehensive study on this matter was conducted. By varying the Al composition in the barrier and buffer layers, we concluded that changes in the barrier height due to the instabilities of the effusion cells was not the reason for the appearance of parallel conduction. However, a slight deviation in the substrate temperature ($\sim 10^\circ\text{C}$) may result in a change in the doping efficiency that is sufficient to introduce parallel conduction in the doping layer. Reliable substrate temperature measurement is hence crucial for the development of reproducible InSb QW heterostructures. An increase in the group V/III flux ratio from 1.5 to 2 was found to eliminate the parallel conduction in standard InSb QW structures, though the mechanism is still unclear. In addition, the parallel conduction appearing in the repeated growths exhibited a slowly increasing trend over time, which might be related to a drift in the chamber environment. Nevertheless, with re-optimized doping profile, the growth of InSb QW structures can be highly reproducible within a reasonable time frame.

Though suffering from severe surface scattering, the InSb true surface QW structures with five Te δ -doping layers showed a promising performance with a mobility of $16\,000\text{ cm}^2/\text{Vs}$ and a carrier density of $8.0 \times 10^{11}\text{ cm}^{-2}$. Unfortunately, all the inverted InSb QW structures were affected with parallel conduction, which cannot be eliminated by tuning the doping density. Possible remedies to this problem were studied by nextnano++ simulations. The inverted InSb QW structures with a Si-doped AlInSb back gate layer were also developed but so far all suffered leakage from the back gate. The possibility of Si segregation during the growth was ruled out by the Secondary ion mass spectrometry (SIMS) measurements. Further optimization of the back-gated structures is currently under development. Successful top gateability has been demonstrated with modulation-doped InSb surface QW structures by using HfO_2 as the gate dielectric. The carrier density was varied by a factor of three by the top gate with minimum hysteresis, yet pinch-off was unachievable due to the parallel conduction channel in the inverted structures.

8.2 Future work and outlook

Optimization of the metamorphic buffers for InSb QW heterostructures with further reduced TDDs motivates an investigation on the application of the IMF growth modes on AlSb and AlInSb buffers.

For applications where high-performance InSb HEMTs are demanded, the design of the active region for the standard QW structure needs to be further optimized to allow for a higher carrier density in the InSb two-dimensional electron gas (2DEG) without parallel conduction. Better doping configuration is preferred such that the modulation of the 2DEG carrier density can be achieved in a wider range by varying the doping density without introducing parallel conduction. High-mobility structures can also be used to study the scattering effect from the surface hillocks by conducting the growths simultaneously on both the on-orientation and offcut substrates.

Further optimization of the InSb surface QW structures is required for the realization of MBS. To overcome the problem of parallel conduction in the modulation-doped inverted structures, the number of the δ -doping layers needs to be reduced as suggested by nextnano++ simulations. Surface treatment can also be developed to further reduce the Schottky barrier at the surface. Furthermore, a higher barrier for the QW is preferred, which motivates the development of strain compensated structures in the active region to increase the 2DEG carrier concentration without the need to decrease the QW thickness or the concern of introducing parallel conduction. For the back-gated inverted InSb QW structures, the solution to leakage from the back-gate to the QW is currently under development. The Si doping density in the back gate layer in the current structures will be decreased further and the thickness of the spacer layer between the QW and the back gate will be increased. A 4 μm linearly graded $\text{Al}_x\text{In}_{1-x}\text{Sb}$ buffer with $x = 0$ near the back gate may also be employed to increase the isolation to the back gate. The development of other InSb surface QW structures is also motivated. Instead of using the modulation doping or back gates, InSb surface QW structures with an additional thin Si-doped InSb layer at the surface are being developed to populate the surface QW and reduce the Schottky barrier at the surface.

The experiments on characterizing and improving the interface between epitaxial Al and III-V materials are currently being carried out in the QNC-MBE lab. In the meantime, the design and fabrication for 2D and 1D superconductor-normal-superconductor (SNS) devices are under development in Prof. Baugh's research group at Waterloo. The induced supercurrent in the Al/InSb-based SNS junctions can then be studied immediately as a preliminary step for the realization of Majorana MBS on a platform that is readily

scalable to logical qubit devices for [MBS](#) manipulation.

Letters of Copyright Permission



Chapter: Chapter 1 Defects in Crystals
Book: Introduction to Dislocations
Author: D. Hull,D.J. Bacon
Publisher: Elsevier
Date: 2011

Copyright © 2011 D. Hull and D. J. Bacon. Published by Elsevier Ltd All rights reserved.

Order Completed

Thank you for your order.

This Agreement between University of Waterloo -- Yinqiu Shi ("You") and Elsevier ("Elsevier") consists of your license details and the terms and conditions provided by Elsevier and Copyright Clearance Center.

Your confirmation email will contain your order number for future reference.

License Number 5133170306810

[Printable Details](#)

License date Aug 20, 2021

Licensed Content

Licensed Content Publisher Elsevier
Licensed Content Publication Elsevier Books
Licensed Content Title Introduction to Dislocations
Licensed Content Author D. Hull,D.J. Bacon
Licensed Content Date Jan 1, 2011
Licensed Content Pages 20

Order Details

Type of Use reuse in a thesis/dissertation
Portion figures/tables/illustrations
Number of figures/tables/illustrations 2
Format both print and electronic
Are you the author of this Elsevier chapter? No
Will you be translating? No

About Your Work

Title Molecular beam epitaxial growth of InSb quantum well heterostructures for applications in topological quantum computing
Institution name University of Waterloo
Expected presentation date Aug 2021

Additional Data

Portions FIGURE 1.19, FIGURE 1.20

Requestor Location

University of Waterloo
200 University Avenue

Tax Details

Publisher Tax ID GB 494 6272 12

Requestor Location

Waterloo, ON N2L 3G1
Canada
Attn: University of Waterloo

Figure 8.1: Reuse and permissions license for Figure 2.2.

 **Taylor & Francis**
Taylor & Francis Group

Accommodation of misfit across the interface between single-crystal films of various face-centred cubic metals

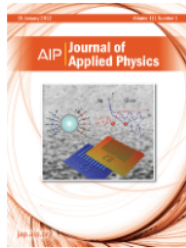
Author: J. W. Matthews
Publication: Philosophical Magazine
Publisher: Taylor & Francis
Date: Jan 6, 1966

Rights managed by Taylor & Francis

Thesis/Dissertation Reuse Request

Taylor & Francis is pleased to offer reuses of its content for a thesis or dissertation free of charge contingent on resubmission of permission request if work is published.

Figure 8.2: Reuse and permissions license for [Figure 2.6](#) and [Figure 2.8](#).



Strain relief mechanisms and the nature of dislocations in GaAs/Si heterostructures

Author: S. Sharan, J. Narayan
Publication: Journal of Applied Physics
Publisher: AIP Publishing
Date: Sep 15, 1989

Rights managed by AIP Publishing.

Order Completed

Thank you for your order.

This Agreement between University of Waterloo -- Yinqiu Shi ("You") and AIP Publishing ("AIP Publishing") consists of your license details and the terms and conditions provided by AIP Publishing and Copyright Clearance Center.

Your confirmation email will contain your order number for future reference.

License Number 5133171290488 [Printable Details](#)

License date Aug 20, 2021

Licensed Content

Licensed Content Publisher	AIP Publishing
Licensed Content Publication	Journal of Applied Physics
Licensed Content Title	Strain relief mechanisms and the nature of dislocations in GaAs/Si heterostructures
Licensed Content Author	S. Sharan, J. Narayan
Licensed Content Date	Sep 15, 1989
Licensed Content Volume	66
Licensed Content Issue	6

Order Details

Type of Use	Thesis/Dissertation
Requestor type	Student
Format	Print and electronic
Portion	Figure/Table
Number of figures/tables	1
Will you be translating?	No

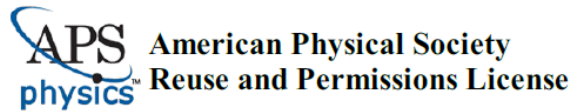
About Your Work

Title	Molecular beam epitaxial growth of InSb quantum well heterostructures for applications in topological quantum computing
Institution name	University of Waterloo
Expected presentation date	Aug 2021

Additional Data

Portions	Figure 4
-----------------	----------

Figure 8.3: Reuse and permissions license for Figure 2.7.



20-Aug-2021

This license agreement between the American Physical Society ("APS") and Yinqiu Shi ("You") consists of your license details and the terms and conditions provided by the American Physical Society and SciPris.

Licensed Content Information

License Number: RNP/21/AUG/043583
License date: 20-Aug-2021
DOI: 10.1103/PhysRevB.14.556
Title: Nonlocal pseudopotential calculations for the electronic structure of eleven diamond and zinc-blende semiconductors
Author: James R. Chelikowsky and Marvin L. Cohen
Publication: Physical Review B
Publisher: American Physical Society
Cost: USD \$ 0.00

Request Details

Does your reuse require significant modifications: No
Specify intended distribution locations: Canada
Reuse Category: Reuse in a thesis/dissertation
Requestor Type: Student
Items for Reuse: Figures/Tables
Number of Figure/Tables: 1
Figure/Tables Details: Figure 8
Format for Reuse: Print and Electronic
Total number of print copies: Up to 1000

Information about New Publication:

University/Publisher: University of Waterloo
Title of dissertation/thesis: Molecular beam epitaxial growth of InSb quantum well heterostructures for applications in topological quantum computing
Author(s): Yinqiu Shi
Expected completion date: Aug. 2021

License Requestor Information

Name: Yinqiu Shi
Affiliation: Individual
Email Id: y84shi@uwaterloo.ca
Country: Canada

Figure 8.4: Reuse and permissions license for [Figure 3.1a](#).

Order Completed

Thank you for your order.

This Agreement between University of Waterloo -- Yinqiu Shi ("You") and AIP Publishing ("AIP Publishing") consists of your license details and the terms and conditions provided by AIP Publishing and Copyright Clearance Center.

Your confirmation email will contain your order number for future reference.

License Number 5136671501196 [Printable Details](#)

License date Aug 26, 2021

✔ Licensed Content

Licensed Content Publisher AIP Publishing
Licensed Content Publication Applied Physics Reviews
Licensed Content Title Quantum confinement in Si and Ge nanostructures: Theory and experiment
Licensed Content Author Eric G. Barbagiovanni, David J. Lockwood, Peter J. Simpson, et al
Licensed Content Date Mar 1, 2014
Licensed Content Volume 1
Licensed Content Issue 1

📄 Order Details

Type of Use Thesis/Dissertation
Requestor type Student
Format Print and electronic
Portion Figure/Table
Number of figures/tables 1
Will you be translating? No

📄 About Your Work

Title Molecular beam epitaxial growth of InSb quantum well heterostructures for applications in topological quantum computing
Institution name University of Waterloo
Expected presentation date Aug 2021

📄 Additional Data


Portions Figure 2

📍 Requestor Location

University of Waterloo
200 University Avenue

📄 Tax Details

Figure 8.5: Reuse and permissions license for Figure 3.2.



Reflection high-energy electron diffraction (RHEED)

Publication: Springer eBook
 Publisher: Springer Nature
 Date: Jan 1, 1999

Copyright © 1999, Springer-Verlag

Order Completed

Thank you for your order.

This Agreement between University of Waterloo -- Yinqiu Shi ("You") and Springer Nature ("Springer Nature") consists of your license details and the terms and conditions provided by Springer Nature and Copyright Clearance Center.

Your confirmation email will contain your order number for future reference.

License Number	5133181489131
License date	Aug 20, 2021

[Printable Details](#)

Licensed Content

Licensed Content Publisher	Springer Nature
Licensed Content Publication	Springer eBook
Licensed Content Title	Reflection high-energy electron diffraction (RHEED)
Licensed Content Date	Jan 1, 1999

Order Details

Type of Use	Thesis/Dissertation
Requestor type	academic/university or research institute
Format	print and electronic
Portion	figures/tables/illustrations
Number of figures/tables/illustrations	1
Will you be translating?	no
Circulation/distribution	1 - 29
Author of this Springer Nature content	no

About Your Work

Title	Molecular beam epitaxial growth of InSb quantum well heterostructures for applications in topological quantum computing
Institution name	University of Waterloo
Expected presentation date	Aug 2021

Additional Data

Portions	Fig. 2.1a,b
----------	-------------

Requestor Location

University of Waterloo	200 University Avenue
Requestor Location	Waterloo, ON N2L 3G1 Canada Attn: University of Waterloo

Tax Details

Figure 8.6: Reuse and permissions license for Figure 4.4.

References

- ¹V. P. Kunets, S. Easwaran, W. T. Black, D. Guzun, Y. I. Mazur, N. Goel, T. D. Mishima, M. B. Santos, and G. J. Salamo, “InSb quantum-well-based micro-Hall devices: potential for pT detectivity”, [IEEE Transactions on Electron Devices](#) **56**, 683–687 (2009).
- ²J. M. S. Orr, P. D. Buckle, M. Fearn, C. J. Storey, L. Buckle, and T. Ashley, “A surface-gated InSb quantum well single electron transistor”, [New Journal of Physics](#) **9**, 261 (2007).
- ³M. Radosavljevic, T. Ashley, A. Andreev, S. D. Coomber, G. Dewey, M. T. Emeny, M. Fearn, D. G. Hayes, K. P. Hilton, M. K. Hudait, R. Jefferies, T. Martin, R. Pillarisetty, W. Rachmady, T. Rakshit, S. J. Smith, M. J. Uren, D. J. Wallis, P. J. Wilding, and R. Chau, “High-performance 40nm gate length InSb p-channel compressively strained quantum well field effect transistors for low-power ($V_{CC} = 0.5V$) logic applications”, [2008 IEEE International Electron Devices Meeting \(IEDM\)](#), 1–4 (2008).
- ⁴R. M. Lutchyn, J. D. Sau, and S. Das Sarma, “Majorana fermions and a topological phase transition in semiconductor-superconductor heterostructures”, [Physical Review Letters](#) **105**, 077001 (2010).
- ⁵Y. Oreg, G. Refael, and F. von Oppen, “Helical liquids and Majorana bound states in quantum wires”, [Physical Review Letters](#) **105**, 177002 (2010).
- ⁶D. Aasen, M. Hell, R. V. Mishmash, A. Higginbotham, J. Danon, M. Leijnse, T. S. Jespersen, J. A. Folk, C. M. Marcus, K. Flensberg, and J. Alicea, “Milestones toward Majorana-based quantum computing”, [Physical Review X](#) **6**, 031016 (2016).
- ⁷C. Beenakker, “Search for Majorana fermions in superconductors”, [Annual Review of Condensed Matter Physics](#) **4**, 113–136 (2013).
- ⁸M. Franz, “Race for majorana fermions”, [Physics](#) **3**, 24 (2010).
- ⁹F. Wilczek, “Majorana returns”, [Nature Physics](#) **5**, 614–618 (2009).

- ¹⁰H. O. H. Churchill, V. Fatemi, K. Grove-Rasmussen, M. T. Deng, P. Caroff, H. Q. Xu, and C. M. Marcus, “Superconductor-nanowire devices from tunneling to the multichannel regime: zero-bias oscillations and magnetoconductance crossover”, [Physical Review B **87**, 241401 \(2013\)](#).
- ¹¹M. T. Deng, C. L. Yu, G. Y. Huang, M. Larsson, P. Caroff, and H. Q. Xu, “Anomalous zero-bias conductance peak in a Nb-InSb nanowire-Nb hybrid device”, [Nano Letters **12**, 6414–6419 \(2012\)](#).
- ¹²Ö. Gül, H. Zhang, J. D. S. Bommer, M. W. A. de Moor, D. Car, S. R. Plissard, E. P. A. M. Bakkers, A. Geresdi, K. Watanabe, T. Taniguchi, and L. P. Kouwenhoven, “Ballistic Majorana nanowire devices”, [Nature Nanotechnology **13**, 192–197 \(2018\)](#).
- ¹³V. Mourik, K. Zuo, S. M. Frolov, S. R. Plissard, E. P. A. M. Bakkers, and L. P. Kouwenhoven, “Signatures of Majorana fermions in hybrid superconductor-semiconductor nanowire devices”, [Science **336**, 1003–1007 \(2012\)](#).
- ¹⁴L. P. Rokhinson, X. Liu, and J. K. Furdyna, “The fractional a.c. Josephson effect in a semiconductor-superconductor nanowire as a signature of Majorana particles”, [Nature Physics **8**, 795–799 \(2012\)](#).
- ¹⁵R. M. Lutchyn, E. P. A. M. Bakkers, L. P. Kouwenhoven, P. Krogstrup, C. M. Marcus, and Y. Oreg, “Majorana zero modes in superconductor–semiconductor heterostructures”, [Nature Reviews Materials **3**, 52–68 \(2018\)](#).
- ¹⁶H. J. Suominen, M. Kjaergaard, A. R. Hamilton, J. Shabani, C. J. Palmstrøm, C. M. Marcus, and F. Nichele, “Zero-energy modes from coalescing Andreev states in a two-dimensional semiconductor-superconductor hybrid platform”, [Physical Review Letters **119**, 176805 \(2017\)](#).
- ¹⁷T. D. Mishima, J. C. Keay, N. Goel, M. A. Ball, S. J. Chung, M. B. Johnson, and M. B. Santos, “Effect of structural defects on InSb/Al_xIn_{1-x}Sb quantum wells grown on GaAs (001) substrates”, [Physica E: Low-dimensional Systems and Nanostructures **20**, 260–263 \(2004\)](#).
- ¹⁸T. D. Mishima, M. Edirisooriya, and M. B. Santos, “Electron scattering by structural defects in InSb quantum wells: analysis with simplified Mayadas-Shatzkes equation”, [Journal of Applied Physics **110**, 093705 \(2011\)](#).
- ¹⁹T. D. Mishima and M. B. Santos, “Impact of structural defects upon electron mobility in InSb quantum wells”, [Journal of Applied Physics **109**, 073707 \(2011\)](#).
- ²⁰J. R. Soderstrom, M. M. Cumming, J. Y. Yao, and T. G. Andersson, “Molecular beam epitaxy growth and characterization of InSb layers on GaAs substrates”, [Semiconductor Science and Technology **7**, 337–343 \(1992\)](#).

- ²¹X. Weng, R. S. Goldman, D. L. Partin, and J. P. Heremans, “Evolution of structural and electronic properties of highly mismatched InSb films”, *Journal of Applied Physics* **88**, 6276–6286 (2000).
- ²²S. D. Wu, L. W. Guo, Z. H. Li, X. Z. Shang, W. X. Wang, Q. Huang, and J. M. Zhou, “Effect of the low-temperature buffer thickness on quality of InSb grown on GaAs substrate by molecular beam epitaxy”, *Journal of Crystal Growth* **277**, 21–25 (2005).
- ²³X. Zhang, A. E. Staton-Bevan, D. W. Pashley, S. D. Parker, R. Droopad, R. L. Williams, and R. C. Newman, “A transmission electron microscopy and reflection high-energy electron diffraction study of the initial stages of the heteroepitaxial growth of InSb on GaAs (001) by molecular beam epitaxy”, *Journal of Applied Physics* **67**, 800–806 (1990).
- ²⁴C. J. McIndo, D. G. Hayes, A. Papageorgiou, L. A. Hanks, G. V. Smith, C. P. Allford, S. Zhang, E. M. Clarke, and P. D. Buckle, “Determination of the transport lifetime limiting scattering rate in InSb/Al_xIn_{1-x}Sb quantum wells using optical surface microscopy”, *Physica E: Low-dimensional Systems and Nanostructures* **91**, 169–172 (2017).
- ²⁵Y. Shi, D. Gosselink, K. Gharavi, J. Baugh, and Z. R. Wasilewski, “Optimization of metamorphic buffers for MBE growth of high quality AlInSb/InSb quantum structures: suppression of hillock formation”, *Journal of Crystal Growth* **477**, 7–11 (2017).
- ²⁶Y. Shi, E. Bergeron, F. Sfigakis, J. Baugh, and Z. R. Wasilewski, “Hillock-free and atomically smooth InSb QWs grown on GaAs substrates by MBE”, *Journal of Crystal Growth* **513**, 15–19 (2019).
- ²⁷M. C. Tam, Y. Shi, D. Gosselink, M. Jaikissoon, and Z. R. Wasilewski, “Temperature monitoring of narrow bandgap semiconductors”, *Journal of Vacuum Science & Technology B, Nanotechnology and Microelectronics: Materials, Processing, Measurement, and Phenomena* **35**, 02B102 (2017).
- ²⁸Y. Shi, D. Gosselink, V. Y. Umansky, J. L. Weyher, and Z. R. Wasilewski, “Threading dislocations in MBE grown AlInSb metamorphic buffers: revealed and counted”, *Journal of Vacuum Science & Technology B, Nanotechnology and Microelectronics: Materials, Processing, Measurement, and Phenomena* **35**, 02B112 (2017).
- ²⁹D. Hull and D. J. Bacon, *Introduction to dislocations*, Vol. 37 (Elsevier, 2011).
- ³⁰J. W. Gibbs, H. A. Bumstead, R. G. Van Name, and W. R. Longley, *The collected works of J. Willard Gibbs* (Longmans, Green and Co., New York, 1928).
- ³¹W. Kossel, “Zur theorie des kristallwachstums”, *Nachrichten von der Gesellschaft der Wissenschaften zu Göttingen, Mathematisch-Physikalische Klasse* **1927**, 135–143 (1927).

- ³²I. N. Stranski, “Zur theorie des kristallwachstums”, [Zeitschrift für Physikalische Chemie](#) **136U**, 259–278 (1928).
- ³³C. Misbah, O. Pierre-Louis, and Y. Saito, “Crystal surfaces in and out of equilibrium: a modern view”, [Reviews of Modern Physics](#) **82**, 981–1040 (2010).
- ³⁴G. Ehrlich and F. G. Hudda, “Atomic view of surface self-diffusion: tungsten on tungsten”, [The Journal of Chemical Physics](#) **44**, 1039–1049 (1966).
- ³⁵R. L. Schwoebel and E. J. Shipsey, “Step motion on crystal surfaces”, [Journal of Applied Physics](#) **37**, 3682–3686 (1966).
- ³⁶M. Siegert and M. Plischke, “Slope selection and coarsening in molecular beam epitaxy”, [Physical Review Letters](#) **73**, 1517–1520 (1994).
- ³⁷D. D. Vvedensky, A. Zangwill, C. N. Luse, and M. R. Wilby, “Stochastic equations of motion for epitaxial growth”, [Physical Review E](#) **48**, 852–862 (1993).
- ³⁸P. Curie, “On the formation of crystals and capillary constants of their different faces”, [Journal of Chemical Education](#) **47**, 636 (1970).
- ³⁹G. Wulff, “Zur frage der geschwindigkeit des wachstums und der auflösung der krystallflächen”, [Zeitschrift für Kristallographie - Crystalline Materials](#) **34**, 449–530 (1901).
- ⁴⁰W. K. Burton, N. Cabrera, and F. Frank, “The growth of crystals and the equilibrium structure of the their surfaces”, [Philosophical Transactions of the Royal Society of London Series a Mathematical Physical and Engineering Sciences](#) **243**, 299–358 (1951).
- ⁴¹J. H. van der Merwe, “Strains in crystalline overgrowths”, [The Philosophical Magazine: A Journal of Theoretical Experimental and Applied Physics](#) **7**, 1433–1434 (1962).
- ⁴²J. H. Van Der Merwe, “Crystal interfaces. part i. semi-infinite crystals”, [Journal of Applied Physics](#) **34**, 117–122 (1963).
- ⁴³J. W. Matthews and A. E. Blakeslee, “Defects in epitaxial multilayers: i. misfit dislocations”, [Journal of Crystal Growth](#) **27**, 118–125 (1974).
- ⁴⁴S. C. Jain, A. H. Harker, and R. A. Cowley, “Misfit strain and misfit dislocations in lattice mismatched epitaxial layers and other systems”, [Philosophical Magazine A](#) **75**, 1461–1515 (1997).
- ⁴⁵A. Rockett and C. J. Kiely, “Energetics of misfit- and threading-dislocation arrays in heteroepitaxial films”, [Physical Review B](#) **44**, 1154–1162 (1991).
- ⁴⁶J. C. Bean, “Silicon-based semiconductor heterostructures: column IV bandgap engineering”, [Proceedings of the IEEE](#) **80**, 571–587 (1992).

- ⁴⁷J. W. Matthews, “Accommodation of misfit across the interface between single-crystal films of various face-centred cubic metals”, *Philosophical Magazine* **13**, 1207–1221 (1966).
- ⁴⁸E. P. Kvam, D. J. Eaglesham, D. M. Maher, C. J. Humphreys, J. C. Bean, G. S. Green, and B. K. Tanner, “The nucleation and propagation of misfit dislocations near the critical thickness in Ge-Si strained epilayers”, *MRS Proceedings* **104**, 623 (1987).
- ⁴⁹S. Sharan and J. Narayan, “Strain relief mechanisms and the nature of dislocations in GaAs/Si heterostructures”, *Journal of Applied Physics* **66**, 2376–2380 (1989).
- ⁵⁰P. M. J. Marée, J. C. Barbour, J. F. van der Veen, K. L. Kavanagh, C. W. T. Bulle-Lieuwma, and M. P. A. Vieggers, “Generation of misfit dislocations in semiconductors”, *Journal of Applied Physics* **62**, 4413–4420 (1987).
- ⁵¹S. Guha, A. Madhukar, and K. C. Rajkumar, “Onset of incoherency and defect introduction in the initial stages of molecular beam epitaxial growth of highly strained $\text{In}_x\text{Ga}_{1-x}\text{As}$ on GaAs(100)”, *Applied Physics Letters* **57**, 2110–2112 (1990).
- ⁵²R. Hull and A. Fischer-Colbrie, “Nucleation of GaAs on Si: experimental evidence for a three-dimensional critical transition”, *Applied Physics Letters* **50**, 851–853 (1987).
- ⁵³D. J. Eaglesham and M. Cerullo, “Dislocation-free stranski-krastanow growth of Ge on Si(100)”, *Phys. Rev. Lett.* **64**, 1943–1946 (1990).
- ⁵⁴V. Gopal, A. L. Vasiliev, and E. P. Kvam, “Strain relaxation and dislocation introduction in lattice-mismatched InAs/GaP heteroepitaxy”, *Philosophical Magazine a Physics of Condensed Matter Structure Defects and Mechanical Properties* **81**, 2481–2501 (2001).
- ⁵⁵Y. Chen and J. Washburn, “Structural transition in large-lattice-mismatch heteroepitaxy”, *Phys. Rev. Lett.* **77**, 4046–4049 (1996).
- ⁵⁶F. K. LeGoues, M. C. Reuter, J. Tersoff, M. Hammar, and R. M. Tromp, “Cyclic growth of strain-relaxed islands”, *Phys. Rev. Lett.* **73**, 300–303 (1994).
- ⁵⁷J. M. Kang, M. Nouaoura, L. Lassabatère, and A. Rocher, “Accommodation of lattice mismatch and threading of dislocations in GaSb films grown at different temperatures on GaAs (001)”, *Journal of Crystal Growth* **143**, 115–123 (1994).
- ⁵⁸W. Qian, M. Skowronski, R. Kaspi, M. De Graef, and V. P. Dravid, “Nucleation of misfit and threading dislocations during epitaxial growth of GaSb on GaAs(001) substrates”, *Journal of Applied Physics* **81**, 7268–7272 (1997).
- ⁵⁹C. J. Kiely, J. I. Chyi, A. Rockett, and H. Morkoç, “On the microstructure and interfacial structure of InSb layers grown on GaAs(100) by molecular beam epitaxy”, *Philosophical Magazine A* **60**, 321–337 (1989).

- ⁶⁰M. Niehle, J.-B. Rodriguez, L. Cerutti, E. Tournié, and A. Trampert, “On the origin of threading dislocations during epitaxial growth of III-Sb on Si(001): a comprehensive transmission electron tomography and microscopy study”, *Acta Materialia* **143**, 121–129 (2018).
- ⁶¹H. L. Tsai and R. J. Matyi, “Generation of misfit dislocations in GaAs grown on Si”, *Applied Physics Letters* **55**, 265–267 (1989).
- ⁶²S. H. Huang, G. Balakrishnan, A. Khoshakhlagh, A. Jallipalli, L. R. Dawson, and D. L. Huffaker, “Strain relief by periodic misfit arrays for low defect density GaSb on GaAs”, *Applied Physics Letters* **88**, 131911 (2006).
- ⁶³E. P. Kvam, D. M. Maher, and C. J. Humphreys, “Variation of dislocation morphology with strain in $\text{Ge}_x\text{Si}_{1-x}$ epilayers on (100)Si”, *Journal of Materials Research* **5**, 1900–1907 (1990).
- ⁶⁴J. Narayan and S. Sharan, “Mechanism of formation of 60° and 90° misfit dislocations in semiconductor heterostructures”, *Materials Science and Engineering: B* **10**, 261–267 (1991).
- ⁶⁵A. Rocher and E. Snoeck, “Misfit dislocations in (001) semiconductor heterostructures grown by epitaxy”, *Materials Science and Engineering: B* **67**, 62–69 (1999).
- ⁶⁶A. Vilà, A. Cornet, J. R. Morante, M. Loubradou, R. Bonnet, Y. González, L. González, and P. Ruterana, “Atomic core structure of lomer dislocation at GaAs/(001)Si interface”, *Philosophical Magazine A* **71**, 85–103 (1995).
- ⁶⁷D. Benyahia, Ł. Kubiszyn, K. Michalczewski, A. Kębłowski, P. Martyniuk, J. Piotrowski, and A. Rogalski, “Optimization of the interfacial misfit array growth mode of GaSb epilayers on GaAs substrate”, *Journal of Crystal Growth* **483**, 26–30 (2018).
- ⁶⁸A. Jallipalli, G. Balakrishnan, S. H. Huang, T. J. Rotter, K. Nunna, B. L. Liang, L. R. Dawson, and D. L. Huffaker, “Structural analysis of highly relaxed GaSb grown on GaAs substrates with periodic interfacial array of 90° misfit dislocations”, *Nanoscale Research Letters* **4**, 1458 (2009).
- ⁶⁹A. Mansoori, S. J. Addamane, E. J. Renteria, D. M. Shima, M. Behzadirad, E. Vadiie, C. Honsberg, and G. Balakrishnan, “Reducing threading dislocation density in GaSb photovoltaic devices on GaAs by using AlSb dislocation filtering layers”, *Solar Energy Materials and Solar Cells* **185**, 21–27 (2018).
- ⁷⁰K. H. Tan, B. W. Jia, W. K. Loke, S. Wicaksono, and S. F. Yoon, “Formation of interfacial misfit dislocation in GaSb/GaAs heteroepitaxy via anion exchange process”, *Journal of Crystal Growth* **427**, 80–86 (2015).

- ⁷¹D. Eaglesham, M. Aindow, and R. Pond, “Defects in large-misfit heteroepitaxy”, [MRS Proceedings](#) **116**, 267 (1988).
- ⁷²Y. Wang, P. Ruterana, S. Kret, S. El Kazzi, L. Desplanque, and X. Wallart, “The source of the threading dislocation in GaSb/GaAs hetero-structures and their propagation mechanism”, [Applied Physics Letters](#) **102**, 052102 (2013).
- ⁷³J. Narayan and S. Oktyabrsky, “Formation of misfit dislocations in thin film heterostructures”, [Journal of Applied Physics](#) **92**, 7122–7127 (2002).
- ⁷⁴C. Choi, N. Otsuka, G. Munns, R. Houdre, H. Morkoç, S. L. Zhang, D. Levi, and M. V. Klein, “Effect of in situ and ex situ annealing on dislocations in GaAs on Si substrates”, [Applied Physics Letters](#) **50**, 992–994 (1987).
- ⁷⁵J. R. Chelikowsky and M. L. Cohen, “Nonlocal pseudopotential calculations for the electronic structure of eleven diamond and zinc-blende semiconductors”, [Physical Review B](#) **14**, 556–582 (1976).
- ⁷⁶E. O. Kane, “Band structure of narrow gap semiconductors”, in *Narrow gap semiconductors physics and applications*, edited by W. Zawadzki (), pp. 13–31.
- ⁷⁷E. G. Barbagiovanni, D. J. Lockwood, P. J. Simpson, and L. V. Goncharova, “Quantum confinement in Si and Ge nanostructures: theory and experiment”, [Applied Physics Reviews](#) **1**, 011302 (2014).
- ⁷⁸S. Birner, T. Zibold, T. Andlauer, T. Kubis, M. Sabathil, A. Trellakis, and P. Vogl, “nextnano: general purpose 3-D simulations”, [IEEE Transactions on Electron Devices](#) **54**, 2137–2142 (2007).
- ⁷⁹E. Majorana, “A symmetric theory of electrons and positrons”, *Nuovo Cimento* **14**, 171–184 (1937).
- ⁸⁰N. Read and D. Green, “Paired states of fermions in two dimensions with breaking of parity and time-reversal symmetries and the fractional quantum Hall effect”, [Physical Review B](#) **61**, 10267–10297 (2000).
- ⁸¹A. Y. Kitaev, “Unpaired Majorana fermions in quantum wires”, [Physics-Uspekhi](#) **44**, 131 (2001).
- ⁸²L. Fu and C. L. Kane, “Superconducting proximity effect and Majorana fermions at the surface of a topological insulator”, [Physical Review Letters](#) **100**, 096407 (2008).
- ⁸³J. D. Sau, R. M. Lutchyn, S. Tewari, and S. Das Sarma, “Generic new platform for topological quantum computation using semiconductor heterostructures”, [Physical Review Letters](#) **104**, 040502 (2010).

- ⁸⁴J. Alicea, “Majorana fermions in a tunable semiconductor device”, [Physical Review B **81**, 125318 \(2010\)](#).
- ⁸⁵A. Das, Y. Ronen, Y. Most, Y. Oreg, M. Heiblum, and H. Shtrikman, “Zero-bias peaks and splitting in an Al-InAs nanowire topological superconductor as a signature of Majorana fermions”, [Nature Physics **8**, 887–895 \(2012\)](#).
- ⁸⁶A. D. K. Finck, D. J. Van Harlingen, P. K. Mohseni, K. Jung, and X. Li, “Anomalous modulation of a zero-bias peak in a hybrid nanowire-superconductor device”, [Physical Review Letters **110**, 126406 \(2013\)](#).
- ⁸⁷C. W. Groth, M. Wimmer, A. R. Akhmerov, and X. Waintal, “Kwant: a software package for quantum transport”, [New Journal of Physics **16**, 063065 \(2014\)](#).
- ⁸⁸*Veeco GEN10 MBE system user manual*, Generic, 2012.
- ⁸⁹W. Braun, *Applied RHEED: reflection high-energy electron diffraction during crystal growth*, Vol. 154 (Springer Science & Business Media, 1999).
- ⁹⁰J. H. Neave, B. A. Joyce, P. J. Dobson, and N. Northon, “Dynamics of film growth of GaAs by MBE from RHEED observations”, *Applied Physics A* **31**, 1 (1983).
- ⁹¹S. Zaefferer and N.-N. Elhami, “Theory and application of electron channelling contrast imaging under controlled diffraction conditions”, [Acta Materialia **75**, 20–50 \(2014\)](#).
- ⁹²J. L. Weyher, “Characterization of compound semiconductors by etching”, in *Handbook on semiconductors: materials, properties and preparation*, Vol. 3, edited by S. Mahajan (Elsevier, Amsterdam, 1994), pp. 995–1031.
- ⁹³J. L. Weyher and J. Van De Ven, “Selective etching and photoetching of GaAs in CrO₃-HF aqueous solutions : iii. interpretation of defect-related etch figures”, [Journal of Crystal Growth **78**, 191–217 \(1986\)](#).
- ⁹⁴E. Bergeron, “Study of surface quantum wells in InSb/AlInSb heterostructures”, Thesis (2019).
- ⁹⁵L. J. Van der Pauw, “A method of measuring the resistivity and hall coefficient on lamellae of arbitrary shape”, *Philips Technical Review* **20**, 220–224 (1958).
- ⁹⁶G. M. Williams, C. R. Whitehouse, N. G. Chew, G. W. Blackmore, and A. G. Cullis, “An MBE route towards CdTe/InSb superlattices”, [Journal of Vacuum Science & Technology B: Microelectronics Processing and Phenomena **3**, 704–708 \(1985\)](#).
- ⁹⁷G. M. Williams, C. R. Whitehouse, A. G. Cullis, N. G. Chew, and G. W. Blackmore, “Growth of CdTe-InSb multilayer structures on (100) InSb substrates using molecular beam epitaxy”, [Applied Physics Letters **53**, 1847–1849 \(1988\)](#).

- ⁹⁸T. D. Golding, S. K. Greene, M. Pepper, J. H. Dinan, A. G. Cullis, G. M. Williams, and C. R. Whitehouse, “Molecular beam epitaxial growth and magneto-transport studies of the InSb/CdTe material systems”, [Semiconductor Science and Technology](#) **5**, S311–S314 (1990).
- ⁹⁹K. J. Mackey, P. M. G. Allen, W. G. Herrenden-Harker, R. H. Williams, C. R. Whitehouse, and G. M. Williams, “Chemical and electronic structure of InSb-CdTe interfaces”, [Applied Physics Letters](#) **49**, 354–356 (1986).
- ¹⁰⁰S. K. Greene, J. Singleton, T. D. Golding, M. Pepper, C. J. G. M. Langerak, and J. H. Dinan, “Fundamental properties of high mobility InSb-CdTe heterojunctions”, [Surface Science](#) **228**, 542–546 (1990).
- ¹⁰¹S. K. Greene, J. Singleton, P. Sobkowicz, T. D. Golding, M. Pepper, J. A. A. J. Perenboom, and J. Dinan, “Subband occupancies and zero-field spin splitting in InSb-CdTe heterojunctions: magnetotransport experiments and self-consistent calculations”, [Journal of Vacuum Science and Technology](#) **7**, 1377–1385 (1992).
- ¹⁰²R. T. Grimes, T. J. B. M. Janssen, M. B. Stanaway, C. J. G. M. Langerak, J. Singleton, D. E. Ashenford, B. Lunn, G. Hill, and J. M. Chamberlain, “The two-dimensional electron gas at the CdTe/InSb interface: cyclotron resonance and Shubnikov-de Haas investigations”, [Surface Science](#) **267**, 133–136 (1992).
- ¹⁰³Y.-D. Zheng, Y. H. Chang, B. D. McCombe, R. F. C. Farrow, T. Temofonte, and F. A. Shirland, “Observation of a quasi-two-dimensional electron gas at an InSb/CdTe interface”, [Applied Physics Letters](#) **49**, 1187–1189 (1986).
- ¹⁰⁴C. A. Lehner, T. Tschirky, T. Ihn, W. Dietsche, J. Keller, S. Fält, and W. Wegscheider, “Limiting scattering processes in high-mobility InSb quantum wells grown on GaSb buffer systems”, [Physical Review Materials](#) **2**, 054601 (2018).
- ¹⁰⁵T. D. Mishima, M. Edirisooriya, N. Goel, and M. B. Santos, “Dislocation filtering by $\text{Al}_x\text{In}_{1-x}\text{Sb}/\text{Al}_y\text{In}_{1-y}\text{Sb}$ interfaces for InSb-based devices grown on GaAs (001) substrates”, [Applied Physics Letters](#) **88**, 191908 (2006).
- ¹⁰⁶X. Weng, N. G. Rudawski, P. T. Wang, R. S. Goldman, D. L. Partin, and J. Heremans, “Effects of buffer layers on the structural and electronic properties of InSb films”, [Journal of Applied Physics](#) **97**, 043713 (2005).
- ¹⁰⁷E. F. Schubert, *Light-emitting diodes*, 2nd ed. (Cambridge University Press, Cambridge, 2006).

- ¹⁰⁸M. K. Saker, D. M. Whittaker, M. S. Skolnick, C. F. McConville, C. R. Whitehouse, S. J. Barnett, A. D. Pitt, A. G. Cullis, and G. M. Williams, “Demonstration of quantum confinement in InSb-In_{1-x}Al_xSb multiquantum wells using photoluminescence spectroscopy”, *Applied Physics Letters* **65**, 1118–1120 (1994).
- ¹⁰⁹J. M. S. Orr, A. M. Gilbertson, M. Fearn, O. W. Croad, C. J. Storey, L. Buckle, M. T. Emeny, P. D. Buckle, and T. Ashley, “Electronic transport in modulation-doped InSb quantum well heterostructures”, *Physics Review B* **77**, 165334 (2008).
- ¹¹⁰K. J. Goldammer, W. K. Liu, G. A. Khodaparast, S. C. Lindstrom, M. B. Johnson, R. E. Doezema, and M. B. Santos, “Electrical properties of InSb quantum wells remotely doped with Si”, *Journal of Vacuum Science & Technology B* **16**, 1367–1371 (1998).
- ¹¹¹W. K. Liu, X. Zhang, W. Ma, J. Winesett, and M. B. Santos, “Molecular-beam epitaxial growth and characterization of Al_xIn_{1-x}Sb/InSb quantum well structures”, *Journal of Vacuum Science & Technology B* **14**, 2339–2342 (1996).
- ¹¹²T. D. Mishima and M. B. Santos, “Effect of buffer layer on InSb quantum wells grown on GaAs (001) substrates”, *Journal of Vacuum Science & Technology B* **22**, 1472–1474 (2004).
- ¹¹³T. Sato, M. Akabori, and S. Yamada, “High-quality highly mismatched InSb films grown on GaAs substrate via thick AlSb and In_xAl_{1-x}Sb step-graded buffers”, *Physica E: Low-dimensional Systems and Nanostructures* **21**, 615–619 (2004).
- ¹¹⁴C. A. Lehner, “On the limitations and prospects of MBE grown high-mobility InSb quantum wells”, Thesis (2019).
- ¹¹⁵J. E. Ayers, “The measurement of threading dislocation densities in semiconductor crystals by X-ray diffraction”, *Journal of Crystal Growth* **135**, 71–77 (1994).
- ¹¹⁶T. D. Mishima, J. C. Keay, N. Goel, M. A. Ball, S. J. Chung, M. B. Johnson, and M. B. Santos, “Anisotropic structural and electronic properties of InSb/Al_xIn_{1-x}Sb quantum wells grown on GaAs (0 0 1) substrates”, *Journal of Crystal Growth* **251**, 551–555 (2003).
- ¹¹⁷K. N. Yaung, S. Kirnstoetter, J. Faucher, A. Gerger, A. Lochtefeld, A. Barnett, and M. L. Lee, “Threading dislocation density characterization in III-V photovoltaic materials by electron channeling contrast imaging”, *Journal of Crystal Growth* **453**, 65–70 (2016).
- ¹¹⁸K. N. Yaung, S. Tomasulo, J. R. Lang, J. Faucher, and M. L. Lee, “Defect selective etching of GaAs_yP_{1-y} photovoltaic materials”, *Journal of Crystal Growth* **404**, 140–145 (2014).

- ¹¹⁹J. L. Weyher, S. Lazar, L. Macht, Z. Liliental-Weber, R. J. Molnar, S. Müller, V. G. M. Sivel, G. Nowak, and I. Grzegory, “Orthodox etching of HVPE-grown GaN”, *Journal of Crystal Growth* **305**, 384–392 (2007).
- ¹²⁰J. L. Weyher, “Defect sensitive etching of nitrides: appraisal of methods”, *Crystal Research and Technology* **47**, 333–340 (2012).
- ¹²¹S. Huang, G. Balakrishnan, and D. L. Huffaker, “Interfacial misfit array formation for GaSb growth on GaAs”, *Journal of Applied Physics* **105**, 103104–5 (2009).
- ¹²²B. W. Jia, K. H. Tan, W. K. Loke, S. Wicaksono, and S. F. Yoon, “Effects of surface reconstruction on the epitaxial growth of III-Sb on GaAs using interfacial misfit array”, *Applied Surface Science* **399**, 220–228 (2017).
- ¹²³H. S. Kim, Y. K. Noh, M. D. Kim, Y. J. Kwon, J. E. Oh, Y. H. Kim, J. Y. Lee, S. G. Kim, and K. S. Chung, “Dependence of the AlSb buffers on GaSb/GaAs(001) heterostructures”, *Journal of Crystal Growth* **301-302**, 230–234 (2007).
- ¹²⁴Y. Wang, P. Ruterana, L. Desplanque, S. El Kazzi, and X. Wallart, “Strain relief at the GaSb/GaAs interface versus substrate surface treatment and AlSb interlayers thickness”, *Journal of Applied Physics* **109**, 023509 (2011).
- ¹²⁵B. W. Jia, K. H. Tan, W. K. Loke, S. Wicaksono, and S. F. Yoon, “Formation of periodic interfacial misfit dislocation array at the InSb/GaAs interface via surface anion exchange”, *Journal of Applied Physics* **120**, 035301 (2016).
- ¹²⁶A. Jasik, I. Sankowska, A. Wawro, J. Ratajczak, D. Smoczyński, and K. Czuba, “GaSb layers with low defect density deposited on (001) GaAs substrate in two-dimensional growth mode using molecular beam epitaxy”, *Current Applied Physics* **19**, 542–547 (2019).
- ¹²⁷S. J. Brown, M. P. Grimshaw, D. A. Ritchie, and G. A. C. Jones, “Variation of surface morphology with substrate temperature for molecular beam epitaxially grown GaSb(100) on GaAs (100)”, *Applied Physics Letters* **69**, 1468–1470 (1996).
- ¹²⁸C. J. K. Richardson, L. He, and S. Kanakaraju, “Metamorphic growth of III-V semiconductor bicrystals”, *Journal of Vacuum Science & Technology B* **29**, 03C126 (2011).
- ¹²⁹G. Balakrishnan, J. Tatebayashi, A. Khoshakhlagh, S. H. Huang, A. Jallipalli, L. R. Dawson, and D. L. Huffaker, “III/V ratio based selectivity between strained Stranski-Krastanov and strain-free GaSb quantum dots on GaAs”, *Applied Physics Letters* **89**, 161104 (2006).
- ¹³⁰J. W. Matthews, A. E. Blakeslee, and S. Mader, “Use of misfit strain to remove dislocations from epitaxial thin films”, *Thin Solid Films* **33**, 253–266 (1976).

- ¹³¹M. Edirisooriya, T. D. Mishima, and M. B. Santos, “Effect of Al composition on filtering of threading dislocations by $\text{Al}_x\text{In}_{1-x}\text{Sb}/\text{Al}_y\text{In}_{1-y}\text{Sb}$ heterostructures grown on GaAs (001)”, *Journal of Vacuum Science & Technology B* **25**, 1063–1065 (2007).
- ¹³²C. Skierbiszewski, H. Turski, G. Muziol, M. Siekacz, M. Sawicka, G. Cywinski, Z. R. Wasilewski, and S. Porowski, “Nitride-based laser diodes grown by plasma-assisted molecular beam epitaxy”, *Journal of Physics D-Applied Physics* **47**, 18 (2014).
- ¹³³H. Turski, M. Siekacz, M. Sawicka, G. Cywinski, M. Krysko, S. Grzanka, J. Smalc-Koziorowska, I. Grzegory, S. Porowski, Z. R. Wasilewski, and C. Skierbiszewski, “Growth mechanism of InGaN by plasma assisted molecular beam epitaxy”, *Journal of Vacuum Science & Technology B* **29**, 03C136 - 03C136-5 (2011).
- ¹³⁴Z. R. Wasilewski, J. M. Baribeau, M. Beaulieu, X. Wu, and G. I. Sproule, “Studies of oxide desorption from GaAs substrates via Ga_2O_3 to Ga_2O conversion by exposure to Ga flux”, *Journal of Vacuum Science & Technology B: Microelectronics and Nanometer Structures Processing, Measurement, and Phenomena* **22**, 1534–1538 (2004).
- ¹³⁵M. C. Bartelt and J. W. Evans, “Kinetic roughening of Fe/Fe(100) epitaxial thin films”, *MRS Online Proceedings Library* **399**, 89 (1995).
- ¹³⁶J. Krug, M. Plischke, and M. Siegert, “Surface diffusion currents and the universality classes of growth”, *Physical Review Letters* **70**, 3271–3274 (1993).
- ¹³⁷J. Villain, “Continuum models of crystal growth from atomic beams with and without desorption”, *J. Phys. I France* **1**, 19–42 (1991).
- ¹³⁸D. E. Wolf and J. Villain, “Growth with surface diffusion”, *Europhysics Letters* **13**, 389–394 (1990).
- ¹³⁹M. D. Johnson, C. Orme, A. W. Hunt, D. Graff, J. Sudijono, L. M. Sander, and B. G. Orr, “Stable and unstable growth in molecular beam epitaxy”, *Physical Review Letters* **72**, 116–119 (1994).
- ¹⁴⁰B. Heying, E. J. Tarsa, C. R. Elsass, P. Fini, S. P. DenBaars, and J. S. Speck, “Dislocation mediated surface morphology of GaN”, *Journal of Applied Physics* **85**, 6470–6476 (1999).
- ¹⁴¹Y. Cui and L. Li, “Suppression of spiral growth in molecular beam epitaxy of GaN on vicinal 6H-SiC(0001)”, *Physica Status Solidi a Applied Research* **188**, 583–586 (2001).
- ¹⁴²J. Mysliveček, C. Schelling, F. Schäffler, G. Springholz, P. Šmilauer, J. Krug, and B. Voigtländer, “On the microscopic origin of the kinetic step bunching instability on vicinal Si(001)”, *Surface Science* **520**, 193–206 (2002).
- ¹⁴³F. Frank, “Capillary equilibria of dislocated crystals”, *Acta Crystallographica* **4**, 497–501 (1951).

- ¹⁴⁴T. D. Mishima, M. Edirisooriya, and M. B. Santos, “Reduction of microtwin defects for high-electron-mobility InSb quantum wells”, [Applied Physics Letters](#) **91**, 062106 (2007).
- ¹⁴⁵W. Yi, A. A. Kiselev, J. Thorp, R. Noah, B.-M. Nguyen, S. Bui, R. D. Rajavel, T. Hussain, M. F. Gyure, P. Kratz, Q. Qian, M. J. Manfra, V. S. Pribiag, L. P. Kouwenhoven, C. M. Marcus, and M. Sokolich, “Gate-tunable high mobility remote-doped InSb/In_{1-x}Al_xSb quantum well heterostructures”, [Applied Physics Letters](#) **106**, 142103 (2015).
- ¹⁴⁶A. M. Gilbertson, W. R. Branford, M. Fearn, L. Buckle, P. D. Buckle, T. Ashley, and L. F. Cohen, “Zero-field spin splitting and spin-dependent broadening in high-mobility InSb/In_{1-x}Al_xSb asymmetric quantum well heterostructures”, [Physical Review B](#) **79**, 235333 (2009).
- ¹⁴⁷W. K. Liu, K. J. Goldammer, and M. B. Santos, “Effect of substrate temperature on Si compensation in δ -doped InSb and In_{1-x}Al_xSb grown by molecular beam epitaxy”, [Journal of Applied Physics](#) **84**, 205–208 (1998).
- ¹⁴⁸S. D. Parker, R. L. Williams, R. Droopad, R. A. Stradling, K. W. J. Barnham, S. N. Holmes, J. Laverty, C. C. Phillips, E. Skuras, R. Thomas, X. Zhang, A. Staton-Bevan, and D. W. Pashley, “Observation and control of the amphoteric behaviour of Si-doped insb grown on GaAs by MBE”, [Semiconductor Science and Technology](#) **4**, 663–676 (1989).
- ¹⁴⁹Z. Lei, C. A. Lehner, E. Cheah, M. Karalic, C. Mittag, L. Alt, J. Scharnetzky, W. Wegscheider, T. Ihn, and K. Ensslin, “Quantum transport in high-quality shallow InSb quantum wells”, [Applied Physics Letters](#) **115**, 012101 (2019).
- ¹⁵⁰M. M. Uddin, H. W. Liu, K. F. Yang, K. Nagase, K. Sekine, C. K. Gaspe, T. D. Mishima, M. B. Santos, and Y. Hirayama, “Gate depletion of an InSb two-dimensional electron gas”, [Applied Physics Letters](#) **103**, 123502 (2013).
- ¹⁵¹N. Cabrera, “Mémoires scientifiques rev”, *Metallurgy* **62**, 205 (1965).
- ¹⁵²W. Jesser, J. Matthews, and K. D., “Accommodation of misfit across interface between different gold-platinum alloys”, in *Journal of vacuum science & technology*, Vol. 2, 5 (1965), p. 276.
- ¹⁵³W. D. Callister and D. G. Rethwisch, *Materials science and engineering: an introduction*, Vol. 9 (Wiley New York, 2018).
- ¹⁵⁴M. Siegert and M. Plischke, “Slope selection and coarsening in molecular beam epitaxy”, [Physical Review Letters](#) **73**, 1517–1520 (1994).
- ¹⁵⁵M. Siegert, “Non-equilibrium ordering dynamics and pattern formation”, in *Scale invariance, interfaces, and non-equilibrium dynamics*, edited by A. McKane, M. Droz, J. Vannimenus, and D. Wolf (Springer Science & Business Media, 1995).

APPENDICES

Appendix A

Device fabrication

A.1 van der Pauw

[Van der Pauw \(vdP\)](#) samples were fabricated by soldering a drop of pure indium at each of the four corners of square samples. The soldering gun was pressed for 30 sec for each application to ensure the diffusion of the metal reaches the [quantum well \(QW\)](#) and an Ohmic contact is achieved. The In solder also connects each of the Ohmic contacts directly to one of the pins on the chip carrier and no wire bonding is needed.

Annealing is not necessary to make Ohmic contacts and in fact is desirable to be avoided in case of deteriorating the sample quality, due to the low thermal budget of InSb material systems.

A.2 Hall-bar

The process for fabricating Hall-bar samples is demonstrated by the step-by-step recipe below:

1. Clean the sample

Ultrasonic cleaning

- (a) Acetone 5 min
- (b) Propanal 5 min

2. Mesa definition

- (a) Pattern by photolithography
- (b) Mesa wet etch
 - i. Buffered oxide etch (BOE) 10 sec
 - ii. $3 \text{ H}_2\text{O}_2 : 4 \text{ H}_3\text{PO}_4 : 9 \text{ citric acid} : 44 \text{ H}_2\text{O}$
To a depth of 200 nm below the InSb QW bottom surface
- (c) Strip photo-resists
Acetone + Propanal

3. Definition of Ohmic contacts

- (a) Pattern by Photolithography
- (b) Ohmic wet etch
 - i. BOE 10 sec
 - ii. $3 \text{ H}_2\text{O}_2 : 4 \text{ H}_3\text{PO}_4 : 9 \text{ citric acid} : 44 \text{ H}_2\text{O}$
To a depth of 5 nm below the InSb QW top surface
- (c) O_2 plasma ash
- (d) BOE dip 10 sec
The above two steps ensure a clean surface prior to the metal deposition
- (e) Ohmic deposition
Ti/Au of thickness 20/100 nm
- (f) Lift-off
PG remover ≥ 1 hr

The above recipe completes the fabrication of un-gated Hall bar devices. For fabricating gated Hall bar devices, additional steps need to be taken following the above recipe:

4. Gate dielectric deposition

atomic layer deposition (ALD) of HfO_2 at 150°C

5. Via definition

- (a) Pattern by photolithography
- (b) Via etch
 - BOE with a rate of 1 nm/min
- (c) Strip photo-resists
 - Acetone + Propanal

6. Gate and bond pads definition

- (a) Pattern by photolithography
- (b) HCl dip 10 sec
- (c) Gate and bond pads deposition
 - Ti/Au of thickness 20/100 nm
- (d) Lift-off
 - PG remover \geq 1 hr

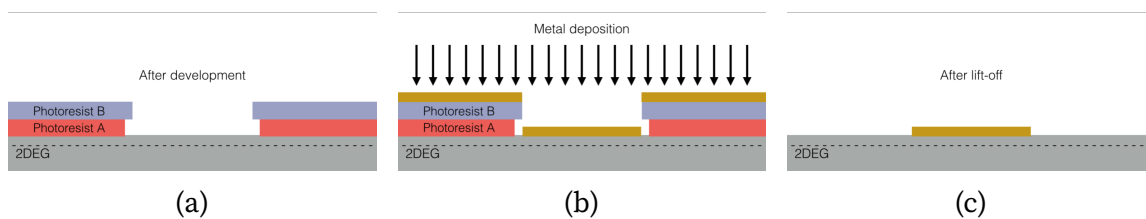


Figure A.1: Schematic illustration of the step-by-step process of Ohmic contact definition, demonstrating the advantageous of the undercut features on the photo-resist sidewalls.

Patterning for mesas, Ohmic contacts, and top gates were all achieved using a stand photolithography process. For the patterning of Ohmic contacts and top gates, a bi-layer of PMGI/S1805 positive photo-resists were used. Due to the faster lateral development rate of PMGI than that of S1805, a large undercut of $\sim 1.5 \mu\text{m}$ can be created on the sidewalls of the developed photo-resists, which ensures the a discontinuous metal deposition and hence a successful lift-off process (Figure A.1). The recipe for the photolithography process using the bi-layer PMGI/S1805 photo-resists is as follows:

1. BOE dip 10 sec

To remove native oxide and improve photo-resist adhesion

2. Spin-coat photo-resists

(a) Bake 5 min at 150 °C

To remove moisture and ensure a good photo-resist adhesion on the surface

(b) Spin PMGI hot

Speed 5000 rpm at a ramp of 1000 rpm/sec for 60 sec

(c) Bake 5 min at 150 °C

To harden the PMGI resist

(d) Spin S1805 hot

Speed 5000rpm at a ramp of 1000 rpm/sec for 60 sec

(e) Bake 90 sec at 120 °C

To harden the S1805 resist

3. Ultraviolet (UV) exposure

25.0 mW/cm² of UV at 365–405 nm for 4.5 sec

4. Develop

MF319 ≤ 4.5 min

5. O₂ plasma Ash 20 sec

To ensure clean edges for the photo-resists

6. Re-flow bake 20 min at 120 °C

To ensure a good photo-resist adhesion after ashing

For mesa and via patterning, no undercut features are needed for the developed resists and a single-layer S1805 positive photo-resist was used. Therefore, Step.2b ‘Spin PMGI hot’ and Step.2c ‘Bake 5min at 150 °C’ were excluded for these processes. Due to the smaller total thickness of the single-layer photo-resist, a shorter develop time was also used.

The low thermal budget of InSb-based material systems prevent the use of thermal annealing to achieve Ohmic contacts. For standard InSb QW structures studied in this thesis, Ohmic contacts to the buried QWs were achieved through a recessed Ohmic wet

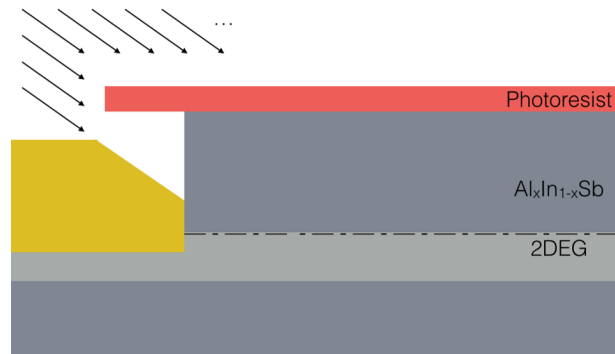


Figure A.2: Schematic diagram showing the 45° deposition of Ti/Au making contact with the sidewalls of the QW in the etched region, where the populated two-dimensional electron gas (2DEG) is indicated by a dashed line.

etching down to ~5nm below the QW surface followed by a quick transfer for an angular deposition of Ti/Au at 45°. Since the recessed Ohmic etch also removes the doping layer and depletes the QW in the etched area, the angular deposition is needed to allow the contact to be made to the populated 2DEG at the sidewalls of the QW in the recessed region (Figure A.2). Similarly the recessed Ohmic contacts were also applied to both the buried QWs and the doped backgate layers in the structures with backgates, as shown in Figure A.3. The Ohmic contacts to the backgate layer were designed off-mesa to avoid the shortage of the QW to the backgate layer through the metal contacts. On the other hand, the angular deposition is not needed for inverted InSb QW structures where the doping layer is below the QW. For InSb surface QWs, Ohmic contacts can be achieved by directly metal deposition on the surface and Step. 3b ‘Ohmic wet etch’ in the above process was omitted.

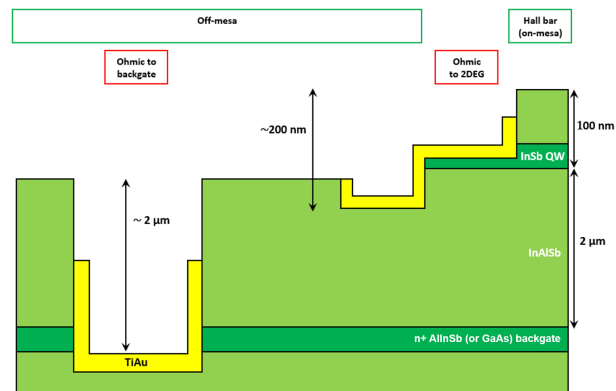


Figure A.3: Schematic diagram showing a finished Hall bar device for a structures with a backgate layer.

Appendix B

Supplementary transport data

Figure B.1 shows the magneto-transport data for the other modulation-doped inverted InSb quantum well (QW) samples included in section 7.2.

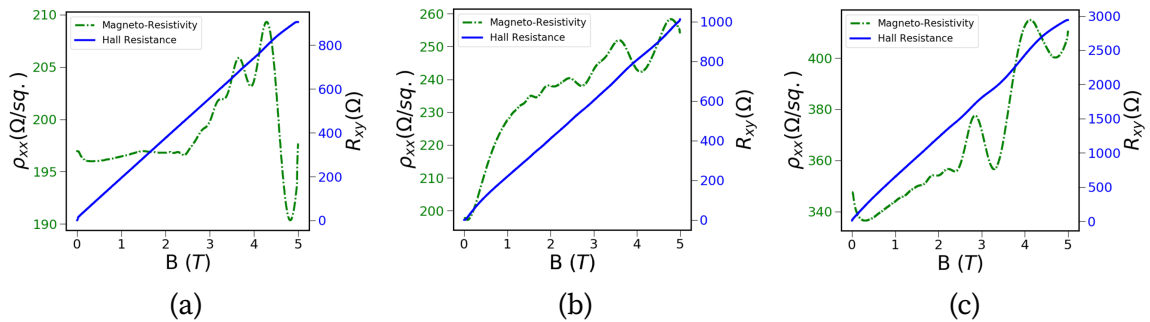


Figure B.1: Plot of the longitudinal resistivity ρ_{xx} (left axis) and the transverse resistivity ρ_{xy} (right axis) as a function of magnetic field B at $T = 1.4$ K for (a) G0381mid, (b) G0383mid, and (c) G0387mid.